The Astbury Centre for
Structural Molecular Biology

UNIVERSITY OF LEEDS

# ANNUAL REPORT 2018

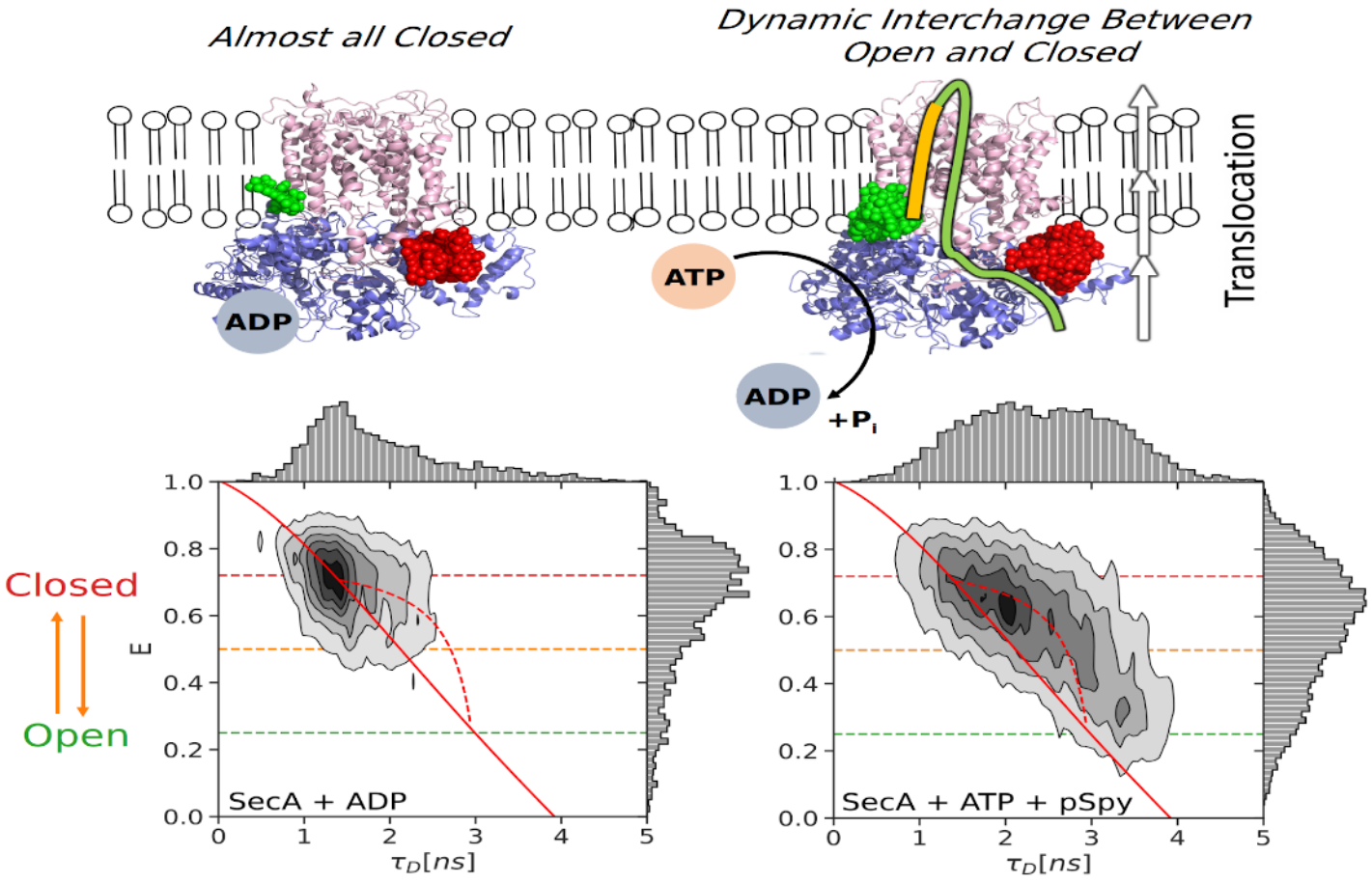

## Front cover illustration

Comparison of joint FRET efficiency and fluorescence lifetime histograms for closed SecYEG:SecA:ADP (left) and translocating complex in the presence of proSpy1 substrate and ATP (right). Top and right sides of each histogram show distribution of lifetimes and FRET efficiencies, respectively. This investigation was a collaboration between Roman Tuma, Joel Crossley, Matthew Watson, Sheena Radford (University of Leeds), and Ian Collinson, Dan Watkins (University of Bristol) and Tomas Fessl (University of South Bohemia).More details can be found on pg 93 of this report.

## Mission Statement

The Astbury Centre for Structural Molecular Biology will promote interdisciplinary research of the highest standard on the structure and function of biological molecules, biomolecular assemblies and complexes using physico-chemical, molecular biological and computational approaches**.**

## Introduction

Welcome to the Annual Report of the Astbury Centre for Structural Molecular Biology 2018. I hope you enjoy reading its contents. It has been yet another busy and successful year for the Centre. The reports in the pages that follow highlight just some of our scientific successes of the last year of our members. We are proud of the strength of our community and our collaborations both locally within the Astbury Centre and University as well as with colleagues from across the globe. I would like to thank every member of the Centre for their hard work over the year: our Support staff, Technicians, Facility Managers, Students, Post-docs, Fellows and Academic staff and, of course, Lucy Gray for her excellent organisation and administrative support. Thank you all.

During 2018 the Astbury Centre continued in its mission to "Understand Life in Molecular Detail" through multiple different activities, including some exciting research discoveries. We continued to enjoy an excellent seminar series (organised by Joe Cockburn), hosting 9 lectures during the year with speakers from the UK and Europe. An inspiring twelfth Annual Astbury Lecture was given by Prof Rick Morimoto, (Northwestern University, Illinois) on the 19th June, entitled "Protein Quality Control and Cell Stress Responses to Protect Cellular Health in Aging and Disease". This annual event was followed by our tradition of a highly competitive sports day and barbecue hosted by the Astbury Society (see http://www.astbury.leeds.ac.uk/about/society.php). On 20th September, 168 members attended the Centre's Biennial Research Away Day held at Headingly Stadium for the first time. The day was a fantastic success and students, post-docs and PIs shared their recent exciting scientific discoveries, through talks, posters and the ever-popular "Flash Poster" presentations. Poster prizes were awarded to Jack Caudwell and Ashley Hancock for the best posters. Well done all! We look forward now to events during 2019, with our 20th birthday and residential retreat in a new location- watch out for an update on these events in the coming months and in next year's report.

The 2018 VC Jordan/PR Radford Prize for the best PhD thesis in the Astbury Centre was awarded to Craig Wilkinson for his thesis "Investigating the catalytic cycle of membrane-bound pyrophosphatases (M-PPases)." performed in Professor Adrian Goldman's laboratory. This annual prize was established in 2017 by a generous donation from Leeds University alumnus Professor Craig Jordan and was presented to Craig by Sir Alan Langmands, Vice Chancellor of the University at the Annual Lecture, http://www.astbury.leeds.ac.uk/prize/.

The Centre welcomed five new PI members in 2018: Rene Frank, Qian Wu, Takashi Ochi, Christos Pliotas (University Academic Fellows) and Yuan Guo (University Lecturer in the School of Food Science). Five research fellows also joined the Centre: Elisabetta Gropelli, Nikesh Patel, Vajinder Kumar, Akshath Uchangi and Jenny Tomlinson (see http://www.astbury.leeds.ac.uk/people/external_fellows.php). We look forward to their involvement in Astbury Centre activities. We were also delighted to welcome our new PhD students and postdocs to the Centre this year, bringing our total number of researchers to >400, including 76 academic staff, 261 PhD students, 99 postdoctoral researchers and 14 Research Fellows.

Astbury Centre members published their research in a wide range of journals in 2018 including Nature Communications, Nature, JACS and Science. A full list can be found at the end of this report. In terms of grant income, Astbury members also enjoyed many successes in 2018. £14M of new project and programme grants brings the Astbury grant portfolio to a striking £69M share of £111.7M of grants: an impressive figure that is testament to the hard work and success of our members. We are much indebted to the funding agencies that support our science, including BBSRC, EPSRC, MRC, the Wellcome Trust, charities, ERC, EU and Industry. We also acknowledge, with thanks, the support of the University of Leeds; the Faculties of Biological Sciences, Maths and Physical Sciences and Medicine and Health, and the Schools of Chemistry, Molecular and Cellular Biology, Biomedical Sciences and Physics and Astronomy for their support of the Centre and our research.

There was continued success in 2018 for members of the Astbury Centre in terms of peer recognition. Adam Nelson was awarded the European Federation for Medicinal Chemistry's 2018 UCB-Ehrlich Award for Excellence in Medicinal Chemistry. The award recognises his implementation of a vision for new chemical synthesis methods to align with drug discovery needs. Our PhD students won a variety of prizes and awards in 2018. Jack Caudwell (Turnbull & Evans group) won a poster prize at the Leeds Microbubble symposium and also won the School of Chemistry postgraduate conference poster conference prize. Emma Cawood (Wilson group) won first prize for her poster at the RSC Chemical Biology and Bioorganic Group Postgraduate Meeting. Kristina Parashiv (Wilson group) won second prize for her poster at the RSC Chemical Biology and Bioorganic Group Postgraduate Meeting. Zsofia Hegedus (Wilson group) won a poster prize at the RSC Peptides and Protein Group Early Stage Research Meeting. Rachel Johnson (Muench group) won a poster prize at the Toronto ACA meeting. Congratulations also go to Ethan Morgan (Macdonald group) who was awarded a WT ISSF award to begin the transition to independent researcher. This funds him for one year to work on his own strand of research, whilst based in the laboratory. Well done all on your wonderful achievements.

The Astbury Centre continued to contribute to public engagement events in 2018 with a significant presence at the 'Be Curious' event in March, 'Light Night Leeds' event in October and the 'One Day At Leeds' event in November. We are currently looking forward to the third Astbury Conversation that will be held at the University of Leeds on 23rd & 24th March 2020 on the topic 'Seeing into Cells' (see https://astburyconversation.leeds.ac.uk). Registration opens in Spring 2019. Do register and join us for a fantastic two days of cutting edge science.

The Astbury Society, led by the presidents David Nicholson and Georgia Pangratiou, played a fantastic role in Astbury activities in 2018. Events included the famous Christmas quiz night, wine and cheese events, and a hugely successful sixth May Ball. With continued fund raising through cake bakes and coffee mornings, the Society continues to support the "Leeds Children's Charity" with donations reaching an impressive £5127 to date. See http://www.astbury.leeds.ac.uk/about/society.php for photos of these events.

I hope that you enjoy reading this Annual Report. Thank you to David Brockwell and Lucy Gray for editing this report, everyone who contributed to it, and all who participated in the Astbury Centre's activities in 2018. The Astbury Centre will celebrate its 20th year in 2019 and we look forward to celebrating this momentous occasion and to continuing our successes in the year ahead.

Sheena E. Radford, FMedSci, FRS

*Director, Astbury Centre for Structural Molecular Biology,*
*Leeds, February 2019*

Please note that this report (as well as those from previous years) is also available as a PDF document which can be downloaded from our website (www.astbury.leeds.ac.uk).

**CONTENTS**

## Contributions indexed by Astbury Centre Principal Investigator

# Understanding the role of light-harvesting proteins in photo-protection and their manipulation for artificial photosynthesis

Ashley Hancock and Peter Adams

## Introduction

Light-Harvesting Complex II (LHCII) is a chlorophyll-protein antenna complex that efficiently absorbs solar energy and transfers electronic excited states to photosystems I and II. Under excess light intensity LHCII can adopt a photoprotective state in which excitation energy is safely dissipated as heat, a process known as Non-Photochemical Quenching (NPQ). In vivo NPQ is triggered by combinatorial factors including transmembrane ΔpH, PsbS protein and LHCII-bound zeaxanthin, leading to dramatically shortened LHCII fluorescence lifetimes. In vitro, LHCII in detergent solution or in proteoliposomes can reversibly adopt an NPQ-like state, via manipulation of detergent/protein ratio, lipid/protein ratio, pH or pressure. Previous spectroscopic investigations revealed changes in exciton dynamics and protein conformation that accompany quenching, however, LHCII-LHCII interactions have not been extensively studied.

## Results and Discussion

Here, we correlated fluorescence lifetime imaging microscopy (FLIM) and atomic force microscopy (AFM) of trimeric LHCII adsorbed to mica substrates and manipulated the environment to cause varying degrees of quenching. AFM showed that LHCII self-assembled onto mica forming 2D-aggregates (25-150 nm width). FLIM determined that LHCII in these aggregates were in a quenched state, with much lower fluorescence lifetimes (~0.25 ns) compared to free LHCII in solution (2.2-3.9 ns). LHCII-LHCII interactions were disrupted by thylakoid lipids or phospholipids, leading to intermediate fluorescent lifetimes (0.6-0.9 ns). To our knowledge, this is the first in vitro correlation of nanoscale membrane imaging with LHCII quenching. Our findings suggest that lipids could play a key role in modulating the extent of LHCII-LHCII interactions within the thylakoid membrane and so the propensity for NPQ activation.

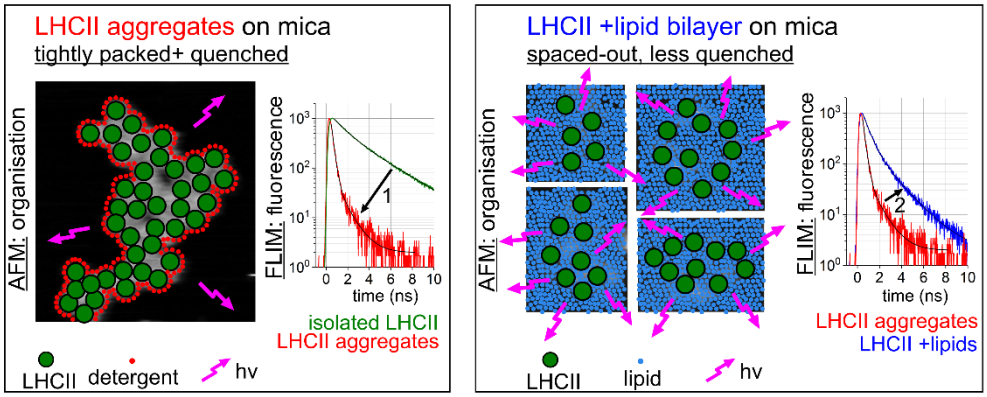


**Figure 1:** LHCII organization and fluorescence quenching. Graphical abstract from the paper referenced below. This shows an AFM height image overlaid with a cartoon display indicating protein arrangement with graphs showing representative fluorescence decay curves.

The combination of chlorophyll and carotenoid pigments within LHCII provide relatively good absorption coverage across the visible spectrum except for a 'green gap' of minimal absorption between 520-620 nm. In an ongoing project, we show that this spectral gap can be effectively filled in a membrane-based assembly of LHCII together with non-covalently incorporated synthetic chromophores (lipid-linked Texas Red). These proteoliposomes (protein-lipid vesicles) act as energy-transferring nanomaterials which offer the modularity to assemble a range of concentrations of donors and acceptors, up to 4% wt/wt Texas Red and 35% wt/wt LHCII, respectively. Our co-assembly procedure effectively mixes both components, shown by fluorescence microscopy images of proteoliposomes that have excellent co-localisation of

signal from our lipids and LHCII (80% and more), suggesting very few protein aggregates or lipid-only vesicles. Donor-to-acceptor energy transfer (FRET) efficiencies up to 95% and a three-fold enhancement of LHCII fluorescence were calculated from bulk steady-state and time-resolved fluorescence spectroscopy data. Membranes could be adhered to surfaces at controlled densities and were found to be optically active, as shown by topographical mapping using atomic force microscopy and photo-bleaching experiments. Energy transfers were investigated at the single-vesicle level by Fluorescence Lifetime Imaging Microscopy (FLIM) and analysis of sub-populations of vesicles suggested that moderate heterogeneities in FRET efficiency are due to variations in LHCII and Texas Red content. In summary, these proteoliposomes provide a platform for controllable distance-dependant energy transfer between synthetic chromophores and native unmodified light-harvesting proteins.

**Publications**

Adams, P.G., Vasilev, C., Hunter, C.N. & Johnson, M.P. (2018) Correlated fluorescence quenching and topographic mapping of Light-Harvesting Complex II within surface-assembled aggregates and lipid bilayers. *BBA, Bioenergetics.* **1859**: 1075-1085.

**Funding**

This work was funded by the BBSRC (fellowship grant # BB/M013723/1 and multi-user equipment grant # BB/R000174/1).

**Collaborators**

*University of Leeds:* Simon Connell, Lars Jeuken
*External:* Cvetelin Vasilev, C. Neil Hunter and Matthew Johnson (University of Sheffield)

## Peroxisome biogenesis and function

Jack Wright, Sophie Moul, Yousef Al Hajaya, Adrian Goldman, Stephen Muench, Stuart Warriner and Alison Baker

### Introduction

Peroxisomes are membrane bound organelles found in almost all eukaryotic cells. They perform a variety of functions which include conserved functions such as β-oxidation of fatty acids and fatty acid-like molecules and reactive oxygen species (ROS) homeostasis, as well as organism and environmentally determined metabolic processes such as photorespiration in photosynthetic cells and methanol metabolism in some yeasts. In humans the critical importance of peroxisomes is underscored by the severe consequences of genetic disorders of the peroxisome. These are divided into biogenesis disorders (Zellweger Syndrome spectrum) where the assembly of the peroxisome is defective, or single gene disorders where a specific enzyme or protein is missing or defective. One example of the latter is X-linked Adrenoleukodystrophy (X-ALD) which is caused by a deficiency in a peroxisome located ABC transporter (ALDP or HsABCD). In X-ALD there is a very poor genotype-phenotype correlation and many mutations lead to reduced levels or absence of protein. The past couple of years have seen extremely rapid progress in the structural biology of ABC transporters but as yet there is no structural information for the peroxisomal subfamily. Furthermore our work and that of others suggest this family may have an unusual mechanism in which their acyl CoA substrate is cleaved and reactivated in the peroxisome.

### Results

A review of recently published ABC transporter structures led us to propose that the widely spaced nucleotide binding domains seen in some ABC transporter structures could be an artefact of detergent solubilisation. We propose the physical properties of the detergent micelle favour a conformation in which the transporter NBDs are spaced widely apart, perhaps due to their behaving like a springe-hinge (Fig 1a black horizontal helix). When reconstituted into nanodiscs; compared to detergent, the more native environment of the nanodisc favours a compact transporter conformation, with NBDs in close proximity Fig 1b). Given that the activity of ABC transporters is generally enhanced when reconstituted into nanodiscs, this conformation is more likely to be physiologically relevant than the wide-open conformation

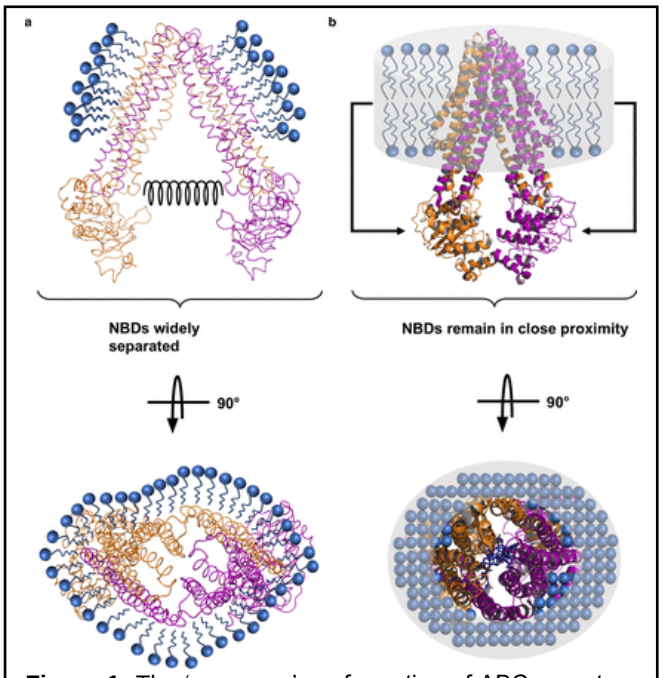


**Figure 1:** The 'open-apo' conformation of ABC exporters may be an artefact of detergent solubilisation. Transporter monomers; purple and orange; detergent; blue, one tail; lipids, blue, two tails; nanodisc annulus, grey halo. This figure was originally published in Wright ltd., 2018.

We are currently working towards a structural determination of the Arabidopsis peroxisomal ABC transporter COMATOSE which is potentially a more stable orthologue of the human protein.

As peroxisome metabolic pathways show a high degree of environmental plasticity we are interested in conserved and differential responses of plant peroxisomes to abiotic stress, since this may impact crop productivity under such conditions. Using a comparative genomics approach we identified 3 groups of proteins: i) those predicted to be delivered to the peroxisome by the major PTS1 signal, ii) PEX genes involved in peroxisome biogenesis, and iii) representative genes of the cellular anti-oxidant network in Arabidopsis, a moss (*Physcomitrella patens*) and

wheat. We showed that genes encoding enzymes involved in β-oxidation and gluconeogenesis were upregulated in response to drought and Abscisic acid (ABA) treatment. ABA is an important plant hormone involved in drought response. It is likely these pathways are involved in production of soluble sugars for respiration or osmotic balance. Peroxisome proliferation was induced by ABA in moss and *PEX3* and *PEX11* genes, key actors in peroxisome proliferation were upregulated and interesting differences were observed between a drought tolerant and drought sensitive wheat cultivar. Catalase also showed conserved upregulation. We are currently investigating the targeting of catalase to peroxisomes and whether this is also regulated under conditions of abiotic stress.

We are additionally looking at developing chemical tools to induce peroxisomal import of proteins lacking a C-terminal PTS1 sequence. These tools have the potential to be used to study specific protein functions and interactions within the environment of the peroxisome. The re-localisation of proteins to peroxisomes from the cytoplasm could be used as a method to modulate their function.

**Publications**

Wright J., Muench S., Goldman A. & Baker A. (2018). Substrate polyspecificity and conformational relevance in ABC transporters: new insights from structural studies. *Biochem, Soc. Trans*. **46**:1475-1484.

Ebeed H., Stevenson S., Cuming A. & Baker A (2018) Conserved and differential transcriptional responses of peroxisome associated pathways to drought, dehydration and ABA. *J. Exp. Bot.* **69**:4971-4985

**Funding**

Work was funded by the BBSRC, Wellcome Trust, Egyptian Mission Sector Ministry of Higher Education and Mu'tah University Jordan.

**Collaborators**

*University of Leeds:* Andy Cuming, Christine Foyer
*External:* Heba Ebeed (Damietta University) and Sean Stevenson (University of Cambridge).

## The structural mechanisms that underpin the regulation of proteins by phosphorylation

Selena Burgess, Manjeet Mukherjee, Mark Richards, Sarah Sabir, Josephina Sampson and Richard Bayliss

### Introduction

Phosphorylation is a common chemical modification of proteins that regulates function through alterations in cellular localisation, biochemical activity, stability, protein-protein interactions, and other mechanisms. Proteomics studies have established there being of the order of 100,000 distinct and known protein phosphorylation sites in a typical human cell. However, there are few examples of structural insights into the molecular mechanisms that underpin the regulation of proteins through phosphorylation. This is partly for a technical reason: the preparation of recombinant proteins that incorporate homogeneous, site-specific phosphorylation suitable for structural studies has been difficult. Indeed, many studies have relied on synthetic production of phospho-proteins, which restricts studies to phosphopeptides of perhaps 20-30 amino acids - for example, studies on the structures of phospho-reader domains (such as SH2). This issue was recently addressed by synthetic biologists, notably Jason Chin at the MRC-LMB, who has developed systems for genetically encoding unnatural amino acids such as phosphoserine and phosphothreonine. We have applied these systems to investigate the mechanisms that underpin phosphoregulation during mitosis, a period in the cell cycle in which there is a peak of serine/threonine kinase activity. Two key families of mitotic protein kinases are the Aurora kinases and the Nek kinases. Although these kinases are known to be critical in mitotic regulation, there have been no reported structures of their substrates in a phosphorylated state. This information is critical in determining the mechanisms by which Aurora and Nek kinases regulate events such as the assembly of the mitotic spindle.

### Results

TACC3 is arguably the best-known substrate of Aurora-A, and we have investigated how TACC3 is recognised by the kinase and the structural consequences of phosphorylation (Burgess, Mukherjee, et al. 2018). Phosphorylation of S558 is required for formation of a robust spindle that is able to segregate chromosomes with minimal errors. TACC3 has a canonical Aurora-A substrate recognition motif that harbours the phosphorylation site S558 (KRxSL). We previously showed that a second mission-critical motif, N-terminal to the phosphorylation site, docks TACC3 to Aurora-A. Here we have determined the crystal structure of the Aurora-A/TACC3 complex, to reveal a binding site that has not been previously implicated in Aurora-A function (Figure 1).

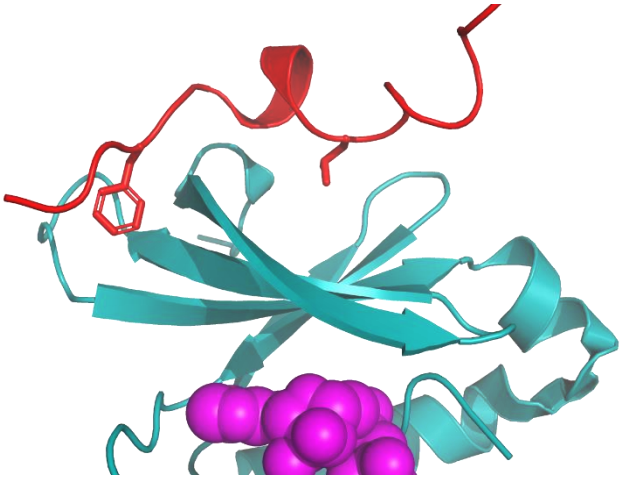

**Figure 1:** Structural basis of the interaction between Aurora-A and TACC3. TACC3 (red) interacts with the N-lobe of the Aurora-A catalytic domain (teal). The two hydrophobic side chains shown (Phe525 and Leu532) of TACC3 interact with hydrophobic pockets on the β-sheet, close to the binding site for ATP/ADP (magenta). The structure was generated from a protein complex comprising aa122-403 of human Aurora-A and aa519-563 of human TACC3, obtained through co-expression in *E. coli*. To prevent phosphorylation of TACC3 by Aurora-A, a mutant kinase was used (D274N), and two further mutations in the kinase (C290A, C393A) were included to improve protein stability. Diffraction data to a limiting resolution of 2.02 Å was collected on beamline I04-1 at Diamond Light Source. PDB code 5ODT.

Phosphorylation of TACC3 on Ser558 drives the formation of a complex with clathrin heavy chain (CHC). During interphase, CHC is a key component of the endocytic machinery.

However, endocytosis is shut down during mitosis and CHC then forms a complex with TACC3. The TACC3-CHC complex binds to microtubules, forming bridges that reinforce these fibres, the loss of which results in weaker spindles. CHC does not possess a known phospho-reader domain, raising the question as to the mechanism by which it recognises phosphorylated TACC3. To address this question, we determined the crystal structure of this complex (Figure 2). The structure revealed an unexpected twist – the region of TACC3 phosphorylated by Aurora-A formed a helix, whereas this region is unstructured in its unphosphorylated state. We confirmed that phosphorylation was the driving force for helix formation, not binding to TACC3, using NMR spectroscopy.

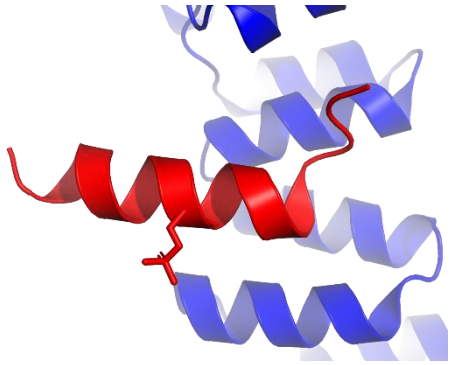

**Figure 2:** Structural basis of the interaction between CHC and TACC3. TACC3 phosphorylated at Ser558 (red) forms an alpha helix that binds between two helices within the ankle region of clathrin (blue). The structure was generated from a chimaeric protein comprising aa1-574 of human CHC and aa549-570 of human TACC3, joined by four repeats of the sequence TGS. The phosphoserine at position 558 of TACC3 was genetically-encoded using a synthetic approach developed by Jason Chin (MRC-LMB, Cambridge). Diffraction data to a limiting resolution of 3.09 Å was obtained using beamline I03 at Diamond Light Source. PDB code 5ODS.

We also investigated the role of phosphorylation in the mitotic regulation of the molecular chaperone Hsp72 (Mukherjee et al., 2018). Hsp72 interacts with exposed hydrophobic peptides within proteins, protecting them from aggregation and helping proteins to fold. Release of hydrophobic peptides from Hsp72 is coupled to the binding of ATP. Nek6 kinase phosphorylates Hsp72 on Thr66, resulting in localisation to the mitotic spindle. At a molecular level, phosphorylation of Hsp72 uncouples ATP binding from peptide substrate release. We generated a crystal structure of the nucleotide binding domain of Hsp72 phosphorylated on residue 66. This revealed that the uncoupling of ATP binding from substrate release is the result of local rearrangements around the phosphorylation site and a network of interactions that connect the phosphate group to an adjacent subdomain.

**Publications**

Burgess S.G., Mukherjee M., Sabir S., Joseph N., Gutierrez-Caballero C., Richards M.W., Huguenin-Dezot N., Chin J.W., Kennedy E.J., Pfuhl M.*, et al.* (2018) Mitotic spindle association of TACC3 requires Aurora-A-dependent stabilization of a cryptic α-helix. *EMBO J* **37**: e97902.

Mukherjee M., Sabir S., O'regan L., Sampson J., Richards M.W., Huguenin-Dezot N., Ault J.R., Chin J.W., Zhuravleva A., Fry A.M.*, et al.* (2018) Mitotic phosphorylation regulates Hsp72 spindle localization by uncoupling ATP binding from substrate release. *Sci Signal* **11**:eaao2464.

**Funding**

This work was funded by the BBSRC and Cancer Research UK.

**Collaborators**

*University of Leeds:* Anastasia Zhuravleva, James Ault
*External:* Jason Chin (MRC-LMB, Cambridge), Fanni Gergely (CRUK Cambridge Institute), Mark Pfuhl (KCL, London), Eileen Kennedy (UGA, Athens, USA), Andrew M Fry (University of Leicester), Stephen J Royle (University of Warwick)

## The interaction of silver nanoparticles with model membranes

Marcos Arribas Perez and Paul Beales

### Introduction

Nanomaterials have wide-ranging potential for applications, including in consumer products and new medicines. Due to the possibility for high levels of human exposure to nanomaterials and their potential toxicity due to their small size, significant focus has been placed on understanding the impacts that nanomaterials may have on living organisms and the environment. However, not all effects are likely to be negative: nanomaterials also hold promise for novel medical therapies where their interactions with biology are advantageous, such as in the formulation and delivery of drugs. The broad parameter space for nanomaterial engineering means that all novel nanoparticles would need to be treated as new entities for screening. In line with the aims of the 3Rs, it would be beneficial to develop a nanoparticle screening platform that could give an early indication of toxicity without proceeding to animal testing. This is the aim of the EU HISENTS project. The HISENTS platform aims to develop a microfluidic screening platform to screen nanoparticle interactions with biomolecular structures, cells and tissue models, where the outputs can be used in a pharmacological model to predict toxicity. One of these modules under development in Leeds is the biomembrane module, consisting of an electrochemical lipid layer on mercury sensor. We are conducting complementary experiments using biophysical membrane models to allow calibration and validation of interactions detected by the HISENTS sensor. One class of particles that we have been using in the early development of this platform are silver nanoparticles, which have established antimicrobial properties that make them of interest for novel therapies and making sterile surfaces.

### Results

Silver nanoparticles have shown very little interaction with the phospholipid layer in the electrochemical biosensor (Fig. 1). These 20-25 nm nanoparticles show no significant changes in the capacitance peaks that are a signature of voltage-induced phase transitions in the structure of the lipid film. Significant interaction with analytes would usually shift the position, height or width of at least one of these peaks.

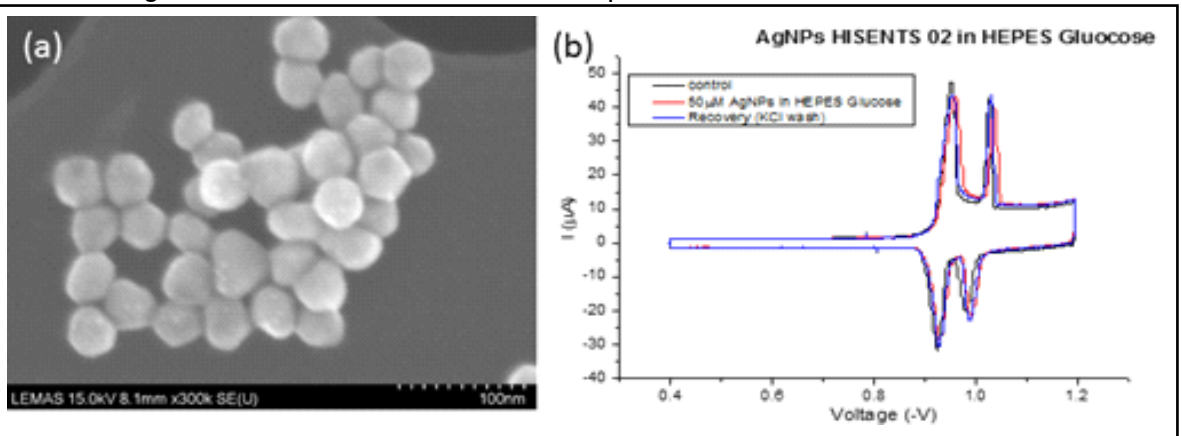


**Figure 1:** Silver nanoparticle interactions on the HISENTS sensor. (a) TEM of silver nanoparticles with an average primary particle diameter of 20-25 nm. (b) Rapid cyclic voltammogram showing no effect of the silver nanoparticles on the capacitance peaks of the lipid layer phase transitions.

Despite not seeing an interaction in the electrochemical sensor, we conducted some high-throughput fluorimetric membrane damage experiments to validate this observation using vesicle membrane models. Interestingly, we found that there were small but significant perturbations of the membrane by the silver nanoparticles, depending on the composition of the solvent environment that the nanoparticles are dispersed in. Sugar-containing buffer solutions tended to stabilise the particles and minimise membrane interaction, but salt-containing buffer had the opposite effect.

The overall interaction of these nanoparticles with vesicle model membranes, even in salt

buffers, saturated well below maximal levels of membrane damage, suggestive that rare, low probability events may occur in these nanoparticle-membrane interactions. Therefore we moved away from ensemble assays that only report average behaviour to use giant unilamellar vesicle (GUV) membrane models that allow microscopy investigation at the single vesicle level. These experiments showed low probability but significant events where the silver nanoparticles could cause membrane leakage, or invagination and vesiculation of the membrane to form new intraluminal vesicles that sequester bulk phase from the external medium (Fig. 2). Early indications from further studies also suggest that the silver nanoparticles may cause a modest increase in membrane tension and small decrease in membrane fluidity.

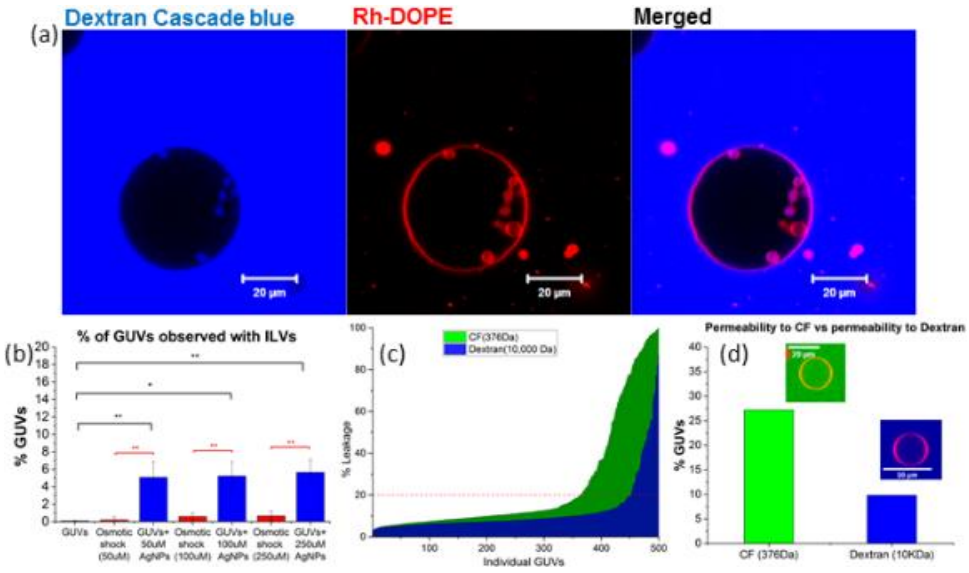


**Figure 2: Interaction of silver nanoparticles with GUVs.** (a) Formation of intraluminal vesicles (ILVs) containing fluorescent dextran from the external medium (blue) suggests curvature-induced membrane remodelling can be facilitated by nanoparticle interactions. (b) The formation of ILVs is a rare event, but significant compared to controls. (c) Membrane damage can also be seen in a sub-population of vesicles as evidenced by the leakage of GUVs to either a 0.3 kDa CF or 10 kDa fluorescent dextran probe. This graph shows the leakage extent of individual GUVs arranged from low to high leakage. (d) The extent of leakage is higher for the smaller leakage marker (CF), but still observed in a minority of GUVs.

In summary, we have found that traditional membrane biophysics approaches can be sensitive to rare events in nanoparticle-membrane interactions that may be below the limit of detection of the HISENTS electrochemical sensor. This might indicate that the interaction of silver nanoparticles with lipid membranes could be weak and transient, but still result in detectable changes in the physical properties of the membrane. However silver nanoparticles are known to have low toxicity, so a negative outcome from the HISENTS sensor could suggest that the system has the potential to discriminate weaker, comparatively harmless interactions from strong, potentially toxic, perturbations to a membrane. Importantly, we find that nanoparticle-membrane interactions are dependent on the solvent environment, which has significant implications for consideration in nanoparticle toxicity screening.

## Publications

Werner M., Auth T., Beales P.A., Fleury J.B., Hook F., Kress H., van Lehn R.C., Muller M., Petrov E.P., Sarkisov L., Sommer J.U. & Baulin V.A. (2018) Nanomaterial interactions with biomembranes: Bridging the gap between soft matter models and biological context. *Biointerphases* **13**: 028501.

## Funding

This work was funded by the EU Horizon2020 programme.

## Collaborators

*University of Leeds:* Andrew Nelson, Nicola William, Alexander Vakurov

## Engineering novel natural products and binding motifs

Ieva Drulyte, Daniel Van, Emily Turri, Adam Nelson and Alan Berry

### Introduction

Natural products form an extensive family of over 200,000 diverse organic molecules discovered and extracted from various plant, animal and microbial sources. Of particular interest are the polyketide, non-ribosomal peptide and isoprenoid classes of natural product since these contribute to the pharmaceutical, cosmetic and biofuel industries. These classes of natural products are synthesised by polyketide synthases, non-ribosomal peptide synthases and terpene synthases, respectively; and our interest lies in understanding the structure-function relationship of these enzymes; facilitating our engineering efforts to synthesise existing, and novel, natural products.

### Structural studies in indanomycin biosynthesis

Indanomycin is an antibiotic active against Gram-positive bacteria, which is produced by a hybrid nonribosomal peptide synthetase-polyketide synthase (NRPS/PKS) from *Streptomyces antibioticus* NRRL 81673. A multi-modular synthase is proposed to produce a linear polyketide which must be modified by 'tailoring' enzymes to complete its final structure. One of these proposed enzymes is IdmH, a putative post-PKS cyclase enzyme, which is thought to catalyze the indane ring formation via a Diels-Alder [4+2] cycloaddition reaction. IdmH was cloned, heterologously expressed and purified. To aid crystallization, we made a mutant of IdmH lacking a flexible loop and solved its crystal structure to 2 Å resolution.

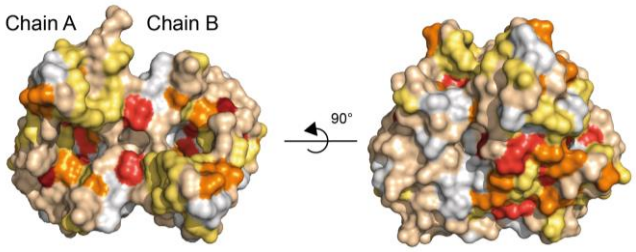


**Figure 1:** NMR chemical shift perturbations (CSP) upon the addition of a ligand (indanomycin) were mapped onto the X-ray structure of IdmH. This identifies a number of changes throughout the structure but highlights active site residues likely to be involved in binding.

We have used NMR to assess whether IdmH can bind the postulated product, indanomycin, and to highlight where the active site might be (Figure 1). Following this, we have used this structure in QM/MM modelling experiments in silico (in collaboration with the University of Bristol) to assess whether IdmH is likely to catalyse indane ring formation via a Diels-Alder reaction. Initial modelling suggests that the structure and proposed catalytic site required for such am mechanism are all present in IdmH, and therefore lends extra weight to the idea that it does indeed represent another enzyme catalyzed Diels-Alderase.

### Structural studies of NRPS/PKS megasynthases

We are interested in elucidating structures of enzymes within biosynthetic gene clusters (BGC). BGC consist of multiple types of proteins involved in the synthesis and release of natural products. NRPSs and PKSs are large proteins that consist of modular domains that come together and form modules. Understanding the structure-function relationship of NRPS/PKS megasynthases is key to understanding why reengineering attempts have been relatively unsuccessful. There are very few structures of modules and therefore we have little understanding of their intramolecular interactions. These large enzymes are a potential source of novel antibiotics. If we can understand their structure-function, we can synthesise novel compounds by taking advantage of their modular nature. We are purifying proteins from the endogenous organisms as well as carrying out recombinant expression in *E.coli* to study them by cryo-electron microscopy and x-ray crystallography. We aim to use the structural data to further our understanding and explain the dynamics of the module to aid in rational protein redesign.

**Engineering selina-4(15),7(11)-diene synthase for novel activities**

In the area of isoprene biosynthesis we have concentrated initial work on the synthesis of selina-4(15),7(11) diene and germacrene B from farnesyl pyrophosphate by the enzyme selina-4(15),7(11)-diene synthase. We are focussing on redesigning the enzyme active site to produce novel activities and novel terpenes. 28 enzyme mutants have been designed and produced using site-directed mutagenesis and screened for altered product profiles to determine their impact on the catalytic reaction. Screening is carried out using gas chromatography, mass spectrometry and novel terpenes are characterized using 2D NMR. The malachite green assay has been adapted to screen the mutants for pyrophosphate cleavage and this has been successfully used on wild type selina-4(15),7(11)-diene synthase. This assay utilizes an inorganic pyrophosphatase, converting pyrophosphate into two inorganic phosphate ions, which consequently form the malachite green complex. The tools are now in place to screen for novel isoprene synthesis by this important class of enzyme.

**Funding**

Our work is funded by BBSRC and The Wellcome Trust.

## Selective TRPC5 channel activation with a xanthine derivative

Aisling Minard, Claudia Bauer, Stuart Warriner and Robin Bon

### Introduction

Transient Receptor Potential Cannonical (TRPC) proteins form non-selective cation channels permeable by $Na^+$ and $Ca^{2+}$. Four TRPC monomers are needed to form a functional ion channel, and channels may consist of homomers or heteromers of subunits, each with their own characteristics and functions. Our work focuses on channels formed by TRPC1, TRPC4 and TRPC5 and their roles in cardiovascular disease. Currently, the best TRPC1/4/5 activator is the natural product (-)-englerin A (EA), which induces strong TRPC1/4/5 currents at nanomolar concentrations. However, its toxicity and instability in rodent serum and in the gastrointestinal tract limit its use for in vivo studies. The most promising TRPC1/4/5 inhibitors are two closely related xanthines, Pico145 and HC-070 (Figure 1A). The compounds exhibit (sub)nanomolar potency against TRPC1/4/5 channels and are highly selective, orally bioavailable and suitable for in vivo studies. Pico145 also distinguishes between different TRPC1/4/5 tetramers, with the highest potency against heteromeric channels. The mechanism by which Pico145 and HC-070 inhibit TRPC1/4/5 channel function is unknown, and a patent describing xanthine-based TRPC5 inhibitors suggests that some xanthines may act as TRPC5 activators instead. Because of the paucity of potent TRPC1/4/5 activators suitable for in vivo studies, and in order to learn more about the remarkable properties of xanthine-based TRPC1/4/5 modulators, we studied the effects of other xanthines on homo- and heteromeric TRPC1/4/5 channels.

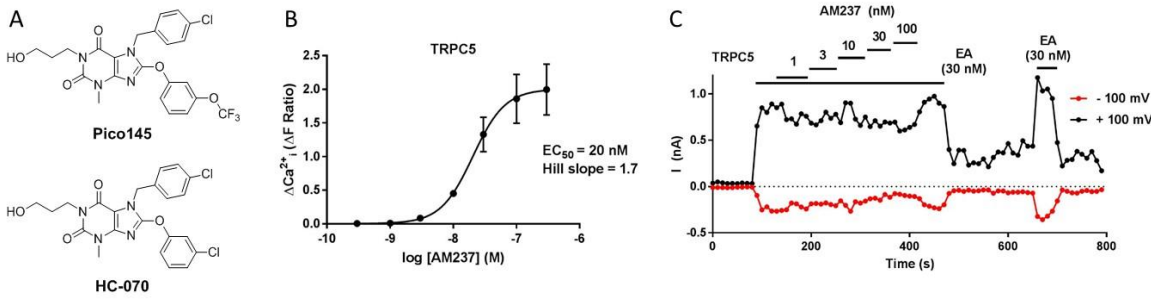


**Figure 1:** A) Structures of the xanthine-based TRPC1/4/5 inhibitors Pico145 and HC-070. B) Concentration-response data for AM237 based on intracellular calcium measurements in HEK cells with fura-2. C) Example outside-out patch clamp data from a hTRPC5-expressing HEK cell showing current sampled at -100 and +100 mV during ramp changes in voltages (all agents were bath-applied).

### Results

We identified several xanthine derivatives, one of which named AM237, that activate homomeric TRPC5:C5 channels (see Figure 1B-C for example data), but inhibit TRPC4:C4, TRPC1:C4 and TRPC1:C5 channels (not shown). Furthermore, Pico145 was a competitive antagonist of AM237 at TRPC5:C5 channels (not shown). This suggests that xanthine-based composition and xanthine substituent pattern, and is consistent with the hypothesis that xanthines bind directly to the channels, through a mechanism different from ion pore blockage. To the best of our knowledge, AM237 is the first TRPC1/4/5 modulator with nanomolar potency that clearly distinguishes homomeric TRPC5:C5 channels from other TRPC1/4/5 tetramers. Therefore, AM237 may be a useful chemical tool to help understand the composition of TRPC1/4/5 channels and the biological roles of specific channels, in different cell types.

### Funding

This work was funded by BBSRC and AstraZeneca.

### Collaborators

*University of Leeds:* Eulashini Chuntharpursat-Bon, Melanie Ludlow, David Beech
*External:* Matthew Burnham (AstraZeneca), Katsuhiko Muraki (Aichi-Gakuin University)

## Recognition of disease mutants of FGFR3 by the Cdc37 co-chaperone

Brendan Farrell and Alex Breeze

### Introduction

Acquired somatic mutations in fibroblast growth factor receptors (FGFRs) are signatures of a number of human cancers, and have been identified as drivers of oncogenic transformation in some tumour types. Several prominent sites for mutation reside in the intracellular tyrosine kinase domain (KD), and act by relieving auto-inhibitory brakes on kinase activity in the absence of growth factor stimulation. However, it is apparent that in some cases these mutations increase dependence of the mutated FGFR on the Cdc37-HSP90 chaperone system, and that this is likely to be due to a reduction in protein stability engendered by the activating mutation. In this study, we sought to identify structural and dynamic features of the KD of FGFR3 that drive the interaction with Cdc37. Thereby, we aim to establish the mechanisms through which Cdc37 is able to discriminate between wild-type KD and disease variants that are 'strong' or 'weak' clients of the co-chaperone, and are thus selected for presentation to the chaperone HSP90.

### Results

In collaboration with colleagues at UCL, MRC LMB (Cambridge) and DESY (Hamburg), we used a combination of structural and biophysical approaches to characterise the interaction between Cdc37 and a disease variant of FGFR3 KD containing a mutation in the 'DFG latch' region (I538F), that we had shown binds with low-μM affinity to Cdc37 and exhibits relatively high levels of occupancy of ternary FGFR3 KD:Cdc37:HSP90 complexes when prepared in vitro. We chose this particular mutant from among several cancer-associated variants with similar properties for reasons of experimental feasibility, as it showed the least impairment of protein expression levels in *E.coli*. Initially, we compared FGFR3$^{I538F}$ with FGFR3$^{WT}$ for levels of deuterium exchange in the presence and absence of Cdc37 using hydrogen-deuterium exchange mass spectrometry (HDX-MS). We found that FGFR3$^{I538F}$ shows significantly increased solvent exchange in the kinase N-lobe, as compared with FGFR3$^{WT}$ (which is almost unaffected) on binding of Cdc37, while some regions of the C-lobe showed slight decreases. These changes are similar to those we also observed for B-Raf$^{V600E}$, another kinase previously studied for its interaction with Cdc37 (Fig. 1).

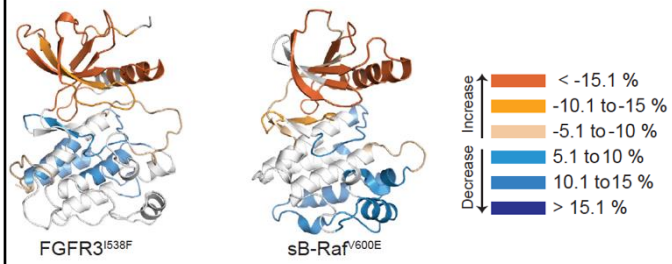


**Figure 1:** Ribbon representations of FGFR3$^{I538F}$ and B-Raf$^{V600E}$ kinase domains with changes in H-D exchange on Cdc37 binding mapped onto them. Peptides with changes >5 % are coloured according to the key.

We then used NMR to further investigate these changes. $^{1}$H-$^{15}$N TROSY-HSQC spectra showed that, compared with FGFR3$^{WT}$, the I538F mutation caused the appearance of additional sharp amide peaks in the random-coil region of the spectrum (Fig. 2A). This implies a degree of localised unfolding that is consistent with the observation that the melting temperature of FGFR3$^{I538F}$ as judged by thermofluor assays is some 10ºC lower than that of FGFR3$^{WT}$ . These same NMR peaks not only matched closely in chemical shift additional peaks induced by the weak binding of FGFR3$^{WT}$ (a weak client; $K_D$ > mM) to Cdc37, but also persisted, and indeed sharpened further, when Cdc37 was added to FGFR3$^{I538F}$ (Fig. 2B & C).

Resonance assignment of these peaks, using a combination of 3D triple-resonance TROSY-based NMR experiments and amino acid-selective $^{15}$N labelling, identified a region at the N-terminal end of the N-lobe as being involved in the transient unfolding of the FGFR3 KD on binding of Cdc37, consistent with the results from our HDX-MS studies. In contrast to the sharpening of these N-lobe peaks, we observed that the majority of the FGFR3$^{I538F}$ KD amide

resonances were strongly broadened in the presence of the co-chaperone, indicative of exchange between free and bound-form conformations on a µs-ms time scale, despite the relatively high affinity of the complex ($K_D$ = 1.8 µM by isothermal titration calorimetry). Analysis by CD spectroscopy indicated that secondary structure is largely conserved on interaction with Cdc37, despite the localised N-lobe disorder we observe by NMR and the changes (both increase and decrease) in solvent exchange rates apparent across the KD from HDX-MS.

Complementary HDX-MS analysis of changes in solvent exposure in Cdc37 on binding to disease-variant FGFR3 KD (in this case, we used the E466K mutant) showed that in contrast to the widespread changes in the client kinase, more limited changes are experienced by the co-chaperone, that are largely restricted to decreased exposure in a small number of regions. These regions are consistent with those previously identified for the interaction between Cdc37 and B-Raf$^{V600E}$ by Keraminsanou et al., implying a common mode of recognition of different kinases on the part of the co-chaperone. Finally, to obtain low-resolution models of the binary FGFR3$^{I538F}$:Cdc37 complex, we used small-angle X-ray scattering (SAXS). Our SAXS envelopes could be fitted to conformations of the complex in which the kinase N-lobe interacts with the N-terminal coiled region of Cdc37 while the C-terminal regions of Cdc37 interact mainly with the C-lobe of FGFR3$^{I538F}$.

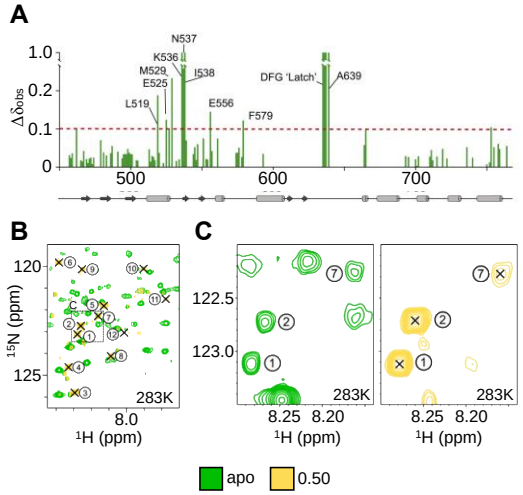


**Figure 2:** (A) Chemical shift perturbation (CSP, Δδobs) analysis of wild-type vs. I538F FGFR3-KD variants. (B and C) Regions of $^{1}H$-$^{15}N$ TROSY-HSQC spectra of FGFR3-KD$^{I538F}$ in *apo* form and in the presence of 0.50 equivalents of unlabelled Cdc37, illustrating random-coil peaks.

Overall, our combined data from multiple structural techniques describe a model in which Cdc37 recognises client kinases (and discriminates between clients and non-clients) by recognising, enhancing and stabilising localised structural disorder in the kinase domain N-lobe. We demonstrate that this model applies to kinases from unrelated families (receptor tyrosine kinases and Ser/Thr kinases), and propose that this represents a common mode of presentation of the client kinase to the chaperone HSP90.

**Publications**

Bunney T.D., Inglis A.J., Sanfelice D., Farrell B., Kerr C.J., Thompson G.S., Masson G.R., Thiyagarajan N., Svergun D.I., Williams R.L., Breeze A.L. & Katan M. (2018) Disease Variants of FGFR3 Reveal Molecular Basis for the Recognition and Additional Roles for Cdc37 in Hsp90 Chaperone System. *Structure* **26**, 446-458.

**Funding**

This work was funded by Cancer Research UK and the Wellcome Trust.

**Collaborators**

*External:* Tom Bunney, Matilda Katan (UCL), Dmitri Svergun (EMBL DESY, Hamburg), Roger Williams (MRC LMB, Cambridge)

## Kinesin-1: Molecular mechanisms of cargo binding and regulation of transport

Sophie Hesketh, Peter Mulhair, Maren Thomsen, Mary O'Connell and Joseph Cockburn

### Introduction

The correct localisation of cellular components is crucial to biological function. Kinesin-1 transports a wide variety of cellular cargoes, including proteins, vesicles, mRNP complexes and organelles, and is implicated in a number of diseases including neurodegeneration, viral and bacterial infections, and cancer. When not bound to cargo, kinesin-1 is autoinhibited to prevent futile ATP hydrolysis. Cargo binding releases autoinhibition, activating microtubule-mediated transport. In animals, kinesin-1 comprises two copies of kinesin heavy chain (KHC), and two copies of kinesin light chain (KLC). In general, cargo binding to both KLC and the KHC tails is required to activate kinesin-1 motility. However, how kinesin-1 binds to multiple, unrelated cargoes, and how these distinct binding events unlock the autoinhibited state, are poorly understood. We have been investigating these issues using the cargo molecules c-Jun N-terminal kinase (JNK) interacting proteins (JIPs) 3 and 4. These proteins function as adaptors that mediate the bidirectional transport of a number of other cargoes by linking them to kinesin-1 and dynein. Kinesin-1-driven motility of JIP3/4 is involved in axonal outgrowth, transport and damage signalling, muscle development, endosomal trafficking, Huntington's disease, and cancer. The JIP3 leucine zipper (LZ) domain binds to the KLC tetratricopeptide-repeat (TPR) domain, inducing an immotile microtubule-bound intermediate. Binding of the JIP3 N-terminal region to the KHC tails then triggers transport. Kinesin-1 recruitment by JIP3/4 is regulated by the GTPase ARF6, which binds to the JIP3/4 LZ domain and prevents KLC binding.

### Results

To investigate the molecular basis for kinesin-1 recruitment and activation by cargoes, we solved the crystal structure of the KLC2 tetratricopeptide-repeat (TPR) domain bound to the JIP3 LZ domain (Fig. 1). The structure revealed a new cargo-binding site on the KLC TPR domain, located on TPR1, conserved in KLC homologs from sponges to humans. Comparison of the structure with the previously solved structure of the JIP4 LZ domain bound to ARF6 revealed how a single copy of active, membrane-anchored ARF6 regulates KLC binding to both sites on the LZ domain. In the crystal structure of the KLC2:JIP3 complex, JIP3 cross-links two KLC2 TPR domains via their TPR1s. Analysis of the available crystal structures of the unbound, intact KLC TPR domain revealed a conserved dimer interface that mimics JIP3 binding. We proposed that cargo-induced dimerisation of the KLC TPR domains via TPR1 is a general mechanism for activating kinesin-1. We related this to activation by tryptophan-acidic cargoes, explaining for the first time how different cargoes activate kinesin-1 through related molecular mechanisms. Our evolutionary analysis also revealed that the cargo-binding and regulatory sites on mammalian KLC evolved at the Bilaterian split, suggesting that allosteric regulation of KLC and its ability to bind to multiple cargoes may have been important for the evolution of Bilaterian body plans and tissues.


**Figure 1:** The KLC2:JIP3 complex

### Publications

Cockburn J.J.B., Hesketh S.J., Mulhair P., Thomsen M., O'Connell M.J., Way M. (2018) Insights into kinesin-1 activation from the crystal structure of KLC2 bound to JIP3. *Structure* **26 (11)**, 1-13.

### Funding

The University of Leeds, BBSRC, The Wellcome Trust and The Royal Society.

## Water clustering drives temperature-dependent segregation in alcohol-water mixtures

Samuel Lenton, Natasha Rhys, James Towey and Lorna Dougan

### Introduction

The importance of hydrogen bonds can be observed in complex solutions such as those containing biological macromolecules or polymers. However, here, we focus on simple alcohol systems, as a model, to provide information about the effect of changing the nonpolar chain on the hydrogen bond network in solution. When two liquids mix, the ideal entropy of the mixture, which is calculated by assuming that the two liquids can completely interpenetrate, has to be greater than the sum of entropies of the pure components on their own. This is because excess work would need to be done on the mixture once it is formed to render it unmixed. In practice, molecular forces between the components can alter the actual mixed-state entropy either above or below the ideal value. In the case of a number of alcohol–water binary mixtures, the excess entropy of mixing is negative compared to the ideal mixing value. Explanations for this negative excess entropy of mixing go back to at least 1945, when Frank and Evans suggested that it indicated some sort of reordering in the solution, and proposed a model of water restructuring itself in an ice-like manner around the hydrophobic sidechains. How this ordering manifests in practice has been the subject of an extensive debate.

### Results

To study the structure of water and alcohol mixtures we exploit the power of neutron diffraction at the ISIS Facility, Rutherford Appleton Laboratories (Figure 1). We use a combination of neutron diffraction with hydrogen isotope labeling and analysis by empirical potential structure refinement (EPSR) to study segregation in binary solutions and the effect of reducing the temperature on cluster formation. The neutron diffraction experiment provides unique information about the hydrogen bonding network by exploiting the difference in neutron scattering lengths between different isotopes of hydrogen, giving direct information about how hydrogen atoms are coordinated in solution.

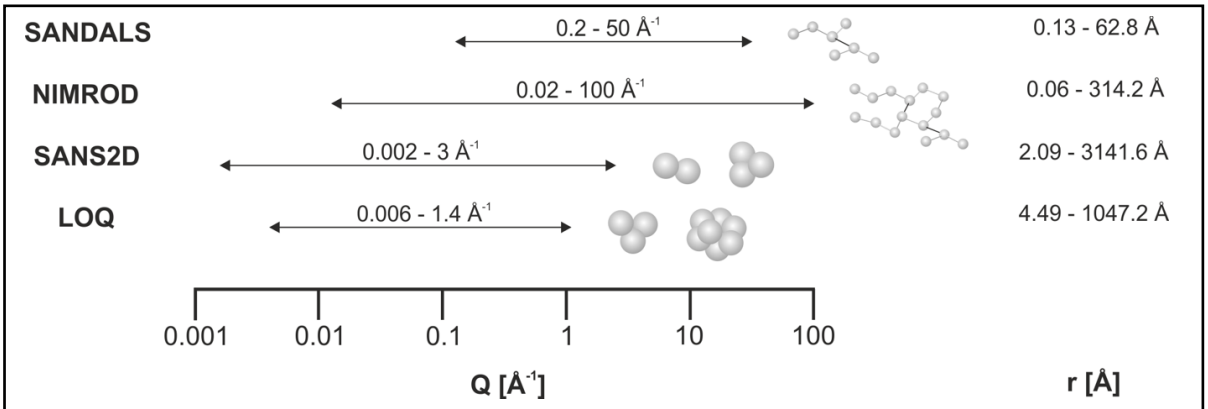


**Figure 1:** A comparison of the Q-range covered by the instruments at ISIS that can probe the structure of biological matter in solution. Whilst SANS instruments such as SANS2D and LOQ can determine bulk structure and the ability of small molecules to associate, diffractometers such as SANDALS and NIMROD aim to study the atomic level interaction of small and larger biomolecules respectively in solution.

Our previous neutron scattering work, combined with computer simulated structure analysis, has established that binary mixtures of methanol and water partially segregate into water-rich and alcohol-rich components. It has furthermore been noted that, between methanol mole fractions of 0.27 and 0.54, both components, water and methanol, simultaneously form percolating clusters. This partial segregation is enhanced with decreasing temperature. The mole fraction of 0.27 also corresponds to the point of maximum excess entropy for ethanol–water mixtures. Here, we studied the degree of molecular segregation in aqueous ethanol solutions at a mole fraction of 0.27 and compare it with that in methanol–water solutions at the same concentration. Structural information is extracted for these solutions using neutron diffraction coupled with empirical potential structure refinement. We show that ethanol, like methanol, bi-percolates at this concentration and that, in a similar manner to methanol, alcohol segregation, as measured by the proximity of neighboring

methyl sidechains, is increased upon cooling the solution (Figure 2). Water clustering is found to be significantly enhanced in both alcohol solutions compared to the water clustering that occurs for random, hard sphere-like, mixing with no hydrogen bonds between molecules. Alcohol clustering via the hydrophobic groups is, on the other hand, only slightly sensitive to the water hydrogen bond network. These results support the idea that it is the water clustering that drives the partial segregation of the two components, and hence the observed excess entropy of mixing.

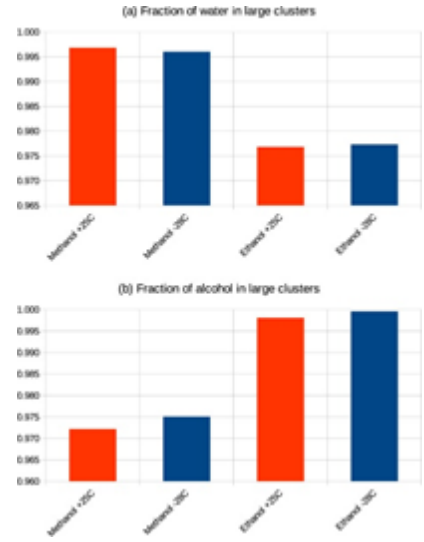


**Figure 2:** To obtain information on the degree of molecular segregation in these solutions, we use cluster size analysis on the water and alcohol molecules in solution. For clusters involving only water molecules, two water molecules were considered to belong to the same cluster if their Ow–Ow distance was less than 3.3 Å, whereas for alcohol clusters, the criterion was for their respective C1 (or C2 in the case of ethanol) atoms, that is the hydrophobic sidechains, to be 5.0 Å or less apart. These distances are determined from the position of the first minimum after the main peak in the corresponding RDF. The bar chart shows the fractions of water (a) and alcohol (b) molecules in large (>100 molecules) clusters at two temperatures in the methanol-water and ethanol-water solutions. For both alcohols, the number of large water clusters increases at low temperature. The temperature-dependent segregation in alcohol-water mixture is driven by water clustering.

## Publications

Lenton S., Rhys N., Towey J., Soper A. & Dougan L. (2018) *Journal of Physical Chemistry B*, **122**, 7884.

## Funding

This work was funded by the European Research Council, Extreme Biophysics 258259

## Collaborators

*External:* Alan Soper (ISIS Facility, Rutherford Appleton Laboratories)

# Structure and function of the Human Respiratory Syncytial Virus proteins M2-1 and P

Muniyandi Selvaraj, Kavestri Yegambaram, Eleanor Todd, Rachel Dods, Georgia Pangratiou, Chi Trinh, Sophie Moul, James Murphy, Jamel Mankouri, John Barr and Thomas Edwards

## Introduction

The negative-stranded RNA virus Human respiratory syncytial virus (HRSV) is a leading cause of respiratory illness, particularly in the young, elderly, and immunocompromised, and has been linked to the development of asthma. HRSV replication depends on the phosphoprotein (P) and polymerase (L), whilst transcription also requires M2-1. M2-1 interacts with HRSV-P and RNA at overlapping binding sites. Whilst these interactions are necessary for transcriptional activity, the mechanism of M2-1 activity is unclear. To better understand HRSV transcription, we solved the crystal structure of M2-1 in complex with the minimal P interaction domain, revealing molecular details of the M2-1/P interface and defining the orientation of M2-1 within the tripartite complex. The M2-1/P interaction is relatively weak, suggesting high-affinity RNAs may displace M2-1 from the complex, providing the basis for a new model describing the role of M2-1 in transcription. Recently, the small molecules quercetin and cyclopamine have been used to validate M2-1 as a drug target.

## Results

HRSV multiplication depends on the replication and transcription of HRSV genes by the virus-encoded RNA-dependent RNA polymerase (RdRp). For replication, this complex comprises P and L proteins. For transcription, M2-1 is also required. M2-1 is recruited to the RdRp through its interaction with HRSV-P. M2-1 binds RNA at overlapping binding sites on the M2-1 surface such that binding of these partners is mutually exclusive. The molecular basis for the transcriptional requirement of M2-1 is unclear, as is the consequence of competition between P and RNA for M2-1 binding, which is likely a critical step in the transcription mechanism. Here, we report the crystal structure at 2.4 Å of M2-1 bound to the P interaction domain, which comprises P residues 90 to 110. The $P_{90–110}$ peptide is alpha helical, and its position on the surface of M2-1 defines the orientation of the three transcriptase components within the complex. The M2-1/P interface includes ionic, hydrophobic, and hydrogen bond interactions, and the critical contribution of these contacts to complex formation was assessed using a minigenome assay. The affinity of M2-1 for RNA and P ligands was quantified using fluorescence anisotropy, which showed high-affinity RNAs could outcompete P. This has important implications for the mechanism of transcription, particularly the events surrounding transcription termination and synthesis of poly(A) sequences.

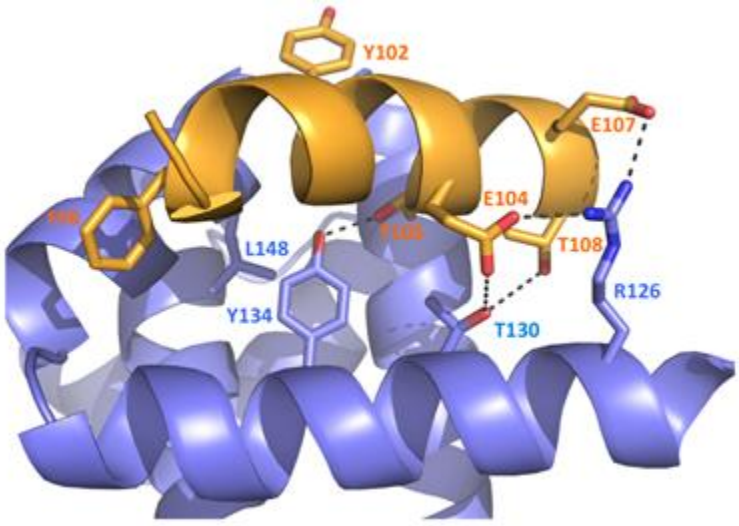


**Figure 1:** Details of M2-1/P electrostatic interactions as revealed by the M2-1/P90–110 co-crystal structure. M2-1 residues are labelled in blue, and P peptide residues are labelled in orange. Hydrophobic residues mutated in replicon experiments are also highlighted.

One possible functional role of M2-1 is that the protein plays a stimulatory role in mRNA polyadenylation. Perhaps the 3′ end of a nascent transcript interacts with M2-1, which in turn induces the P/L RdRp complex to switch from a processive templated polymerization mode into a reiterative polymerization mode, in which the short gene end U-tract is repeatedly copied to generate the 3′ poly(A) tail. Such a role would be consistent with previous reports of truncated mRNAs detected in the absence of M2-1, as tail-less RNAs would be rapidly degraded. Further structural, biochemical, and cellular investigations of M2-1 and its binding partners will aid in resolving these critical questions surrounding the role of M2-1 in HRSV gene expression.

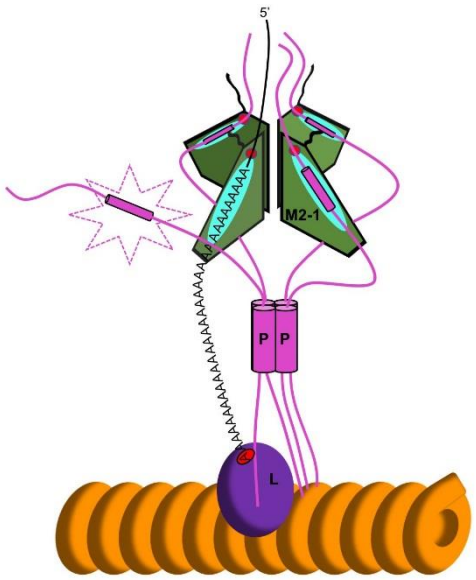


**Figure 2:** Schematic representation of the interaction between M2-1 and P in the context of the transcribing HRSV polymerase complex. The orange helix represents RNP. L (purple) and P (pink) form the complex that generates mRNA. M2-1 (green) is recruited to the complex via P. The P90–110 peptide is displaced from one of the P binding sites on M2-1 by A-rich RNA.

## Publications

Selvaraj M., Yegambaram K., Todd E., Richard C.A., Dods R.L., Pangratiou G.M., Trinh C.H., Moul S.L., Murphy J.C., Mankouri J.*, et al.* (2018) The structure of thehumanrespiratory syncytial virus m2-1 protein bound to the interaction domain of the phosphoprotein p defines the orientation of the complex. *MBio* **9**:e01554-18.

## Funding

This work was funded by the Wellcome Trust, BBSRC, the University of Leeds and the MRC.

## Collaborators

*External:* Charles-Adrien Richard and Jean-François (Éléouët. Unité de Virologie et Immunologie Moléculaires (UR892), INRA, Université Paris-Saclay, Jouy-en-Josas, France)

## Raman spectroscopy is a promising technique for the study of photodynamic therapy on colorectal cancer

Julia Gala de Pablo, Fern Armistead, Sally Peyman and Stephen Evans

### Introduction

Less than half of patients with colorectal cancer will survive the disease, and around one in five of the tumours of diagnosed patients have metastasis. Understanding how cancer develops and progresses can help defeat it. Understanding the links between biochemical changes and pathology represents a major challenge in cancer research. Raman confocal microspectroscopy is a label-free technique that can obtain information about the composition of a sample without damaging it, where a laser spot is focused onto live single cells to prove the vibrations of their molecules and obtain their spectra.

Photodynamic therapy is a cancer treatment that uses photosensitizing drugs along with light. The drugs selectively accumulate in cancerous cells and can then be activated by using special light onto the cells, killing the cancer cells but sparing the surrounding tissue. These treatments have shown very promising results with colorectal cancer, and some of these agents have also strong Raman signals. The aim of this project is to use Raman to understand the different spectral signatures of colorectal cancer cell lines and for detection of photodynamic drugs on colorectal cancer cells.

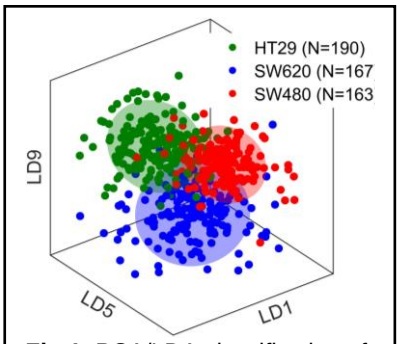


**Fig 1**: PCA/LDA classification of CRC adenocarcinoma cells from Duke's B stage (SW480), Duke's C stage (HT29) and Duke's C metastasis (SW620).

### Results

Here, cell lines derived from different stages of colorectal adenocarcinoma – from a primary tumour to a metastasis (SW480, HT29, SW620) – were measured using Raman and compared. Hundreds of single cells were measured using Raman and their spectra showed differences in the chemical composition of the cells, aiding the search of biomarkers that could be used for diagnosis of patient's samples. As shown in Figure 1, the cells showed biochemical differences and could be classified with >92% accuracy. Two bands – labelled as lipids and lactate - appeared to be dependent on the colorectal adenocarcinoma stage, and were labelled as possible biomarkers that will need to be confirmed in patients.

Further experiments were done to detect the novel photosensitizer DC473, that shows a very specific Raman signal thanks to the presence of two alkyne groups in its structure. To understand its photosensitizing effects, DC473 was chemically imaged within a fixed SW480 cell confirming its presence in the cytosol and in lipid droplets, and showing presence inside the nucleus. Fig. 2 shows the Raman mapping results when imaging the intensity of different bands for a cell with DC473 and a control cell with DMSO. Due to its solvatochromatic properties, information about the

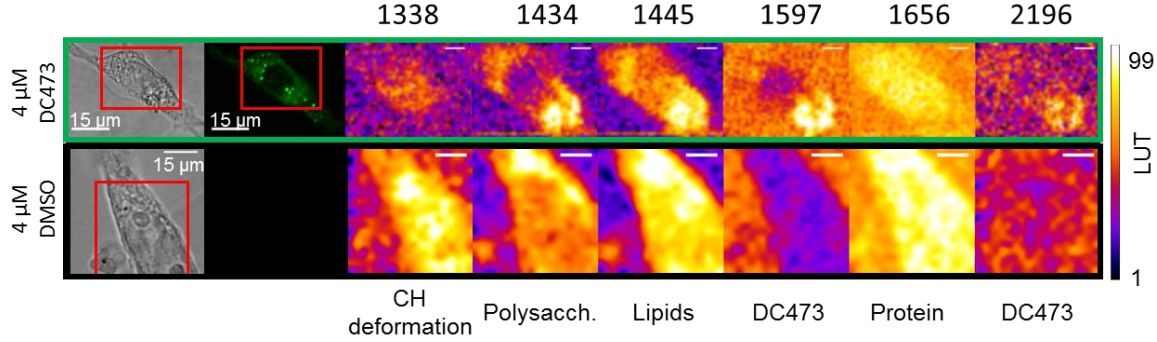


**Fig 2**: Raman mapping on a cell treated with DC473 or with an equivalent amount of DMSO as a control. DC473 could be tracked using the 1597 and 2196 $cm^{-1}$ bands, showing strong presence in vesicles around the nucleus. This correlates with the fluorescence data. Other information such as lipid, protein or polysaccharydes could be obtained in a label free manner and could be correlated with the drug location.

polarity of each of these locations was also obtained. Results show that Raman spectroscopy has great potential for single-cell cancer progression and drug treatment studies, in particular with photodynamic therapy agents.

## Publications

De Pablo J.G., Armistead F.J., Peyman S.A., Bonthron D., Lones M., Smith S. & Evans S.D. (2018) Biochemical fingerprint of colorectal cancer cell lines using label-free live single-cell raman spectroscopy. *J Raman Spectrosc* **49**:1323-1332.

De Pablo J.G., Chisholm D.R., Steffen A., Nelson A.K., Mahler C., Marder T.B., Peyman S.A., Girkin J.M., Ambler C.A., Whiting A.*, et al.* (2018) Tandem fluorescence and raman (fluoraman) characterisation of a novel photosensitiser in colorectal cancer cell line SW480. *Analyst* **143**:6113-6120.

## Funding

This work was funded by MRC grant (MR/M009084/1), the NIHR grant (MIC-2016-004) and the EPSRC PhD grant (EP/P023266/1).

## Collaborators

*External:* Michael Lones (School of Mathematical and Computer Sciences, Heriot-Watt University), Stephen Smith (Department of Electronics, University of York), David R. Chisholm, John M. Girkin, Carrie A. Ambler and Andrew Whiting (LightOx Limited and Department of Chemistry, Durham University), Andreas Steffen, Amanda K. Nelson, Christoph Mahler and Todd B. Marder (Institut für Anorganische Chemie, Julius-Maximilians-Universität Würzburg).

## Lipid coated liquid crystal droplets for the on-chip detection of AMPs

Peng Bao, Daniel Paterson, Patrick Harrison, Keith Miller, Sally Peyman, Cliff Jones, Jonathan Sandoe, Richard Bushby, Helen Gleeson and Stephen Evans

### Introduction

For many decades, liquid crystal (LC) materials have been widely used in industry for LC display (LCD) applications, due to their well-known electrooptic modulation effects. More recently, LC materials have shown great potential in the field of biosensors. They have been demonstrated for the successful detection of surfactants, lipids, heavy metals, glucose, enzymes, volatile organic compounds, DNAs and proteins, bacteria/mammalian cells and antigens. Recently, LC biosensors have also been demonstrated useful for the detection of cationic antimicrobial peptides (AMPs). Here, we are using Smp43 as a model peptide to develop LC based biosensors for the detection of AMPs utilizing a lipid coated liquid crystal droplet using a mechanism shown schematically in Figure 1. Monodisperse lipid-coated liquid crystal droplets were produced using a microfluidic approach and confined in a trap structure that allowed gradients of AMPs to be flowed across the LC droplets in a controlled way. Smp43 was used at different (micromolar) concentrations and the switching of LC droplets from radial to bipolar configurations was demonstrated by in-situ polarized optical microscopy.

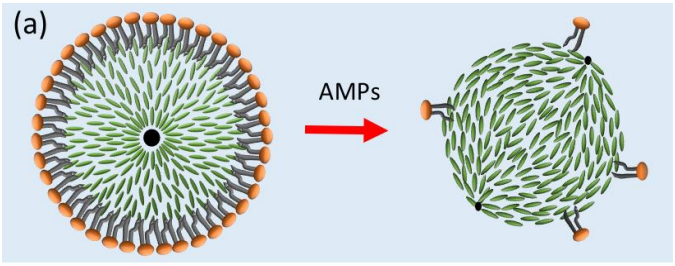


**Figure 1:** Schematic diagram showing the bio-sensing mechanism. The lipid coating on the liquid crystal droplet initially induces a radial director geometry. Exposure to the AMP removes the lipid coating, inducing a planar surface alignment and bipolar droplet geometry. LC molecules: green rods.

### Results

Monodisperse lipid-coated droplets (diameter = 17 μm) were produced using a flow focus droplet microfluidic device [35]. A schematic diagram of the droplet formation process in the device is shown in Figure 2(a). The liquid crystal material (E7) entered the nozzle and was pinched-off by the buffer solution surrounding it due to the shear force.[35]. Lipid vesicles in solution adsorbed and ruptured at the hydrophobic LC /water interface to form a monolayer on the surface, Figure 2 (a) and (c).

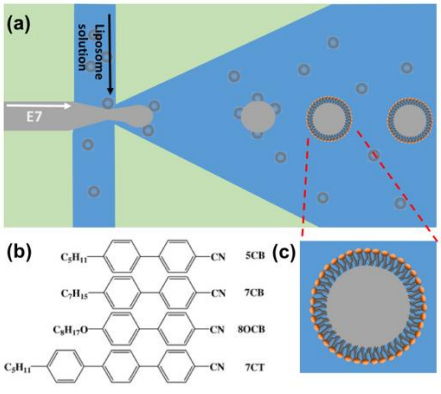


**Figure 2:** (a) Schematic of the microfluidic device used to form lipid-coated E7 droplets. (b) The molecular structure of the compositions in the mixture of E7. The weight percentages are 51%, 25%, 16%, and 8%, respectively. (c) The schematic diagram of the lipid coated LC droplet.

For the *in-situ* observation of the radial to bipolar switching of droplets on exposure to Smp43, we deployed our novel trap structure with its concentration gradient generator on a single chip, as shown in Figure 3. After the LC droplets were trapped in the device, the droplet inlet was blocked and the buffer inlet and Smp43 inlet were connected, feeding the device with buffer and Smp43 at a flow rate of 0.4ul/min. The concentration of SMP43 was 6 μM at the Smp43 inlet. After the concentration gradient generator, the concentration of Smp43 in the different trap chambers was 6, 4.8, 3.6, 2.4, 1.2, and 0 μM (from top to bottom in Figure 3).

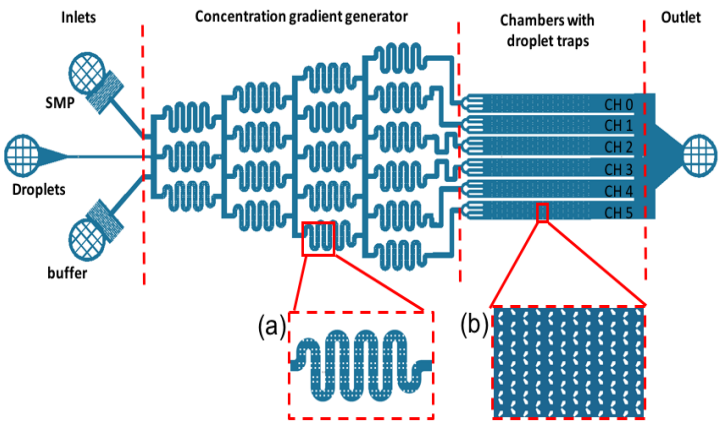


**Figure 3:** The trap structure with a concentration gradient generator used to evaluate the Smp43 detection by the lipid-coated LC droplets. The device has four main parts: inlets, concentration gradient generator, chamber with droplet traps, and outlet. (a) an expanded view of the serpentine channel and pillars in the channel to promote mixing; (b) an expanded view of the trap region indicating how the droplets are trapped in the swallowtail features.

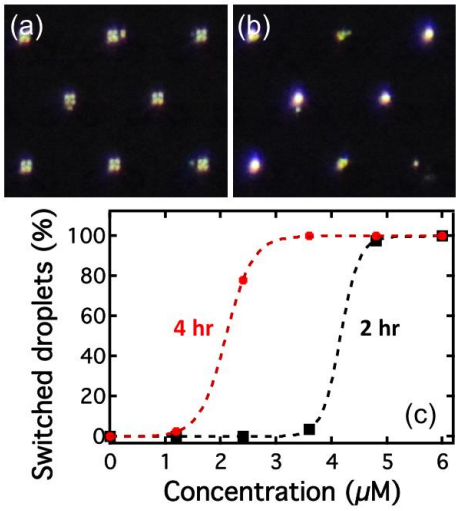


**Figure 4:** (a) and (b) are typical images of arrays of droplets in traps under polarizing microscopy before and after Smp43 (4.8 μM) treatment, respectively. The images clearly show the switching from radial to bipolar states ((a) and (b) respectively). (c) The percentage of switched LC droplets, after two hours (black squares) and four hours (red dots) as a function of Smp43 treatment at different concentrations. The dashed lines are fits to these two sets of data using Sigmoid function. In this case, the concentrations that show full switching are 4.8 and 3.6 μM for the two-hour and four-hour treatment, respectively.

Initially, all the droplets had the Maltese cross birefringence pattern indicative of a radial structure, Figure 4(a). As the droplets are exposed to the Smp43, they begin to change appearance with the crossed patterns first transforming to an irregular texture before exhibiting a birefringence pattern characteristic of a bipolar structure, Figure 4(b). The percentages of the droplets that had switched director orientation at two hours in the different chambers are shown as the black squares in Figure 4 (c). After 2 hours, almost all of the droplets rinsed with Smp43 at concentrations of 4.8 and 6 μM had switched from the radial to the bipolar state (98% and 100% respectively.), Figure 4 (c). However, only 4% of droplets exposed to the 3.6 μM Smp43 had switched and for lower concentrations of Smp43, no switching was detected. The data suggested that the detection limit for Smp43 by the lipid-coated E7 droplets was 4.8 μM at two hours. After four hours of exposure (red circles in Figure 4(c)), more droplets in the chambers (with Smp43 concentration of 2.4 and 3.6 μM) had switched to bipolar state causing most or all of the droplets to change configuration. The detection limit at four hours was 3.6 μM.


## Funding

This work was funded by the EPSRC(EP/P024041/1).


## Collaborators

*External:* P. L. Harrison (Department of Chemistry and Biochemistry, University of Hull), K. Miller (Biomolecular Research Centre, Sheffield Hallam University, Sheffield)

## Development of Small Molecule Inhibitors of Ebola Virus Genome Replication

Martin McPhillie, Victoria Easton, Sam Stephen, John Barr, Thomas Edwards, Richard Foster, Mark Harris and Colin Fishwick

### Introduction

EBOV was first identified in 1976 and has caused sporadic outbreaks in remote villages in Central Africa since then. The global importance of the virus came into sharp focus with the 2014-2016 major outbreak in West Africa which involved both urban and rural areas. This outbreak resulted in 28,000 confirmed cases and more than 11,000 deaths with a small number occurring outside West Africa indicating the potential for world-wide spread. Although that outbreak was successfully contained, the very recent 2017 outbreak in Democratic Republic of Congo reinforces the need for an effective response to inevitable future outbreaks. In this regard, an efficacious small molecule inhibitor of EBOV replication that had broad range activity against multiple different strains of the virus would be a valuable component of an emergency preparedness strategy. If used therapeutically at an early stage (e.g. at first sign of symptoms), it would have the potential to reduce both the clinical severity of disease and duration of infection, thereby directly impacting the health of infected individuals and limiting the transmission of the virus.

### Results

The EBOV viral genome encodes for seven proteins, of which the nucleoprotein (NP), VP35 and VP30 cofactors and the RNA polymerase are required to form a complex that transcribes and replicates the EBOV genome. This complex is essential for genome replication and viral pathogenesis, and therefore an attractive target for drug development. The protein-protein interaction (PPI) between VP35 and NP is a critical component of the complex and has recently been characterised using X-ray crystallography (Fig 1A). Such detailed structural information allowed us to apply our computer-aided drug design (CADD) expertise to design small molecules targeted to the EBOV NP. Within the hydrophobic interface between NP and VP35, three 'hotspots' (Fig 1B) were identified that were amenable to CADD techniques. Each 'hotspot' region contained a suitable hydrophobic pocket with the potential to make hydrogen-bonding interactions with putative ligands.

A virtual screening cascade was setup to evaluate a number of commercially available 'drug-like' small molecules predicted to bind with high affinity for a number of 'hotspots'. A number of candidate molecules (150) were identified using eHiTS and AutoDock software and were subjected to a robust screening cascade starting with an EBOV mini-genome (MG) assay coupled with assessment of cytotoxicity. As the readout of the MG assay is firefly luciferase (Fluc), compounds are simultaneously screened for any effects on EBOV-independent Fluc expression.

After a triage process, four compounds were identified that exhibited robust inhibition of EBOV RNA synthesis (<4 μM $EC_{50}$ values) with low cytotoxicity. Computational analysis of the four compounds revealed that they share a common binding mode (in 3/4 cases) by traversing 'hotspots' 1 & 2 (Fig 1C). The four compounds represent distinct chemical series and further chemical development was performed via structure-activity relationship (SAR) studies which resulted in some significant improvements in both $EC_{50}$ and selective index ($EC_{50}$ ratio vs cytotoxicity). Mutational analysis of the residues close to or within 'hotspots' 1-3 confirmed target identification in some cases (Fig 1D).

In summary, we have identified four distinct series of small-molecular inhibitors of EBOV gene expression via a suite of CADD tools. Our inhibitors also have good selectivity indices (SI) with no activity against a Fluc control, and low cytotoxicity and as such are regarded as validated hits. We are now conducting hit-to-lead studies and complementary biophysical assays which will aim at progressing one or more of these series into lead antivirals by providing unambiguous target identification

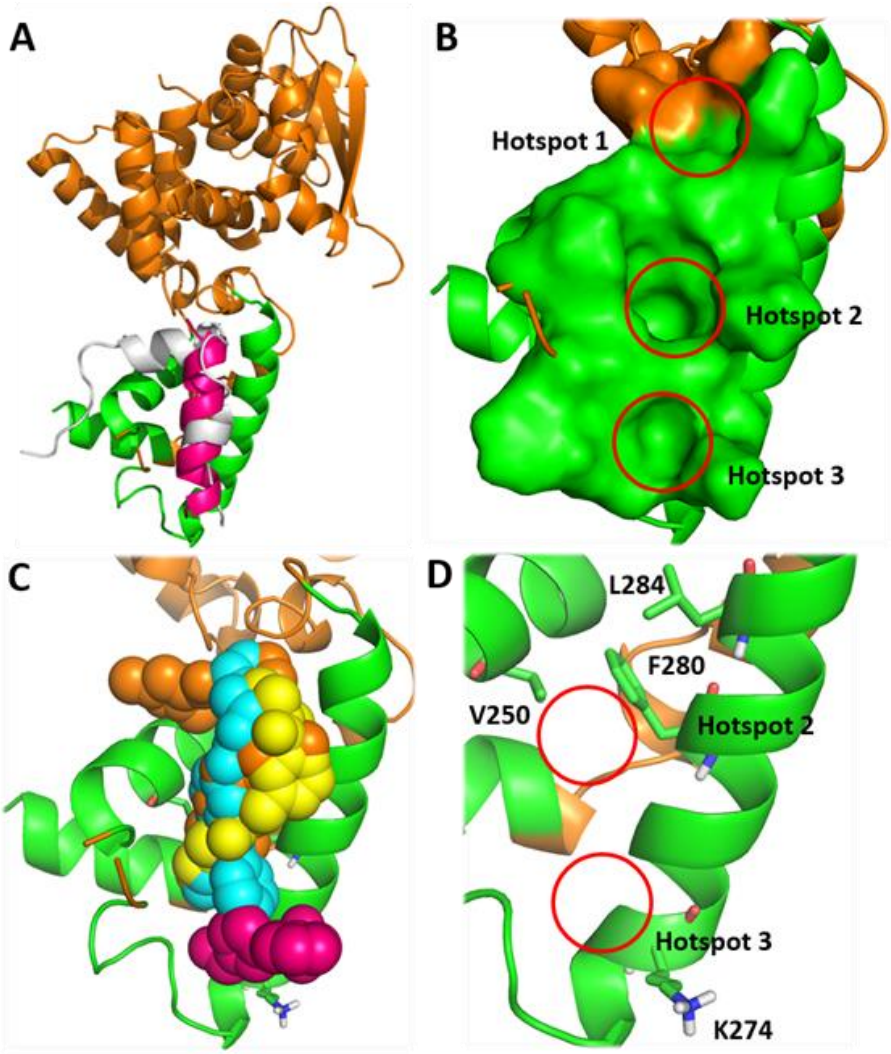


**Figure 2:** Nucleocapsid protein (NP) from EBOV. A) Overlay of EBOV NP crystal structures (PDB IDs 4YPI & 4Z9P) showing that VP35 (white ribbons) and helix-20 (pink ribbons) bind to the same hydrophobic channel (green ribbons) within NP (orange ribbons). B) Surface representation of the hydrophobic channel (VP35/helix-20 removed) highlighting three distinct hotspots for inhibitor design. C) Graphic showing the putative binding mode of each inhibitor series. Series 1-3 (orange, blue and yellow spheres) occupy the same hotspot regions (1 & 2). Series 4 occupies hotspot 3. D) Identified sites for mutagenesis: K274, V250, F280 and L284.

## Publications

Easton, V., McPhillie, M.J., Barr, J., Edwards, T.E., Foster, R., Fishwick, C.W.G., Harris, M. (2018) Identification of a small molecule inhibitor of Ebolavirus genome replication and transcription using in silico screening *Antiviral Research*,**156**, 46-54.

## Funding

This work was funded by a Wellcome Trust Pathfinder Award 2016-2018.

## Potassium is a trigger for conformational change in the fusion spike of an enveloped RNA virus

Emma Punch, Samantha Hover, Henry Blest, Jack Fuller, John Barr, Jamel Mankouri and Juan Fontana

### Introduction

The order Bunyavirales represents the largest group of enveloped segmented negative-stranded (SNS) RNA viruses, and many are associated with serious disease of humans, animals, and plants. The order includes over 500 named isolates classified into nine families, with four of these including members that cause serious human disease; namely, the Nairoviridae, Peribunyaviridae, Hantaviridae, and Phenuiviridae.

All members of the Nairoviridae family are arboviruses, including Crimean–Congo hemorrhagic fever virus (CCHFV), which is an emerging threat because of the expanding habitat of its tick host. CCHFV is the causative agent of a lethal hemorrhagic fever in humans, with case fatality rates of over 60% in certain outbreaks. There is no vaccine or therapy to prevent or treat CCHFV-mediated disease, and consequently, CCHFV is one of a small group of human pathogens classified in hazard group 4. Hazara virus (HAZV) is closely related to CCHFV, and they share the same CCHFV serogroup and high structural homology, although HAZV has not been documented to cause human disease and is currently classified within hazard group 2.

Bunyavirus infection starts with attachment to the host cell and entry through endocytosis. This is followed by fusion of the viral and endosomal membranes, a process orchestrated by the Gn and Gc glycoproteins located on the virion exterior, which allows the viral ribonucleoproteins to access the cytoplasm of the cell.

Recently, using the model bunyavirus Bunyamwera virus (BUNV), we showed that pharmacological inhibition of endosomal $K^+$ channels blocked BUNV entry by reducing $K^+$ accumulation in the endosomal system. Although this work revealed [$K^+$] as a newly identified biochemical cue required for efficient infectivity, the identity of the viral component that responds to the $K^+$ was unknown, as was the nature of the underlying mechanism of enhanced infection.

### Results

Here we demonstrate that entry of HAZV, like BUNV, is also influenced by [$K^+$], showing that $K^+$ enhances infectivity across multiple families within the Bunyavirales order. We further report the first visualization of any nairovirus using cryo-EM, which revealed the HAZV ultrastructural characteristics and surface glycoprotein architecture in high detail (Fig. 1A – C). By performing cryo-electron tomography (cryo-ET) of HAZV and subtomogram averaging (STA) of HAZV spikes, we show that exposure of virions to elevated [$K^+$] alone is associated with dramatic spike conformational changes and, furthermore, promotes interactions with membranes (Fig. 1D – E). We propose that these conformational changes and membrane interactions occur during the HAZV entry pathway and initiate virus fusion within endosomal compartments in which the [$K^+$] trigger is present. Finally, we show that the cellular $K^+$ channels that mediate endosomal $K^+$ influx are a druggable target that can be targeted to block HAZV infectivity (Fig. 2).

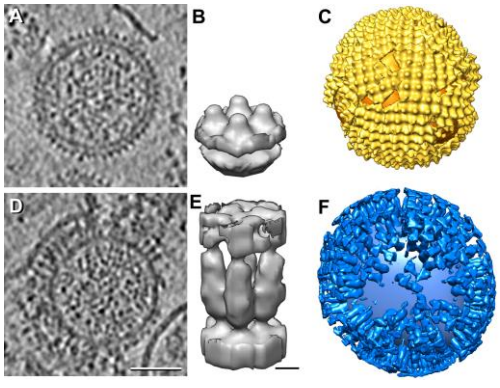


**Figure 1:** Cryo-ET and STA of HAZV virions treated with low or high [$K^+$] at pH 7.3. A – C, HAZV virions at low [$K^+$] (5 mM). D – F, HAZV virions at high [$K^+$] (140 mM). A & D, central tomographic sections. Changes in [$K^+$] resulted in extension of the glycoprotein spikes and interactions with adjacent membranes co-purified with HAZV virions are apparent. B & E, isosurface rendering STA of HAZV spikes. Although the high $K^+$ average is ~3 times longer than the low $K^+$ average, the low $K^+$ average shows a continuous density parallel to the viral envelope that is absent in the high $K^+$ average. C & F, 3D models of full virions. Scale bars = 50 nm in A & D, 5 nm in B & E.

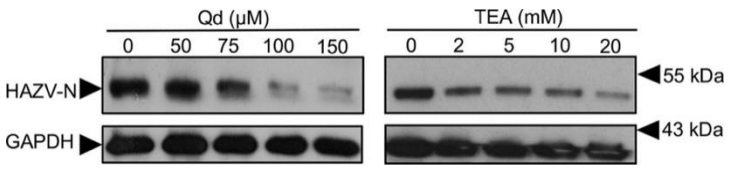


**Figure 2:** HAZV multiplication can be blocked by broad-spectrum inhibition of cellular $K^+$ channels. Representative western blots of A549 lysates following pretreatment with the indicated channel blockers (TEA, and Quinidine - Qd) prior to infection with HAZV (multiplicity of infection of 0.1). After 24 h, cell lysates were probed by Western blotting with sheep anti-HAZV N serum and GAPDH as a loading control. No-treatment controls were included for each inhibitor.

Taken together with our previous findings, showing that multiple bunyaviruses require elevated [$K^+$] for entry, we suggest that the [$K^+$] trigger is a common feature of bunyaviral entry and that cellular $K^+$ channels represent a new target for the development of antiviral molecules that broadly impede bunyavirus growth.

**Publications**

Punch E.K., Hover S., Blest H.T.W., Fuller J., Hewson R., Fontana J., Mankouri J., Barr J.N. (2018) Potassium is a trigger for conformational change in the fusion spike of an enveloped RNA virus. *J. Biol. Chem.* **293**: 9937-9944.

**Funding**

This work was supported by the Academic Fellow scheme at the University of Leeds (to J. Fontana and J. M.), The Royal Society (to J. M.), EPSRC Grant EP/L504993/1 (to E. P.), and Public Health England (to J. Fuller).

**Collaborators**

*External:* Roger Hewson (Public Health England).

## Structure of specialized ribosomes

Tayah Hopes, Michaela Agapiou, Amy Turner, Emily Levitt, Albert Blady, Ellen Temple, Julie Aspden and Juan Fontana

### Introduction

Our understanding of 'the ribosome' and mRNA translation has been transformed by the discovery that specialised ribosomes exist and regulate the translation of specific mRNAs. It is now evident that not all ribosomal proteins (Rp) are equally important to the translation of all mRNAs. For example, RpL38 is required for the specific translation of Hox mRNAs, which is essential for neural specification in mice. This project aims to determine the underlying structural implications of changes to ribosomal protein composition and how this facilitates specialised ribosome function. This will enable us to dissect how changes in ribosome composition result in ability to translate specific pools of mRNA, and how differences in the ribosome structure mechanistically regulate mRNA translation events.

### Results

To profile specialised ribosomes composition we purified ribosomes from *D. melanogaster* testes, ovaries, heads, embryos and S2 cells (embryo derived cell line). Tandem Mass Tag (TMT) mass spectrometry analysis revealed that the overall protein composition of ribosomes in the testis is substantially different from the other tissues (Fig. 1A). Hierarchical clustering identified a group of 6 RPs that are more abundant in testis 80S than other tissues e.g. RpL22-like, and under-represented in heads and ovaries. Importantly, several pairs of paralogs were present, indicating that different populations of ribosome exist. In fact, switching of paralogs was evident from increased incorporation of one paralog and decreased incorporation of its pair e.g. S19 a and b.

Purified 80S ribosomes from *D. melanogaster* testes were also studied by cryo-electron microscopy (cryo-EM). This allowed us to generate a 3D reconstruction to 3.9 Å (Fig. 1B). Rigid body fitting of RpL37a into the testis ribosome EM reconstruction shows that there is no density for the C-terminus (Fig. 1C, circled). Combined with our TMT data, this suggests that this testis ribosome population contains RpL37b, instead of RpL37a, and that a population of specialised ribosomes exist in *D. melanogaster* testes.

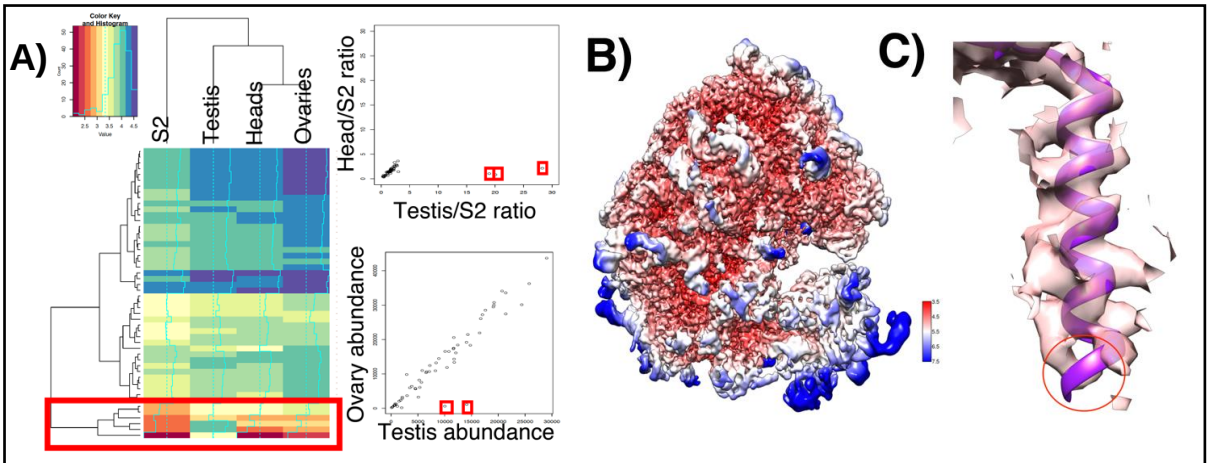


**Figure 1:** Characterisation of specialised ribosomes from *Drosophila* testis. A) Left, Hierarchical clustering of RP abundances (log10) from TMT of whole 80S ribosome complexes isolated from S2 cells, testes, heads and ovaries. Right, correlation of Rp ratios in testis and heads relative to "standard" S2 cells (top); and correlation of RP abundances in testis and ovary 80S complexes (bottom). B) 3.9 Å cryo-EM reconstruction of 80S purified from testes showing local resolution (from 3.5Å – red, to 7.5Å – blue). C) Rigid body fitting of RpL37 in testis 80S.

### Funding

This work was funded by BBSRC (BB/S007407/1), Royal Society (RSG\R1\180102), and White Rose University Consortium Collaboration Fund.

## Development of a novel small molecule anticoagulant with minimal bleeding risk

Charlotte Revill, Emma Hethershaw, Colin Fishwick, Helen Philippou and Richard Foster

### Introduction

There is an urgent need for the development of new anticoagulants with a reduced risk of bleeding. As part of a long-standing collaboration with a group in the Faculty of Medicine & Health at University of Leeds we have identified small molecule modulators of a critical enzyme involved in the coagulation cascade which demonstrate exceptional efficacy and minimal bleeding risk in animal models of thrombosis.

### Results

We have identified potent small molecule inhibitors of a serine protease of the coagulation cascade with exceptional *in vivo* efficacy using a number of mouse models of thrombosis. The inhibitors were identified using a number of parallel hit-identification approaches, including virtual drug design and fragment and high-throughput screening of drug-like small molecule libraries. Presently, we are optimising the inhibitors for on-target potency, specificity and drug-like physicochemical properties using iterative rounds of medicinal chemistry optimisation and screening *via* a panel of orthogonal *in vitro* bioassays. The current series of inhibitors demonstrate high aqueous solubility, metabolic stability, plasma stability and low levels of plasma protein binding consistent with an orally bioavailable agent. The compounds also demonstrate no adverse toxicity at high concentrations, including absence of cardiotoxicity (e.g. hERG and sodium channel inhibition). The compounds are highly potent (<10 nM $IC_{50}$) and demonstrate >1000× selectivity for 10 structurally (and functionally) related protein targets. The aim of our on-going work is to further develop the leads to generate a candidate compound with suitable pharmaceutical properties consistent with an optimised lead ready for progression into Phase 1 clinical trials. A second series of inhibitors identified by fragment-based screening is undergoing optimisation for potency driven by structure guided design. The second series of ligands bind at a different site to the primary series and offer a possibility of generating inhibitors with a complementary selectivity and property profile to the current lead series.

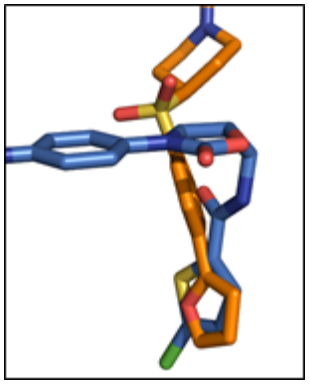

Ligand alignment model used for vHTS

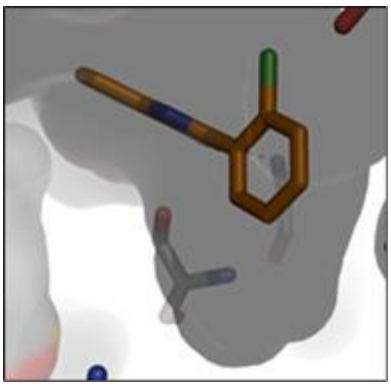

Co-crystallised protein (grey): fragment (orange) complex

### Publication

Patent: UK15217111

### Funding

Our work is funded by the Wellcome Trust, MRC and BHF

## Cryo-electron microscopy of FCHSD2, a BAR domain-containing, actin-organizing component of endocytosis

René Frank

### Introduction

The uptake of large macromolecules including proteins and pathogens by cells is dependent on the formation of dome-shaped membrane invaginations that internalize a patch of the plasma membrane; cupping a sample of solute from outside the cell in a process called endocytosis. Clathrin-mediated endocytosis (CME), is characterized by the formation of a triskelion cage of clathrin that assembles under the cytoplasmic leaflet of the membrane causing the membrane to invaginate. Several other proteins adhere to the inner leaflet of the membrane via domains that recognize or induce membrane curvature (Fig 1A). Branched filamentous actin polymerizes from the plasma membrane towards the clathrin pit, suggesting that the dynamics of filamentous actin contribute to the force that propels the pit inwards.

FCH and double SH3 domains protein 1 and 2 (FCHSD1 and FCHSD2) are the mammalian homologs of the *Drosophila* Nervous Wreck protein (Nwk). They are part of the BAR super-family of dimeric membrane binding domains. Nwk mutant flies are paralyzed under non-permissive temperatures and show abnormal neuronal morphology. The Nwk protein interacts with components of the CME and actin cytoskeleton machinery. Using GST-pulldowns our collaborators discovered that FCHSD2, like Nwk, interacts with N-WASP and intersectin via its SH3-1 and SH3-2, respectively. *In vitro* assays indicated that FCHSD1 is the major activator of membrane-dependent actin polymerization. Using STED super-resolution light microscopy, our collaborators also showed that FCHSD1 is a bona fide component of CME machinery, assembling as an annulus at the base of CME pits in cells (Fig 1B). To understand the structural basis of FCHSD2 in orchestrating actin polymerization at CME pits, we used single-particle cryo-electron microscopy (cryoEM).

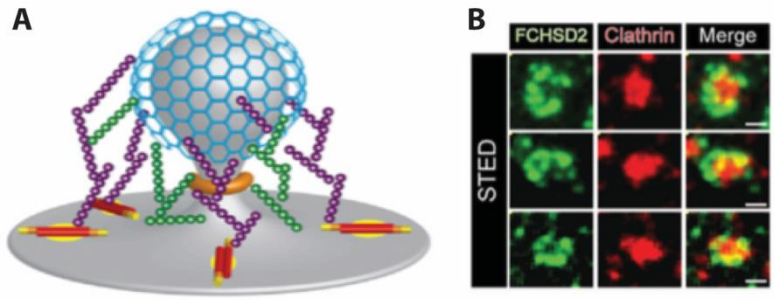


**Figure 1:** FCHSD2 is a bona fide component of clathrin-mediated endocytosis. **A** Schematic showing an elaborate network of proteins, including clathrin (blue), actin (green and purple), and membrane-binding proteins (red and orange), orchestrate endocytosis at the plasma membrane (grey) . **B** STED microscopy of HeLa cells stably transfected with FCHSD2-Venus (green). Clathrin (red) was detected with antibodies. Scale, 250 nm.

### Results

Recombinant FCHSD2 was over-expressed in *E. coli* and purified using a poly-histidine tag. Size-exclusion chromatography suggested FCHSD2 assembles into a 125 kDa homodimeric complex. Given the small size of this complex, a screen of cryoEM grid preparation was performed to minimize ice thickness. In thin ice, 135 Å × 25 Å rod-like particles were identified, usually at too high a concentration to resolve individual particles for further image processing. Surprisingly, varying sample concentration with a dilution series had little effect on the apparent concentration of particles in holey-carbon grids, suggesting particles partitioned to the air-water interface of the blotted cryoEM grids. Concordantly, we found the time interval between applying sample on the grid, blotting and plunge freeze was a critical variable

enabling the preparation of cryoEM grids with not too high a concentration of particles (Fig 2A).

Data were collected with a Titan Krios electron microscope (FEI) operated at 300 kV equipped with a K2 Summit direct electron detector (Gatan) mounted after a Gatan Imaging Filter (GIF) with a 20-eV slit. 20-frame image stacks were collected in electron-counting mode with a flux of 2 $e^-/Å^2/s$ and a total dose of 40 $e^-/Å^2$ and a calibrated pixel size of 1.1 Å. Frames were aligned and averaged with MOTIONCORR. Contrast-transfer-function parameters were calculated with Gctf. All subsequent particle picking and data processing was done in a pre-release of Relion 2.0. From 766 micrographs, Relion autopick selected 230954 particles using as a reference 2D averages derived from a manually picked particle set. Autopicked particles were used for reference free 2D classification (Fig 2B). The best 2D classes, containing 30270 particles, were selected for further processing. 3D classification generated classes that looked very similar to each other. Therefore, we used all particles from the best 2D classes for 3D refinement using a 40 Å low-pass filtered FES F-BAR structure (pdb 4DYL) as an initial model and applying C2 symmetry.

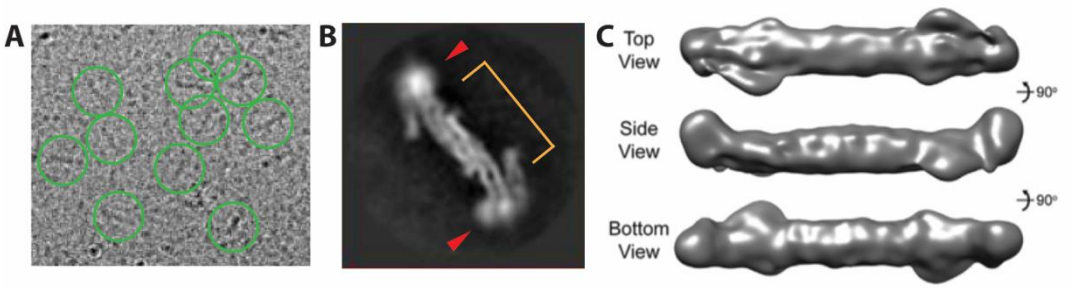


**Figure 2:** Single-particle cryo-electron microscopy of FCHSD2. **A** Typical electron micrograph of purified FCHSD2. ~135 Å rod-like particles are highlighted with green circles. **B** One of the 2D class averages reveals the helix arrangement within the BAR domain (orange bracket) of FCHSD2. Electron density of SH3-1 domain was more diffuse (red arrow heads). **C** 9.6 Å resolution electron density map, shows atypical flat conformation of FCHSD2 BAR domain.

The final electron density map (Fig 2C) reached 9.6 Å resolution revealing the overall shape of the BAR domain of FCHSD2. The SH3 domain was slightly less well resolved than the BAR domain, suggesting its connection with the BAR domain is flexible. BAR domains are usually crescent-shaped with a curved surface that matches the curvature of the membrane to which it binds. The structure of the FCHSD2 BAR domain presents a flat rather than curved surface for association with the membrane. This atypical conformation suggests a preference of this domain to associate with flat or low curvature membranes and provides a structural explanation for the discovery that FCHSD2 associates at the base of CME pits, rather than on the pit itself. *In vitro* binding assays by our collaborator confirmed the preference of this domain for less curved membranes. Overall, the discovery of a flat BAR domain structure is consistent with the role of FCHSD2 in organizing actin polymerization from the base of CME pits.

**Publications**

Almeida-Souza L., Frank R.A.W, Garcia-Nafria J., Colussi A., Gunawardana N., Johnson C.M., Yu M., Howard G., Andrews B., Vallis Y., McMahon H.T. (2018) A flat BAR protein promotes actin polymerisation at the base of clathrin-coated pits. *Cell* **73**: 74, 325.

**Funding**

This work was funded by the Medical Research Council.

**Collaborators**

*External:* Leonardo Almeida-Souza. Javier Garcier-Nafria, Adeline Colussi, Nishan Gunarwadana, C. Michael Johnson, Min Yu, Gill Howard, Byron Andrews, Yvonne Vallis and Harvey McMahon (MRC Laboratory of Molecular Biology)

## Integral membrane proteins as drug targets

Keni Vidilaseris, Steven Harborne, Craig Wilkinson, Aaron Wilkinson, Jannik Strauss, Sarah Harris, Roman Tuma, Lars Jeuken, Christos Pliotas and Adrian Goldman

### Introduction

Membrane pyrophosphatases (M-PPases) occur in plants, protozoan parasites and prokaryotes. They are associated with low-energy stress: overcoming saline or drought conditions in plants or rapid changes in pH or osmotic pressure in protozoan parasites. M-PPases couple pyrophosphate hydrolysis to the pumping of sodium ions and/or protons across the inner membrane of prokaryotes or the vacuole/acidocalcisome membranes of plants/parasites. These proteins are important in the lifecycle of several pathogenic species of parasites, including *Plasmodium falciparum*, which causes malaria, and in several species of pathogenic bacteria, such as *Clostridium botulinum* and species of *Bacteroides* that can cause severe opportunistic infections. There are no analogues in mammals, so M-PPases are an important potential drug target[1]. Continuing from our initial M-PPase structure using X-ray crystallography, we are completing a model of the catalytic cycle using additional structural and biochemical data and are using this in drug design.

### Results

We have solved the first structures of *Thermotoga maritima* M-PPase (TmPPase) in complex with an allosteric inhibitor, *N*-[(2-amino-6-benzo-thiazolyl)-methyl]-1*H*-indole-2-carboxamide (ATC) at a resolution of 3.4-4.0 Å as determined by the StarAniso server. The crystals contain two biological dimers AB and CD, with imidodiphosphonate (IDP) bound in the active site of all of them, but the ATC molecule, bound as a dimer, occurs between the AD and BC monomers (Fig. 1). In the AD interface, two molecules of ATC π-stack head-to-tail (Fig. 2) into a hydrophobic cleft. The cleft is principally formed by strands β1–2 (loop6–7), loop8–9, and

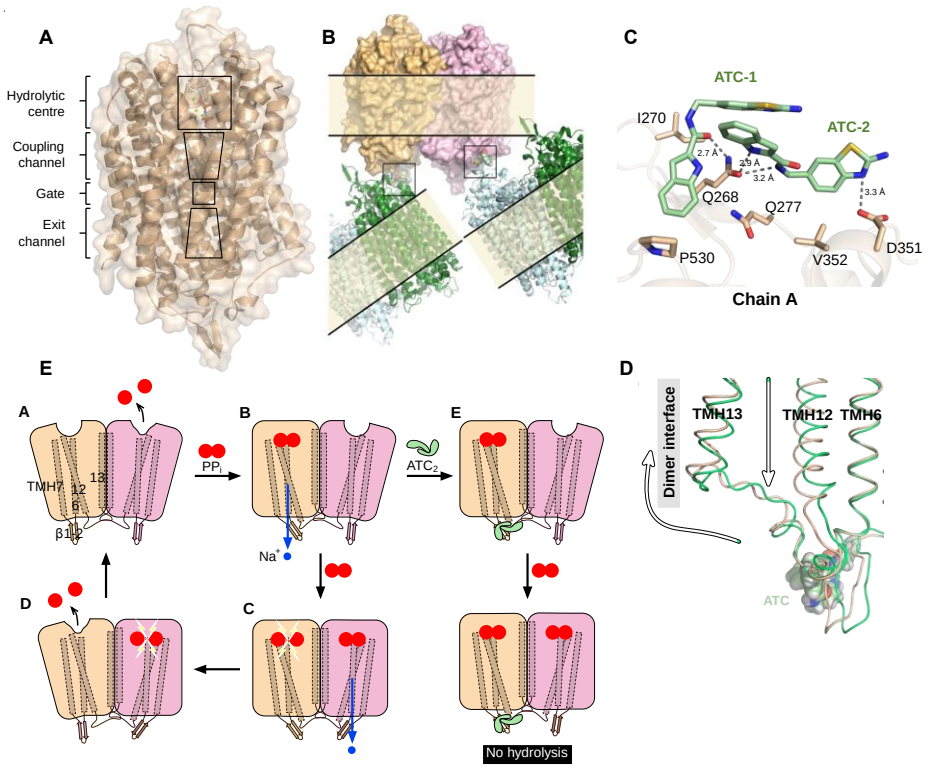


**Figure 1**. A: Overall view of TmPPase monomer, showing the parts of the catalytic site. B: Overall view of the crystallographic AB-CD tetramer, showing where ATC binds (boxed). C: View of the ATC dimer bound beside the exit channel of TmPPase (β1-β2). D: Difference between ATC-bound (straw) and ATC-free structures, showing how binding of ATC near helices 6 and 12 influences the dimer interface. E: Revised mechanism of M-PPases, suggesting how binding of $PP_i$ to one monomer potentiates binding at the other active site, but also enables $ATC_2$ binding.

loop12–13 near the exit channel of chain A. The binding of ATC appears to stabilize an asymmetric structure of TmPPase, especially in the loops that interact with the inhibitor (rmsd/Cα 1.25 Å) when the A monomer (ATC bound) is compared with the B monomer (no ATC bound). Our other TmPPase structures are much more symmetric in this region. We also performed extensive kinetics studies, which demonstrate (Fig. 2) that, as in the structure, *two* molecules of ATC are required for inhibition of the TmPPase *dimer*, and that inhibition is uncompetitive: ATC only binds in the presence of substrate. Indeed, we could only obtain the TmPPase:ATC complex in the presence of ATC. ATC is the first non-phosphorus and the first allosteric inhibitor identified for M-PPases.

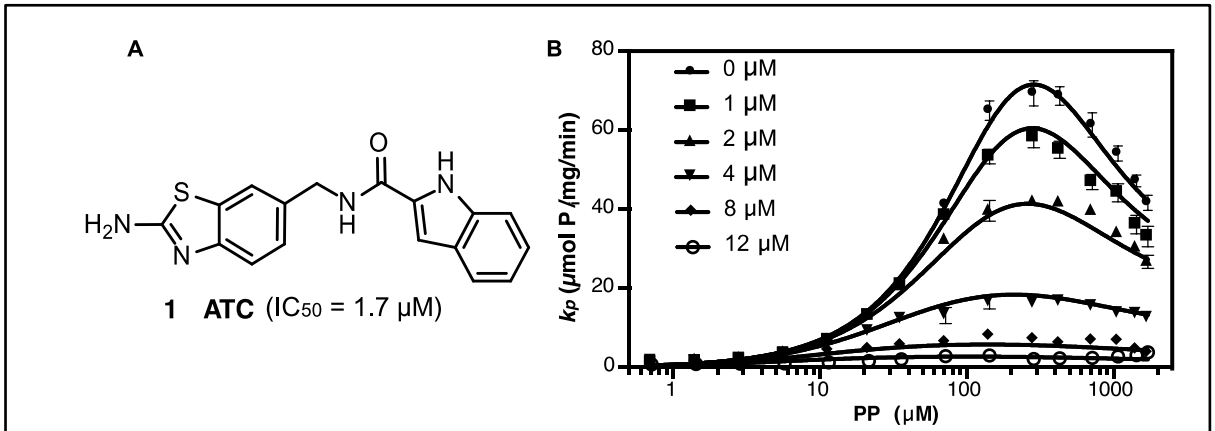


**Figure 2**. A: Structure of ATC. B: Non-linear fit of the uncompetitive model where there are two $K_m$ for binding of substrate to the $E_2$ and $E_2S$, similarly two $k_{cat}$, and the ATC dimer can bind either to $E_2S$ ($K_{I1}$) or $E_2S_2$ ($K_{I2}$) but not to $E_2$. This model, which fits the data very well, $K_{m1} = 8K_{m2}$; $k_{cat1} = 0.05\ k_{cat2}$, and $K_{I1} = 1.4$ µM, while $K_{I2} = 3.2$ µM.

We then endeavoured to see if ATC was a viable inhibitor of protozoan M-PPases. It did not inhibit *P. falciparum* M-PPase, and it did not inhibit the growth of malaria parasites in the red blood cell killing assay. This is not surprising, as the β1-2 loop where ATC binds is one of the variable regions in M-PPases. However, we have developed other compounds (A. Wilkinson, *unpublished*) that bind to conserved regions near the monomer-monomer interface in TmPPase and *do* kill malaria parasites at concentrations of 1-5 µM. They also bind in an allosteric manner, and are being further optimized. Overall, we now have a novel understanding of how to inhibit M-PPases: this work will allow the development of drugs against significant human and animal parasites.

**Publications**

Robinson, J. I., Baxter, E. W., Owen, R. L., Thomsen, M., Tomlinson, D. C., Waterhouse, M. P., Win, S. J., Nettleship, J. E., Tiede, C., Foster, R. J., Owens, R. J., Fishwick, C. W. G., Harris, S. A., Goldman, A., McPherson, M. J. & Morgan, A. W. (2018) Affimer proteins inhibit immune complex binding to FcγRIIIa with high specificity through competitive and allosteric modes of action. *Proc Natl Acad Sci USA* **115,** E72–E81.

Harborne, S. P. D., Strauss, J., Turku, A., Watson, M. A., Tuma, R., Harris, S. A. & Goldman, A. (2018) Defining Dynamics of Membrane-Bound Pyrophosphatases by Experimental and Computational Single-Molecule FRET. *Methods Enzymol* **607,** 93–130.

Vidilaseris, K., Kiriazis, A., Turku, A., Khattab, A., Johansson, N.G., Leino, T.O., Kiuru, P.S., Boije af Gennäs, G., Meri, S. Yli-Kauhaluoma, J., Xhaard, H. & Goldman, A. (2018) Asymmetry in catalysis by *Thermotoga maritima* membrane-bound pyrophosphatase demonstrated by a non-phosphorous allosteric inhibitor. BioRxiv, doi: 10.1101/423954.

**Funding**
This work was funded by the BBSRC, the University of Leeds, the European Union, the Academy of Finland and the Erkko Foundation and the EPSRC.

**Collaborators**
*University of Leeds:* Antreas Kalli, Colin Fishwick
*External:* University of Helsinki, University of St. Andrews

## Bimodal prophylactic therapy for hepatitis C virus

Joseph Shaw, Rajendra Gosein, Jayakanth Kankanala, Toshana Foster, Claire Scott, Matthew Bentham, Laura Wetherill, Abigail Bloy, Adel Samson, Mark Harris, Andrew Macdonald, David Rowlands, Jamel Mankouri, Richard Foster and Stephen Griffin

### Introduction

Ion channels are amongst the most druggable of biological targets. However, those encoded by viruses, known as “viroporins”, have been largely ignored with only a single class of agent, adamantanes targeting influenza A virus M2, licensed in the 1960s. The widely perceived failures of these drugs in terms of resistance and lack of clinical efficacy represent a spectre that has effectively hampered the development of new viroporin-targeted agents in recent years.

However, some of the most clinically and economically important viruses known, including both established and emerging pathogens encode essential viroporins. Hepatitis C virus (HCV) remains a major public health issue, infecting over 100 million people and accounting for over a third of all primary liver cancers. Whilst new successful HCV drugs are on the market, these exclusively target the viral replicase and so treat established infections, which are usually diagnosed when liver disease is already severe.

We describe a step-change in viroporin-targeted drug design, applying rational methods to define a potent lead-like inhibitor of the HCV p7 viroporin. Use of this inhibitor and related tool compounds elucidated a newly described role for p7 channel activity during virus entry, in addition to its known role during virus egress. Hence, targeting p7 represents a bimodal antiviral approach suited to prophylaxis, which could conceivably reduce the ~6 million new HCV cases that occur annually.

### Results

p7 plays an essential role during virion secretion and so provides an alternative target stage of the virus life cycle compared to current DAAs; these unanimously target the viral replicase. We previously described a first generation series of inhibitors derived by *in silico* screening using a heptameric channel model template derived from our monomeric NMR structure (PDB 3DZ0). Based upon hit compounds with sub-micromolar potency, we undertook a second round rational screening, capitalising upon rapid-throughput analysis of secreted HCV infectivity based upon the Incucyte Zoom. The resulting second-generation series yielded an oxindole-based lead, JK3/32 (Figure 1), as well as an extensive structure-activity relationship (SAR) comprising ~50 derivatives with >3 $\log_{10}$ range in potency. Atomistic molecular dynamics simulations of JK3/32 binding further validated its SAR.

JK3/32 displayed pan-genotypic activity against HCV chimaeric viruses expressing p7 from multiple genotypes, with a cell culture $IC_{50}$ of 184 nM versus genotype 1b viruses and sub-micromolar activity across the range tested. The compound displayed no off-target activity against cellular kinases, ion channels or other viroporins, had no activity against viral replication, and had a toxicity-based selectivity index of >500 (>100 000 nM in Huh7 cells). In addition, our extensive SAR enabled the generation of both stabilised fluoridated JK3/32 derivatives as well as chemical probes with fluorescent or biotin tags for use in mechanistic studies.

Based upon our previous studies describing a link between p7 and the acid stability of secreted HCV particles, we used JK3/32 and derivatives to investigate whether virion-resident channel complexes might influence virus entry and uncoating in addition to secretion. Excitingly, JK3/32 specifically inhibited HCV entry, albeit at higher concentrations compared with when targeting secretion. This was evident by genotype-specific potency, a lack of effect upon virion binding and cell fusion, and the maintenance of normal cellular endocytosis in the presence of the compound. Furthermore, a structurally related inactive derivative “R21” had no effect upon HCV infectivity and JK3/32 had no effect upon the infectivity of other viruses retaining virion-resident viroporin complexes. Moreover, whilst it was not possible to select JK3/32 resistance in culture, specific resistance polymorphisms for prototypic p7 inhibitors provided

genetic evidence of target engagement. Time of addition assays confirmed that JK3/32, but not R21 was only active when present during the infection process.

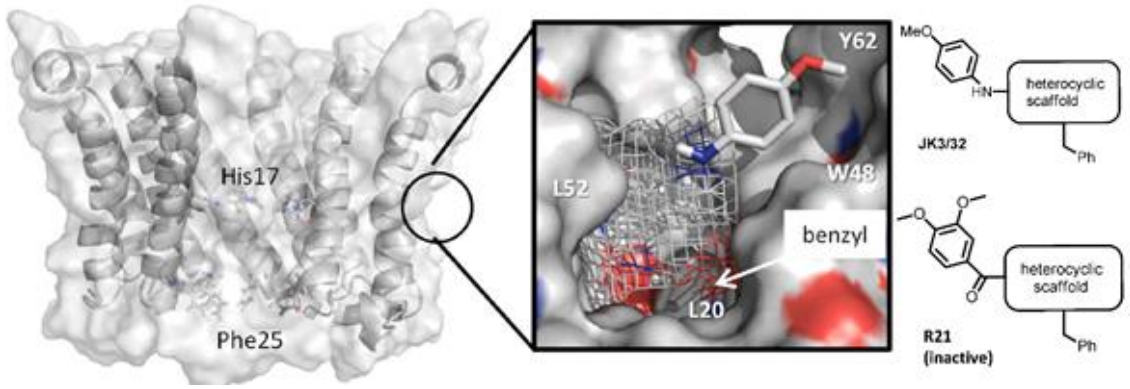


**Figure 1**. Rational development of JK3/21 Oxindole-based inhibitor of HCV p7. Left panel shows NMR-based (PDB 3DZ0) structure model of the heptameric p7 channel complex with His17 proton sensor and Phe25 gating heptads. Circle indicates position of peripheral membrane-exposed JK3/32 binding site (central panel). Right panel shows northern functional groups of JK3/32 and related inactive R21 derivative which serves as a control for p7-specific activity.

Finally, we were able to show using a fluorescent JK3/32 derivative that the inhibitor exerted an irreversible effect upon HCV particles which, following purification away from free compound using iodixinol gradients, were unable to productively infect cells whilst being otherwise structurally intact. Thus, the potency and selectivity of JK3/32 not only represents a step-change in therapeutic development targeting viroporins, but has provided an excellent molecular tool for the study of p7 channel function, identifying a second role during HCV entry. Hence, drugs based upon JK3/32 could deliver effective antiviral prophylaxis against *de novo* exposure or transplanted graft re-infection, in addition to use in conventional combination therapies treating chronic HCV infection.

**Funding**
This work was funded by the Wellcome Trust, the University of Leeds and the MRC.

**Collaborators**
*University of Leeds:* Richard Foster, Jamel Mankouri, Andrew Macdonald, David Rowlands, Mark Harris, Adel Samson
*External:* Wolfgang Fischer (Taipei), Alexander Tarr (Nottingham).

## Ultra-coarse grained biomolecular simulation with Fluctuating Finite Element Analysis

Rob Welch, Ben Hanson, Daniel Read, Oliver Harlen and Sarah Harris

### Introduction

FFEA is a novel simulation tool for modelling very large biomolecular complexes based on low resolution structural data, such as from cryo-EM or SAXS. It can also make use of restraints provided by biophysical tools such as FRET or ion mobility mass spectrometry. FFEA treats biomolecules as soft continuum materials that change shape continuously due to thermal motion. It represents globular regions of proteins using a triangular finite element mesh, and linear regions of biomolecules (such as coiled-coils or dsDNA) using flexible rods. It can represent stiff and flexible regions of proteins or nucleic acids by tuning the material parameters (specifically the Young's modulus) associated with each of the finite elements. It describes biomolecular interactions by placing sticky forces on the surface of the mesh, which allows proteins to interact in a specific manner with their substrates based on experimentally measured binding affinities.

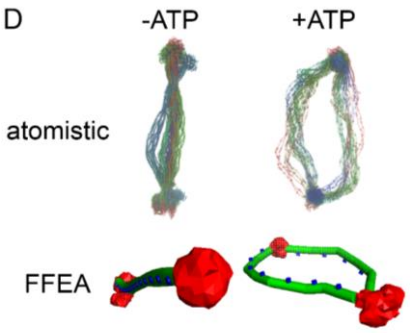


Example of atomistic MD simulations (top) of the Structural Maintenance of Chromosomes (SMC) protein, compared with the corresponding ultra-coarse grained rod-blob FFEA model (bottom).

We have recently developed methodology to obtain FFEA parameters (e.g. the variable Young's moduli throughout proteins) from atomistic molecular dynamics simulations. For FFEA rods, this is achieved by locally matching the moduli associated with each rod element to achieve the same magnitude of thermal fluctuations observed in the more detailed simulations. For globular proteins, FFEA simulations are performed with a variety of moduli, and the value chosen that best fits the atomistic simulations. For biomolecules with complex shapes, such as the molecular motor dynein, the molecule is split into manageable domains (e.g. stalk/motor domain/tail) and the fitting performed separately for each. The validity of this approach of matching local flexibilities to global dynamics is validated by comparing principal components calculated for the whole biomolecular complex.

### Results

By analysing the conformers generated by the FFEA modelling, we will be able to compare with cross-sectional areas and binding interfaces obtained by mass-spec (Element 2) and with the distances measured by smFRET (Element 3). We will also use FFEA to optimise the experimental design by prior testing of the potential effect of biochemical perturbations *in silico*. For example, we can use FFEA to locate the most effective positions for mutations or FRET probes. Key predictions from the modelling will be validated (or disproved) by subsequent experiments. FFEA includes functionality to enable switching between known biomolecular conformations at a defined

### Publications

Solernou, A., et al., (2018) Fluctuating Finite Element Analysis (FFEA): A continuum mechanics software tool for mesoscale simulation of biomolecules. *PLoS Comput Biol*. **14**: p. e1005897.

## Investigating novel redox partners for bacterial lytic polysaccharide monooxygenase activation

Badri Rajagopal, Jessie Branch, Alan Berry and Glyn Hemsworth

### Introduction

Lytic polysaccharide Monooxygenases (LPMOs) are copper dependant enzymes that require oxygen and an electron donor to catalyse the oxidative cleavage of glycosidic bonds in polysaccharides. These enzymes have been under intense study in recent years due to their potential application in improved enzymatic biomass processing. An area that has been of increasing importance is the mechanism by which electrons can be delivered to these enzymes. For many fungal LPMOs, another enzyme called cellobiose dehydrogenase (CDH) can deliver electrons to the LPMO and hence activate it for polysaccharide cleavage. This is thought to be mediated via a *b*-type cytochrome-like domain present in CDH. There is no equivalent enzyme to CDH in bacteria, but many of these organisms also make use of LPMOs in order to break down polysaccharide substrates. We are, therefore, investigating a series of previously uncharacterised, putative, redox capable proteins as potential LPMO activators. Our current focus is on proteins from two prolific cellulose degrading bacteria, *Teredinibacter turnerae* (Tt) and *Cellvibrio japonicus* (Cj). By understanding the natural mechanisms by which LPMOs are activated, we aim to harness this knowledge in the development of novel LPMO activators for deployment in the biomass processing industry.

### Results

Working with Prof Bernard Henrissat, founder of CAZy (www.CAZy.org), we have identified a set of target proteins that contain X-domains, which have unknown functions but are often appended to Carbohydrate Binding Modules (CBMs) suggesting a role in polysaccharide processing (Figure 1A). We have successfully expressed, purified, crystallised and determined high resolution X-ray structures of two X183 domains, TtX183A and CjX183 (Figure 1B & C). These structures confirm that these domains are *c*-type cytochromes in which an iron containing haem molecule is covalently linked to the protein via thioether bonds. These types of domains are often associated with an electron transfer function further supporting the notion that these proteins could be involved in LPMO activation.

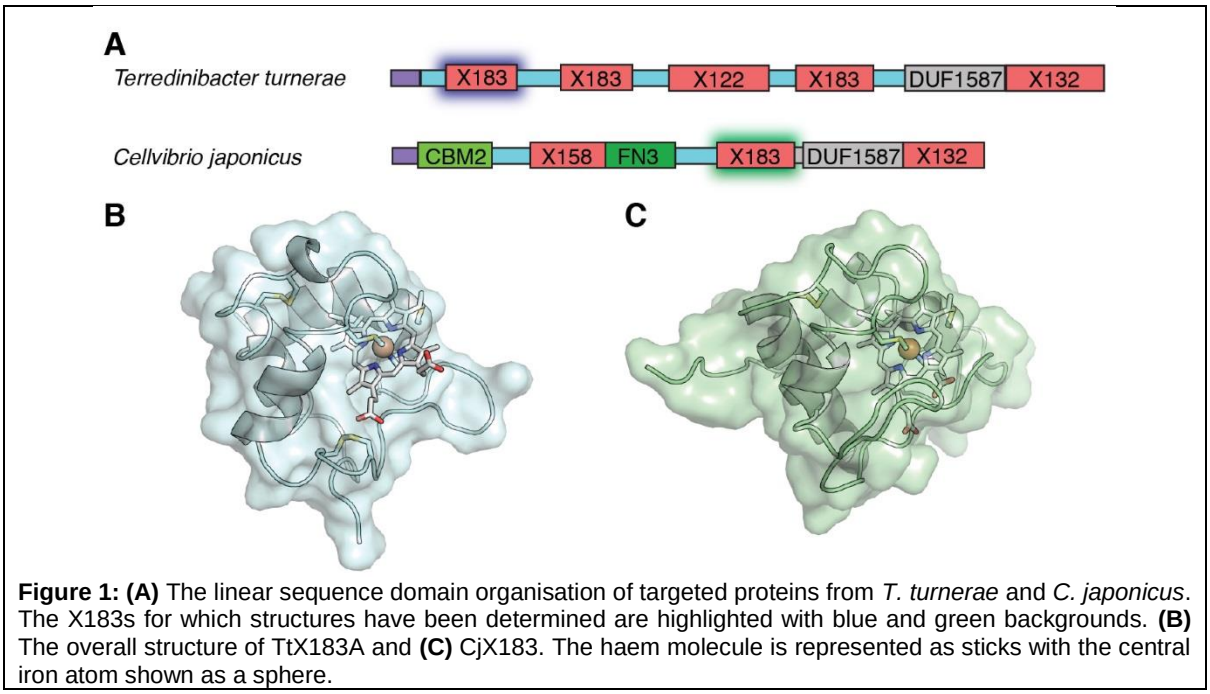


**Figure 1: (A)** The linear sequence domain organisation of targeted proteins from *T. turnerae* and *C. japonicus*. The X183s for which structures have been determined are highlighted with blue and green backgrounds. **(B)** The overall structure of TtX183A and **(C)** CjX183. The haem molecule is represented as sticks with the central iron atom shown as a sphere.

The UV-Visible absorption spectrum of *c*-type cytochromes provides a convenient means of assessing the redox state of the haem molecule present in the protein. The alpha and beta bands between 500 and 600 nm form distinct peaks in the reduced state, which broaden to

form a single peak when the cytochrome is oxidized (Figure 2A). We have used this property to monitor whether there are any changes in rate of oxidation of the X183 haem in response to the addition of LPMO. With the exception of TtX183A, an increased rate of haem oxidation was observed in an LPMO concentration dependent manner in all cases suggesting that these domains can indeed donate electrons to the enzyme (Figure 2B). Interestingly, from our structures we can see that TtX183A has its haem propionates considerably more exposed to solution in comparison to the orthologue from *C. japonicus*, which may account for its rapid oxidation when exposed to oxygen. Following up on these data, we have used MALDI-ToF mass spectrometry to show that CjX183 is capable of activating its cognate LPMO to oxidise cellulose as indicated by the production of oxidised oligosaccharides (Figure 2C).

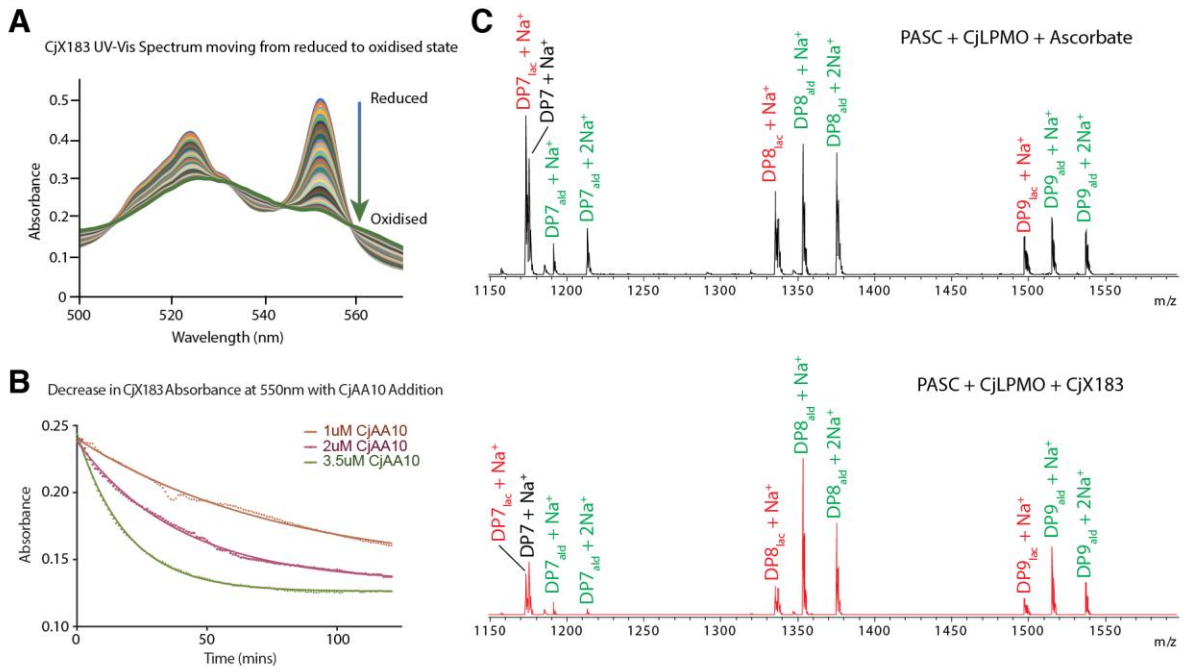


**Figure 2: (A)** Example UV-Vis spectrum for CjX183 showing the transition from reduced to oxidised state over time. **(B)** Observed rate of oxidation for CjX183 in the presence of varying concentrations of the cognate LPMO. **(C)** MALDI-ToF data showing the production of oxidised cello-oligosaccharides from PASC using the CjLPMO and either ascorbate or CjX183 as the electron source.

Our current data suggest that the electron transfer domains found within the unusual, multimodular bacterial proteins that we have identified are capable of activating LPMOs for activity. We are now following this up with more detailed kinetic analyses and molecular interaction studies to further probe the efficiency of this system in addition to characterising the functions of the other domains from these proteins. We will then attempt to engineer these domains for improved LPMO activation as we seek to increase the efficiency with which biomass can be degraded industrially.


**Funding**
This work is funded by the BBSRC and the University of Leeds.


**Collaborators**
*External:* Prof Bernard Henrissat (Aix Marseille University), Prof Paul Walton and Dr Alison Parkin (University of York)

## A thiol-reactive Ru(II) ion explains the antimicrobial properties of [Ru(CO)$_3$Cl(glycinate)]

Hannah Southam and Peter Henderson

### Introduction

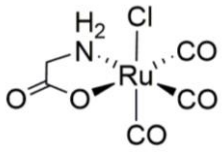


Scheme 1. Structure of the widely used Ru-carbonyl CO-releasing molecule, CORM-3.

Over the past decade, novel transition metal-based carbon monoxide-releasing molecules (CORMs) have been developed to deliver physiologically relevant levels of CO experimentally or therapeutically, not only in clinical and physiological applications, but also as anticancer drugs and novel antimicrobials. One of the earliest and widely used CORMs is the water-soluble [Ru(CO)$_3$Cl(glycinate)] ('CORM-3', Scheme 1). CORM-3 not only inhibited growth and respiration of *Pseudomonas aeruginosa in vitro*, but also decreased bacterial counts in the spleen of both immunocompetent and immune-suppressed mice. CORM-3 is toxic against laboratory strains and clinical isolates of *Escherichia coli*, *Campylobacter jejuni*, *Lactobacillus lactis*, *P. aeruginosa*, *Staphylococcus aureus* and *Salmonella enterica* serovar Typhimurium. Since CORM-3 accumulates in bacterial cells (as assessed by ruthenium uptake) and inhibits respiration, an early assumption was that activity was due to intracellular release of CO, which binds to terminal oxidases, thereby inhibiting respiration. In contrast, CORM-3 has beneficial therapeutic effects to mammalian cells in numerous *ex vivo* and whole-animal models (vasodilatory, renoprotective, cardioprotective, neuroprotective, anti-inflammatory etc.) without any onset of adverse effects to host organs. A radically different explanation for the toxic biological activities of these ruthenium carbonyl CORMs is that, rather than acting via release of CO, they are sources of Ru(II), which can react with a range of cellular targets. Here, we investigate this hypothesis.

### Results

When CORM-3 (60 μM) is added to cultures of *E. coli* growing on glucose in minimal salts media, growth ceases immediately (Figure 1). However, if the CORM-3 solution is mixed with a 2-fold excess of cysteine immediately before addition, then the inhibitory effect on growth is essentially abolished (Figure 1). A less effective protection against CORM-3 follows its preincubation with histidine or methionine, but not with any other amino acid (only serine or alanine are shown in Figure 1). Furthermore, other sulphydryl-containing compounds like reduced glutathione, abrogated the inhibitory activity of CORM-3 in minimal media.

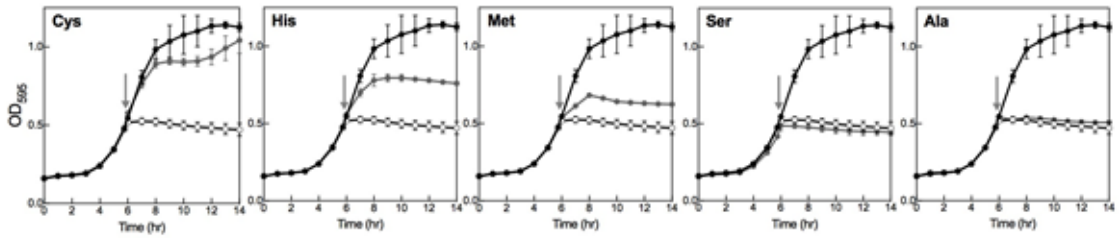


**Figure 1:** Effects of amino acids on the growth inhibitory effects of CORM-3. *E. coli* cell cultures were grown aerobically at 37°C in Glucose Defined Minimal Media in 96-well plates and then 60 □M CORM-3 alone (black line, open circles) or CORM-3 pre-mixed with 120 μM amino acid (grey line, grey circles) was added. Growth without reagent is shown for comparison (black line, closed circles). In controls 120 μM amino acid had no deleterious effects on growth. In order to test whether CORM-3 was reacting directly with the agents that attenuated its potency it was titrated against peptides Ala3XAla3 containing X=Cys or His or Met or Asp, and against reduced or oxidized glutathione, using NMR to monitor formation of complexes (Figure 2). With solution conditions similar to those of the growth experiments the strengths of interactions with CORM-3 were best with GSSH = cysteine >> His > Met > GSSG >> Asp. Consistently, CORM-3 was ineffective against growth of bacteria or mammalian cells when it was added to rich media already containing cysteine, glutathione, histidine, or methionine.

The buffer was 30 mM KPi pH ~ 7 – 7.6. Arrows show the direction of signal intensities upon increasing CORM-3 additions. (b) Binding curves of the decrease in intensity of $^1$H-NMR signals corresponding to: Cys (i), His (ii), Met (iii), GSH (iv) and GSSG (v). The estimated $K_d$ of CORM-3 to each peptide was determined to be: 5±3 µM for Cys, 800±100 µM for His, 4700 µM for Met, 4±2 µM for GSH and 9190±1000 µM for GSSG.

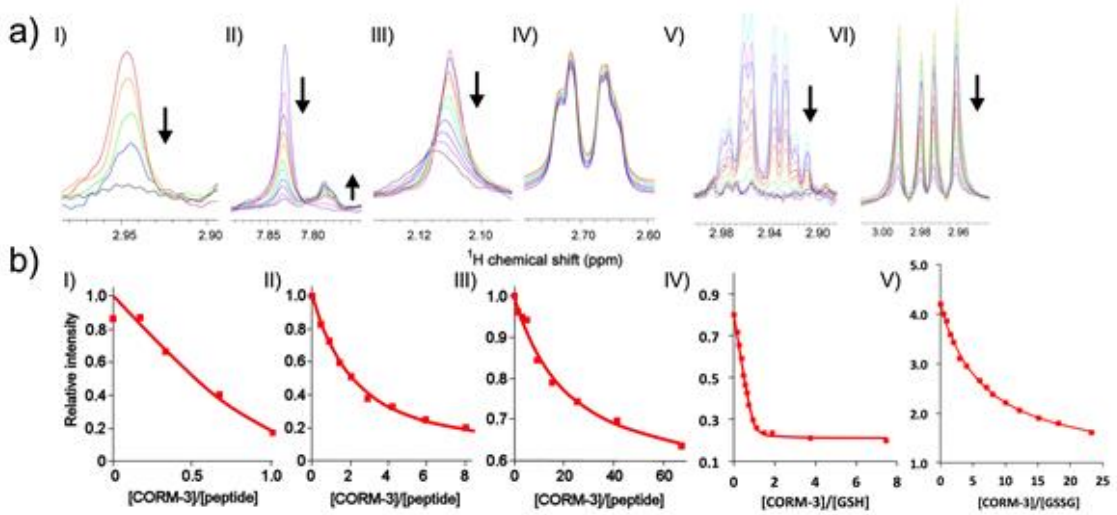


**Figure 2**: Binding affinities of CORM-3 to selected amino acids or glutathione determined by $^1$H-NMR. (a) $^1$H-NMR spectra of: (i) Cys Hβ of $A_3CA_3$ peptide titrated with 0-1.0 equivalents CORM-3; (ii) His aromatic proton region of $A_3HA_3$ with 0-18 equivalents CORM-3; (iii) Met Hε region of $A_3MA_3$ with 0 -134 equivalents CORM-3; (iv) Asp Hβ region of $A_3DA_3$ with 0 - 20 equivalents CORM-3; (v) GSH with **0**-5 equivalents CORM-3; and (VI) GSSG with 0 - 23 equivalents CORM-3.

A radically different explanation for the toxic biological activities of ruthenium carbonyl CORMs is that, rather than acting via release of CO, they are sources of Ru(II), which we now demonstrate can react with a range of cellular targets containing thiols and amino acids. These findings have important implications for understanding the pharmacological development of these agents against both bacterial and mammalian cells.

**Publications**

Southam, H.M., Smith, T.W., Lyon, R.L., Liao, C., Trevitt, C.R., Middlemiss, L.A., Cox, F.L., Chapman, J.A., El-Khamisy, S.F., Hippler, M., Williamson, M.P., Henderson, P.J.F. and Poole, R.K. (2018). A thiol reactive Ru(II) ion, not CO release, underlies the antimicrobial and cytotoxic properties of CO-releasing molecule-3 ($Ru(CO)_3Cl$(Glycinate)). *Redox Biol*. (**18**), 114-123.

Majd, H., King, M., Palmer, S.M., Smith, A., Elbourne, L.D.H., Paulsen, I.T., Sharples, D., Henderson, P.J.F. and Kunji, E.R.S. (2018) Screening of candidate substrates and coupling ions of transporters by thermostability shift assays. *Elife*. doi: 10.7554/eLife.38821.

Dilworth, M.V., Pie, M., Bettaney, K.E., Ma, P., Lu, J., Sharples, D., Poyne, D.R., Gros, S.R., Moncoq, K., Henderson, P.J.F., Miroux, B. and Bill, R.M. (2018). Microbial expression systems for membrane proteins. *Methods* 147, 3-39.

Papadaki, G.F., Ma, P., Ahmad, I., Calabrese, A.N., Baldwin, S.A. (deceased), Henderson, P.J.F., Diallinas, G. (2018) Membrane transport proteins. The nucleobase-cation-symport-1 family. In: Roberts G., Watts A., (eds) *Encyclopedia of Biophysics*. Springer, Berlin.

**Funding**

BBSRC, MRC and the Leverhulme Trust.

**Collaborators**

*University of Leeds*: Irshad Ahmad, Alison Ashcroft, Anton Calabrese, David Sharples.
*External*: Robert Poole, Mike Williamson, Edmund Kunji, Roslyn Bill, George Diallinas.

## Bacteria sensing their redox environment: tactic response of *Shewanella oneidensis* MR-1

Joseph Oram and Lars Jeuken

### Introduction

Exoelectrogenic bacteria can couple their metabolism to extracellular electron acceptors, including macroscopic electrodes, and this has applications in energy production, bioremediation and biosensing. Optimisation of these technologies relies on a detailed molecular understanding of extracellular electron transfer (EET) mechanisms, and *Shewanella oneidensis* MR-1 (MR-1) has become a model organism for such fundamental studies. Besides EET efficiency, performance is dependent on the exoelectrogens' ability to migrate towards and colonize insoluble electron acceptors (minerals). There has been a steady flow of reports focused on MR-1's tactic response to soluble electron acceptors, which can form concentration gradients, but, notably, contrasting models have been proposed for both EET and taxis of MR-1 to insoluble electron acceptors. Here, we have used electrochemical tools and video tracking experiments to study the mechanism of EET and taxis. Three distinct mechanisms have previously been proposed for MR-1 EET: 1) direct electron transfer (DET) between MR-1 and insoluble electron acceptors; 2) long-ranged DET through conductive "wires" formed by extrusions of the outer membrane and periplasm, in which electrons are thought to "hop" between the cytochromes that decorate these membrane extrusions; 3) mediated electron transfer (MET) achieved through self-secreted redox mediators, in particular riboflavin (RF) and flavin mononucleotide (FMN), which shuttle electrons between the outer membrane cytochromes and electrodes.

### Results

In order to distinguish between DET and MET mechanisms, an electrode surface was developed that was almost unable to react with flavins, in effect abolishing the MR-1 ability for MET. It was found that gold surfaces, modified with a self-modified monolayer (SAM) containing negatively-charged carboxylic acid groups, displayed irreversible electrochemistry with riboflavin, meaning that kinetics of flavin oxidation and reduction by the electrode are very slow. When these electrode surfaces were incubated with MR-1 for > 16 h, very small currents were observed around -0.2 V (vs Standard Hydrogen Electrode, SHE), consistent with the fact that these electrodes are unable to convert (ribo)flavin, which has a potential of ~ -0.2 V vs SHE. Instead, a clear signal is observed with an onset of about 0.2 V vs SHE, consistent with a potential that has previously been ascribed to a DET mechanism (Fig. 1, blue line).

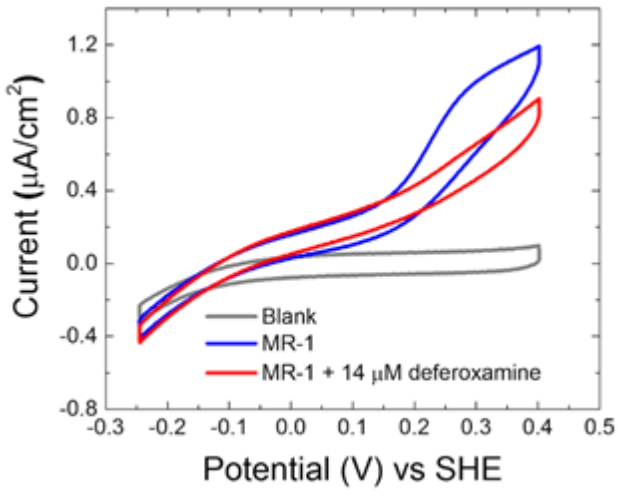


**Figure 1:** Cyclic voltammograms of MR-1 ($OD_{600}$=0.55) in 10 mM lactate, 20 mM MOPS, 30 mM $Na_2SO_4$ (pH 7.4), measured after 23 h incubation at +0.25 V (vs SHE, blue) and after addition of 14 μM deferoxamine and a further 30 min at 0.25 V (red), using an electrode modified with a mixed SAM of 8-mercaptooctanol and 8-mercapto-octanoic acid. The baseline (grey) was measured before addition of MR-1. All scans start at the 0 V. Scan rate=0.01 V/s.

Importantly, after a long and detailed characterisation of the growth media and bacterial suspension, it was observed that the signal onset of ~ +0.2 V also coincides with the reduction potential of iron-lactate, where iron is a required nutrient of MR-1 and lactate an extremely common carbon and energy source in these types of experiments. Addition of an iron chelator

like deferoxamine, indeed resulted in an immediate and strong reduction of the signal with an onset of +0.2 V. We thus conclude that signals at +0.2 V previously attributed to a DET mechanism could in many cases be attributed to a MET mechanisms where electron transfer is mediated by iron or iron-lactate.

To study the tactic behaviour of MR-1, an experimental platform was developed that can specifically inspect taxis of MR-1 around electrodes with defined electrode potentials (in a three electrode system). In these systems the redox state of extracellular redox compounds such as flavins can be controlled close to the electrode. Within the first 20 minutes after loading and sealing an electrochemical cell with MR-1, a high proportion (>70%) of bacteria displayed high motility throughout the cell with no relationship towards the electrode. This is expected as after sealing the cell, MR-1 will consume oxygen still dissolved in the medium. Between 20 to 60 min, however, the motility gradually decreases as oxygen is consumed. Taxis of MR-1 was quantified by video tracking experiments. Two key parameters are presented here: average velocity of all motile bacteria within an area (for bacteria with velocities >4 µm/s) and motile population density, which is the density of bacteria with mean velocities >4 µm/s in a specified area. Tracking analysis shows that when oxidative potentials are applied (0.3 V vs SHE), motile MR-1 bacteria accumulate close to the electrode (Fig. 2). These effects are stronger if an additional 2 µM riboflavin is added to the capillary cell and importantly, a switch in behaviour is observed at a potential of about -0.2V, i.e. the redox potential of riboflavin. This strongly suggests that MR-1 is able to sense the redox state of flavin in its surrounding and migrate towards regions in which the flavins are more oxidised, i.e. towards the electrode.

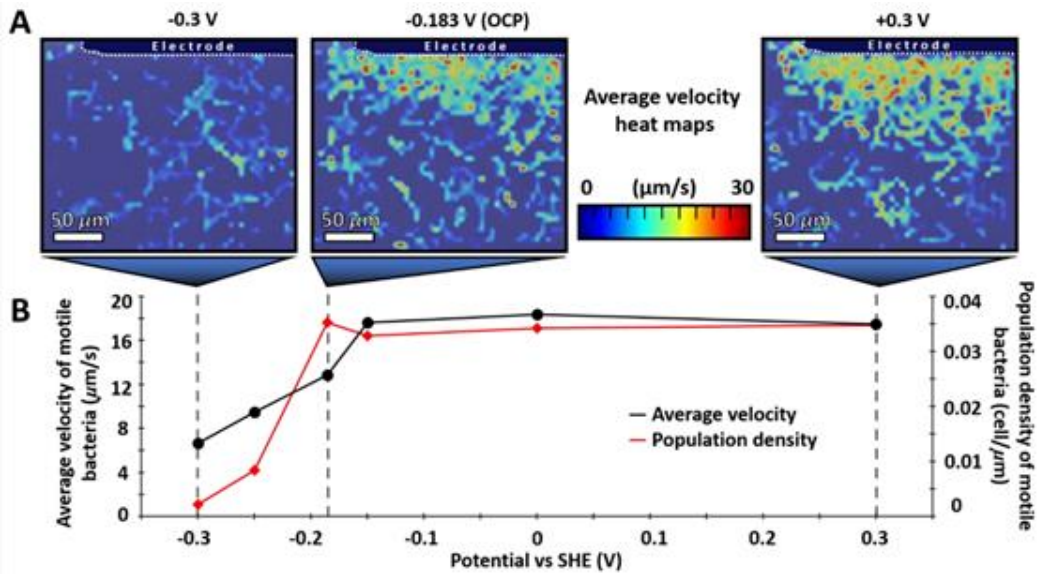


**Figure 2**: A) Average velocity of MR-1 (presented as heatmaps) for three potentials (-0.3, -0.183, and +0.3 V vs SHE). B) Overlaid plots of the motile population density (red) and average velocity (black) of MR-1, within 20 µm of the electrode surface as a function of the electrochemical potential.

In summary, we propose that besides self-secreted flavins, MR-1 can utilise iron or iron lactate to transport respiratory electrons to insoluble electron acceptors. Furthermore, excreted flavins do not only act as redox mediators, but also as redox sensors, and could be an important factor for MR-1's survival in electron acceptor limited niches.

**Publications**

Oram, J., Jeuken, L.J.C. (2018) Tactic response of *Shewanella oneidensis* MR-1 towards insoluble electron acceptors, *mBio*, **10**, e02490-18.

**Funding**

This work was funded by the ERC and the BBSRC

## Molecular dynamics simulations reveal a near full-length model of the anion exchanger 1 and its interactions with lipids

Dario De Vecchis and Antreas Kalli

### Introduction

Anion exchanger 1 (AE1, Band 3, SLC4A1) is a glycoprotein responsible for the exchange of bicarbonate and chloride across the red blood cell plasma membrane. Mutations found on AE1 result in diseases such as Southeast Asian ovalocytosis and distal renal tubular acidosis. Human AE1 is a dimer consisting of a N-terminal cytoplasmic domain (cdAE1) and a C-terminal membrane domain (mdAE1) responsible for its transport function. The mdAE1 monomer consists of 14 transmembrane (TM) helices organized as two 7+7 inverted repeats. Each monomer consists of a core domain (TM helices 1-4 and 8-11) and a gate domain (TM helices 5-7 and 12-14). It is the relative movement of these two domains that allows ion transport, although the molecular details of this movement are still unknown. The cdAE1 functions as an anchoring site for cytoplasmic proteins. Crystal structures of both the mdAE1 and the cdAE1 domains have been obtained separately but a structure of the complete AE1 is not available. Additionally, it has been shown that AE1 function is regulated by lipids, e.g. enriched levels of cholesterol decrease AE1 transport activity.

In mature red blood cells AE1 interacts with Glycophorin A (GPA) to form the Wright (Wr) blood group antigen. This interaction involves the specific interaction of Glu658 in AE1 with Arg61 in GPA. Whilst there are structural data for both the AE1 and GPA, the molecular details of this complex are elusive. In this study we integrated molecular modelling and molecular dynamics simulations at different resolutions (i.e. coarse-grained and all-atom simulations) to study the interaction of AE1 with GPA, and to construct a near full-length model of AE1. Moreover, our simulations were performed in a complex bilayer that resembles the native red blood cell plasma membrane. This enabled us to gain novel insights into the dynamic interactions of AE1 with lipids.

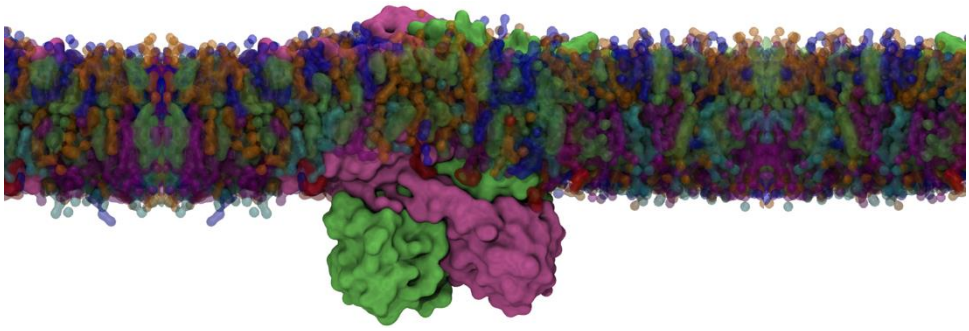

**Figure 1: AE1 in a complex bilayer.** Structure of the dimeric form of AE1 inserted in a complex bilayer that resembles the red blood cell plasma membrane. The AE1 dimer subunits are shown in green and pink, respectively. The different lipids in the bilayer are shown in different colors.

### Results

To study the interactions of AE1 with lipid molecules, we first inserted the transmembrane region of AE1 (mdAE1) in an asymmetric native-like model red blood cell plasma membrane, containing POPC, sphingomyelin, POPE and cholesterol in the outer leaflet and POPC, sphingomyelin, POPE, cholesterol, POPS and $PIP_2$ lipids in the inner leaflet. Analysis of the interactions of mdAE1 with the different lipids revealed that a discontinuous anionic annulus was formed around mdAE1 in the inner bilayer leaflet. Cholesterol also interacted preferentially with mdAE1. The crystal structure of the mdAE1 revealed a rather large cavity in the interface between the two mdAE1 monomers. Interestingly, in our simulations this cavity is occupied by cholesterol. This suggests that lipids may regulate the interaction between the mdAE1 monomers.

As mentioned above AE1 interacts directly with GPA to form the Wright (Wr) blood group antigen. To study the AE1/GPA interactions, we added the transmembrane helical region of the GPA and two mdAE1 dimers in a complex bilayer. These simulations demonstrated that GPA associates with mdAE1 not only via an interaction of Arg61 with Glu658 but also via additional interactions of the transmembrane and extracellular parts of GPA with mdAE1. The interactions of the mdAE1 in the GPA/mdAE1 complex with lipids were similar to the interactions seen for mdAE1 alone (above). Interactions of basic residues on the cytosolic site of GPA with $PIP_2$ molecules were also observed.

To model the complete AE1, the mdAE1 and the cdAE1 domains were positioned away from each other and a linker region was modelled to connect these two domains. The model of the complete AE1 was inserted in an asymmetric native-like red blood cell bilayer and simulated at the coarse-grained and the atomistic resolutions. During the simulations the cdAE1 diffuses in the aqueous environment before interacting with the membrane domain and the lipid bilayer (Figure 1). Interestingly, our results reveal that the linker region is positioned at the interface of mdAE1 and cdAE1. AE1 residues that were shown to interact with cytoskeleton proteins are exposed to the solvent in some of our models indicating that those models are in good agreement with available biophysical and biochemical data.

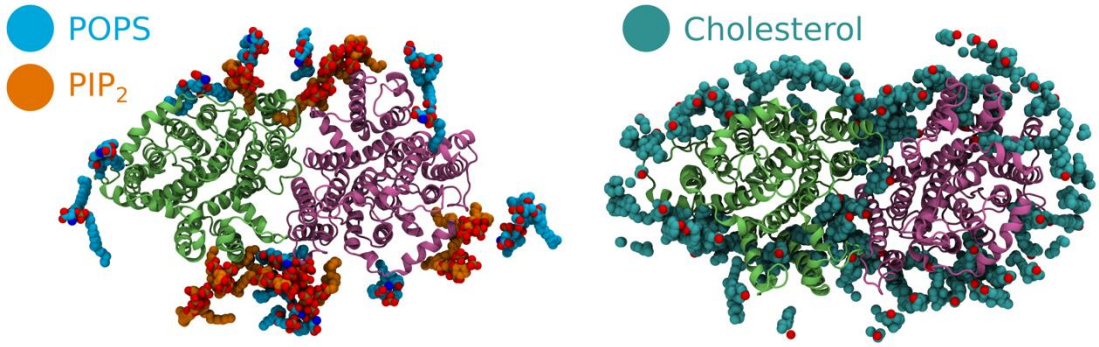


**Figure 2: Interaction of AE1 with lipids.** Snapshots from a simulation with our AE1 model showing the interactions of mdAE1 dimer (green and pink ribbon) with anionic lipids (POPS and $PIP_2$) and cholesterol. The cdAE1 is omitted for clarity.

Analysis of the interactions of AE1 with different lipids showed that in the presence of the cdAE1, the mdAE1 still interacts preferentially with anionic phospholipids present in the inner leaflet (i.e. $PIP_2$ and POPS) via conserved positive residues (Figure 2). Similar to the simulations with the mdAE1, the cavity between the two monomers is occupied by cholesterol (Figure 2). This augments our previous observation that cholesterol may stabilize the mdAE1 dimer interface.

In summary, our results provide novel information about the interaction of AE1 with lipid molecules and with its partner protein GPA. Using simulations, we were also able to construct a near-complete model of AE1 that demonstrates the orientation of the cdAE1 with respect the mdAE1.

**Publications**

Kalli, A. C. & Reithmeier, R. A. F. (2018) Interaction of the human erythrocyte Band 3 anion exchanger 1 (AE1, SLC4A1) with lipids and glycophorin A: Molecular organization of the Wright (Wr) blood group antigen. *PLOS Comput. Biol.* **14**, e1006284.

**Funding**

This work was funded by the Academy of Medical Sciences and the Wellcome Trust.

**Collaborators**

*External:* Reinhart Reithmeier (Dept. of Biochemistry, University of Toronto).

## Direct, rigorous determination of the pre-exponential factor of protein folding dynamics

Sergei Krivov

### Introduction

A fundamental problem in the analysis of protein folding dynamics, and an active area of research, is the determination of the free energy barrier ΔF and the pre-exponential factor $k_0$, which are related to the folding rate as $k_f = k_0 e^{-\Delta F/kT}$. *Direct* determination of these quantities by experiment has been hampered by very limited spatial and temporal resolution. The situation has significantly improved recently. For example, one can now directly estimate the transition path times by counting single photons. However, the interpretation of the experiments still assumes a particular shape of the folding free energy landscape, which cannot be established in a direct manner. Thus, even state of the art experimental techniques cannot determine the pre-exponential factor in a direct and rigorous manner.

### Results

Protein folding dynamics can be described as a diffusion on a free energy landscape – free energy as a function of reaction coordinates (RC). For the description to be quantitatively accurate, RCs should be chosen in an optimal way. In this case the corresponding diffusive model can be used to compute some properties of the dynamics exactly. For protein folding dynamics, such a coordinate is known as the committor or $p_{fold}$ - the probability to fold before unfolding, starting from the current position. Diffusion on a free energy profile as a function of $p_{fold}$ can be used to compute exactly the equilibrium flux, the mean first passage times, and the mean transition path times between any two points on the profile. Thus, it suggests a possible way for direct and rigorous determination of the pre-exponential factor. However, determination of the $p_{fold}$ for a practical system is a very difficult problem. Recently we have suggested an adaptive non-parametric approach to accurately determine the committor RC for an equilibrium trajectory of a realistic system. The non-parametric nature of the approach means that it determines numerical values of the $p_{fold}$ coordinate for every snapshot of the trajectory, rather then the parameters of some functional form approximating the RC. The approach is completely data-driven and requires no system-specific information.

Using the developed approach, we have determined the $p_{fold}$ coordinate for an equilibrium folding−unfolding trajectory of HP35 Nle/Nle double mutant consisting of 1509392 snapshots at 380 K, obtained by the Shaw group. Fig. 1 shows the corresponding free energy profile.

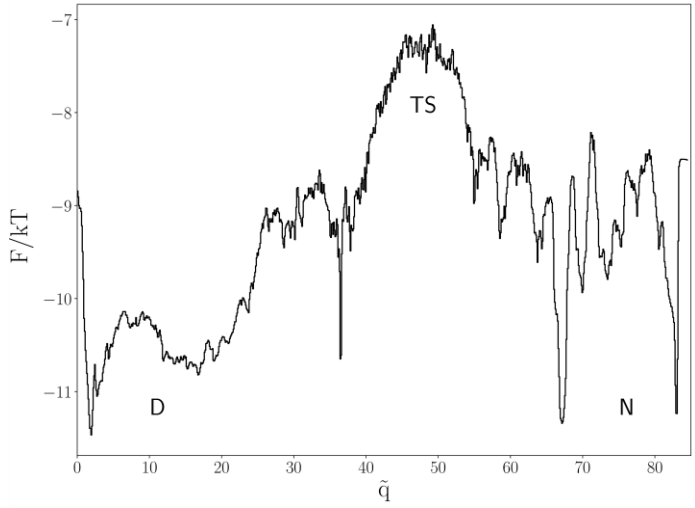


**Figure 1:** The free energy profile of HP35 as a function of rescaled $p_{fold}$ coordinate. The $p_{fold}$ reaction coordinate is monotonically transformed (rescaled) to new coordinate q̃, so that the diffusion coefficient is constant D(q̃)=1. The landscape shows the denatured (D), native (N) and transition (TS) states. The native state has sub-states, separated by high barriers, in agreement with experiment.

The free energy profile F(q̃) with the diffusion coefficient D(q̃)=1 define a diffusive model of the protein folding dynamics. According to the theory this model can be used to compute exactly the equilibrium flux $J_{AB} = N_{AB}/T$, where T is the trajectory length and $N_{AB}$ is the number of transitions between the boundary states A and B; the mean first passage times (mfpt); and the mean transition path times (mtpt); between any two points on the profile. Table 1 compares these quantities computed from the model and directly from the trajectory.

**Table 1. Comparison of the dynamical quantities computed from the diffusive model and directly from the trajectory.** The numbers show the latter, while percentages in the brackets show the relative difference between the two. Times are given in ns.

| q̃(a) | q̃(b) | $N_{ab}$ | $mfpt_{ab}$ | $mfpt_{ba}$ | $mtpt_{ab}$ |
|---|---|---|---|---|---|
| 0 | 84.5 | 73 (0.1%) | 3034 (0.1%) | 1101 (-0.1%) | 234 (-4%) |
| 1.7 | 83 | 75 (2%) | 3032 (-3%) | 1102 (-2%) | 208 (-8%) |
| 17 | 68 | 89 (3%) | 2547 (-3%) | 962 (-3%) | 66 (-13%) |
| 36.5 | 58.6 | 115 (8%) | 2027 (-7%) | 750 (-7%) | 10.7 (-1%) |
| 38 | 55 | 127 (12%) | 1959 (-11%) | 712 (-11%) | 7.8 (-13%) |

Having determined the optimal RC q̃ and the corresponding FEP F(q̃), which provide a quantitative description of the folding dynamics, we are now in a position to rigorously determine the pre-exponential factor in a direct manner. For example, taking the folding barrier of 4kT (Figure 1) and $k_f^{-1}=\tau_f$=3034 ns (Table 1), one finds a rough estimate of $k_0^{-1}$ of 55 ns. Two other, more accurate estimates, the harmonic approximation to the Kramer's equation and Szabo's relation between $k_0$ and the mtpt, give $k_0^{-1}$ equal to 27 ns and 24 ns, respectively.

In summary, we have determined, for the first time, the $p_{fold}$ coordinate for a realistic protein folding trajectory, and the corresponding free energy landscape, which provides a quantitatively accurate description of the folding dynamics. In particular, it reproduces the important dynamical quantities exactly, up to statistical uncertainty. We emphasize that no fitting of the parameters of the diffusive models was employed and that an accurate description is achieved at the trajectory time scale of 0.2 ns. Based on that, we have obtained a direct rigorous estimate for the pre-exponential factor of folding dynamics.

**Publications**

Krivov S.V. (2018) Protein Folding Free Energy Landscape along the Committor – the Optimal Folding Coordinate. *J. Chem. Theor. Comput.* **14 (18)**, 3418-3427.

**Funding**

This work was partially funded by BBSRC.

## Receptor tyrosine kinase signalling in the absence of growth factor stimulation: response to cellular stress

Eleanor Cawthorne, Janne Darell, Christopher Jones, Sabine Knapp,
Chi-Chuan Lin, Dovile Milonaityte, Arndt Rohwedder, Caroline Seiler and John Ladbury

### Introduction

Receptor tyrosine kinases (RTKs) expressed on the plasma membrane of cells in normal tissue are rarely exposed to high concentrations of extracellular growth factors. Nonetheless they express proteins associated with kinase-mediated signalling. We are interested in the signalling associated with these proteins that occurs under basal conditions (which are close to the conditions experienced by normal tissue. In the absence of extracellular stimulation or genetic mutation, an oncogenic response can be driven by the competitive binding of SH3 domain-containing downstream effector proteins to proline-rich sequences on growth factor receptors. Of the approximately 50 plasma membrane receptor tyrosine kinases (RTKs) the majority have proline-rich sequences in their C-termini. These have a propensity to bind to the >300 proteins expressed in human cells which contain SH3 domains. These interactions occur in the absence of any extracellular stimulation (e.g. growth factors, cytokines). Proline-rich sequence binding to SH3 domains are promiscuous and the observed interactions with RTKs are dependent on the relative concentrations of the proteins involved.

We previously established that under non-stimulatory conditions the fibroblast growth factor receptor 2 (FGFR2) recruits the adaptor protein, growth factor receptor binding protein 2 (Grb2) through its C-terminal SH3 domain. In cells depleted of Grb2 other proteins can access the proline-rich motif on FGFR2. One of these proteins, phospholipase C(gamma)1 (Plcγ1) is activated on binding and through turnover of plasma membrane phospholipids to produce second messengers, raises cellular calcium levels which are responsible for increased cell motility and invasive behaviour. In ovarian and lung adenocarcinoma patients with low levels of Grb2 and increased expression of Plcγ1 higher incidence of metastasis leads to greatly reduced survival outcomes.

The dependence of signalling described above on respective concentrations of RTKs and SH3 domain containing proteins mean that there is no on-off switch for this form of signalling, the outcomes are dictated solely by fluctuations of protein concentrations. As a result one key driver for this form of signalling is cellular stress. We are working to establish how stresses experienced by tissue (e.g. pH change associated with acid reflux in the oesophagus) can lead to cancer outcomes.

### Results

We have extended our studies in this area to explore other RTK-SH3 domain-containing protein interactions to establish whether the up-regulation of signal transduction through these interactions is a general phenomenon. This leads to the hypothesis that two tiers of intracellular signalling can be derived from receptors with intrinsic protein kinase activity:
1) Ligand-induced elevation in kinase activity resulting in tyrosylphosphate-mediated effector protein recruitment and committal to a defined cellular outcome (e.g. proliferation).
2) Receptor phosphorylation-independent activation of downstream effectors through SH3 domain/proline-rich sequence interactions, which appear to be required for cell homeostasis/metabolic control.

Hyperactivity of the tier 1 signalling is a feature of receptor tyrosine kinase-related cancers arising from genetic mutation. Although the tier 2 signalling mechanism occurs under basal conditions, and is thus likely to be associated with cellular maintenance, we have shown that fluctuations in expression levels of SH3-containing proteins can drive cells into pathological phenotypes including proliferation and metastasis.

We are testing this hypothesis with a range of methods extending from cell-based assays (including fluorescence lifetime imaging microscopy) through to structural and in vitro biophysical analysis.

We are optimising a screening protocol to establish the extent of tier 2 signalling in a range of cells and conditions. We have identified novel interactions involving well studied proteins as well as less understood systems. These are being validated and phenotypic outcomes of knocking down these interactions are being explored to establish the effects of signalling in normal tissue.

We have focused on gastro-intestinal cancers we have begun to explore the effects of stress on intracellular protein expression and the outcomes on tier 2 signalling. We have shown that by mimicking conditions experienced in the GI tract we can affect expression of receptor tyrosine kinases.

In addition to identifying the signalling pathways which are initiated as a result of fluctuations in protein concentrations in cell-based assays, we are exploring the interactions associated with up-regulation of Tier 2 signalling using both biophysical and structural biological methods. High resolution structural detail on the receptor-ligand interactions are providing invaluable detail on the mode of recruitment of signalling proteins as well as information towards potential inhibition of aberrant pathways that lead to pathogenic outcome.

**Publications**

Honda A., Kita T., Seshadri S.V., Misaki K., Ahmed Z., Ladbury J.E., Richardson G.P., Yonemura S. & Ladher R.K. (2018) FGFR1-mediated protocadherin-15 loading mediates cargo specificity during intraflagellar transport in inner ear hair-cell kinocilia. *Proc Natl Acad Sci USA* **115**:8388-8393.

Suen K.M., Lin C.C., Seiler C., George R., Poncet-Montange G., Biter A.B., Ahmed Z., Arold S.T. & Ladbury J.E. (2018) Phosphorylation of threonine residues on Shc promotes ligand binding and mediates crosstalk between MAPK and Akt pathways in breast cancer cells. *Int J Biochem Cell Biol* **94**:89-97.

**Funding**

This work is funded by Cancer Research UK.

**Collaborators**

*University of Leeds:* Prof. Phillip Quirke, Prof. Susan Short, Prof. Alex. Breeze, Dr. Darren Tomlinson

*External:* Prof. Zamal Ahmed, Prof. Mien-Chie Hung, Swathi Arur (University of Texas MD Anderson Cancer Center, USA), Mikhail Bogdanov (University of Texas, USA), Richard Grose (Barts Cancer Institute, London).

## Understanding the mechanisms by which small DNA tumour viruses cause disease

Ethan Morgan, Margarita Panou, David Kealy, Gemma Swinscoe, Michelle Antoni, James Scarth, Molly Patterson, Corinna Brockhaus, Eleni-Anna Loundras and Andrew Macdonald

### Introduction

Small DNA tumour viruses are the causative agents of severe diseases in humans. Notable examples include cervical cancer, which is exclusively associated with infection with human papillomaviruses, and polyomavirus-associated nephropathy (PVAN) and Merkel cell carcinoma (MCC) caused by the BK and MCV polyomaviruses. We undertake a broad ranging analysis of these viruses to identify new targets for therapeutic intervention.

### Results

Human papillomavirus: Infection with HPV causes ~6% of human cancers, including nearly all cervical carcinomas as well as head and neck squamous carcinomas (HNSCC). Despite FDA-approved prophylactic vaccines, the burden of HPV-associated malignancy will remain high for decades due to their limited availability in low income countries, poor coverage where access is possible, and the long latency period separating infection from carcinogenesis. Although HPV-specific antivirals are needed, their development is hindered by an incomplete understanding of the virus life cycle and essential interactions with host factors within the infected keratinocyte.

Using an approach incorporating molecular and cellular biology with cutting edge cell culture and cancer models further informed by patient samples we explore the roles of the HPV oncoproteins in the virus life cycle and in transformation. We demonstrated that the host transcription factor STAT3 is absolutely essential for the HPV18 life cycle in primary human keratinocytes. Ablation of STAT3 function using small molecule inhibitors, siRNA depletion or expression of dominant negative forms of STAT3 impaired HPV transcription and led to a loss of the characteristic proliferation observed in keratinocytes infected with HPV. Using cytology samples from patients with cervical disease we saw an increase in STAT3 activation that correlated with cervical disease progression. Together, these studies show that STAT3 is an essential host factor for HPV, that STAT3 is deregulated in HPV cancers and as such is a potential target for anti-HPV therapeutics in cancer.

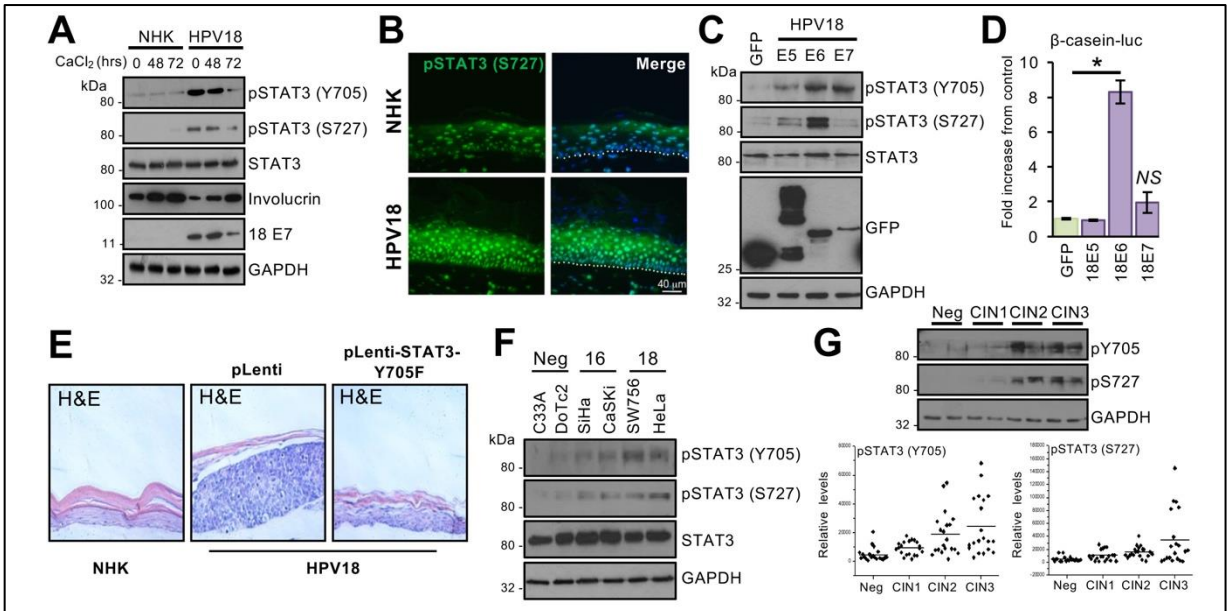


**Figure 1: STAT3 is activated during the productive HPV18 life cycle and in HPV positive cancer.** Levels of STAT3 phosphorylation are increased in primary human foreskin keratinocytes harbouring the HPV18 genome differentiated in (A) monolayer culture or (B) stratified in three dimensional organotypic raft culture. (C) Expression of the E6 oncoprotein leads to the dual phosphorylation of STAT3. (D) Expression of the E6 oncoprotein increases STAT3 activity. (E) Active STAT3 is essential for the hyperplasia observed in HPV18 containing stratified epithelia. (F) Levels of total and phosphorylated STAT3 are increased in HPV positive compared to HPV negative cervical cancer lines. (G) Western blot analysis of cervical biopsy samples (n=80) correlates increased STAT3 phosphorylation with cervical disease progression. *p<0.05.

Human polyomaviruses: Despite their clear association with disease there is a paucity of understanding of polyomavirus biology and as such we aim to understand their life cycles and to identify novel targets for antiviral therapeutics. With Prof. Adrian Whitehouse we identified mechanisms of MCV-mediated cancer metastasis. With Prof. Neil Ranson we are using the latest advances in cryo-electron microscopy to gain an unprecedented understanding of the fundamental make-up of polyomavirus particles and how they mediate their interactions with host receptor molecules. This information may herald crucial advances in antiviral drug design.

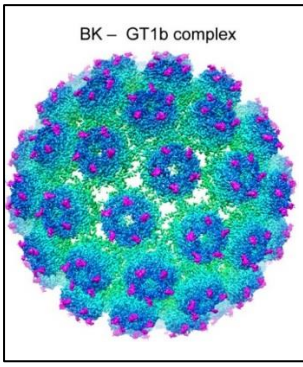


**Figure 2: High-resolution structure of infectious BKV alone or in complex with GT1b ganglioside.** Frozen, hydrated native BKV particles were individually recorded using a direct electron detecting camera to obtain a 3.4 angstrom resolution structure.

## Publications

Nwogu N., Boyne J.R., Dobson S.J., Poterlowicz K., Blair G.E., Macdonald A., Mankouri J. & Whitehouse A. (2018) Cellular sheddases are induced by Merkel cell polyomavirus small tumour antigen to mediate cell dissociation and invasiveness. *PLoS Pathog* **14**: e1007276.

Wetherill L.F., Wasson C.W., Swinscoe G., Kealy D., Foster R., Griffin S. & Macdonald A. (2018) Alkyl-imino sugars inhibit the pro-oncogenic ion channel function of human papillomavirus (HPV) e5. *Antiviral Res* **158**:113-121.

Morgan E.L., Wasson C.W., Hanson L., Kealy D., Pentland I., Mcguire V., Scarpini C., Coleman N., Arthur J.S.C., Parish J.L*., et al.* (2018) STAT3 activation by E6 is essential for the differentiation-dependent HPV18 life cycle. *PLoS Pathog* **14**:e1006975.

Hurdiss D.L., Frank M., Snowden J.S., Macdonald A. & Ranson N.A. (2018) The structure of an infectious human polyomavirus and its interactions with cellular receptors. *Structure* **26**:839-847.

Panou M.M., Prescott E.L., Hurdiss D.L., Swinscoe G., Hollinshead M., Caller L.G., Morgan E.L., Carlisle L., Muller M., Antoni M*., et al.* (2018) Agnoprotein is an essential egress factor during BK polyomavirus infection. *Int J Mol Sci* **19**: E902.

Stakaityte G., Nwogu N., Dobson S.J., Knight L.M., Wasson C.W., Salguero F.J., Blackbourn D.J., Blair G.E., Mankouri J., Macdonald A*., et al.* (2018) Merkel cell polyomavirus small t antigen drives cell motility via Ro-GTPase-induced filopodium formation. *J Virol* **92**:e00940-17.

Stakaityte G., Nwogu N., Lippiat J.D., Blair G.E., Poterlowicz K., Boyne J.R., Macdonald A., Mankouri J. & Whitehouse A. (2018) The cellular chloride channels CLIC1 and CLIC4 contribute to virus-mediated cell motility. *J Biol Chem* **293**:4582-4590.

## Funding

This work was funded by Wellcome Trust, the MRC, the BBSRC, Kidney Research UK and the Faculty of Biological Sciences, University of Leeds.

## Collaborators

*University of Leeds:* Neil Ranson (FBS), Adrian Whitehouse (FBS), Richard Foster (MAPS) Adel Samson (FMH) and Stephen Griffin (FMH).
*External:* Sally Roberts and Joanna Parish (University of Birmingham).

## Bunyavirus requirement for endosomal $K^+$ reveals new roles of cellular ion channels during infection

Samantha Hover, Becky Foster, Juan Fontana, John Barr and Jamel Mankouri

### Introduction

To penetrate cells and cause disease most viruses traverse the cellular endocytic network and exploit its environment to trigger the release of their genetic material into the cytosol. Endosomal pH, virus-receptor interactions, proteolytic cleavage, and the lipid composition of membranes have all been previously reported to act as endosomal triggers. Here, we reveal the identity of an additional critical endosomal trigger for virus entry, namely a requirement for exposure to specific $K^+$ ion concentrations, which we demonstrate is regulated by cellular $K^+$ channels. We show that by blocking $K^+$ channels, we can disrupt the $K^+$ concentration across the endosomal system, impeding virus trafficking.

### Results

Previously we demonstrated that several bunyaviruses, which comprise the largest family of negative sense RNA viruses, require the activity of cellular potassium ($K^+$) channels to cause productive infection. Specifically, we demonstrated a surprising role for $K^+$ channels during virus endosomal trafficking. In this study, we have used the prototype bunyavirus, Bunyamwera virus (BUNV), as a tool to understand why $K^+$ channels are required for progression of these viruses through the endocytic network. We report three major findings: First, the production of a dual fluorescently labelled bunyavirus to visualize virus trafficking in live cells (Figure 1). Secondly, we show that BUNV traffics through endosomes containing high [$K^+$] and that these $K^+$ ions influence the infectivity of virions. Thirdly, we show that $K^+$ channel inhibition can alter the distribution of $K^+$ across the endosomal system and arrest virus trafficking in endosomes. These data suggest high endosomal [$K^+$] is a critical cue that is required for virus infection, and is controlled by cellular $K^+$ channels resident within the endosome network. This highlights cellular $K^+$ channels as druggable targets to impede virus entry, infection and disease.

### Publications

Selvaraj M., Yegambaram K., Todd E., Richard C.A., Dods R.L., Pangratiou G.M., Trinh C.H., Moul S.L., Murphy J.C., Mankouri J.*, et al.* (2018) The structure of the human respiratory syncytial virus m2-1 protein bound to the interaction domain of the phosphoprotein p defines the orientation of the complex. *MBio* **9**:e01554-18.

Nwogu N., Boyne J.R., Dobson S.J., Poterlowicz K., Blair G.E., Macdonald A., Mankouri J. & Whitehouse A. (2018) Cellular sheddases are induced by Merkel cell polyomavirus small tumour antigen to mediate cell dissociation and invasiveness. *PLoS Pathog* **14**: e1007276.

Punch E.K., Hover S., Blest H.T.W., Fuller J., Hewson R., Fontana J., Mankouri J. & Barr J.N. (2018) Potassium is a trigger for conformational change in the fusion spike of an enveloped RNA virus. *J Biol Chem* **293**:9937-9944.

Stakaityte G., Nwogu N., Lippiat J.D., Blair G.E., Poterlowicz K., Boyne J.R., Macdonald A., Mankouri J. & Whitehouse A. (2018) The cellular chloride channels CLIC1 and CLIC4 contribute to virus-mediated cell motility. *J Biol Chem* **293**:4582-4590.

Hover S., Foster B., Fontana J., Kohl A., Goldstein S.A.N., Barr J.N. & Mankouri J. (2018) Bunyavirus requirement for endosomal $K^+$ reveals new roles of cellular ion channels during infection. *PLoS Pathog* **14**:e1006845.

Stakaityte G., Nwogu N., Dobson S.J., Knight L.M., Wasson C.W., Salguero F.J., Blackbourn D.J., Blair G.E., Mankouri J., Macdonald A.*, et al.* (2018) Merkel cell polyomavirus small t antigen drives cell motility via Ro-GTPase-induced filopodium formation. *J Virol* **92**:e00940-17.

**Funding**
This work was funded by the Royal Society and the University of Leeds.

**Collaborators**
*External:* Alan Kohl (MRC-University of Glasgow Centre for Virus Research), Steve Goldstein (Loyola University Chicago).

## Electron microscopy of membrane proteins to underpin structure guided inhibitor design

David Klebl, Rachel Johnson, Dimitrios Kontziampasis and Stephen Muench

### Introduction

Structure based drug design has traditionally been underpinned by X-ray crystallography and NMR. However, recent developments in the electron microscopy (EM) field have led to a step change in our ability to solve the “high resolution” structure of previously intractable systems. This is exemplified by the sudden expansion in membrane protein structures solved revealing new insights into structure, mechanism and regulation. My group are developing new opportunities within the EM field in two areas. The first is by developing new grid making technology that can rapidly freeze grids and capture changes in structure in the low ms timeframe (>10ms) during catalysis/function. The second is in in the use of new methodologies for stabilizing membrane proteins, for example, styrene maleic acid co-polymer lipoproteins (SMALPs).

### Results

Our fundamental understanding of biological processes is often underpinned by structural biology, which ultimately may assist our ability to design tailored medicines through structure-based drug design. However, current structural biology methods typically yield structural snapshots of a given stable state of an otherwise dynamic protein system. Time-resolved structural biology approaches aim to trigger a reaction and then capture structural changes after defined time delays to capture new catalytic states. The progress of time-resolved methodologies within EM has been slow due to limitations with microscope design, data collection throughput, resolution and reproducibility of the grids. Backed by the significant investment in EM at Leeds our group (in collaboration with Prof White) have developed a unique apparatus that is capable of using voltage assisted spraying of a sample to trigger a reaction and trap different states after ~7ms time delay. The first approach relies on an EM grid being pre-blotted before spraying a substrate to trigger a reaction on the EM grid which is subsequently vitrified in liquid ethane to stop the reaction within >7ms. The second approach relies on the mixing of two samples (substrate and reactant) as they are sprayed onto an EM grid which is subsequently vitrified in liquid ethane. We have now used this setup to prepare EM grids capable of producing sub 4Å structures (Figure 1A).

The group have been using single particle cryo-EM to inform on inhibitor binding to a range of target proteins. This year we published our work on imidazoleglycerol-phosphate dehydratase (IGPD), a herbicide and antimicrobial target that is involved in histidine biosynthesis (Figure 1B). Through single particle cryo-EM we have shown that differences in potency between plant and yeast IGPD is a result of an ~30 amino acid insert that forms additional interactions with the inhibitor binding loop. The group have also been studying cytochrome *bc*1, a validated antimalarial drug target. Through single particle cryo-EM we have now established a robust structure determination pipeline to produce several inhibitor bound structures of cytochrome *bc*1 to a resolution where we can identify the bound inhibitor to feed into our structure based drug design pipelines. The group is also working with pharmaceutical partners, (GlaxoSmithKline and UCB pharma) through a joint BBSRC grant to study a range of systems and develop new methodologies for EM.

To improve our structural data on membrane proteins the group have been studying new ways to extract and isolate membrane proteins in more “native” environments through the use of styrene maleic acid (SMA) co-polymers. These polymers cut the membrane into lipid particles (SMALPs) enclosing the membrane protein by native lipid, which often results in higher activity than detergent solubilized counterparts. This year we published *Escherichia coli* multidrug efflux transporter AcrB in a SMALP scaffold to sub-nm resolution using single particle cryo-EM and now have ~4.0Å single particle structures using SMA based polymers.

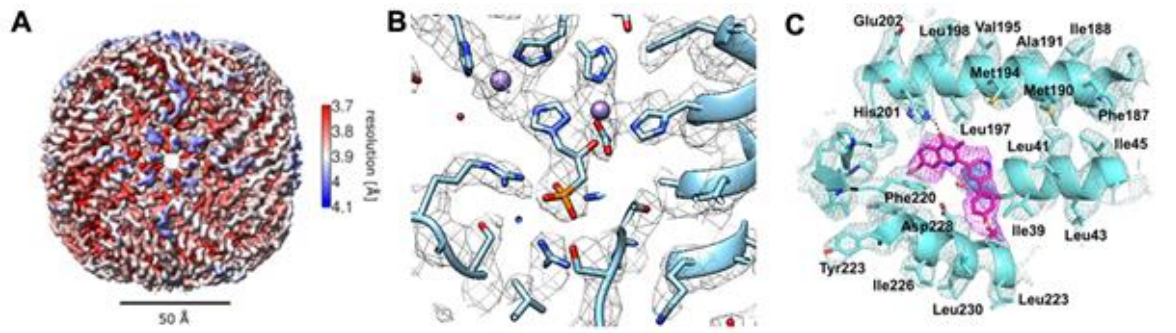


**Figure 1.** A) Single particle cryo-EM reconstruction of apoferritin from grids prepared on the new freezing setup. Cryo-EM maps of Arabidopsis IGPD (B) and bovine cytochrome *bc*1 (C) with bound inhibitor.

## Publications


Rawson, S., Bisson, C., Hurdiss, D., Fazal, A., McPhillie, M., Sedelnikova, S., Baker, P., Rice, D.W., Muench, S.P. (2018) Elucidating the structural basis for differing enzyme inhibitor potency by cryo-EM. *Proc. Natl. Acad. Sci.* **115**: 1795-1800.

Amporndanai, K., Johnson, R.M., O'Neil, P.M., Fishwick, C.W.G., Jamson, A.H., Rawson, S., Muench, S.P., Hasnain, S.S. & Antonyuk, S.V. (2018) X-ray and cryo-EM structures of inhibitor-bound cytochrome $bc_1$ complex for structure-based drug discovery. *IUCrJ*. **5**: 200-210.

Agip, AN.A, Blaza, J.N., Bridges, H.R., Viscomi, C., Rawson, S, Muench, S.P. & Hirst, J. (2018) Cryo-EM structures of complex I from mouse heart mitochondria in two biochemically defined states. *Nat. Struct. Mol. Biol*. **25**: 548-556.

Drulyte, I., Johnson, R.M., Hesketh, E.L., Hurdiss, D.L., Scarff, C.A., Porav, S.A., Ranson, N.A., Muench, S.P. & Thompson, R.F. (2018) Approaches to altering particle distributions in cryo-electron microscopy sample preparation. *Acta D* **74**: 560-571.

Harrison, M.A. & Muench, S.P. (2018) The Vacuolar ATPase – A Nano-scale motor that drives cell biology. *Subcell Biochem*. **87**: 409-459.

Vasilca, V., Sadeghpour, A., Rawson, S., Hawke, L.E., Baldwin, S.A., Wilkinson, T., Bannister, D., Postis, V.L.G., Rappolt, M., Muench, S.P. & Jeuken, L.J.C. (2018) Spherical-supported membranes as platforms for screening against membrane protein targets. *Anal Biochem* **549**: 58-65.


## Funding


This work was supported by the BBSRC and Wellcome Trust.


## Collaborators

*University of Leeds:* Colin Fishwick and Frank Sobott
*External:* Howard White (Eastern Virgina Medical School), Martin Trebbin (State University of New York), Prof Samar Hasnain & Dr Svetlana Antonyuk (University of Liverpool), Dr Chun-wa Chung (GlaxoSmithKline), Dr Tom Ceska (UCB Pharma).

## Unified synthetic approaches to diverse biologically-relevant molecular scaffolds

Anthony Aimon, Shiao Chow, Philip Craven, Mark Dow, Daniel Foley, Haitham Hassan, George Karageorgis, Samuel Liver, Jacob Masters and Adam Nelson

### Introduction

The discovery of biologically-active small molecules is an enduring theme in chemical biology and medicinal chemistry. However, the historical exploration of chemical space has been highly uneven and unsystematic: a sixth of known cyclic organic compounds are based on just 30 (of 2.5 million) known molecular scaffolds! This uneven exploration stems, in large part, from the narrow toolkit of reliable reactions that currently underpins molecular discovery. We have an ongoing and vibrant research program that is focused on the development of unified approaches to explore novel and diverse regions within chemical space.

### Results

We developed a unified synthesis of a set of bridged fragments containing a bridgehead nitrogen (Scheme, left panel). Many of these fragments contain twisted lactams whose modulated electronic properties may present unusual opportunities for interaction with target proteins. The demonstrated novelty, three-dimensionality and molecular properties of the set of 22 fragments may provide valuable, and highly distinctive, starting points for fragment-based drug discovery.

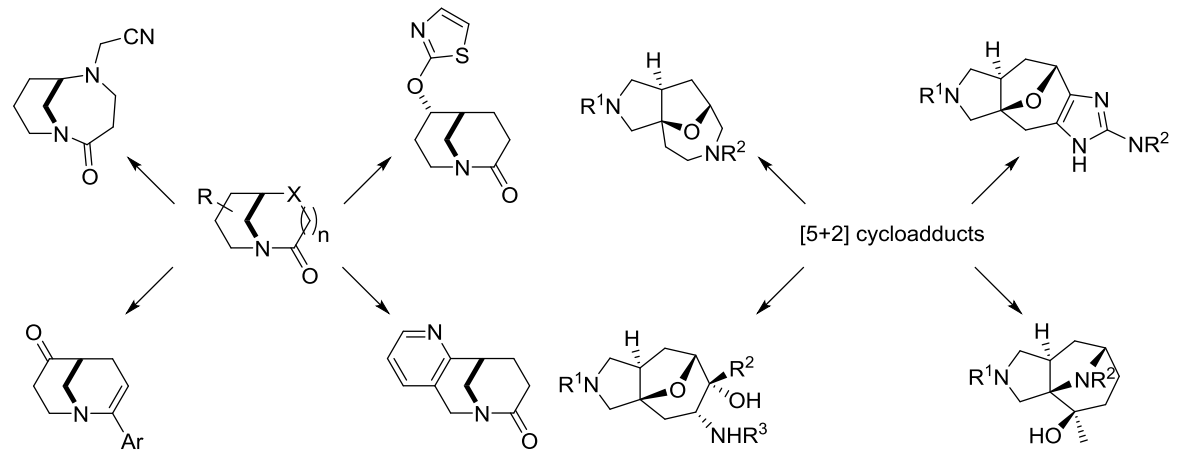


**Figure 1:** Exemplar unified synthetic approaches to diverse molecular scaffolds. Left: Synthesis of bridged fragments containing a bridgehead nitrogen atom. Right: Synthesis of four natural product-like compound libraries.

We have also exploited our "top-down" lead-oriented synthetic approach to enrich the diversity of a large small molecule screening collection (Scheme, right panel). The approach enabled complex intermediates formed by [5+2] cycloaddition to be converted into scaffolds that have broad natural product-like features, but that are only distantly related to specific natural products. In each case, a library was nominated for production, leading to a total of >2900 screening compounds that augmented the Joint European Compound Library of the European Lead Factory.

The development of unified strategies that are able to deliver skeletally diverse scaffolds is demanding. In addition, it is critical to demonstrate the biological relevance of novel scaffolds that are prepared, for example through fragment screening or phenotypic screening. We have translated many of our unified diversity-oriented synthetic approaches into the €196M European Lead Factory in which Leeds was a partner. Publications from this programme, and

other programmes under active development in the group, are listed below. Further details of research within the Nelson group may be found at www.asn.leeds.ac.uk.

**Publications**

Hassan, H., Marsden S. P., Nelson, A. (2018) "Design and synthesis of a fragment set based on twisted bicyclic lactams", *Bioorg. Med. Chem.* **26**, 3030-3033.

Aimon, A., Karageorgis, G., Masters, J., Dow, M., Craven, P. G. E., Ohsten, M., Willaume, A., Morgentin, R., Ruiz-Llamas, N., Lemoine, H., Kalliokoski, T., Eatherton, A. J., Foley, D. J., Marsden, S. P., Nelson, A., (2018) "Realisation of small molecule libraries based on frameworks distantly related to natural products", *Org. Biomol. Chem.* **16**, 3160-3167.

Morgentin, R., Dow, M., Aimon, A., Karageorgis, G., Kalliokoski, T., Roche, D., Marsden, S. P., Nelson, A., (2018) "Translation of innovative chemistry into screening libraries: an exemplar partnership from the European Lead Factory", *Drug Discov. Today* **23**, 1578-1583.

Chow, S., Liver, S., and Nelson, A., (2018) "Streamlining bioactive molecular discovery through integration and automation", *Nat. Rev. Chem.* **2**, 174-183.

ed. Westwood N. J., Nelson, A., (2018) "Chemical and Biological Synthesis: Enabling Approaches for Understanding Biology", Royal Society of Chemistry, ISBN: 978-1-78262-948-1.

Westwood N. J., Nelson, A., (2018) "Synthetic Tools for Elucidating Biological Mechanisms", DOI: 10.1039/9781788012805-00001, in Chemical and Biological Synthesis, ed. Westwood N. J., Nelson, A., Royal Society of Chemistry, pp 1-7.

Liver, S., Masters, J., Nelson, A., (2018) "Function-driven Discovery of Bioactive Small Molecules", DOI: 10.1039/9781788012805-00138, in Chemical and Biological Synthesis, ed. Westwood N. J., Nelson, A., Royal Society of Chemistry, pp 138-152.

**Collaborators**

*University of Leeds:* Professor Steve Marsden, Dr Remy Morgentin, Dr Didier Roche and colleagues,
*External:* Dr Remy Morgentin, Dr Didier Roche and colleagues (Edelris), Dr Tuomo Kalliokoski (Lead Discovery Center), Andy Eatherton (AstraZeneca) and Professor Nick Westwood (University of St Andrews).

We also acknowledge other scientific collaborators who have also contributed strongly to other aspects of our on-going research programme.

**Funding**

We thank EPSRC, the EU and AstraZeneca for support.

## XRCC4-superfamily proteins work in non-homologous end joining and centrosomal & ciliary functions

Takashi Ochi

### Introduction

XRCC4 superfamily is comprised of five different protein families namely XRCC4, XLF, PAXX, SAS6 and CCDC61, which all share a similar protein fold. These proteins play roles in two different biological systems; non-homologous end joining (NHEJ) and centrosome/basal body function. NHEJ is one of major DNA-repair pathways for DNA double-strand breaks (DSBs) (Figure 1). Since NHEJ directly joins two separated DNA ends without any templates, it is considered to be error prone. Indeed, this characteristic of introducing indels is used knockout genes by CRISPR-Cas9. In addition to repairing DSBs, NHEJ is critical for generating T-cell receptors and immunoglobulins *via* V(D)J recombination and class-switch recombination. Three of the XRCC4-superfamily members XRCC4, XLF and PAXX have been known to have important functions in NHEJ. XRCC4 and XLF interact each other in a "head-to-head" manner to make spiral protofilaments whereas XLF and PAXX have a redundant function. Since PAXX has been identified recently by myself and others as a NHEJ factor interacting with core NHEJ proteins Ku70/80, its exact function has yet to be revealed. The two other XRCC4 superfamily proteins SAS6 and CCDC61 are known to be centrosomal proteins. The centrosome is a major microtubule-organising centre and probably the largest protein complex found in eukaryotes. The centriole is the core structure of the centrosome and has a 9-fold rotational symmetry. SAS6 is key to generate this symmetry and indeed itself forms a ring structure having the symmetry in a similar head-to-head manner to the XRCC4/XLF complex. I have recently discovered that the fifth member of the superfamily CCDC61 is a previously known member of the XRCC4 superfamily. Here, I describe a recent finding about PAXX, which has been published this year, and a progress in understanding a function of CCDC61.

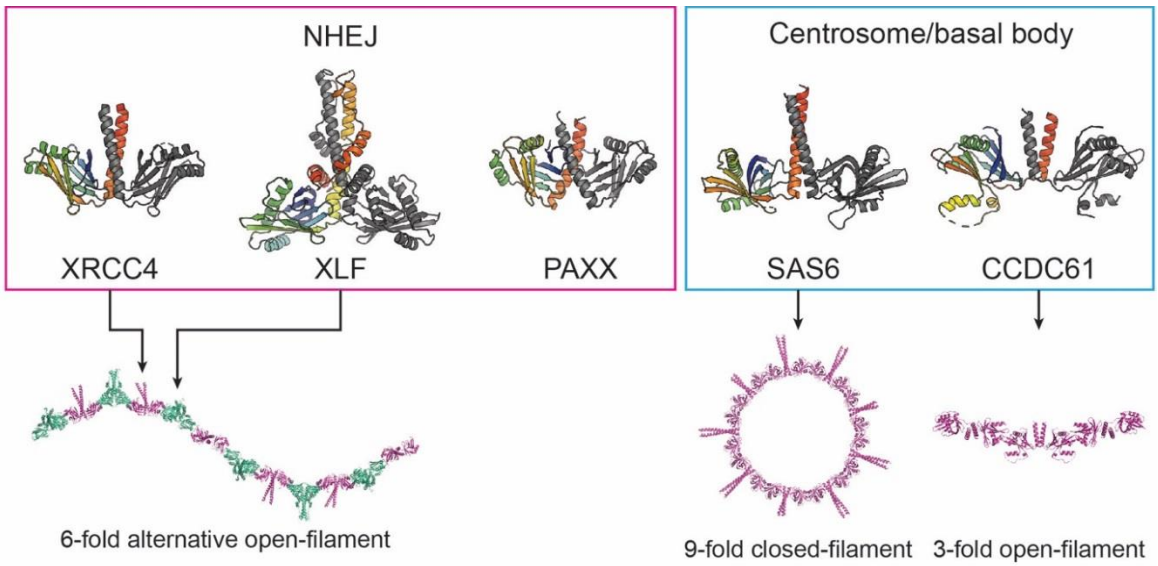


**Figure 1:** The structures of the XRCC4-superfamily proteins. The crystal structures of XRCC4, XLF, PAXX, SAS6 (PDB codes: 1IK9, 2QM4, 3WTD and 2Y3W respectively) and CCC61 (unpublished) homodimers are shown in a cartoon representation. The colour of each monomer progresses from blue (N-terminus) to red (C-terminus). Protofilaments of XRCC4/XLF (magenta and green respectively; PDB code: 3W03), SAS6 (PDB code: 4CKP) and CCDC61 (unpublished) are shown below their homodimer structures.

**Results**
In collaboration with Dr. Terence Strick and his colleagues, we studied the DNA synapsis by NHEJ proteins at the single-molecule level. We showed that PAXX stabilises the DNA synapsis by interacting with core NHEJ proteins Ku70/80 heterodimer and retains the synapsis by the heterodimers in complex with DNA-PKcs longer than the complex without PAXX, indicating that PAXX supports the DNA synapsis by the complex. A role of PAXX in the DNA synapsis is consistent with that of the XRCC4/XLF complex. Thus, we now can conclude that the XRCC4 superfamily members in NHEJ have a common role in the DNA synapsis. This work was done when I was a research associate in Professor Tom Blundell's laboratory (Department of Biochemistry, University of Cambridge). Structural and biochemical studies of CCDC61 revealed that CCDC61 forms homo-oligomers in a similar manner to the SAS6 ring but instead makes linear filaments. This suggests that a common feature of the XRCC4 superfamily is the formation of open or closed protofilaments. I also found that the coiled-coil domain of CCDC61 binds to microtubules. Next, I would like to answer how the filament formation and microtubule binding of CCDC61 plays a role in cells and where exactly CCDC61 filaments exist. Experiments related to CCDC61 were carried out while I was a postdoctoral fellow in Dr. Mark van Breugel's laboratory (MRC Laboratory of Molecular Biology).

**Publications**
Wang, J. L., Duboc, C., Wu, Q., Ochi, T., Liang, S., Tsutakawa, S. E., Lees-Miller, S. P., Nadal, M., Tainer, J. A., Blundell, T. L. & Strick, T. R. (2018). Dissection of DNA double-strand-break repair using novel single-molecule forceps. *Nat. Struct. Mol. Biol* **25**, 482-487.

**Funding**
These works were mainly funded by the Wellcome Trust for Prof. Tom Blundell and MRC for Dr. Mark van Breugel. I am currently supported by the University of Leeds.

**Collaborators**
*External:* Prof. Sir Tom L. Blundell (University of Cambridge, UK), Dr. Mark van Breugel (MRC Laboratory of Molecular Biology, UK), Dr. Terence Strick (Université Paris Diderot, France), Dr. Fanni Gergely and Dr. Valentina Quarantotti (CRUK Cambridge Institute, UK), Prof. Susan K. Dutcher and Dr. Huawen Lin (Washington University School of Medicine, USA), Dr. Jerome Jullien (The Gurdon Institute, UK), Prof. Stephen P. Jackson (The Gurdon Institute, UK), Prof. Raymond E. Goldstein and Dr. Francesco Boselli (University of Cambridge, UK), Dr. Dr. Yuu Kimata (ShanghaiTech University, China), Dr. Andrew N. Blackford (University of Oxford, UK).

## How does *Staphylococcus aureus* resist the antibiotic nisin?

Christopher Randall, Arya Gupta, Bret Utley-Drew, Siu Yi Lee, Genevieve Morrison-Williams and Alex O'Neill

### Introduction

Nisin and related peptide antibiotics are of interest as candidates for the treatment of human infections caused by Gram-positive pathogens such as *Staphylococcus aureus.* An important potential liability of nisin in this regard is the ease with which *S. aureus* acquires resistance. We have previously shown that such resistance is usually the result of mutations in *nsaS*, a gene that encodes the sensor kinase of the NsaRS two-component regulatory system. Here we describe a series of studies to explore how these mutational changes result in reduced nisin susceptibility.

### Results

In our earlier study, we speculated that nisin resistance mutations in *nsaS* confer a gain of function on the encoded protein, with resistance resulting from consequent upregulation of the NsaRS regulon. In line with this idea, engineered loss of function in *nsaS* as a consequence of insertional inactivation of the gene resulted in complete loss of resistance, and comparative transcriptomic analysis by RNAseq revealed upregulation of the NsaRS regulon in a nisin-resistant mutant of *S. aureus* versus its otherwise-isogenic progenitor.

Deletion studies subsequently established that two putative ABC transporters (BraDE and VraDE) encoded within the NsaRS regulon – both of which have been reported to provide a degree of intrinsic protection against nisin - are required for the observed nisin resistance phenotype. These transporter proteins were found to play distinct roles in resistance. As has been described for intrinsic nisin resistance, nisin detoxification was ultimately mediated by VraDE, with artificial overexpression of *vraDE* alone providing high-level nisin resistance. By contrast, BraDE participates in the signaling cascade underlying VraDE expression; bacterial two-hydrid analysis revealed that BraDE physically interacts with NsaRS, and deletion of *braDE* resulted in a ~9 fold drop in *vraDE* expression as determined by qRT-PCR.

Our results establish that *S. aureus* naturally possesses the cellular machinery to detoxify nisin, but that the transporter responsible (VraDE) is not ordinarily produced to a degree sufficient to yield substantial resistance. Acquired nisin resistance mutations prompt activation of the regulatory circuit controlling expression of *vraDE*, thereby unmasking an intrinsic resistance determinant. These findings offer new insights into the complex mechanism by which expression of *vraDE* is regulated, and suggest that a potential route to overcoming the resistance liability of nisin could involve chemical modification of the molecule to prevent its recognition by the VraDE transporter.

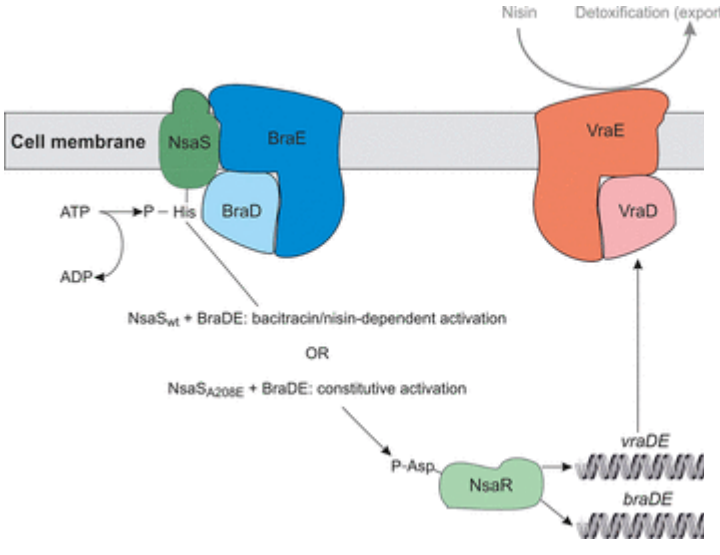


**Figure 1:** Predicted roles of NsaRS, BraDE, and VraDE in intrinsic and acquired NIS resistance. In intrinsic resistance, the presence of peptide antibiotics (e.g. nisin and bacitracin) in the extracellular space is detected by the NsaS/BraDE complex, which in turn activates the cognate response regulator NsaR via phosphotransfer to upregulate BraDE/VraDE expression. Detoxification of antibiotics is ultimately achieved by VraDE through an as-yet unknown mechanism. In acquired resistance, an amino acid substitution in NsaS (e.g. $A_{208}E$) uncouples sensing from activation of NsaR, leading to constitutively high levels of BraDE/VraDE expression and high-level resistance.

**Publications**

Randall C.P., Gupta A., Utley-Drew B., Lee S.Y., Morrison-Williams G., O'Neill A.J. (2018) Acquired Nisin Resistance in Staphylococcus aureus Involves Constitutive Activation of an Intrinsic Peptide Antibiotic Detoxification Module. *mSphere*. doi: 10.1128/mSphereDirect.00633-18.

## Neuron-induced TCS regulates organismal proteostasis and protects against amyloid beta toxicity

Daniel O'Brien, Laura Jones, Sarah Good, Jay Miles, Rebecca Aston, Vijay Shanmugiah, David Westhead and Patricija van Oosten-Hawle

### Introduction

In metazoans, tissues experiencing proteotoxic stress induce "transcellular chaperone signalling" (TCS), that activates molecular chaperones, such as *hsp-90*, in distal tissues. Thus, conserved stress responses such as the heat shock response initiate inter-cellular communication that allows protective chaperone expression to be signalled and spread from one tissue to another, a process known as transcellular chaperone signalling (TCS). One key observation of TCS is that an imbalance of proteostasis in only one tissue (e.g. neurons) through altered expression of the major chaperone *hsp-90*, can lead to an upregulated *hsp-90* chaperone response in receiving tissues that is spread throughout the organism[1,2]. How this form of inter-tissue communication is mediated to upregulate systemic chaperone expression and whether it can be utilised to protect against protein misfolding diseases remains an open question to date.

### Results

Using *C. elegans*, we identified key nodes of a neuronal induced transcellular signalling cue that couples the PQM-1 zinc finger transcription factor and components of the innate immune response with the regulation of systemic proteostasis. This study was recently published in Cell Reports[3]. We show that perturbation of proteostasis in the neurons, via neuron-specific overexpression of HSP-90, activates TCS via PQM-1 and the innate immunity-associated transmembrane protein CLEC-41. This activation of neuronal PQM-1/CLEC-41 signalling is required to induce *hsp-90* expression in muscle cells. Importantly, using *C. elegans* models of Alzheimer's Disease, we show that increased expression of Hsp90 in the neurons suppresses Aβ aggregation expressed in muscle cells (Fig.1A &1B) and ameliorates muscle-expressed *Aβ3-42* associated toxicity (paralysis; Fig. 1C).

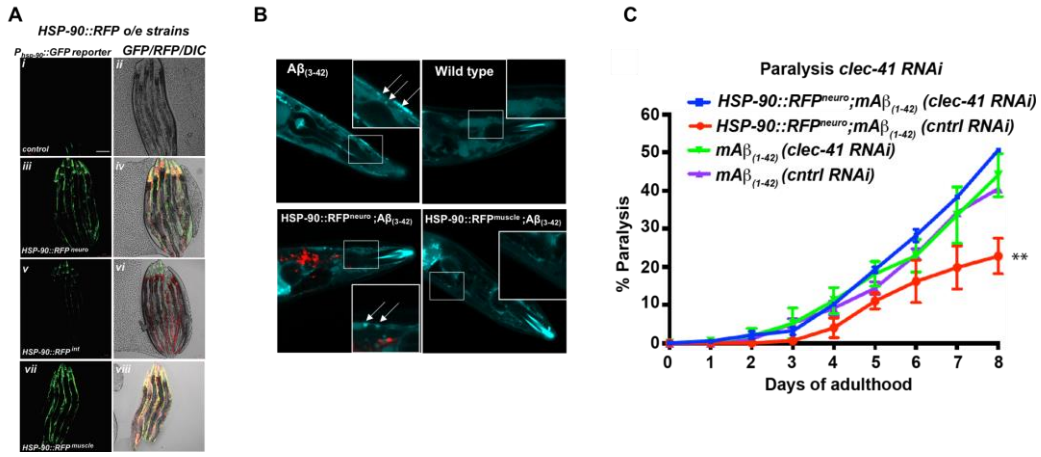


**Figure 1: (A)** *C. elegans* strains overexpressing HSP-90::RFP in the neurons (iii, iv), the intestine (v, vi) and the muscle (vii, viii), leading to TCS-mediated upregulation of *hsp-90* expression in muscle cells. **(B)** Increased expression of Hsp90 reduces Aβ aggregates in the muscle of mAβ (3-42) animals. Aβ deposits were stained in live worms (Day 5 of adulthood) with the amyloid-specific dye X-34 (a derivative of Congo Red) that specifically stains aggregates, but not oligomeric intermediates. **(C)** Paralysis assays of *C. elegans* overexpressing HSP-90 in the neurons, which protects against amyloid associated toxicity throughout aging (red line). RNAi mediated knockdown of *clec-41* reverses this protective effect (blue line).

This intercellular and neuronally induced signalling cue depends on glutamatergic neurons and requires the transmembrane channel CLEC-41. Thus, our results reveal elements of a neuronal signalling cue that promotes cell nonautonomous *hsp-90* chaperone expression and protects against age-associated proteostasis dysfunction (See Figure 2 for a model).

Further elucidating components of this neuronal TCS pathway to understand how it activates the increased cell-non-autonomous expression of Hsp90 in *C. elegans* may provide a powerful tool that could be utilised for the treatment of protein misfolding diseases such as AD.

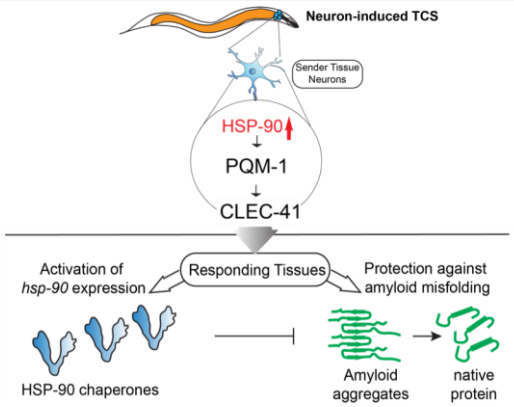


**Figure 2:** Model of Transcellular Chaperone Signalling induced by overexpression of Hsp90 in the neurons. This activates a neuronal signalling cue dependent on PQM-1 and CLEC-41 and triggers hsp-90 expression in the muscle, which protects against amyloid beta aggregates expressed in the muscle.

## Publications

O'Brien, D. *et al.* (2018) A PQM-1-Mediated Response Triggers Transcellular Chaperone Signaling and Regulates Organismal Proteostasis. *Cell Rep.* **23,** 3905–3919.

## Funding

We are grateful for support from the Wellcome Trust, the NC3Rs, and a BBSRC and MRC doctoral studentship.

## Collaborators

*University of Leeds:* David Westhead.

## Experimental data and physical models in protein science

Emanuele Paci

Our research focuses on the development and application of novel computational tools to investigate structure and functional dynamics of biomolecules. One of our aims is fully exploit the wealth of experimental data that is increasingly available thanks to the development of more advanced and higher throughput techniques. Most of our research involves experiments performed in collaboration with colleagues from the Astbury Centre and further afield.

One topic where models and simulations provided information that experiments cannot provide and suggestions for more insightful experiments relates to the structural propensity of polypeptides with specific sequence patterns. These range from the simplest repeat, a homopolypeptide, i.e., repeats of the same amino acid, or repeats short patterns of amino acids. While polymer theory suggests that most of these sequences are unstructured, we found evidence of the emergence of structural preferences and unique, sequence and length dependent, dynamical properties. In collaboration with Michelle Peckham at Astbury we have been exploring the properties of polyampholyte repeat sequences that are strongly helical using experiment and simulation.

Characterization kinetics and thermodynamics of disordered states is one of the current focuses of our group. We explored the rate of contact formation in a number of peptides and proteins. Results explain and reconcile experimental results that show an anomalous time dependence of the contact formation rate. The anomalous kinetics turns out to be in part due to the ruggedness of the free energy landscape, and in part due to the polymeric nature of peptides and proteins.

Much of our work involves molecular simulation of the dynamics and interactions within and between protein systems. Data generated from simulation are used to interpret and direct experimental measurements such as hydrogen-deuterium exchange probed by mass spectroscopy, NMR and SAXS.

Among our current interests is the development of *ab initio* methods to determine the structure of proteins and protein complexes. All available structure predictors share the inconvenience of not being able to score the correct model higher than decoys. Atomistic simulation can be used to assess the stability of different models. In this way we could determine the correct structure of designed antibody analogs interacting with domain IV of Human Epidermal Growth Factor Receptor 2.

Such approach, while it demonstrates the ability of *ab initio* methods such as Rosetta to generate correct structures of complexes and the reliability of simulation to assess their kinetic and thermodynamic properties, is still very expensive in terms of computation required.

We are now able to show that sparse information from hydrogen-deuterium exchange protection factors is sufficient to assess the quality of *ab initio* models. Even more promising is the fact that the deuterium uptake measured by mass spectrometry, which is currently only used to fingerprint regions that form intra or intermolecular contacts, can be converted into protection factors for individual residues. Hence, we anticipate that a relatively fast measurement, that can be performed on tiny samples of unlabelled protein, can be sufficient to assess high resolution structural models.

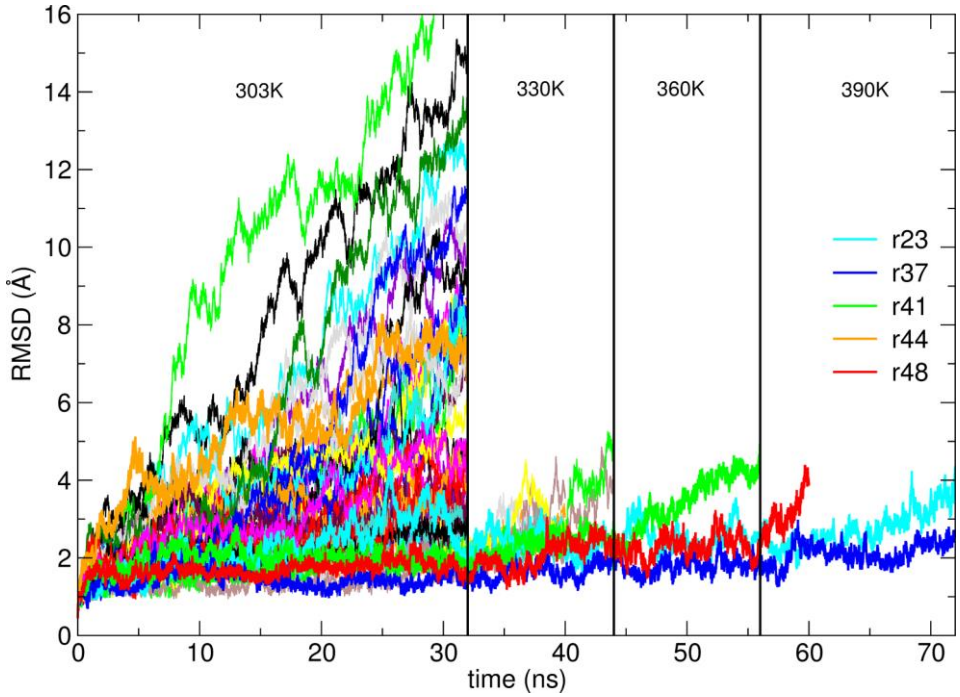


**Root-mean-square deviation from the position of Cα atoms in the respective models of G3:HER2_IV complex as a function of simulation time.** Rosetta has been used to generate 100 models of the complex. From each of these models a simulation was started. While some models rapidly move away from the initial pose, others only deviate from the initial structure when temperature is increased (i.e., they are wrong but metastable). The only model that even after 20 ns simulation at a temperature of 390 K remains close to the initial structure (i.e., the kinetically most stable) is model r37, that is, the one closest to the correct structure.

## Publications

Radom F., Pluckthun A. & Paci E. (2018) Assessment of *ab initio* models of protein complexes by molecular dynamics. *PLoS Comput Biol* **14**:e1006182.

Gomez Santiago, C., E. Paci and D. Donnelly (2018) A mechanism for agonist activation of the glucagon-like peptide-1 (GLP-1) receptor through modelling & molecular dynamics. *Biochem Biophys Res Commun* **498**: 359-365.

Batchelor M. & Paci E. (2018) Helical polyampholyte sequences have unique thermodynamic properties. *J Phys Chem B* **122**:11784-11791.

## Collaborators

*University of Leeds:* R. Tuma, J. Houwing-Duistermaat**,** B. Turnbull, R. Bayliss, D. Brockwell, R. Richter, D. Donnelly, M. Peckham
*External:* J. Clarke (Cambridge), A. Plückthun (Zurich), C. Kleanthous (Oxford), J. Potts (York), R. Maillard (Georgetown), Freeline Therapeutics (Stevenage)

## Super-resolution imaging of the cytoskeleton

Alistair Curd, Ruth Hughes, Anna Lopata, Christian Tiede, Darren Tomlinson & Michelle Peckham

### Introduction

The cytoskeleton is critical for normal cellular function. It is made up of three different types of filaments, composed of actin, tubulin or intermediate filament proteins. The actin cytoskeleton is used as a track for motor proteins called myosins. Most cells continuously change and remodel their actin cytoskeleton in response to the environment. Actin organisation is critical to cellular function. We have developed super-resolution imaging to investigate the organisation of the cytoskeleton and associated proteins in cells using our home-built 3D PALM/STORM microscope, which provides resolutions of ~20nm. To capitalise on this high level of resolution, we have now developed the use of small, fluorescently labelled, non-antibody binding proteins called 'Affimers' (with Darren Tomlinson) as alternatives to antibodies in PALM and STORM. As a test case, we tested Affimers to F-actin. We also tested these anti-actin Affimers in a related super-resolution approach called DNA-PAINT (with Ralf Jungman). In principle, their small size (~10kDa, ~2nm) places the fluorescent dye label very close to the target protein, compared to antibodies (>10nm), enabling us to more accurately determine the position of the labelled protein in super-resolution imaging.

### Results

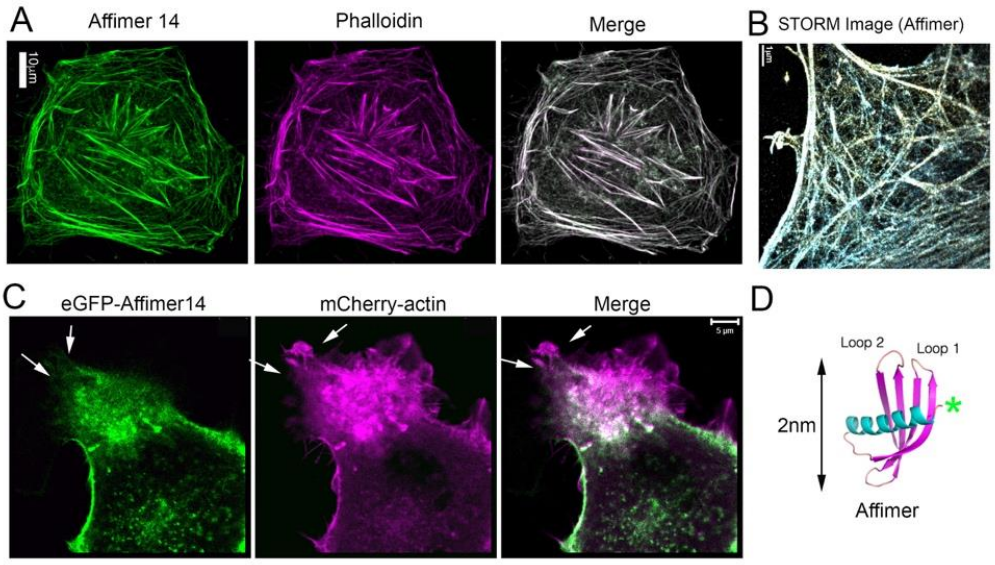


**Figure 1**: Labelling of F-actin in fixed and live cells by anti-actin Affimer. A) Labelling in fixed cells compared to phalloidin. B) STORM image of part of a cell obtained with the Affimer. C) Live cell imaging with eGFP-Affimer 14 shows it does not label dynamic actin in ruffles, labelled with mCherry actin (indicated by white arrows). D) the structure of the Affimer. Star indicates position of fluorescent label. Loop 1 and Loop 2 bind to F-actin.

We raised 4 different Affimers to filamentous actin (F-actin) and confirmed that 3 of the 4 bound with high affinity (~250nM) to F-actin (4). When we tested fluorescently labelled Affimers for their ability to label the actin cytoskeleton in fixed cells, we found that all 4 Affimers labelled actin in methanol fixed cells, but only one (Affimer 14) worked in paraformaldehyde fixed cells (Fig. 1). Methanol is known to have a small effect on the structure of F-actin, which means that a commonly used small cyclic peptide (phalloidin) does not bind to methanol fixed F-actin. Therefore, it's possible that the Affimers are also sensitive to these small structural changes, providing a potential explanation for this difference in labelling of methanol and paraformaldehyde fixed cells.

Affimer 14 was then used in dSTORM experiments (Fig. 1), and worked well, providing detailed images of the actin cytoskeleton. In collaboration with Ralf Jungmann's group, we also found that this Affimer worked will in labelling F-actin using DNA-PAINT (1). Finally, we tested the ability of eGFP-Affimers to label actin in live cells. Three of Affimers labelled F-actin. Interestingly, the Affimers are excluded from regions of dynamic actin, labelled with mCherry actin (C). This may again either reflect minor structural differences between dynamic and stable actin. The eGFP-Affimers could be useful tools in imaging stable actin in living cells.

In summary, our work with Affimers, in this and other studies demonstrate their potential for specifically recognising proteins in fixed and live cells, their potential sensitivity to the conformation of the protein, and their usefulness in super-resolution microscopy from dSTORM to DNA-PAINT.

**Publications**

Schlichthaerle T., Eklund A.S., Schueder F., Strauss M.T., Tiede C., Curd A., Ries J., Peckham M., Tomlinson D.C. & Jungmann R. (2018) Site-specific labeling of affimers for DNA-paint microscopy. *Angew Chem Int Ed Engl* **57**:11060-11063.

Remenyi R., Gao Y., Hughes R.E., Curd A., Zothner C., Peckham M., Merits A. & Harris M. (2018) Persistent replication of a chikungunya virus replicon in human cells is associated with presence of stable cytoplasmic granules containing nonstructural protein 3. *J Virol* **92**:e00477-18.

Parker F., Batchelor M., Wolny M., Hughes R., Knight P.J. & Peckham M. (2018) A1603P and K1617del, mutations in β-cardiac myosin heavy chain that cause Laing early-onset distal myopathy, affect secondary structure and filament formation *in vitro* and *in vivo*. *J Mol Biol* **430**:1459-1478.

Lopata A., Hughes R., Tiede C., Heissler S.M., Sellers J.R., Knight P.J., Tomlinson D. & Peckham M. (2018) Affimer proteins for f-actin: Novel affinity reagents that label f-actin in live and fixed cells. *Sci Rep* **8**:6572.

Batchelor M., Wolny M., Kurzawa M., Dougan L., Knight P. J. and Peckham M. (2018) Determining Stable Single Alpha Helical (SAH) Domain Properties by Circular Dichroism and Atomic Force Microscopy. *Methods Mol Biol* **1805**: 185-211

Batchelor M. & Paci E. (2018) Helical polyampholyte sequences have unique thermodynamic properties. *J Phys Chem B* **122**:11784-11791.

Bartlett C., Curd A., Peckham M. & Harris M. (2018) Visualisation and analysis of hepatitis C virus non-structural proteins using super-resolution microscopy. *Scientific Reports* **8**:13604.

**Funding**

This work was funded by BBSRC, MRC, the British Heart Foundation and the Wellcome Trust.

**Collaborators**

*University of Leeds:* Mark Harris, Darren Tomlinson, Christian Tiede, Peter Knight, Emanuele Paci, Arnout Kalverda

*External:* Thomas Schlichthaerle & Ralf Jungmann (Max Planck Institute of Biochemistry, Martinsried, Germany), Emily Baker (University of Bristol, UK), James Sellers (National Institutes of Health, Bethesda, USA).

## Allosteric activation of the large conductance mechanosensitive channel in the absence of membrane tension

Bolin Wang and Christos Pliotas

### Introduction

Mechanosensation is the ability of ion channels to sense changes in membrane tension and respond by altering their structure and function. It is an ancient fundamental biophysical property of the lipid bilayer and mechanical regulation of ion channels occurs through sites which are accessible to the lipid bilayer. Previously, the degree of lipid chain availability within transmembrane nano-pockets (NPs) of ion channels has been linked with mechanosensitivity and it is known as the "lipid moves first" model. However, the direct effect of lipid chain disruption within the NPs on mechanical activation has not been demonstrated yet. We have identified NPs on the large conductance mechanosensitive (MS) channel MscL, the ion channel with the highest-pressure activation threshold across life kingdoms. We have restricted lipid chain access within NPs by covalent cysteine modification on sites spanning all protein domains and monitored channel conformation, by PELDOR (DEER) spectroscopy. For a single site located at the entrance of the NPs we promoted allosteric channel opening in the absence of pressure. Single channel recordings in the presence of applied tension of this modified channel revealed a dramatic decrease in pressure activation threshold than WT channel and a novel sub-conducting state. The modification restricted lipid chain access to the NPs and thus the final contact lipid chains make with the protein to mediate bilayer tension. We propose this method could be used to reversibly generate allosteric responses in mechanically gated channels.

### Results

Pulsed Electron DOuble Resonance (PELDOR, also known as DEER) spectroscopy could measure distances (1.5 – 8) nm between unpaired electrons introduced to selected sites of a protein. This approach combines the specificity and reversibility of cysteine modification, with the accuracy of PELDOR in reporting stoichiometry and conformation of ion channels, in a lipid environment. We have coupled PELDOR with cysteine modification (nitroxide spin labels) on multiple sites of MscL targeting the nano-pocket (NP) itself, its entrance, and proximal regions and interrogated changes in channel conformation (Fig 1a). Our hypothesis was that NP disruption would prevent acyl chain occupancy and consequently cause an allosteric MS channel structural/functional response in the absence of membrane tension.

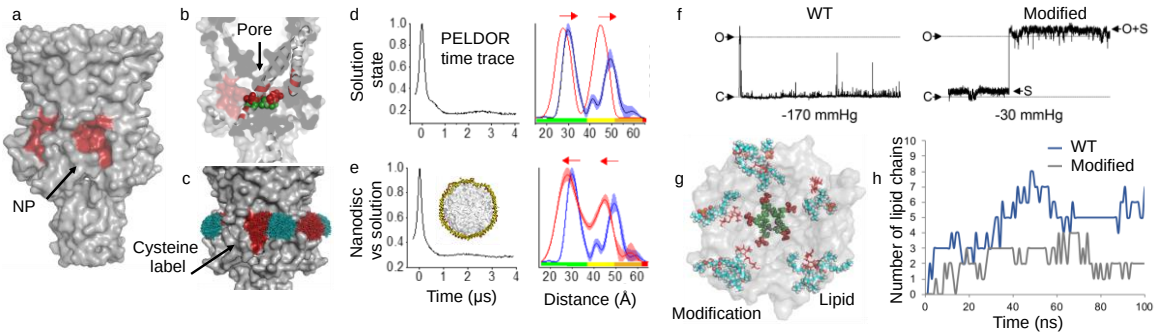


**Figure 1: a.** NP-forming region residues (red surface view) **b.** NP-bottom (red spheres) and pore constriction site (green spheres) forming residues. **c.** modification (red sticks) disrupting access to NPs. **d.** Raw PELDOR traces (left columns) and resulting distance distributions (right columns). Red lines correspond to closed state modelled distances. Blue shade areas correspond to measured distances. Modified channel distance distribution shift (highlighted by red arrows) between the "closed structure MscL model" and "PELDOR distances in solution. **e.** Distance shift between modified MscL solution and nanodiscs suggesting a reversible change in the presence of membrane tension. **f.** Single channel recordings from GUVs containing WT or modified MscL protein. The pressure applied during the recording is indicated. Current levels representing the closed ("C"), fully opened ("O") and subconductance ("S") channels. **g.** MD simulation top pore view snapshots of modified channel (transparent grey surface view), pore constriction (green spheres) and NP bottom (red spheres). NP-associated lipids are shown in cyan sticks. Only a couple of chains make contact with constriction site in the modified channel as label (red sticks) clashes with lipids. **h.** Comparison of the number of lipid chains residing within the NPs over time between WT (blue) and modified (grey) MscL channels.

If the essential feature of MS channel activation is lipid removal from the NPs, then opening should occur by sterically excluding lipid chain contacts to NP-forming residues (Fig 1a,b & c). 20 single-cysteine TbMscL mutants were generated with respect to the NPs and for thirteen positions we obtained PELDOR time traces, with clear dipolar oscillations in the raw data, which allowed the extraction of well-defined distance distributions. For a single site located in the proximity of the NP entrance subgroup and its moderately bulky side chain could "sweep" penetrating acyl chains away from NPs we observed a significant conformational change, consistent with a helical movement of ~6 Å and pore expansion (Fig 1d).

We then sought to identify any associated endogenous membrane lipids with MscL, by ES-MS and 31P-NMR, which should be included in the liposome and nanodisc reconstitutions for our PELDOR measurements. We observed lipid preference but no specificity, consistent with our initial hypothesis that no specific lipid-protein interactions are required to activate MscL. A significant distance shift was observed after reconstitution into nanodiscs (Fig 1e). The distances shorten, in agreement with the closed state modelled distances, suggesting a reversible induced change, from the open to closed state.

To evaluate the functional effects of the covalent attachment on this specific site, single channel recordings were taken from excised patches from Giant Unilamellar Vesicles (GUVs) containing WT or modified protein, in the presence of applied tension. From GUVs containing WT protein patches exhibited single channel openings with a mean conductance of ~3 nS, but only when pressures of at least -140 mmHg were applied (Fig 1f). In contrast, patches excised from GUVs containing modified MscL exhibited similar unitary currents, but activated at threshold pressures lower than WT, ranging between -30 and -120 mmHg (Fig 1f).

Molecular dynamic (MD) simulations were carried out to "observe" acyl chain blocking by the spin label at the modified site. We spin labelled MscL, set up and performed fully atomistic simulations within lipid bilayers to monitor the degree of NP lipid chain penetration over time and the effect of lipids on spin label conformation in respect to NP lipid penetration (Fig 1g). Lipid chain NP occupancy was significantly lower in the modified *versus* the WT channel (Fig 1h). We observed that each MscL pocket could fit up to two single acyl chains. More than half of the WT channel's available NPs were continuously occupied by lipid chain(s), in contrast to the modified channel NPs which were empty for the majority of the simulations (Fig 1h).

In summary, we have demonstrated that disruption of lipid chain penetration within NPs generates a mechanosensitive ion channel structural and functional response. We designed and implemented the first direct test of the "lipid moves first" hypothesis and provided substantial experimental evidence for its validity. Importantly, we offer insights into how lateral tension is transmitted from the membrane through the lipid chains to the NP and gates ion channels. We demonstrate that allosteric mechanical gating of ion channels can be achieved by disulfide cysteine modification on sites located at the entrance of the NP and distal to the channel pore.

**Funding**
This work was funded by Royal Society of Edinburgh, Tenovus Scotland, Carnegie Trust and the Universities of Leeds and St Andrews.

**Collaborators**
*University of Leeds:* JD Lippiat
*ExternaL:* J Schnell (University of Oxford), C Kapsalis, H El Mkammi, SJ Pitt, TK Smith, BE Bode (University of St Andrews)

## Structures of $\beta_2$-microglobulin amyloid fibrils by cryoEM

Matthew Iadanza, Matthew Jackson, Joshua Boardman, Hugh Smith, Theodoros Karamanos, Eric Hewitt, Neil Ranson and Sheena Radford

### Introduction

The protein beta-2-microglobulin ($\beta_2$m) is a component of the class 1 major histocompatibility complex (MHC-1) found on the surface of all nucleated cells and essential for immune response. Free $\beta_2$m is normally cleared by the kidneys, but when this does not occur, such as in patients undergoing kidney dialysis, the $\beta_2$m concentration in blood becomes elevated leading to the formation of amyloid fibrils. This can result in debilitating arthritis and joint damage. Using a combination of cryo electron microscopy (cryoEM) and magic angle spinning NMR (MAS-NMR), we determined the structure of a $\beta_2$m amyloid fibril to 3.9Å resolution. The structure represents a complete refolding of the protein from its native state and but also, intriguingly, preserves many of the secondary structure elements of the native fold. The $\beta_2$m fibril contains structural features common to all amyloid fibrils, but also has motifs that have not been observed in amyloid fibrils previously.

### Results

When $\beta_2$m fibrils were assembled *in vitro* from purified protein a variety of fibril morphologies were found (figure 1). We used helical reconstruction techniques to produce a 3.9Å map of the most common morphology (figure 1c) and built an atomic model into the EM density using constraints determined by MAS-NMR (figure 2). The $\beta_2$m fibrils consist of two twisted protofilaments each made up of flat subunits containing a single molecule of $\beta_2$m. These subunits are stacked in-register with an even spacing of 4.83Å down the fibril axis and a twist of -0.608° per subunit. This 'cross-β' conformation has long been a defining feature of amyloid fibrils. The subunit structure is stabilised by a variety of interactions which are also considered hallmarks of amyloid fibril structure, a 'steric zipper' of interdigitated hydrophobic residues and hydrophobic packing. In addition, the $\beta_2$m fibril subunit fold contains two features never before observed in an amyloid fibril: a π-stacking interaction between three tyrosine sidechains and a disulfide bond, which is also present in the native structure and has been shown to be required for fibril formation.

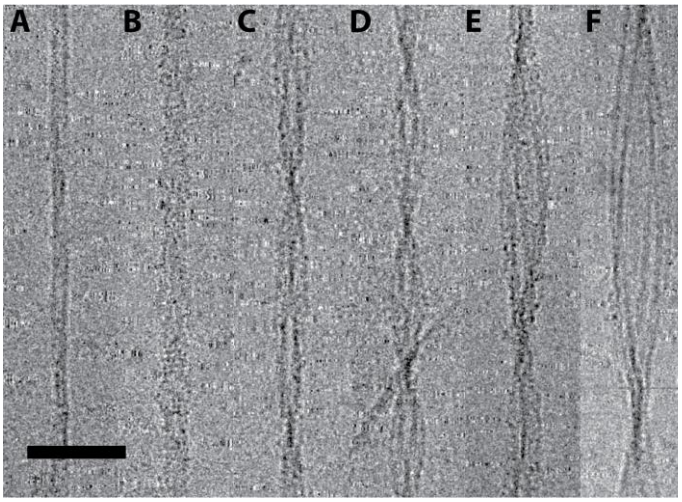


**Figure 1: Polymorphism in $\beta_2$m amyloid fibrils.** Electron micrographs of six polymorphs of the $\beta_2$m amyloid fibril. Scale bar is 50 nm.

The two protofilaments are held together by solvent exclusion as well as weak π-stacking and sidechain hydrogen bond interactions running down the axis. This interface is, so far, unique to $\beta_2$m fibrils. When we compare subunit folds and protofilament interface interactions of known amyloid structures we begin to see the very different structural features that can underpin the gross morphology that amyloid fibrils share. Although amyloid fibrils all have a twisted ribbon appearance and 'cross-β' morphology, this same overall cross-β structure is formed proteins that are completely unrelated in structure or sequence. The subunit structures that make up amyloid fibrils vary widely and, although they sometimes share common structural motifs such as the 'steric zipper', each fibril structure is unique. This has wide ranging implications for design of drugs for treatment of amyloid diseases. One strategy may be to target the shared features to develop general inhibitors of amyloidosis. Conversely, the

unique nature of each amyloid fibril on the subunit level may lead to very specific drugs that could target individual fibril types.

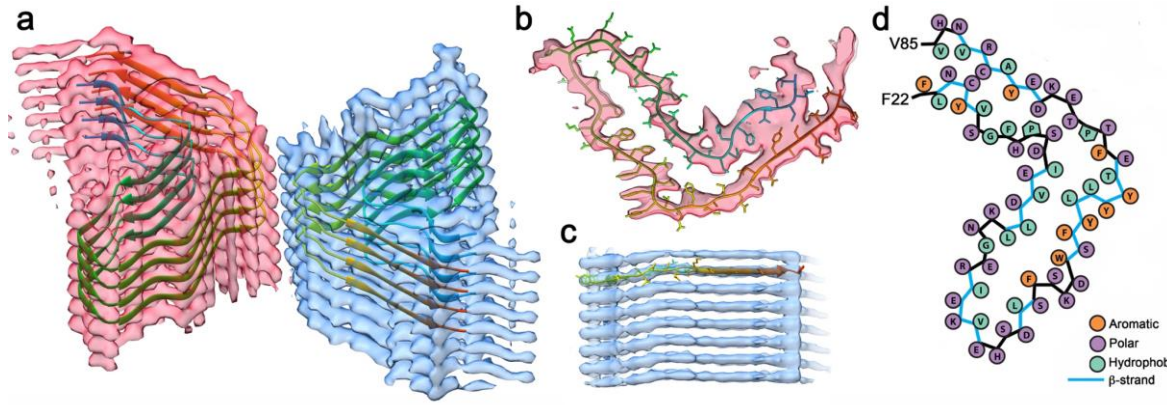


**Figure 2: The structure of a $\beta_2$m amyloid fibril.** (a) Oblique view of the cryo-EM map, with four layers of the atomic model built into each protofilament (coloured pink and blue). (b) Cross-section and (c) side view of a single layer of the atomic model, showing the fit of model to density across the $\beta_2$m subunit. (d) Schematic view of a single $\beta_2$m subunit showing polar (purple), hydrophobic (cyan) and aromatic residues (orange) in the fibril core.

Interestingly, the MAS-NMR analysis of the $\beta_2$m fibrils showed single peaks for all, but one, of the amino acid residues that make up the amyloid core. This suggests that, although the fibril sample is highly polymorphic, all of the individual polymorphs are constructed out of the same identical subunit. This phenomenon has been observed in other amyloid fibrils, reinforcing the observation that, despite the differences, there appear to be common pathways to fibril formation and assembly. To investigate this further we determined two additional $\beta_2$m fibril structures from other polymorphs (figure 1b and 1f). Because these polymorphs were much less common we were not able to determine their structure to the same high resolution as polymorph C. The lower resolution reconstructions suggest polymorph B contains a single protofilament while polymorph F is composed of four identical protofilaments. This suggests a hierarchical assembly pathway for the different polymorphs, with protofilaments forming and twisting together to form fibrils that can in turn self-associate to form even larger structures.

The high-resolution model of the $\beta_2$m amyloid fibril is one of the first glimpses of the molecular basis of an amyloid structure. This and other recently determined amyloid structures will give new insight into the features that stabilise misfolded proteins in amyloid fibrils. Although some common features are becoming apparent, it also appears that each amyloid fibril is unique. This will hopefully lead to a better understanding of the pathways of amyloid formation and improved diagnostics and treatments for amyloid associated disease.

**Publications**

Iadanza M.G., Jackson M.P., Hewitt E.W., Ranson N.A. & Radford S.E. (2018) A new era for understanding amyloid structures and disease. *Nat Rev Mol Cell Biol* **19**:755-773.

Iadanza M.G., Silvers R., Boardman J., Smith H.I., Karamanos T.K., Debelouchina G.T., Su Y.C., Griffin R.G., Ranson N.A. & Radford S.E. (2018) The structure of a $\beta_2$-microglobulin fibril suggests a molecular basis for its amyloid polymorphism. *Nat Commun* **9**:4517.

**Funding**

This work was funded by the European Research Council (ERC), the Wellcome Trust and the National Institutes of Health (NIH).

**Collaborators**

Robert Silvers, Galia Debelouchina, Yongchao Su and Robert Griffin (MIT).

## Rapid mapping of protein interactions using tag-transfer photocrosslinkers

Jim Horne, Martin Walko, Antonio Calabrese, Mark Levenstein, David Brockwell, Nikil Kapur, Andrew Wilson and Sheena Radford

### Introduction

Interactions between proteins are at the heart of many of the processes in living cells and their study is crucial for our understanding of non-pathogenic, as well as pathological pathways. The challenge in studying protein-protein interactions, however, stems from their transient nature. An efficient approach is to trap the interacting proteins in a covalently bound complex using crosslinkers. Chemical crosslinking combined with mass spectrometry has become a major tool to enable characterisation of protein complexes and how they change with time and/or post-translational modification of one or more of the interacting partners. The most commonly used crosslinkers for mapping protein-protein interactions rely on the presence of specific functional groups at the surface of the proteins (e.g. Lys-Lys), which limits the information that can be gained on the interacting interfaces. This drawback can be overcome, however, by using photoactivable crosslinkers. These crosslinking groups are 'activated' upon irradiation with UV light into highly reactive species with indiscriminate reactivity, thus removing the residue bias inherent in chemical crosslinkers relying on particular functional groups.

### Results

We have developed several new crosslinkers comprising a cysteine-selective binding group, methanethiosulphonate (MTS), and a photoactivatable diazirine group. The crosslinker is attached to a cysteine uniquely introduced into a "bait" protein which is then allowed to interact with the target protein. Upon irradiation with 365 nm UV light, the diazirine is transformed to a highly reactive carbine, with broad and unspecific reactivity which immediately reacts with the target protein. The bait and target thus become covalently crosslinked. Up to this point the procedure is similar to the majority of crosslinking methods. However, the fact that the crosslinker is attached to the bait protein via a disulphide bond means that it is possible to perform a subsequent reduction step to separate the bait from the target protein. The target now bears an additional thiol-containing tag transferred from the "bait" protein (Figure 1a). This can then be used to enrich the crosslinked target, improving the signal-to-noise ratio in downstream mass spectrometry analysis. The signal-to-noise can also be enhanced by digesting the tagged proteins captured in thiol-beads, allowing all non-thiol containing (and therefore non-crosslinked) peptides to be removed from the sample prior to analysis by mass spectrometry (Figure 1b). The fact that the position of this thiol group is at, or in a close proximity, to the interaction interface allows the use of the transferred tag location, identified via mass spectrometry, as a proxy for the site of the target-bait interaction. As a final and important step, we developed an LED platform to irradiate the samples. This system enables crosslinking to reach completion in ~10 seconds with minimal

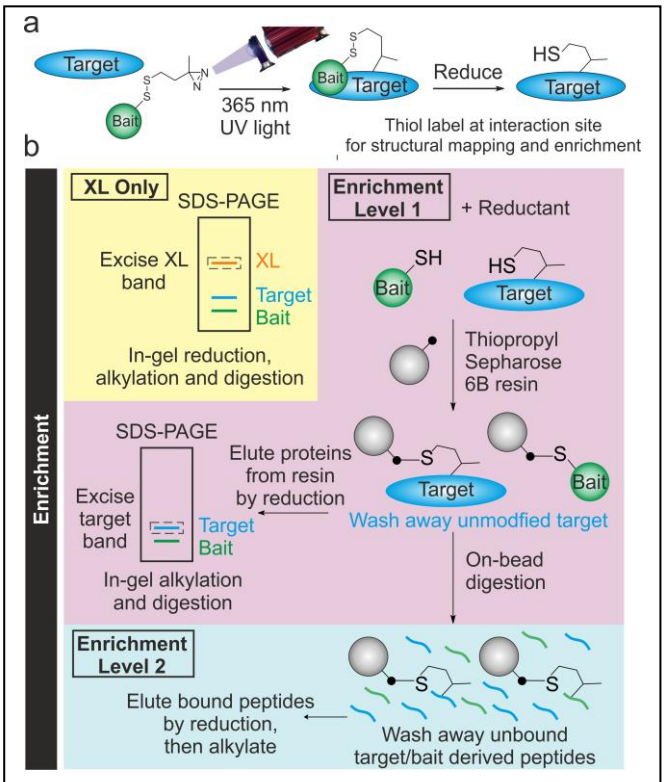


**Figure 1:** Schematic of the tag transfer strategy. (a) Overview of the method. (b) Tag-transfer crosslinking (XL) allows varying degrees of enrichment of the XL product.

heating, compared with >30 minutes needed to form the same extent of cross-linking using a traditional UV lamp source.

The new crosslinkers, as well as the enrichment and mass spectrometry workflow were showcased on two protein-protein interactions with different modes of binding. BID is the regulatory partner of the pro-apoptotic human protein, MCL-1. A derived peptide, $BID_{80-102}$, has been shown to interact via a tight helix-in-groove interaction with MCL1 with nanomolar affinity. On the other hand, the *E. coli* periplasmic chaperone Skp interacts with its substrates, such as the outer membrane protein OmpA, by sequestering them inside its tentacle-like legs and holding it an unstructured, dynamically tumbling state. Introducing the small MTS-diazirine crosslinker (Figure 1a) to single-Cys mutants of the $BID_{80-102}$ bait peptide and incubating with MCL-1 showed minimal perturbation to the binding affinity of this tight interaction upon introduction of the cross-linking moiety (Figure 2a). Subsequent crosslinking (without enrichment) was used to map the interaction interface between BID and MCL-1 (Figure 2b). Using the same method with the chaperone-substrate pair OmpA and Skp, we were able to map this highly dynamic interface from just a single position on OmpA. For this dynamic and heterogeneous interaction interface, enrichment of the cross-linked protein was found to be essential to yield sufficient crosslinks to map the interface, highlighting the enhanced sensitivity afforded by the enrichment methodology (Figure 2c, d).

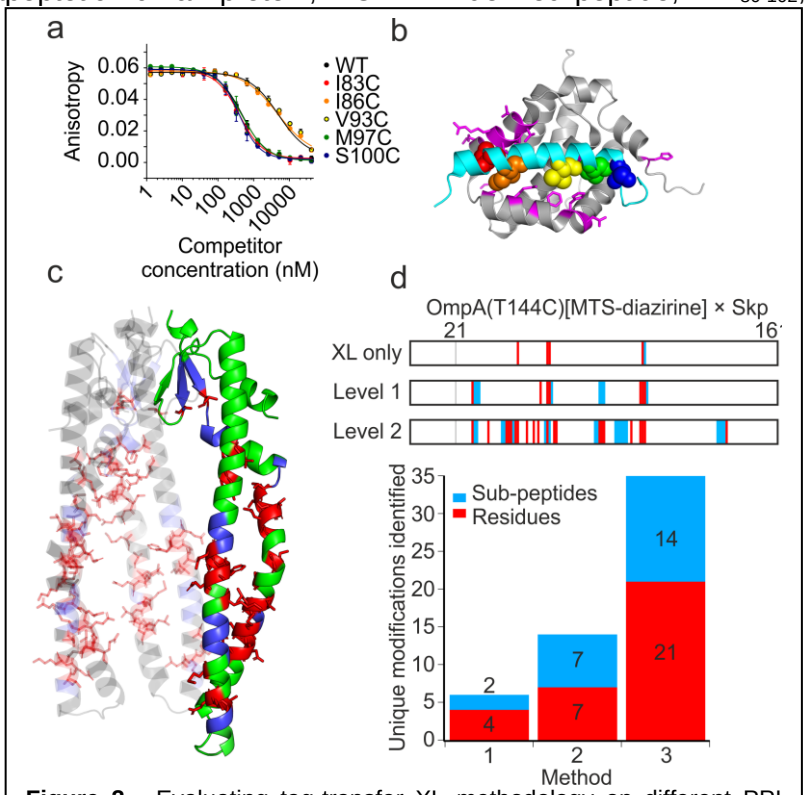


**Figure 2:** Evaluating tag-transfer XL methodology on different PPI interfaces. (a) Introduction of MTS-diazirine onto $BID_{80-102}$ at its interaction interface minimally perturbs binding to its regulatory partner MCL-1 as measured by fluorescence anisotropy. (b) Crosslinks (shown in purple) derived from a series of individual labelled 'bait' $BID_{80-102}$ peptides (backbone shown in cyan, mutated residues shown as space-fill) onto the 'target' MCL-1 (grey) agree well with the NMR structure of this interaction. (c) The dynamic interactions of a single Cys variant of OmpA mapped in detail into the cavity of Skp defined by its tentacle-like legs. Residue level information is shown as red-sticks, while crosslinks mapped to a region >1 residue are shown in blue. (d) Crosslink yield for the three enrichment methods shown in Fig. 1b mapped onto the primary structure of Skp (top) with the total number of unique modifications identified for each method shown below.

In summary, the methodology we have developed enables rapid and efficient crosslinking of interacting proteins, enrichment and isolation of the crosslinked target protein from the mixture and extremely sensitive localisation of the interacting interface. The crosslinkers are now available commercially from Redbrick Molecular and Fluorochem.

**Publications**

Horne J.E., Walko M., Calabrese A.N., Levenstein M.A., Brockwell D.J., Kapur N., Wilson A.J. & Radford S.E. (2018) Rapid Mapping of Protein Interactions Using Tag-Transfer Photocrosslinkers. *Angew. Chem. Int. Ed.* **57 (51)**: 16688-16692.

**Funding**

This work was funded BBSRC, EPSRC, Wellcome Trust, RAEng, GSK and ERC.

## Fluid flows and their role in therapeutic protein aggregation

Leon Willis, Amit Kumar, John Dobson, Ioanna Panagi, Lorna Kelly, Samantha Lawrence, Nikil Kapur, David Brockwell and Sheena Radford

### Introduction

Monoclonal antibodies (mAbs) represent the fastest growing class of protein-based drugs, with over 70 approved to date. The successful development of mAbs as medicines is hindered by the likelihood of these proteins unfolding, misfolding and aggregating. Aggregates have been linked to adverse immunological effects in patients and in the failure of developing early leads into 'manufacturable' products. Therefore, identifying non-aggregation prone but efficacious mAbs is a great challenge for industry. It is well-understood how certain physico-chemical changes, such as in temperature and pH, can trigger protein aggregation. For biopharmaceuticals, the hydrodynamic forces proteins encounter during their manufacture have long been linked to causing them to aggregate. Despite ~50 years of both fundamental and applied research, our understanding of this link remains tenuous due to: the structural and topological diversity of proteins investigated, the types of flow that the proteins were subjected to and the presence or absence of other factors, such as air-water interfaces, in such studies. Here, we describe the use of a previously characterised extensional and shear flow device (EFD) to subject three mAbs and BSA to defined fluid fields, with the resulting aggregates quantified using a protein pelleting assay.

### Results

The EFD consists of two Hamilton syringes connected together with a glass capillary. Protein solution is driven from one syringe to the other at a defined velocity. The design of the device, validated by Computational Fluid Dynamics (CFD), means proteins are exposed to both extensional flow and shear flow (Figure 1).

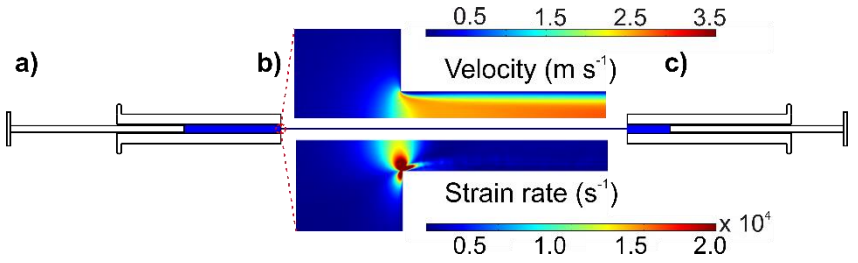


**Figure 1:** Schematic of the extensional flow device (EFD). a) 0.5 mL of protein solution is driven from one syringe to the other *via* a glass capillary. b) Computational Fluid Dynamics (CFD) shows that the 15:1 contraction ratio between the syringe and capillary causes a 238-fold increase in the velocity of the fluid (top profile). The bottom profile shows the rapid change in strain rate at the contraction point, indicative of an extensional flow. When the plunger is pushed at a velocity of 8 mm $s^{-1}$, proteins are exposed to a strain rate = 11,750 $s^{-1}$ for ~18 μs, followed by a shear rate = 52,000 $s^{-1}$ for 40 ms of shear flow in the capillary. c) The device then reciprocates on the next pass, expelling the contents of the right-hand syringe into the left and so on. Upon completion of the desired number of passes, the EFD is disassembled and the sample analysed using a pelleting assay.

In addition to the model protein BSA, which has been shown to aggregate under different fluid fields, three IgG1 mAbs were procured from MedImmune: WFL- a difficult to manufacture mAb targeting nerve growth factor; STT-a mutant of WFL designed to have favourable biophysical properties, despite differing by only 6 residues; mAb1- a 'generic' IgG1 with no known target. Under controlled flow conditions, the three mAbs were shown previously to be inherently more sensitive to aggregation under flow than BSA, with WFL being most sensitive and STT being the least sensitive.

For BSA, we also showed that when both the strain rate and pass number (the number of times the solution was exposed to the flow field) were varied independently, the extent of

aggregation varied. In this study, both the strain rate and number of passes were varied in the EFD when stressing BSA, STT and WFL (Figure 2).

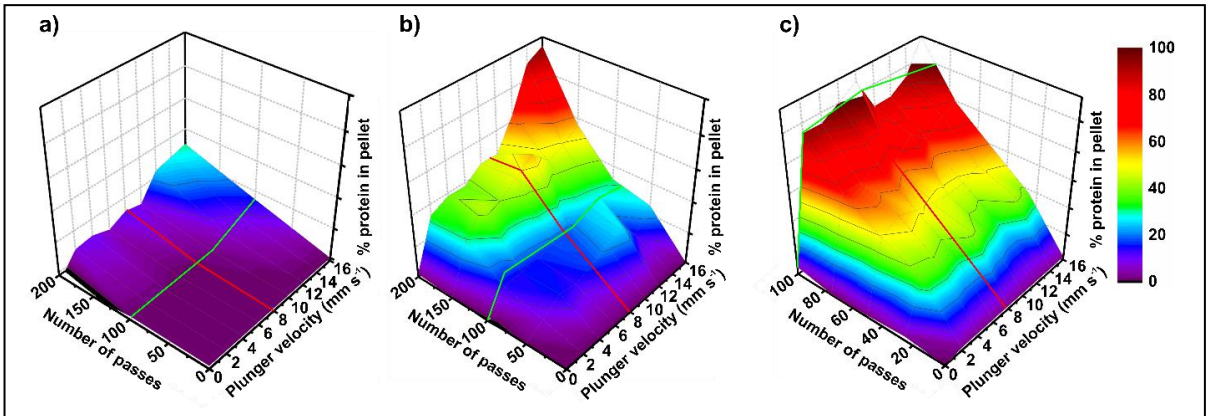


**Figure 2:** Aggregation landscapes for a) BSA, b) STT and c) WFL. Following stress in the EFD for the stated number of passes at a given plunger velocity (strain rates from 3,184–23,421 $s^{-1}$), samples were centrifuged for 30 mins at ~35,000 *xg*, with the amount of protein in the pellet fraction then quantified using UV-vis spectroscopy. [BSA] = 5 mg $mL^{-1}$, whilst [STT] and [WFL] = 0.5 mg $mL^{-1}$. Red lines highlight the data for 8 mm $s^{-1}$, whilst green lines highlight the data obtained after 100 passes of stress.

BSA possesses a very flat aggregation landscape (Figure 2a), with aggregation most pronounced at high strain rates (equivalent to plunger velocities >10 mm $s^{-1}$) after 200 passes, as observed previously. STT, on the other hand, has a more complex landscape (Figure 2b). Under harsh flow conditions (high pass numbers and high plunger velocities), STT is rendered almost completely insoluble due to aggregation. Additionally, a large, blue region of the landscape exists where relatively low levels (<30%) of STT aggregation occurs. In contrast, WFL possesses a strain-independent, pass-dependent aggregation landscape (Figure 2c). After 100 passes, almost all of the protein is rendered insoluble, accentuating the sensitivity of WFL to flow compared to its mutant, STT. It also suggests the energy mediated through flow to put proteins into an aggregation-prone state varies widely, even for closely-related proteins.

In further work, mAb1 was shown to have flow-induced aggregation behaviour in between that of WFL and STT, i.e. greater strain sensitivity than WFL, as well as aggregating to approximately twice the extent of STT after 100 passes of stress. IgG aggregation was also found to be highly dependent on the buffer used in the experiment. The work discussed above was conducted in 150 mM ammonium acetate, pH 6.0. By stressing the three IgGs in 125 mM L-arginine + 20 mM sodium succinate, pH 6.0 for 100 passes (plunger velocity = 8 mm $s^{-1}$), aggregation levels were greatly suppressed, even for WFL. This approach could be used by industry to scout for favourable flow conditions and map these onto plant-scale equipment. This would allow manufacturing processes to be altered to minimise flow-induced aggregation of mAbs, increasing yields and decreasing the overall cost of manufacture. Furthermore, the buffer data open up the possibility of using the EFD as a formulation tool. Work is currently ongoing to determine the exact pathways by which mAbs aggregate under flow.

## Publications

Willis L.F., Kumar A., Dobson J., Bond N.J., Lowe D., Turner R., Radford S.E., Kapur N. & Brockwell D.J. (2018) Using extensional flow to reveal diverse aggregation landscapes for three IgG1 molecules. *Biotechnol. Bioeng.* **115**: 1216-1225.

## Funding

This work was funded by the University of Leeds, MedImmune and the EPSRC

## Collaborators

*External*: Nick Bond, Richard Turner, Paul Varley, David Lowe (MedImmune plc)

## Hydrogen deuterium exchange and fast photochemical oxidation of proteins: method development and characterisation of aggregation-prone proteins

Owen Cornwell, James Ault, Antonio Calabrese, Yong Xu, Alison Ashcroft and Sheena Radford

### Introduction

The study of protein structure and dynamics is essential for the understanding of protein folding, function, misfolding, and aggregation. Hydrogen deuterium exchange (HDX) is a chemical labelling technique, frequently used in conjunction with mass spectrometry (MS), where deuterium exchange for protons in the backbone amide groups of the protein sequence can be used to reveal changes in solvent accessibility and hydrogen bonding, over long timescales (typically sec-hours). We sought to compare HDX-MS with fast photochemical oxidation of proteins (FPOP), a comparatively new technique for probing protein solvent accessibility and dynamics, using hydroxyl radicals liberated from photolysis of hydrogen peroxide to covalently oxidise solvent-accessible side-chains on the µs-ms timescale. Unlike HDX, the effect of solution conditions and nearby side-chains in FPOP are not well understood, although the irreversible nature of the covalent labelling in FPOP allows ergodic fragmentation techniques to be used for sequencing enabling information at the single amino acid level without any back-exchange of the label; both of which are common issues with HDX-MS. Given the propensity of FPOP to label large hydrophobic side chains, the solvent exposure of which is often implicated in protein aggregation, we applied FPOP and HDX-MS to the study of aggregation-prone proteins, specifically $\beta_2$-microglobulin ($\beta_2$m) and its aggregation-prone variant, ΔN6, which lacks the six N-terminal residues.

### Results

Comparison of the properties of wild-type and ΔN6 $\beta_2$m using HDX-MS showed three regions of significantly increased deuterium uptake in ΔN6 at the earliest labelling time point (30 s), all of which are proximal to the six residue N-terminal truncation present in ΔN6, highlighting changes in solvent accessibility and hydrogen bonding associated with the loss of the N-terminal hexapeptide (Fig. 1a,c). After 2 hours of deuterium labelling, smaller differences (<5%) were observed throughout the sequence of the proteins, consistent with the known difference in stability of the two $\beta_2$m variants (Fig. 1d).

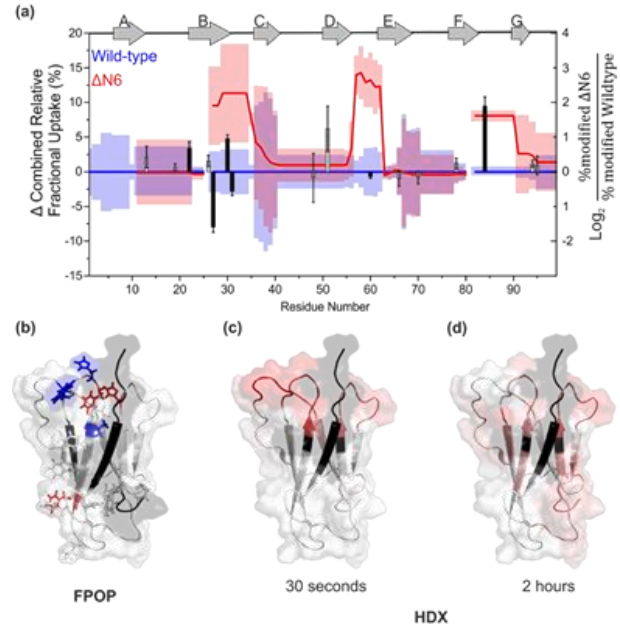


**Figure 1**: Differences in main chain dynamics between wild-type and ΔN6 $\beta_2$m monitored by HDX and FPOP. (a) HDX difference plot using PAVED showing difference in combined relative fractional uptake after 30 secs deuterium labelling (left y-axis) between ΔN6 (red line) and wild-type $\beta_2$m (blue line, set to zero for reference). Shaded regions show combined standard deviation per residue. A bar chart of the FPOP data is overlaid, showing residues modified by FPOP as a ratio of %modified ΔN6/%modified wild-type $\beta_2$m plotted on a $Log_2$ scale (right y-axis, $p < 0.05$ = solid black, no significant change = grey). (b) Side-chains of residues modified by FPOP mapped onto the structure of $\beta_2$m. No significant difference = grey, more labelling in wild-type = blue, more labelling in ΔN6 = red. (c, d): Statistically significant relative fractional uptake differences in HDX ($p < 0.05$) after (c) 30 secs) and (d) 2 hours. Red regions indicate significantly higher deuterium uptake in ΔN6 relative to wild-type. In (b), (c), and (d) missing residues and the N-terminal truncation are shown in black. PDB: 2XKS

The two proteins were also analysed using FPOP under identical solution conditions to those used for HDX-MS. LC-MS/MS analysis of chymotryptic peptides of the oxidised proteins revealed that 6 of the 17 identified oxidised residues showed statistically significant degrees of modification in the wild-type protein and ΔN6 (Fig. 2a). Five of these residues are located proximal to the N-terminal truncation, and in regions that also showed differences in deuterium uptake at the earliest labelling time point (Fig. 1a,b).

More detailed analysis of the FPOP LC-MS/MS data showed a surprising complexity, with multiple retention times observed for the same modified peptide. This is consistent with hydroxyl radical oxidation at different positions on amino acids containing aromatic rings (Phe, Tyr, Trp). For example, for modified Phe30, differences in FPOP modification for each of the potential positional isomers (ortho-, meta- and para-oxidised) were observed, with quantification of each (based on their known, different retention times on LC) (Fig. 2c), correlated well with changes in solvent accessibility between the two proteins, determined from their NMR structures (Fig. 2a-c). Similarly, modified Trp60 showed a total of nine different oxidation products (Fig. 2d), consistent with hydroxyl radical attack on both the pyrrole and benzene rings of the side chain, and known tryptophan oxidation chemistry.
Side-chain movements of this nature are difficult, if not impossible, to detect using HDX measurements and highlight the utility of FPOP to probe changes in solvent accessibility, particularly for large hydrophobic side chains, at sub-amino acid level resolution. As such, FPOP may provide invaluable new information for the study of protein folding, dynamics, and conformational change, including the conformational changes that drive aggregation into amyloid.

Note also that during the development of this work a new algorithm to enable easy comparison on the difference in HDX profiles of two proteins, or the same protein under to different conditions. This algorithm, named PAVED (Positional Averaging for Visualising Exchange Data) was used to generate Fig. 1a and can be downloaded from https://biologicalsciences.leeds.ac.uk/facilities/doc/mass-spectrometry/page/5

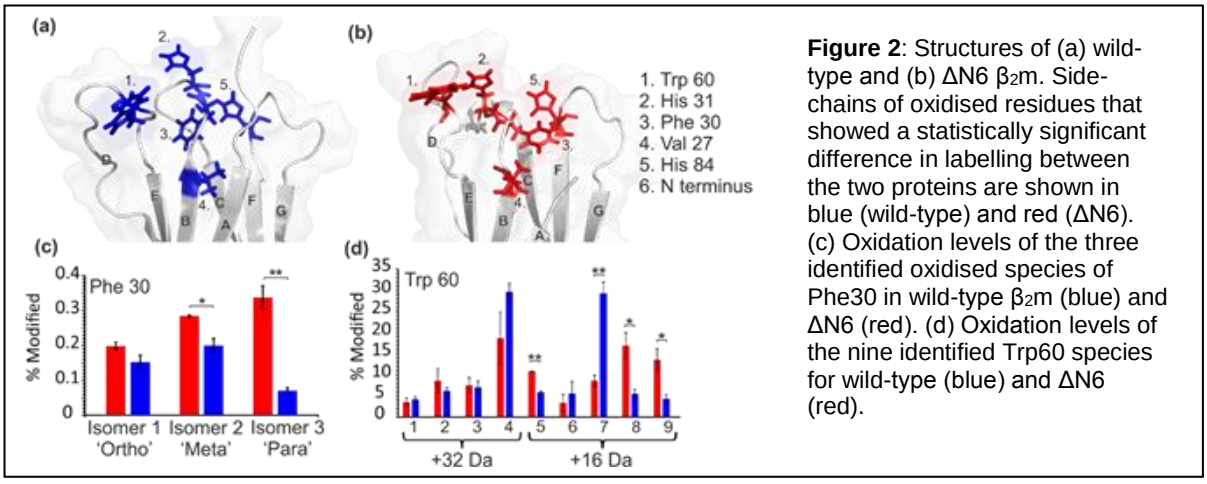


**Figure 2**: Structures of (a) wild-type and (b) ΔN6 $\beta_2$m. Side-chains of oxidised residues that showed a statistically significant difference in labelling between the two proteins are shown in blue (wild-type) and red (ΔN6). (c) Oxidation levels of the three identified oxidised species of Phe30 in wild-type $\beta_2$m (blue) and ΔN6 (red). (d) Oxidation levels of the nine identified Trp60 species for wild-type (blue) and ΔN6 (red).

**Publications**

Cornwell O., Radford S. E., Ashcroft A. E. & Ault J. R. (2018) Comparing hydrogen deuterium exchange and fast photochemical oxidation of proteins: A structural characterisation of wild-type and ΔN6 $\beta_2$-microglobulin. *J. Am. Soc. Mass spectrum*. **29**: 2413-2426.

**Funding**

This work was funded by Medimmune plc and the BBSRC

**Collaborators**

*External*: Nick Bond (Medimmune plc)

## Doubling Up! How to build a geminivirus capsid

Emma Hesketh, Chloe Fisher and Neil Ranson

### Introduction

Geminiviruses are major threats to food security and agricultural economies globally, being the causative agents for diseases that include: maize streak disease and cassava mosaic disease in Africa; golden mosaic disease of beans in the Americas; tomato yellow leaf curl disease across much of the globe; and cotton leaf curl disease across India and Pakistan. They are single-stranded DNA viruses with complicated genetics. Many geminiviruses have two different (A & B) genomes, each about 2.7 kilobases in length and encoding multiple gene products. Geminiviruses also have satellite genomes ($\alpha, \beta, \delta$ etc) of ~1.0-1.3 kilobases in length, that enhance infectivity. Their closest relatives are the nanoviruses, which have multipartite genomes each of ~1 kilobase in length, and each encoding a single gene product. Geminiviruses thus appear to be able to package much larger amounts of DNA than nanoviruses, and to achieve this, they have evolved a unique capsid structure. Whereas nanoviruses have *T*=1 icosahedral capsids of ~18nm in diameter, geminiviruses are formed from two such isometric particles, or 'hemicapsids', fused to form a geminate particle which gives the virus family its name. Until recently, no high-resolution structure for a geminivirus was available to describe how this architecture was realized. However, low-resolution cryo-EM studies suggested that the geminivirus coat protein (CP) adopts a structure similar to that of satellite tobacco necrosis virus (STNV), a single-stranded RNA virus. However, STNV also has a much smaller genome than a geminivirus (~1250 vs ~2700 nucleotides), so geminate capsids again can package more genetic material than a simple *T*=1 particle, despite encoding a single, similar, capsid protein. Conceptually, this is the same leap in packaging capacity to that made by other viruses in the transition from *T*=1 to *T*=3 capsids described by Caspar & Klug in classical quasi-equivalence. In the absence of a truly high resolution structure for a geminivirus capsid, many questions of fundamental biological interest remain unanswered in geminivirus biology. Firstly, how does a single capsid accommodate the different conformations required to build a geminate particle? Secondly, no empty geminivirus particles have ever been reported, implying that DNA binding is intimately linked to capsid assembly; but how is DNA recognized and packaged?

### Results

Here we present the first atomic resolution structure of a geminivirus capsid: the cryo-EM structure of Ageratum yellow vein virus (AYVV) at 3.3 Å resolution (See Figure 1).

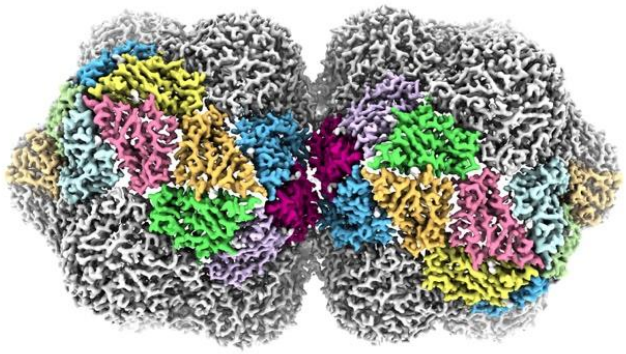

**Figure 1:** The structure of Ageratum yellow vein virus at 3.3 Å resolution. The density is segmented and coloured to highlight the 11 unique copies of the single AYVV coat protein subunit in the D5 asymmetric unit. The fivefold symmetry axis is horizontal and through the centre of the particle in this view. Three distinct conformations of the CP are seen (see Figure 2).

Geminiviruses have an obligate arthropod vector and are strictly phloem-limited, and so are not mechanically transmissible. They are thus extremely difficult to propagate and grow in the quantities required for structural studies. To overcome this, we used an agrobacterium transformed with a plasmid containing the AYVV DNA-A to agro-infect *N. benthamiana* plants. Geminate particles were then purifiable from the leaves of infected plants in quantity. The structure shows that the capsid is built from three distinct conformations of a single CP subunit, and that these conformational differences facilitate the formation of the interface between

hemicapsids. In figure 1, the blue and magenta subunits at the 'waistline' of the particle are in different conformations to all other positions in the capsid.

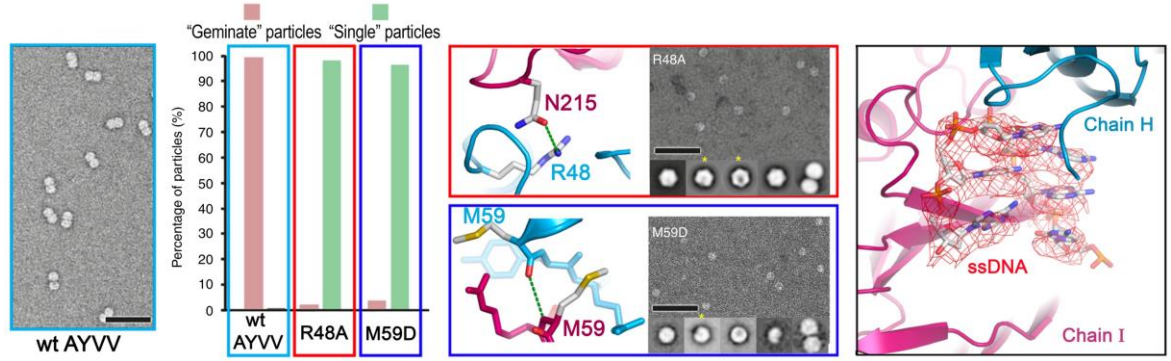


**Figure 2:** wt AYVV only forms geminate particles. The R48A and M59D mutations were designed based on the cryo-EM structure to disrupt the geminate interface, and in both cases, a clear switch from geminate to 'single' particles is are introduced is observed in an in vivo assembly assay with the α-satellite DNA. Contacts to the packaged DNA for Chain H (at the interface) are different to those at any other position in the capsid.

At the interface, the N-terminus of the CP, which is disordered throughout the rest of the capsid, adopts two different conformations. In the H subunit (blue), a new helix-loop-helix motif is formed, and a new β-strand interaction is formed with a segment of the N-terminus from the I subunit (magenta). Collectively these two interactions form the interface between the two geminate half capsids. To test the importance of these interactions for geminate capsid assembly, we designed two mutations that disrupt the different parts of this interface. Using *in vivo* assembly assays with a satellite DNA molecule, we saw a complete switch from geminate to single particles, suggesting that the interactions we observe are critical for correct assembly. We do not yet fully understand how the different CP conformers are specified – i.e. how does a CP 'know' where it sits within a capsid? However, we do also see differences in ssDNA binding at the interface between hemicapsids, with a unique interaction between the DNA backbone and Arg42 in subunit H, which when mutated to alanine completely abolishes all assembly *in vivo*. We hope that in the future, higher resolution studies without symmetry averaging will allow us to see the molecular details of this protein:DNA interaction.

**Publications**

Hesketh E. L., Saunders K., Fisher C., Potze J., Stanley J., Lomonossoff G. P. , & Ranson N. A. (2018). The 3.3 Å structure of a plant geminivirus using cryo-EM. *Nat. Commun.*, *9*: 2369.

**Funding**

This work was funded by the BBSRC.

**Collaborators**

*External:* Keith Saunders, Joran Potze, John Stanley & George Lomonossoff (John Innes Centre, Norwich, UK).

## Collection, pre-processing, and on-the-fly analysis of data for high-resolution, single-particle cryo-electron microscopy

Rebecca Thompson, Matthew Iadanza, Emma Hesketh and Neil Ranson

### Introduction

The dramatic growth in using cryo-electron microscopy to generate high resolution structures of macromolecular complexes has changed the landscape of structural biology. The majority of structures deposited in the electron microscopy data bank at higher than 4 Å resolution were collected on Titan Krios microscopes. While the pipeline for single particle data collections is becoming routine, there is much variation in how sessions are set up. Furthermore, when collection is underway there are a range of approaches to efficiently move and pre-process this data.

### Results

Here we present a standard operating procedure for single particle data collection with Thermo Fisher Scientific EPU software, using the two most common direct electron methods, and a strategy for structuring this data to enable efficient pre-processing and on-the-fly monitoring of data collection. By performing microscope data collection set-up in a consistent and systematic way, it increases the likelihood of collecting high quality data, and makes troubleshooting more straightforward. In addition, we describe a pipeline to organise and pre-process the multiple terabytes of data each microscope produces in a standard session. This not only makes the handling of such datasets more practical and decreases time taken to generate a structure, but also helps to assess the quality of data 'on-the-fly' and allow adjustments to be made to acquisition parameters where required, to improve data quality (Figure 1).

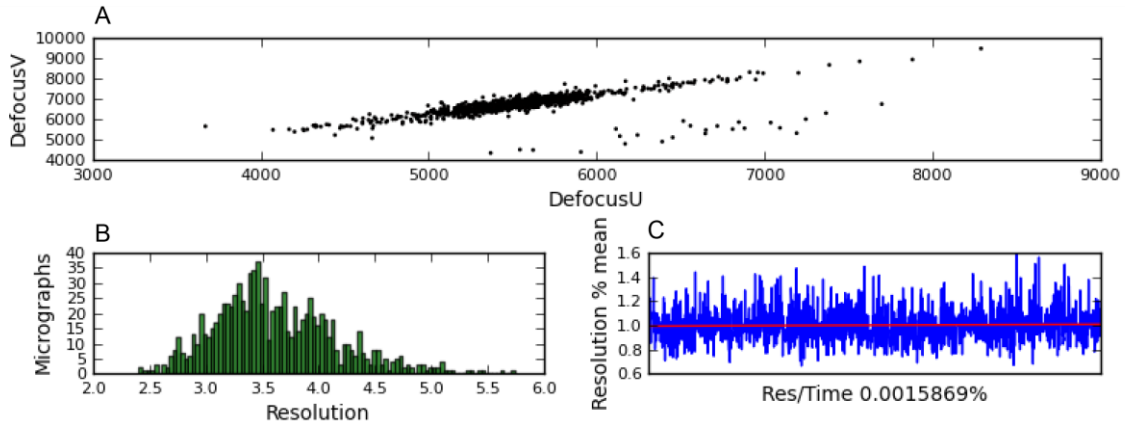


**Figure 1:** Example output from the micrograph analysis script. A scatter plot of the two orthogonal defocus measurements (A) provides a quick visual assessment of the range of defocus values in the dataset. Histograms in the left column describe the overall dataset estimated resolution (B) and resolution values for each micrograph in the order they were acquired, expressed as a percentage of the mean values for the entire dataset (C). Large changes in these values over time suggest a problem may have occurred during the data acquisition run.

### Funding

The Titan Krios microscopes were funded by the University of Leeds and Wellcome Trust. ELH is partially funded by BBSRC. MGI received funding from the European Research Council under European Union's Seventh Framework Programme and the MRC.

### Collaborators

*External:* Shaun Rawson (Harvard Medical School).

## Sugars give blood cells a push

Ralf Richter

### Introduction

The softness of the blood vessel could repel blood cells away from the vessel walls. Streaming towards the centre of vessels ensures that red blood cells move freely to deliver oxygen and do not clump together and get stuck. It was long thought that this is largely due to the softness of the red blood cells themselves, since they deform under blood flow and lift away from walls. Our research now shows that the soft, sugar-rich lining of blood vessel walls, the endothelial glycocalyx, may play an equally important role in this process. This finding highlights the importance of glycan-rich cell coats and their physical cues (next to biochemical cues) in the communication of cells with their environment.

### Results

To demonstrate the lift effect of the endothelial glycocalyx, we built a model glycocalyx using its main sugar component hyaluronan and imaged the movement of cell-sized beads. The beads lifted substantially away from the wall under flow conditions found in blood vessels, and softer hyaluronan 'brushes' caused an even bigger effect. These experimental data are the first of their kind and are supported by physical theory.

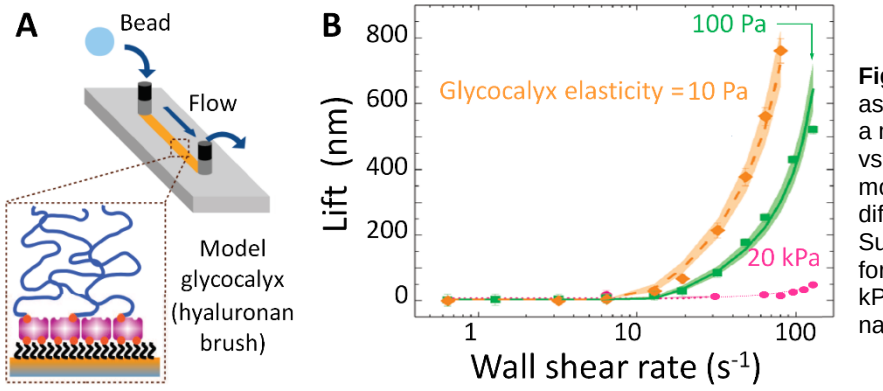


**Figure 1:** (**A**) Laminar flow assay with microbeads and a model glycocalyx. (**B**) Lift vs. wall shear rate for model glycocalyces of different elasticity. Substantial lift is observed for elasticities in the sub-kPa range characteristic for native endothelial

The lift effect arises from coupling the hydrodynamics of flowing blood and elastic glycocalyx deformation. This study thus emphasizes the importance of elastohydrodynamics in blood circulation and unveils a new mechanism by which the glycocalyx may be involved in regulating the interactions between circulating cells and vascular walls.

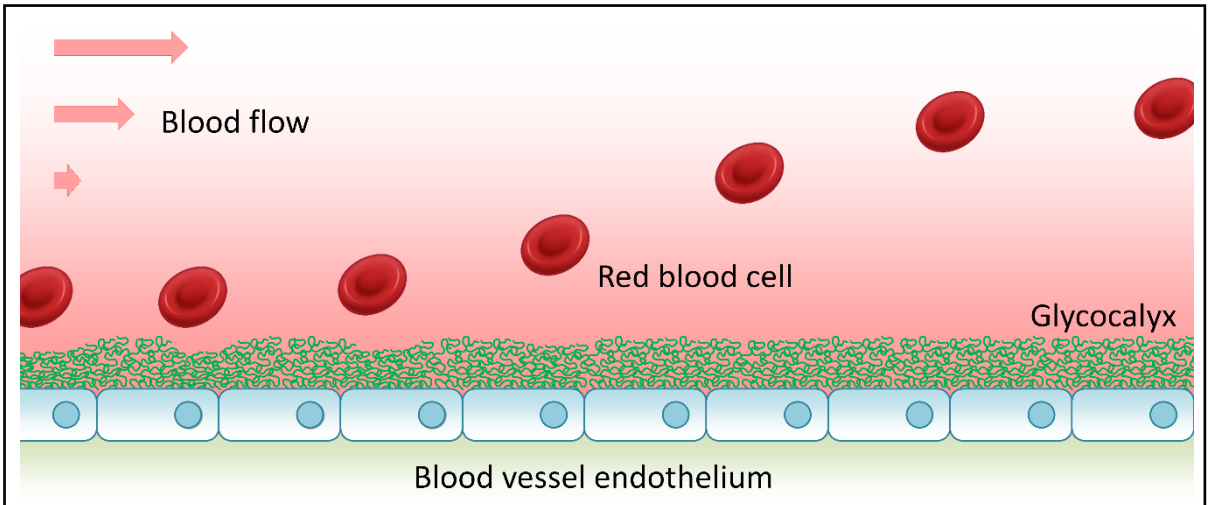


**Figure 2:** The physics of sugar coats conditions how circulating cells interact with the blood vessel wall. The inner walls of all blood vessels are lined with the endothelial glycocalyx, a soft and swollen coat made from polysaccharides and proteins (here illustrated as a green mesh). Cells circulating in the blood, such as red blood cells, deform the glycocalyx owing to the hydrodynamic liquid flow around them. This physical effect pushes the cells off the wall and retains them in the centre of the vessel.

We have a particular interest in understanding how such effects condition the selective traffic of circulating cells (e.g. immune and stem cells) into inflamed or damaged tissues. We also show how the observed phenomenon can be used to characterize the mechanical properties of thin soft coatings.

**Publications**

Davies H. S., Débarre D, El Amri N., Verdier C., Richter R. P. & Bureau L. (2018) Elastohydrodynamic lift at a soft wall. *Phys. Rev. Lett.* **120**: 198001.

Davies H. S., Baranova N. S., El Amri N., Coche-Guérente L., Verdier C., Bureau L., Richter* R. P. & Débarre* D. (2018) An integrated assay to probe endothelial glycocalyx-blood cell interactions under flow in mechanically and biochemically well-defined environments. *Matrix Biol.* in press, **DOI:** 10.1016/j.matbio.2018.12.002.

**Funding**

Thiswork was funded by the European Union (PRESTIGE programme and European Research Council), the Royal Society, the University Grenoble Alpes (France), the French National Research Agency and the French National Centre for Space Studies.

**Collaborators**

*External:* Heather Davies (University Grenoble Alpes; now Blueberry Therapeutics), Lionel Bureau, Liliane Coche-Guérente, Delphine Débarre, Nouha El Amri & Claude Verdier (all University Grenoble Alpes), Natalia Baranova (CIC biomaGUNE, Spain; now IST Austria)

## Biosynthesis of the 15-membered ring depsipeptide neoantimycin

Divya Thankachan, Kenneth McDowall and Ryan Seipke

### Introduction

*Streptomyces* species produce an incredible array of high-value specialty chemicals and medicinal therapeutics. Neoantimycins are 15-membered ringed depsipeptides produced by *Streptomyces orinoci* (Fig. 1). Neoantimycins were recently identified as downregulators of GRP78/BiP expression. Growth of cancerous cells is energetically expensive and as a result cells often exist in a state of hypoxia, which necessitates the overproduction of the molecular chaperone GRP78/BiP for survival. Thus, modulating the activity or indeed the level of cellular GRP78/BiP represents an exciting therapeutic target for the treatment of diverse cancers. Despite being known for >50 years, remarkably little is known about the biosynthesis of neoantimycins and thus the opportunity for bioengineering new drug variants is limited. Here we identified and cloned the neoantimycin biosynthetic gene cluster and engineered its overproduction by *Streptomyces coelicolor.* This expression chassis can be used in the future to bioengineer neoantimycin analogues and evaluate structure-activity relationships.

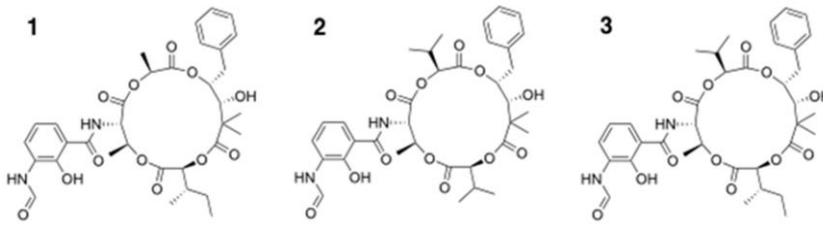


**Figure 1:** Chemical structures of neoantimycins

### Results

We sequenced the genome of the neoantimycin producer, *Streptomyces orinoci* using Pacific Biosciences SMRT RSII platform and identified a ~38 kb biosynthetic gene cluster (BGC) composed of 18 genes whose deduced functionalities were consistent with a pathway that may produce neoantimycins. A key aim of this study was to first determine if this BGC does indeed confer the production of neoantimycins and then develop an expression system by which new variants could be bioengineered in the future. To achieve this, the BGC was inserted into two plasmids harbouring orthologous phage integrate sites so that they could be stably maintained in a *Streptomyces* host without selection. Next, a suite of promoter engineering recombineering templates were developed and used to replace native promoters with strong constitutive ones such that the entire BGC would be overexpressed. The engineered neoantimycin plasmids were moved to *Streptomyces coelicolor* and the resulting strains were examined for their ability to produce neoantimycins using liquid chromatography high resolution electrospray ionisation mass spectrometry (LC-HRESIMS). As anticipated, molecular formulae for neoantimycins were observed in chemical extracts prepared from the *S. coelicolor* double integrant (Fig. 2). Current work is now aimed at using this platform to bioengineer new neoantimycin analogues.

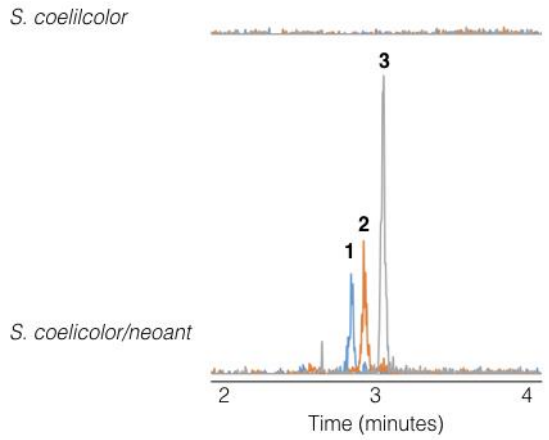


**Figure 2:** Engineered heterologous production of neoantimycins by *Streptomyces coelicolor* M1146. The empty *S. coelicolor* host (top) does not produce neoantimycins while neoantimycins are readily detectable from chemical extracts prepared from *S. coelicolor* harbouring the engineered neoantimycin plasmids (bottom). Shown are extracted ion chromatograms $[M+H]^+$ for **1, 2, 3** depicted in Figure 1.

**Publications**

Skyrud W., Liu J., Thankachan D., Cabrera M., Seipke R.F. & Zhang Z. (2018) Biosynthesis of the 15-membered ring depsipeptide neoantimycin. *ACS Chem Biol.* **13 (5)**, 1398-1406.

**Funding**

This work was funded by the University of Leeds and the BBSRC.

**Collaborators**

*External:* Will Skyrud, Joyce Liu, Maria Cabrera, Wenjun Zhang (University of California at Berkeley).

## Self-assembly of fractal liquid crystal colloids

Nikita Solodkov, Cliff Jones and Jung-uk Shim

### Introduction

Nematic liquid crystals are anisotropic fluids that self-assemble into vector fields, which are governed by geometrical and topological laws. Because of this, particulate or droplet inclusions self-assemble in nematic domains through a balance of topological defects. We use double emulsion droplets generated in a microfluidics device and controlled agitation to create multiple water droplets with radial boundary conditions inside larger radial nematic droplets. We observe spontaneous formation of fractal shapes due to the topological and elastic properties of nematic liquid crystals. We find that the size differences between the water droplets play a key role in the formation of complex three-dimensional (3D) structures. To explain our observations, we use numerical analysis to relate the basic formation of colloidal structures in radial nematic droplets to the solutions of the Thomson problem and extend the analogy to the formation of fractal structures. The results are relevant to a variety of inclusions, ranging from colloids suspensions to multi-emulsion systems. Such systems have potential applications in novel switchable photonic structures, and also provide wider insights into the packing of self-assembled structures.

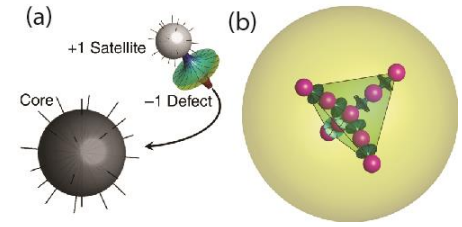


**Figure 1:** (a) Illustration of the satellite to core attachment process. (b) Diagram showing a colloidal structure with tetrahedral symmetry: water droplets are shown by magenta balls, hyperbolic defects are shown in cyan and the nematic region is shown in yellow.

### Results

Consider the domain of a nematic droplet with radial (normal to the surface) boundary conditions. From topological principles, a topological discontinuity with a charge of +1 is formed inside it and centralized to minimize the free energy of the system. Adding an inclusion (such as a particle coated with a homeotropic surfactant, or a second, smaller water droplet) with normal boundary conditions does not create any additional distortion to the radial director field. Instead, the inclusion minimizes the free energy by creating a virtual, highly splayed defect at the centre of the particle and moving the inclusion to the centre of the system. Once a satellite enters the director field, elastic forces drag it towards the point of highest splay, at which point it enters the core's primary orbit. All other satellites entering this primary orbit are attracted to the core but repel each other. This suggests that there exists a maximal capacity of satellites in the primary orbit. By symmetry, the second satellite must attach itself on the opposite side of the core to the first satellite, to minimise elastic distortion. A third satellite then has a choice between attaching itself either to the core or to one of the two existing satellites. It is the relative sizes of the droplets that determine the resulting structure. For droplets of similar size, the third and fourth droplets will become arranged at the tetrahedral angles to the core, and additional droplets beyond the fourth attach as satellites to the higher orbitals, four per orbital, to create a characteristic tetrahedral structure. Figure 1 shows the satellite attachment process and a tetrahedral structure with linear chains extending radially outward from the core that results from near equivalent sized internal droplets.

To determine the maximal orbit capacity, we first study the solution sets for distributions of repulsive points around the boundary of a circle in 2D and on the surface a sphere in 3D. In 2D systems, primary satellites distribute themselves along the vertices of regular polygons. Similarly, in 3D the structures follow the solutions to the Thomson problem (originally used to describe the electronic structure of atoms for the superseded "plum-pudding" model), which include some regular polyhedrons. Two satellites can continue to move closer together until the director reaches a critical distortion (this is equivalent to adding more satellites to the orbit). By symmetry of the director field, primary orbit satellites share a network of mirror planes and symmetry axes of rotation (Figure 2). We can see that the highest amount of distortion in the

director field occurs in the plane containing the core and two nearest neighbour satellites. As the two satellites in the same orbit approach each other, the critical separation point will be reached first in this plane, which reduces the 3D problem to 2D.

The maximal number of satellites in the primary orbit, $N_c$, can be calculated by comparing $\theta_c$ with the angles generated by the closest neighbouring vertices of the Thomson problem solutions. As $r$ tends to infinity, exact solutions of $N_c$ can be found using the Fejes inequality. The value of $N_c$ serves as the maximal achievable number of primary satellites for a given core to satellite ratio of the system. We find that our ansatz is closely matched by the numerical solution and, therefore, can be used as a quicker estimation method for $N_c$ as a function of $r$. This can be seen in Figure 2b, which shows the allowed solutions for the primary orbit satellites alongside a representative selection of experimental results. We see that the relationship between $N_c$ and $r$ is weakly non-linear for small values of $r$ and increases in a step-function-like fashion. The numerical results indicate that for systems in which the satellites are identical in size to their cores, triangular configurations are expected and we may expect tetrahedral structures to form once $r$ reaches $1.12 \pm 0.01$. In practice, there always exists a small size distribution of water inclusions, which creates enough variation in $r$ to allow tetrahedral structures.

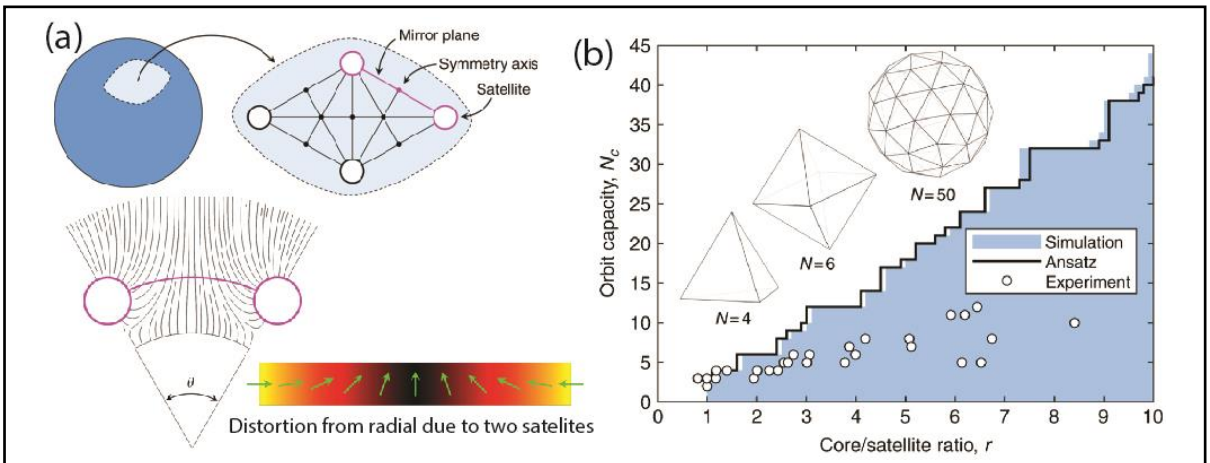


**Figure 2:** (a) Subdomain of the spherical surface corresponding to the primary satellite orbit. Large unfilled circles represent satellites, small filled circles represent symmetry axes of rotation with radial director profiles and solid lines represent unfolded mirror planes. The plane of highest disturbance (repeated in the structure) is highlighted in magenta. Distortion of the director field in the radial reference frame as a function of the polar angle between two neighbouring satellites along their orbital path with and without the presence of satellites. (b) Orbit capacity as a function of the core to satellite size ratio illustrating numerical space of possible values (blue shading), estimated maximal orbit capacity from the ansatz (black line), and a representative selection of experimental results achieved with water in a liquid crystal in water double emulsions (circles).

In conclusion, we have investigated the properties of spontaneous self-assembly of geometric structures formed from water inclusion with normal boundary conditions inside radial nematic liquid crystal droplets. Due to the vector like behaviour of nematic liquid crystals, all disturbances in the director field are governed by topological rules. We created permanent disturbances by adding small water droplets with normal boundary conditions to the nematic droplet domains, which resulted in the formation of stabilizing hyperbolic defects these emulsions. Our results indicate that in geometrically unbiased nematic droplets, radial inclusions spontaneously form 3D structures with symmetry properties matching those described by the solutions to the Thomson problem. Using numerical simulations of the director field, we have shown that the ratio between the core and the satellite inclusions plays a key role in the resulting shapes of these self-assembled colloidal structures. We also provide a simple model to describe the maximal capacity of satellites around the core as a function of their size ratios and the elastic constants of the nematic liquid crystal. As expected, it suggests that as the ratio between the bend and the splay elastic constants gets bigger, a core can accommodate more satellites in its primary orbit. Similarly, a larger core can provide more room for director deformation and therefore, a higher number of satellites. The most common shape found experimentally consisted of a core with four dipolar satellite chains extending radially away from it with tetrahedral symmetry. The shape was then altered by physical

agitation of the samples near the nematic to isotropic phase transition and deformation of spherical droplets to 2D disks to obtain single linear chains and triangular structures. Following this, we found that in systems with large distributions of satellite sizes, the colloids self-assembled in fractal structures. The number of symmetry evolutions depended on the distributions of satellite sizes. Systems with large distributions were able to achieve several evolutionary steps, surpassing the resolution of optical microscopy. Due to the length scales of director fields, the structures formed in nematic liquid crystals have a finite number of possible fractal evolution steps in the formation process of fractal colloids.

**Funding**
This work was supported by a Merck iCASE studentship for N.S. and an Advanced Fellowship in Manufacturing from the EPSRC for C.J. (EP/L015188/2).

## Fast photochemical oxidative labelling of an adenovirus

Charlotte Scarff, Binta Bedeau, Eric Blair and Frank Sobott

### Introduction

Fast photochemical oxidation of proteins (FPOP) is a chemical footprinting technique whereby exposed amino-acid side-chains are covalently labelled with hydroxyl radicals. Labelling is induced by short UV laser pulses on the sub-millisecond timescale, and down-stream mass spectrometry (MS) analysis can be used to provide information about protein structure, solvent accessibility, ligand-binding, protein-protein interactions, protein folding and dynamics.
To date, FPOP-MS has been applied to address a diverse range of problems in structural biology but has never been used previously to report on a virus structure. Here we asked the question, can FPOP-MS analysis be used to identify the surface-exposed regions of an intact virus? (Ad5, 15-17 MDa, Figure 1).

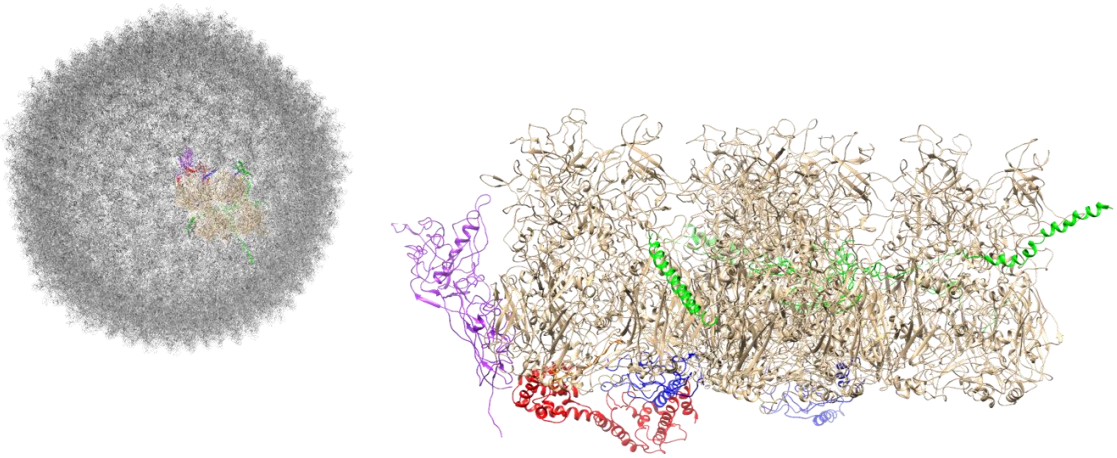

**Figure 1:** Crystal structure (PDB ID: 6CGV) of adenovirus 5 with one asymmetric unit highlighted. 60 copies of the 21-mer asymmetric unit assemble to form the intact capsid. The 21-mer consists of four hexon-protein trimers (beige), four copies of the hexon interlacing-protein IX (green), two copies of the pre-hexon linking protein VIII (dark blue), one penton protein (purple), one pre-hexon linking protein VIII (red) and one pre-protein VI (orange).

### Results

All of the main protein components of the capsid were identified by LC-MS/MS analysis. High sequence coverage was obtained for the majority of these components: 74 %, 74 %, 66 %, 63 % and 53 % for the hexon protein, hexon-interlacing protein IX, pre-protein VI, pre-hexon linking protein IIIa and the penton protein respectively. The major component of the capsid is the hexon protein with four trimers per asymmetric unit making a total of 720 copies per capsid. Three peptides within the hexon protein were found to be labelled with a hydroxyl radical in the hydrogen peroxide FPOP treated sample and not in the control. These peptides were all located on the periphery of the capsid (Figure 2). Two peptides were also found to be labelled by FPOP in the pre-hexon linking protein IIIa. Unfortunately, the full structure of the pre-hexon linking protein IIIa is not resolved in the crystal structure so whether or not these peptides are solvent-exposed is unknown. As such our results indicate that FPOP-MS can be used to inform on surface-exposed regions of an intact virus. This suggests that FPOP-MS could be used in the future to study virus breathing and virus-host interactions.

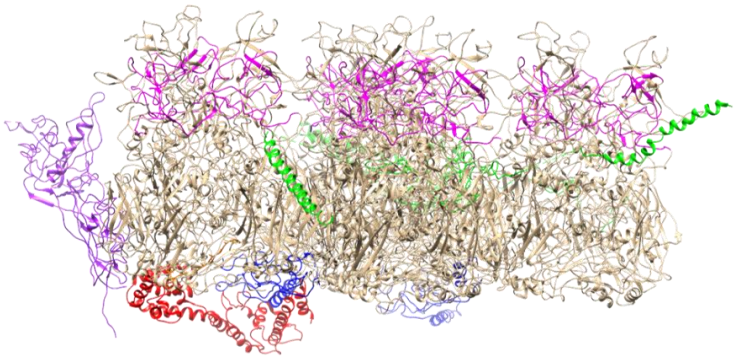

**Figure 2:** The 21-mer asymmetric unit of adenovirus 5 (coloured as in figure 1.) with the FPOP-labelled peptides of the hexon protein highlighted in magenta.

**Funding**
We thank the Wellcome Trust, BBSRC Alert and the University of Leeds for funding.

## Identification of a cyanobacterial aldehyde dehydrogenase that produces retinoic acid *in vitro*

Jennifer Miles, Michael Webb and Paul Taylor

### Introduction

Retinoic acid is a key signalling molecule in healthy development and in differentiation of stem cells. In eukaryotes retinoic acid is made by oxidation of all-*trans*-retinal by retinal/aldehyde dehydrogenases (ALDH1). This step is preceded by the production of retinal from either retinol or *beta*-carotene. As yet, this canonical signalling pathway has only been characterised in animals. Our earlier phylogenetic analysis identified orthologues of human ALDH1A1 in cyanobacteria that have a very high sequence conservation (>60%) and retain the catalytic GQCC motif. We have now characterised *in vitro* a cyanobacterial ALDH and demonstrated that it can convert retinal to retinoic acid.

### Results

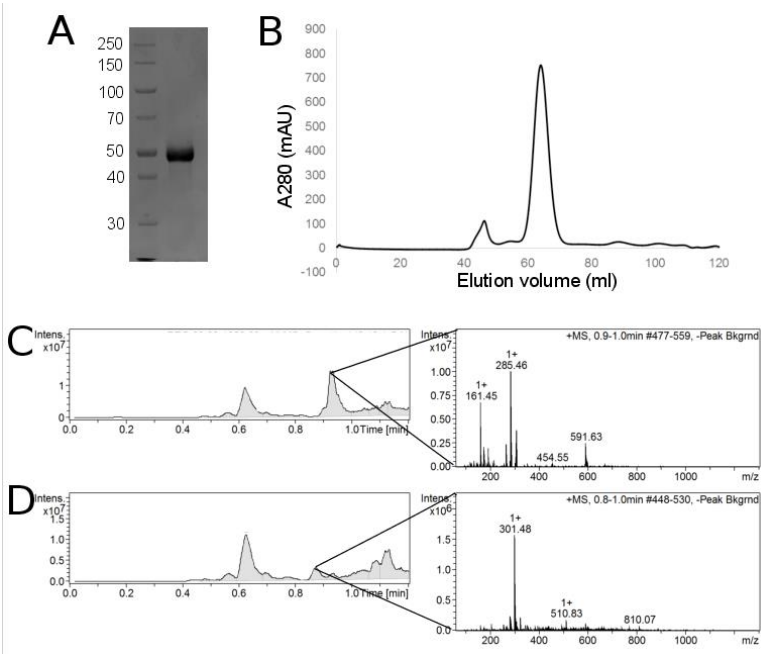


**Figure 1:** (a) SDS-PAGE analysis of purified cfALDH. (b) Size-exclusion chromatography of purified cfALDH on Hiload Superdex 200 16/60. c) LC-MS analysis indicating that retinoic acid is produced when cfALDH is incubated with retinal and NAD. cfALDH incubated with all-trans-retinal, indicating that no retinoic acid is produced without the cofactor NAD (MW all-trans-retinal 284.4). d) cfALDH incubated with 1mM NAD and all-trans-retinal, indicating that retinoic acid (MW 300.4) is produced.

We elected to strudy an ALDH1 orthologue (cfALDH) from the cyanobacterium *Chlorogloeopsis fritschii*. To ascertain the activity of the protein, cfALDH was cloned from genomic DNA and over-expressed in *E. coli*. SDS-PAGE analysis showed the purified protein has a MW ~50 kDa (Figure 1a), with analysis by accurate mass spectrometry giving a mass of 53613.60 Da whilst the calculated mass is 53614.19 Da. The protein purified as a homo-tetramer on size-exclusion chromatography (calculated mass of ~239 kDa, Figure 1b).

To establish whether retinoic acid is produced by this putative retinal dehydrogenase, an LC-MS based method was used. The purified protein was incubated in the presence of NAD and all-*trans*-retinal to determine the conversion to retinoic acid. Samples were extracted into hexane and analysed by LC-MS. After incubation at 37°C for 90 minutes retinoic acid was clearly produced when all components were present, but not without inclusion of the cofactor NAD (Figure 1c & d).

A fluorescence based assay was then used to measure NADH production and therefore calculate the levels of retinoic acid production. The concentration of all-*trans*-retinal was varied between 0.1-10 µM, whilst $NAD^+$ remained at a high concentration of 1mM andcfALDH was kept low at 200 nM (Figure 2a). The concentration of cfALDH was varied and a relationship between activity and enzyme concentration is seen as expected (Figure 2b). This process was optimal at a basic pH of 8.5 - 9.5 (Figure 2c) and enhanced by the presence of $Mg^{2+}$ in the assay buffer (Figure 2d), as seen with other ALDH1s. This is the first time a cyanobacterial ALDH has been seen to produce retinoic acid from all-*trans*-retinal. Future work should focus on establishing whether this aldehyde dehydrogenase is responsible for retinoic acid production *in vivo* and defining the role of retinoic acid in cyanobacteria.

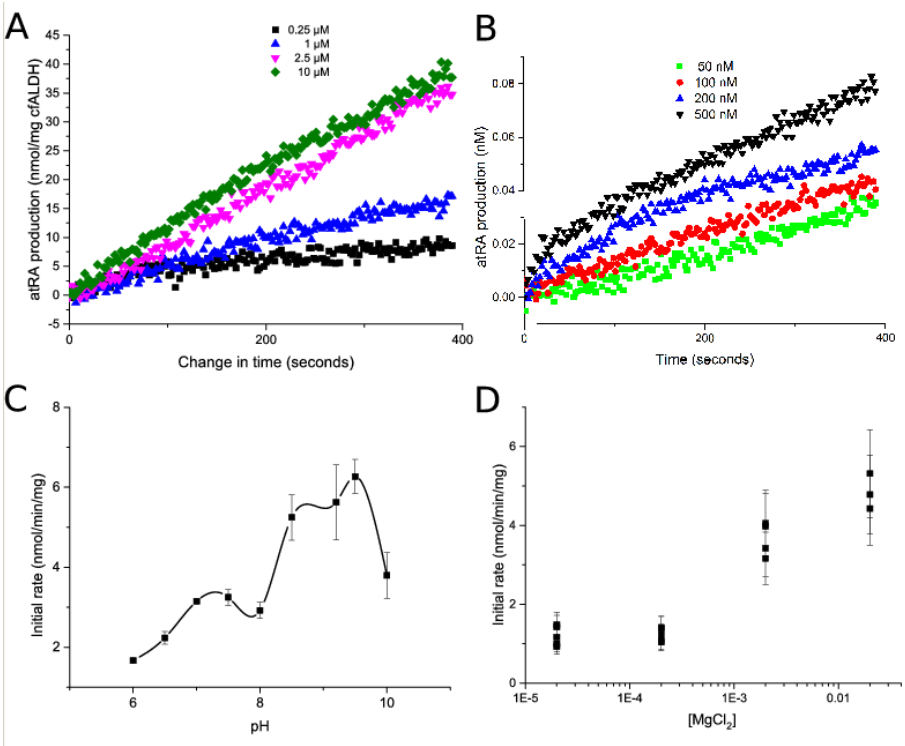


**Figure 2:** (a) Change in fluorescence seen when the concentration of all-trans-retinal is altered in the presence of cfALDH and NAD. (b) Change in retinoic acid (RA) production when the concentration of cfALDH is altered in the presence of all-trans-retinal and NAD. c) The effect of pH on cfALDH activity with the initial rate shown in µmol/mg/min. The activity is higher between pH 8.5-9.5. d) The effect of Mg2+ ion concentration on cfALDH activity with the initial rate shown in nmol/mg/min, with 20 mM giving the highest activity of the concentrations tested.

**Funding**
This work was funded by the University of Leeds.

**Collaborators**
*University of Leeds:* P. Machattou, D. Nevin-Jones
*External:* A. Millard (University of Leicester), D.J. Scanlan (University of Warwick).

## The use of affimers for DNA-paint microscopy

Alistair Curd, Christian Tiede, Michelle Peckham and Darren Tomlinson

### Introduction

Super-resolution microscopy is becoming a standard tool in cellular biology. Due to the use of target-specific fluorescent labels, super-resolution enables high-contrast imaging in complex 3D cellular architectures, and thus combines the advantages of increased spatial resolution with molecular affinity probes. Although antibodies are commonly used for fluorescence microscopy they have severe limitations for super-resolution approaches, particularly when the method used reaches localization precisions on the order of only a few nanometers. The reason for this is that antibodies are large, and the fluorescent dye label being imaged is placed some distance from the target protein. In the case of primary and secondary antibodies, the size of the probes easily adds an additional linkage error of around 10–15 nm to the actual position of the molecule of interest. Using antibodies can mean that high-performance super-resolution techniques actually report the location of the probe rather than the position of the biomolecules under investigation.

Affimer reagents (1) are artificial antibodies (ca. 10–12 kDa, ca. 2 nm) that are isolated from large phage-display libraries (approx. $10^{10}$ members). The ability to quickly isolate Affimers with high specificity and affinity that can be used in a range of applications highlights their potential as alternatives to traditional antibodies. In super resolution microscopy, Affimer reagents are particularly good as their small size means that the fluorophore is placed in close proximity to the target proteins. Affimers have been used to image actin, tubulin and a receptor tyrosine kinase by site-specific labelling with a fluorophore (1, 2). Moreover, they can be used in a range of super-resolution applications including DNA-PAINT, which provides very high resolution images.

### Results

To site-specifically modify Affimers for DNA-PAINT, we first labelled a reduced C-terminal cysteine residue with maleimide-DBCO which was then linked to azide-functionalized DNA using a strain-promoted azide–alkyne cycloaddition (SPAAC) reaction (Figure 1).

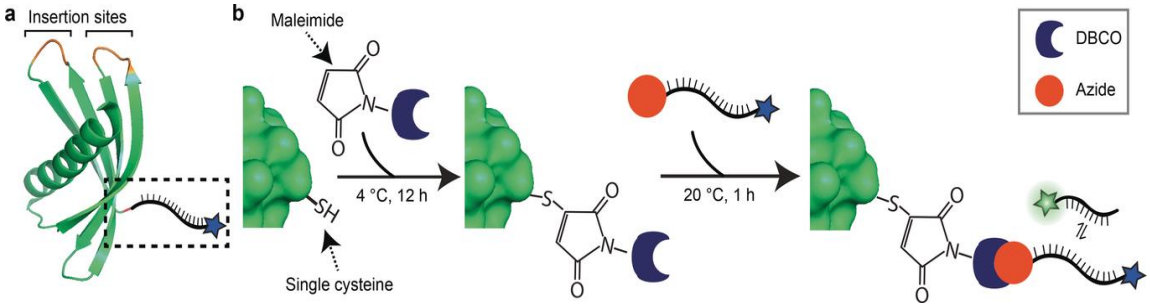


**Figure 1:** Site-specific DNA labeling of Affimer reagents. The site-specifically attached DNA strand (dotted box) contains an additional Atto488 fluorophore. b) Azide-labeled DNA is added and binds covalently to the DBCO reagent. Finally, DNA-labeled Affimers can be used for DNA-PAINT imaging. Affimer cartoons modified from PDB ID: 4N6T

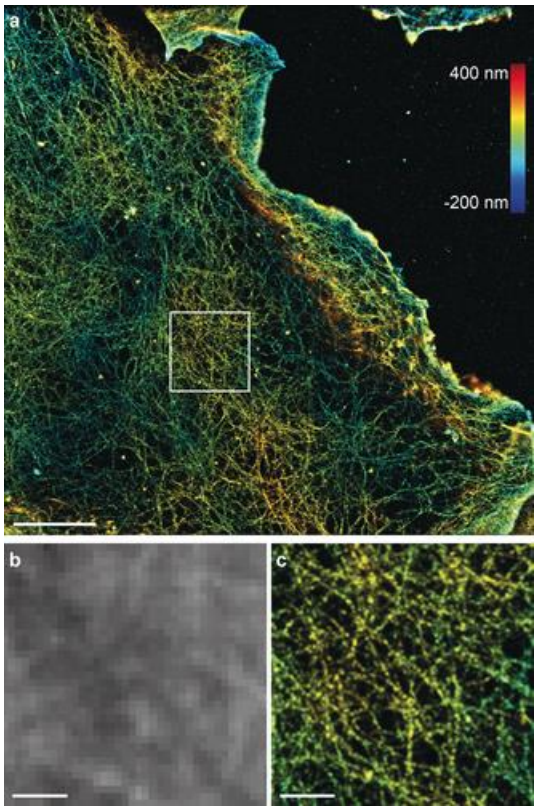


**Figure 2:** DNA-PAINT imaging of Affimer-labelled actin network in fixed Cos7 cells (colour indicates height). b) Diffraction-limited zoom-in of the highlighted area in (a). c) Super-resolved zoom-in of the highlighted area in (a) shows increased spatial resolution and dense actin labelling. Scale bars: 5 µm (a), 1 µm (b, c).

Actin filaments were then labelled in fixed Cos7 cells with purified DNA–Affimer conjugate and 3D DNA-PAINT microscopy was performed (Fig. 2a). Comparison of the diffraction-limited image (Fig. 2b) acquired shows the clear improvement in resolution obtained by DNA-PAINT (Fig. 2c) and highlights the high labelling specificity and efficiency of the DNA-conjugated actin Affimer.

**Publications**

Lopata A., Hughes R., Tiede C., Heissler S.M., Sellers J.R., Knight P.J., Tomlinson D., Peckham M. (2018) Affimer proteins for F-actin: novel affinity reagents that label F-actin in liveand fixed cells. *Sci Rep*. **8**: 6572

Schlichthaerle T., Eklund A.S., Schueder F., Strauss M.T., Tiede C., Curd A., Ries J., Peckham M., Tomlinson D.C., Jungmann R. (2018) Site-Specific Labeling of Affimers for DNA-PAINT Microscopy. *Angew Chem Int Ed Engl*. doi: 10.1002/anie.201804020

**Collaborators**

*External:* Ralf Jungmann and team (Max Plank Institute of Biochemistry, Martinsried).

## Dynamic energy landscape steering in ATP driven translocation of proteins across membranes

Joel Crossley, Matthew Watson, Sheena Radford and Roman Tuma

### Introduction

Sec machinery is universally conserved and mediates transport and insertion of proteins across and into lipid membranes. In *E. coli* the SecYEG integral membrane complex transiently associates with a cytoplasmic SecA ATPase and together they drive translocation of unfolded polypeptides into the periplasm. Recently, it was proposed that translocation is effected by gated diffusion of the unfolded polypeptide though the central channel of SecY. Channel gating is performed by the SecY lateral gate (LG) and controlled by allosteric changes elicited by nucleotide binding and hydrolysis at SecA. Likewise, passage of bulky residues within the translocating substrate is communicated back to the ATP binding site to accelerate the rate limiting step. Thus, the translocation mechanism relies on a two way communication between the peripheral SecA and the transmembrane SecY channel. Two way communication can be mediated by tightly coupling between LG gating and nucleotide cycle, i.e. open and closed LG states correspond to ATP and ADP bound SecA states, respectively. Alternatively, the coupling can be through dynamic steering in which LG remains mobile and SecA nucleotide cycle modulates the energy landscape on which the LG motion takes place. In the former case LG dynamics will be slow, essentially following the ATPase cycle on a 100 ms time scale. The latter case will be compatible with multiple states, rapidly interchanging within milliseconds. However, the time scale on which gating takes place remained elusive.

### Results

Further advances in single molecule detection and data analysis permitted us to monitor conformational changes associated with translocation initiation on the millisecond to minutes time scale (Fessl et al 2018). Recently, we have added fluorescent life time analysis to our interrogation of fast dynamics of the SecYEG:SecA complex. This, in combination with recurrence analysis, permitted us to detect fast LG dynamics and extract kinetic information on the sub-millisecond time scale. Figure 1 illustrates how simultaneous measurement of FRET efficiency and fluorescence life time enables us to distinguish between static and dynamic states. In the static case, like that of the SecYEG:SecA complex, which is locked in a closed state by ADP, fluorescence lifetime decreases linearly with increasing FRET efficiency. In contrast, during translocation SecYEG adopts a whole range of interconverting states as manifested by the departure of the joint histogram from the diagonal E-τ line. Thus, LG undergoes fast dynamics on the time needed to collect data, i.e. 0.5 ms up to 500 milliseconds. Further analysis of

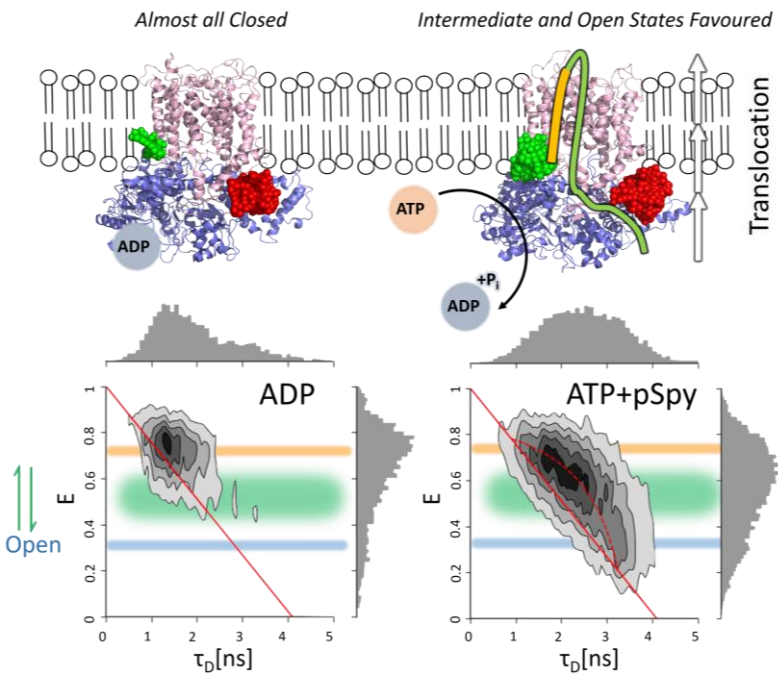


**Figure 1:** Comparison of joint FRET efficiency and fluorescence lifetime histograms for closed SecYEG:SecA:ADP (left) and translocating complex in the presence of proSpy1 substrate and ATP (right). Top and right sides of each histogram show distribution of lifetimes and FRET efficiencies, respectively.

individual time resolved trajectories (Figure 2) identified three states, open (low FRET), part open (intermediate FRET) and closed (high FRET) and frequent transitions between them. The dwell times are on the millisecond time scale, while transitions take less than a few milliseconds to complete, i.e both are faster than the ATPase cycle. Dwell times and occupancy of different states depend on the nucleotide state of SecA (Figure 2C). Hence the two way coupling seems to steer dynamics via changes to both energy of states as well as barriers associated with transitions between them.

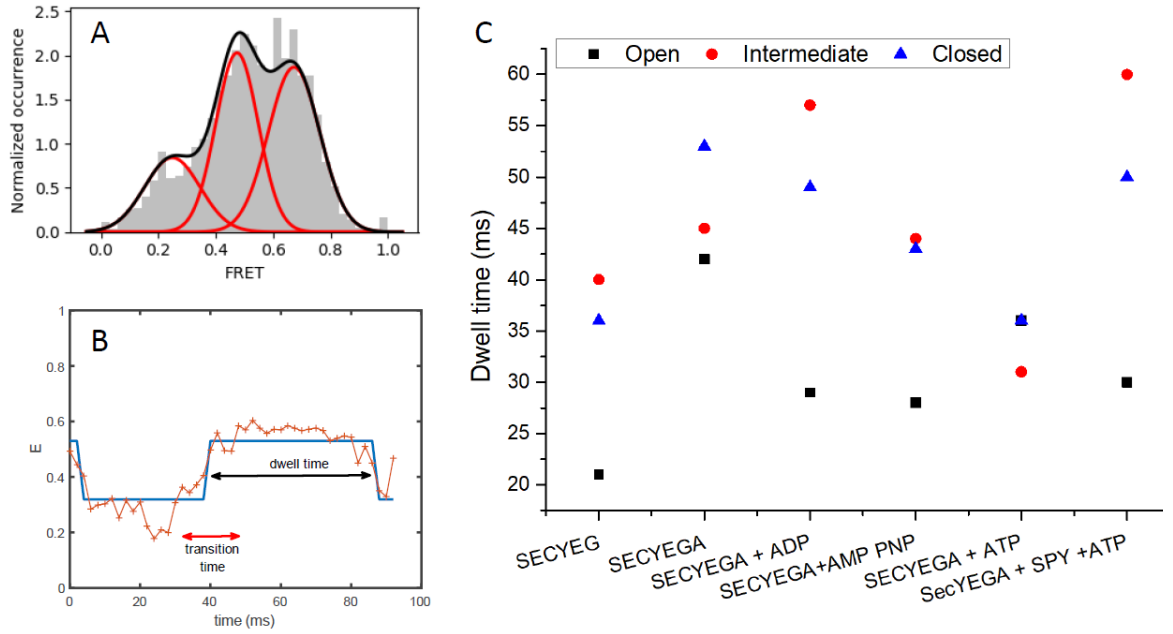


**Figure 2:** (A) Three states were identified by hidden Markov model analysis of many individual time resolved FRET trajectories that fit the combined FRET histogram well. (B) Example of a time resolved FRET trajectory with dwell time and transition time indicated. (C) Dwell times depend on SecYEG:SecA state.

In summary, we provide evidence of dynamic coupling between the ATPase subunit and integral membrane complex and reveal transitions on the millisecond and faster time scale.

**Publications**

Fessl T., Watkins D., Oatley P., Allen W.J., Corey R.A., Horne J., Baldwin S.A., Radford S.E., Collinson I., Tuma R. (2018) Dynamic action of the Sec machinery during initiation, protein translocation and termination. *Elife* **7**, e35112.

**Funding**

This work was funded by BBSRC, Leeds Beckett University, Wellcome Trust and EU ERDF

**Collaborators**

*External:* Ian Collinson, Dan Watkins (University of Bristol), Tomas Fessl (University of South Bohemia)

## Arbovirus replication and host cell interactions

Andrew Tuplin

### Introduction

Chikungunya virus (CHIKV) is a re-emerging *Alphavirus* causing fever, joint pain, skin rash, arthralgia, and occasionally death. Antiviral therapies and/or effective vaccines are urgently required. CHIKV biology is poorly understood, in particular the functions of the non-structural protein 3 (nsP3). Here we present the results of a mutagenic analysis of the alphavirus unique domain (AUD) of nsP3. Informed by the structure of the Sindbis virus AUD and an alignment of amino acid sequences of multiple alphaviruses, a series of mutations in the AUD were generated in a CHIKV sub-genomic replicon. This analysis revealed an essential role for the AUD in CHIKV RNA replication, with mutants exhibiting species- and cell-type specific phenotypes. To test if the AUD played a role in other stages of the virus lifecycle, the mutants were analysed in the context of infectious CHIKV. This analysis indicated that the AUD was also required for virus assembly. In particular, one mutant (P247A/V248A) exhibited a dramatic reduction in production of infectious virus. This phenotype was shown to be due to a block in transcription of the subgenomic RNA leading to reduced synthesis of the structural proteins and a concomitant reduction in virus production. This phenotype could be further explained by both a reduction in the binding of the P247A/V248A mutant nsP3 to viral genomic RNA *in vivo*, and the reduced affinity of the mutant AUD for the subgenomic promoter RNA *in vitro*. We propose that the AUD is a pleiotropic protein domain, with multiple functions during CHIKV RNA synthesis.

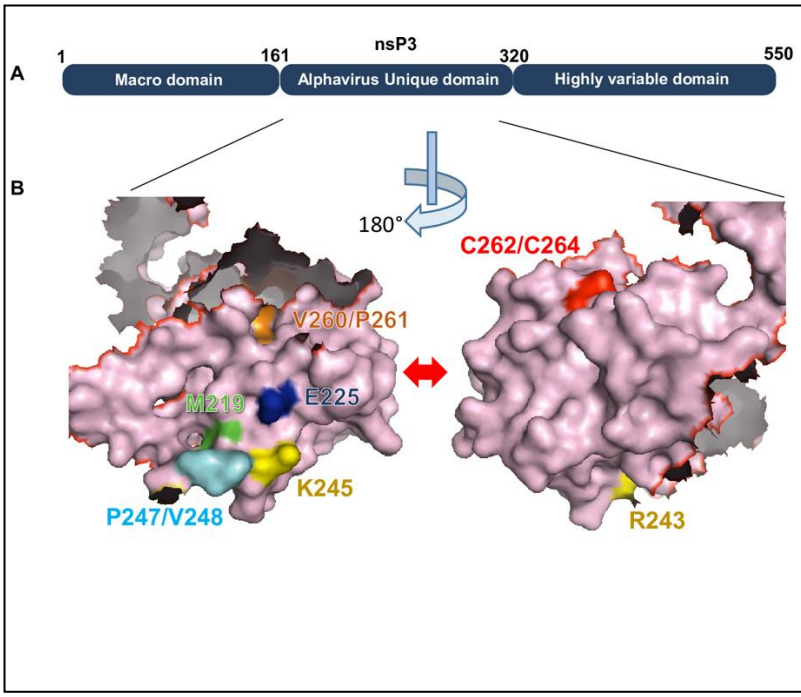


**Figure 1:** (A) Schematic representation of the domain structure of the alphavirus nsP3 protein. (B) Surface representation of the Sindbis virus nsP3 AUD structure (PDB ID code 4GUA) (residues 161–320), including the 40 amino acid flexible linker between the macrodomain and the AUD. The locations of the mutated residues in nsP3 are highlighted in colour with their designation alongside in text of the same colour. The two images show opposite faces of the structure, rotated 180$^{o}$ along the vertical axis.

### Publications

Bentley K., Cook J.P., Tuplin A.K., Evans D.J. (2018) Structural and functional analysis of the roles of the HCV 5′ NCR miR122-dependent long-range association and SLVI in genome translation and replication *PeerJ* 6 -, DOI:10.7717/peerj.5870

### Funding

MRC New Investigator Research Grant.

**Collaborators**

*University of Leeds:* Prof. M. Harris, Dr. A. Zhuravleva, Prof. Nic Stonehouse and Dr. J. Mankouri

*External:* Dr. Alain Kohl (MRC Centre for Virus Research, UK), Dr. Andrew Davidson (University of Bristol, UK) and Prof. Andres Merits (University of Tartu, Estonia).

## Inhibitors of bacterial toxin adhesion

Vajinder Kumar, Ryan McBerney, Kristian Hollingsworth, Michael Webb and Bruce Turnbull

### Introduction

Protein-carbohydrate interactions at cell surfaces mediate many important processes in biology, from fertilisation to adhesion of viruses, bacteria and their toxins. Individually, protein-sugar interactions are usually very weak, but both affinity and binding selectivity can be enhanced through a phenomenon called multivalency: multiple binding sites on the protein interact simultaneously with multiple copies of the sugar ligand to achieve a high avidity and enhance binding selectivity. The multivalency phenomenon can be reproduced using synthetic molecules that incorporate multiple copies of the carbohydrate ligands.

### Results

An important class of carbohydrate-binding proteins are the $AB_5$ protein toxins released by enterotoxigenic bacteria in the intestine, which bind specific glycolipids that mediate their endocytosis. The most common of these are the cholera toxin from *Vibrio cholerae* and the shiga-like toxin from *E. coli* O157. We are developing methods to make artificial glycoproteins that match the spacing and valency of the target pentameric protein toxins using a combination of enzymatic oligosaccharide synthesis and site-specific bioorthogonal modification of protein scaffolds. We are also investigating the use of synthetic polymer scaffolds for multivalent glycans. Such multivalent inhibitors have proven effective in cellular assays using intestinal organoids.

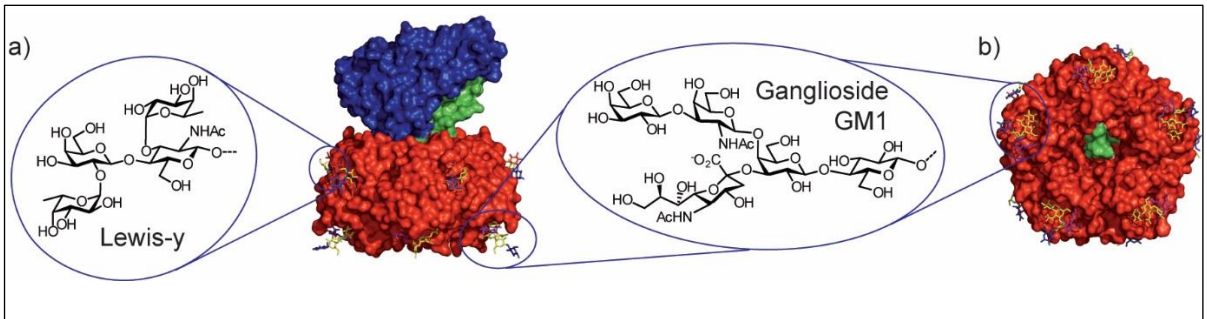


**Figure 1:** a) Cholera toxin showing the toxic A-subunit in Blue and green, and the carbohydrate-binding B-subunit in red; the location of the two carbohydrate binding sites are indicated with the structures of the preferred carbohydrate ligands; b) the five-fold symmetry of the ganglioside-binding lower face of the B-pentamer.

### Publications

Turnbull W.B., Kumar V. (2018) Carbohydrate inhibitors of cholera toxin. *Beilstein J. Org. Chem.* **14**: 484-498.

Guo Y., Turnbull W.B., Zhou D. (2018) Probing Multivalent Protein–Carbohydrate Interactions by Quantum Dot-Förster Resonance Energy Transfer. *Methods Enzymol*. **598**: 71-100.

### Funding

This work was funded by the European Union, the BBSRC and EPSRC.

### Collaborators

*External:* Clare Mahon (University of York), Roland Pieters (Utrecht University).

## Biophysical studies of multisite protein-ligand interactions

Danuta Witkowska, Zoe Arnott, Holly Morgan, Tomasz Kaminski, Heather Cox, Darren Machin, Gemma Wildsmith and Michael Webb

### Introduction

Understanding the molecular basis for protein-ligand interactions is fundamental to both understanding enzyme mechanism and the rational design of inhibitors. A wide variety of biophysical techniques are available to study these interactions including fluorescence spectroscopy, surface plasmon resonance and isothermal titration calorimetry. We were interested in understanding ligand-binding in more complex systems and investigated the bifunctional enzyme aminoimidazolecarboxamide ribonucleotide formyltransferase: inosine monophosphate cyclohydrolase (ATIC), which catalyses the last two steps of the human *de novo* purine biosynthesis pathway and is a validated target for anticancer drug development. The protein is both bifunctional and dimeric and our challenge was therefore to understand how to interpret nucleotide ligand binding data when there were four potential ligand binding sites.

### Results

Our initial interest in human ATIC was to understand several unusual aspects of the kinetic behaviour of the formyl transferase active site - despite the involvement of a histidine residue in catalysis, it is pH-independent and activity is dependent upon potassium. As part of these studies, we decided to investigate ligand binding using ITC but we rapidly realised that we could not readily distinguish binding at the formyl transferase active site and the cyclohydrolase active site, both of which bind nucleotides. For different nucleotides (AICAR, AMP, IMP and XMP) we observe different stoichiometries of binding and in the case of XMP a complex multiphase binding curve suggesting negative cooperativity in binding at either the cyclohydrolase or formyltransferase active sites.

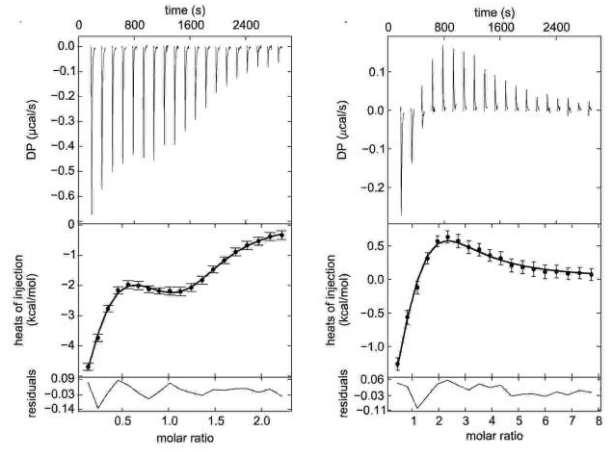


**Figure 1:** Example of complex thermogram traces obtained for multisite binding in human ATIC. Some ligands bind at both distinct binding sites in the symmetrically disposed monomers. Left: In this case (XMP), binding in the IMP cyclohydrolaase active site shows negative cooperativity but binding to the AICAR formyltransferase site is not cooperative, leading to an overall complex curve shape. Right: Saturation of the AICAR formyltransferase active site with AICAR enables clear analysis of the two phases of XMP binding in the IMP cyclohydrolase active site.

We used a combination of site-directed mutagenesis and protein truncation to distinguish between the binding sites – ultimately we were able to demonstrate that binding of ligand in one cyclohydrolase active site perturbed the site in the other half of the dimer, but that binding in the two formyltransferase sites was independent. This work demonstrates that by careful use and selection of experiments it is possible to understand complex binding patterns using calorimetry and that it is always worth following up unusual curve shapes.

### Publications

Witkowska, D., Cox, H.L., Hall, T.C, Wildsmith, G.C., Machin, D.C. & Webb, M.E. (2018) Analysis of substrate binding in individual active sites of human ATIC *Biochem. Biophys. Acta* **1866 (2)**, 254-263.

### Funding

This work was funded by the EU (MSC fellowship to DW) and BBSRC.

## Virus-host cell interactions required for oncogenic virus replication and transformation

Oliver Manners, James Murphy, Sam Dobson, Sophie Schumann, Belinda Baquero-Perez, Tim Mottram, Becky Foster, Zoe Jackson, Holli Carden, Katie Harper, Euan McDonnell and Ade Whitehouse

### Introduction

Infection is a major cause of cancer worldwide. Viruses are associated with ~15% of human cancers, which approximates to about 2 million new cases every year in the world. We have utilised a range of cutting-edge transcriptomic and quantitative proteomic approaches to globally identify how the oncogenic viruses Kaposi's sarcoma-associated herpesvirus (KSHV) and Merkel cell polyomavirus (MCPyV) affect the cellular environment to enhance their own replication and drive tumorigenesis.

### Results

KSHV, like all herpesviruses, establishes a life-long infection; however how it achieves this is yet to be fully understood. In an unbiased quantitative affinity purification coupled to mass spectrometry (q-AP-MS) approach, we identify that the Interferon-stimulated gene (ISG) OASL interacts with the KSHV ORF20 protein. We showed that the interaction with OASL is conserved among ORF20 isoforms and UL24 family members present in other herpesviruses. We further analysed the OASL interactome by q-AP-MS and found that OASL and ORF20 share numerous ribosomal interaction partners. Furthermore, both proteins co-purify with 40S and 60S ribosomal subunits. Moreover, when expressed together they associate with polysomes, but do not have a global effect on translation. Interestingly, ORF20 upregulates OASL mRNA expression downstream of RIG-I in an IRF3-dependent manner, but independently of IFNAR signalling. Lastly, OASL enhances KSHV infection in an ORF20-dependent manner, suggesting that KSHV has commandeered this ISG to benefit KSHV infection.

The MCPyV small tumour antigen (ST) is considered to be the main viral transforming factor; however potential mechanisms linking ST expression to the highly metastatic nature of Merkel cell carcinoma are yet to be fully elucidated. We have determined that MCPyV ST affects multiple stages of the metastatic cascade.

(i) We firstly demonstrated that MCPyV ST affects the actin cytoskeleton to promote the formation of filopodia, through a mechanism involving the catalytic subunit of protein phosphatase 4 (PP4C). We also showed that MCPyV ST-induced cell motility is dependent upon the activity of Rho-family GTPases Cdc42 and RhoA. In addition, our results indicated that the MCPyV ST-PP4C interaction results in the dephosphorylation of β1 integrin, likely driving the cell motility pathway.

(ii) We have also demonstrated that Cl- channel modulation can reduce MCPyV ST-induced cell motility and invasiveness. Proteomic analysis revealed that MCPyV ST upregulates two Cl- channels; CLIC1 and CLIC4, which, when silenced, inhibited MCPyV ST-induced motility and invasiveness, implicating their function as critical to MCPyV-induced metastatic processes. Consistent with these data, we confirmed that CLIC1 and CLIC4 are upregulated in primary MCPyV-positive MCC patient samples. We therefore, for the first time, implicated cellular ion channels as a key host cell factor contributing to virus-mediated cellular transformation.

(iii) Finally, we have shown that MCPyV ST expression disrupts the integrity of cell-cell junctions, thereby enhancing cell dissociation, and have implicated the cellular sheddases, ADAM 10 and 17 proteins, in this process. Inhibition of ADAM 10 and 17 activity reduced MCPyV ST-induced cell dissociation and motility, attributing their function as critical to the MCPyV-induced metastatic processes. These novel findings implicate cellular sheddases as key host cell factors contributing to virus-mediated cellular transformation and metastasis.

**Publications**

Bussey K.A., Lau U., Schumann S., Gallo A., Osbelt L., Stempel M., Arnold C., Wissing J., Gad H.H., Hartmann R., Brune W., Jänsch L., Whitehouse A. & Brinkmann M.M. (2018). The interferon-stimulated gene product oligoadenylate synthetase-like protein enhances replication of Kaposi's sarcoma-associated herpesvirus (KSHV) and interacts with the KSHV ORF20 protein. *PLoS Pathogens*, **14**(3):e1006937.

Nwogu N., Boyne J.R., Dobson S.J., Poterlowicz K., Blair G.E., Macdonald A., Mankouri J. & Whitehouse A. (2018). Cellular sheddases are induced by Merkel Cell Polyomavirus Small Tumour Antigen to mediate cell dissociation and invasiveness. *PLoS Pathogens*, **14**(9):e1007276.

Stakaityte G., Nwogu N, Dobson S.J., Knight L.M., Wasson C.W., Salguero Bodes F.J., Blackbourn D.J., Blair G.E., Mankouri J., Macdonald A. & Whitehouse A. (2018). Merkel cell polyomavirus small T antigen enhances cell motility via Rho-GTPase induced filopodia formation. *Journal of Virology*, **92**:e00940-17.

Stakaityte G., Nwogu N., Lippiat J.D., Blair G.E., Poterlowicz K., Boyne J.R., Macdonald A., Mankouri J. & Whitehouse A. (2018). The cellular chloride channels CLIC1 and CLIC4 contribute to virus-mediated cell motility. *Journal of Biological Chemistry*, **293**, 4582–4590.

Manners O., Murphy J., Coleman A., Hughes D.J. & Whitehouse A. (2018). Contribution of the KSHV and EBV Lytic Cycles to Tumourigenesis. *Current Opinions in Virology*, **32**, 60–70.

**Funding**

This work was funded by the BBSRC, MRC, Rosetrees Trust, Wellcome Trust.

**Collaborators**

*University of Leeds:* Andrew Macdonald, Jamel Mankouri, John Lippiat, Eric Blair
*External:* James Boyne (University of Bradford), David Hughes (University of St Andrews), David Blackbourn (University of Surrey), Melanie Brinkmann (University of Hannover, Germany).

## Inhibition of protein-protein interactions using designed molecules

Emma Cawood, Som Dutt, Zsofia Hegedus, Fruzsina Hobor, Kris Parashiv, Sonja Srdanovic, Martin Walko, Thomas Edwards, Adam Nelson and Andrew Wilson

### Introduction

This Report summarises our ongoing efforts to develop ligands that recognise protein surfaces to act as competitive inhibitors of protein-protein interactions (PPIs). Development of inhibitors of PPIs represents a major challenge both in terms of providing tools to understand biomacromolecule structure/function and tools to elaborate chemical probes. Peptide and peptidomimetic chemical probes, particularly incorporating non-natural and bespoke modifications to enhance biophysical and pharmacokinetic properties, are essential reagents in the armoury of tools needed to study biological molecular mechanism. For instance our group can readily prepare and provide reagents that can be used in biophysical and structural analyses of protein-protein interactions e.g. we recently supported a study of the PABP1–eIF4E4 interface, a novel PPI found in *Leishmania*. This reports highlights two bespoke methods for modifying the properties of peptide-based inhibitors of protein-protein interactions.

### Results

A significant proportion of PPIs involve the docking of a helical epitope from one protein into a cleft on its partner. An ongoing area of investigation centres on development of methods to constrain peptides in a bioactive helical conformation; this can confer enhanced proteolytic stability, enhanced cell-uptake, and, in some cases enhanced target affinity of constrained peptide sequences.

For a strategy applying covalent constraints we focused on the histone H3-ASF1 (anti-silencing function 1) PPI, which represents a potential approach for treatment of numerous cancers. As an α-helix mediated PPI, constraint of the key histone H3 helix (residues 118-135) was seen as an attractive starting point for development of inhibitors. $H3_{118\text{-}135}$ peptides bearing pentenyl glycine residues at *i* and *i* + 4 positions were constrained by olefin metathesis. Subsequent biophysical analyses revealed that promotion of a bioactive helical conformation was dependent on the position at which the constraint was introduced, but that potency of binding towards ASF1 is unaffected by the constraint and instead that enthalpy-entropy compensation occurs. Moreover, differential protection against proteases was observed for different constraining positions.

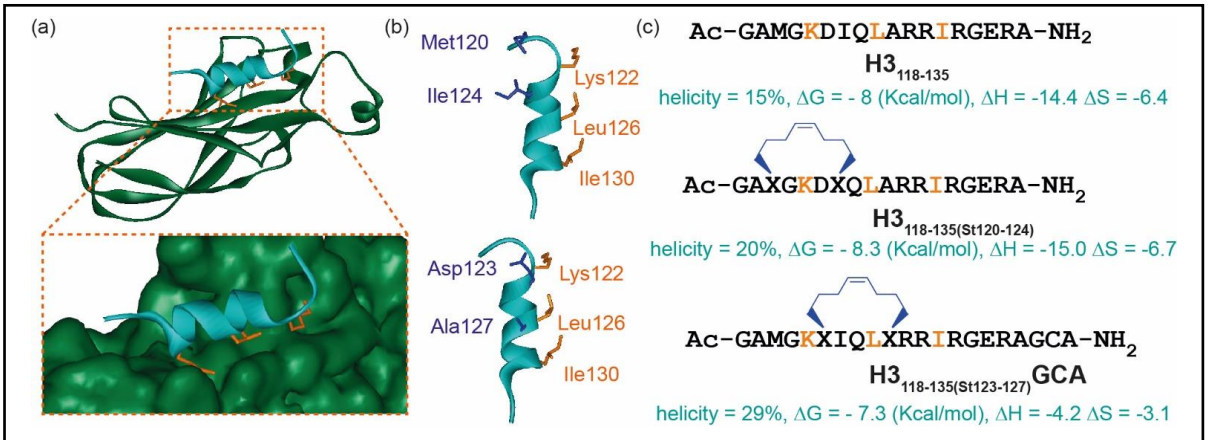


**Figure 1:** ASF1 as a target for constrained peptides (a) Structure of the Histone H3(118-135) (cyan)/ASF1A (1-156) (forest green) interaction as determined by NMR (PDB ID: 2IIJ) – Histone side chains located on one face perceived to be important for binding are shown as orange sticks (b) Key H3 helix (cyan), highlighting key side chains (orange) and residues at i, i + 4 positions considered suitable for introduction of a constraint (top: M120/I124, bottom: D123/A127), (c) Sequences of peptides used in this studied, highlighting position of hydrocarbon constraint, together with key biophysical properties.

In a second collaborative study with the University of Bristol, we explored the use of a non-covalent approach that exploits *de novo* coiled-coil assemblies and applied this to the MCL-1/NOXA-B PPI. First, computational alanine scanning was used to identify key α-helical residues from NOXA-B that contributed to recognition of MCL-1, then these residues were grafted onto the exposed surfaces of *de novo* designed homodimeric or heterodimeric coiled-coil peptides. The resulting coiled-coil assemblies were shown to inhibit the MCL-1/BID complex in the mid-nM range and were selective over helical PPIs involving BCL-$x_L$ and *h*DM2. In addition, the heterodimeric system only inhibited the interaction when both the grafted peptide and its designed partner were present. Such inhibitory dependence upon supramolecular assembly offers new possibilities for the application of supramolecular approaches to regulate PPI inhibition.

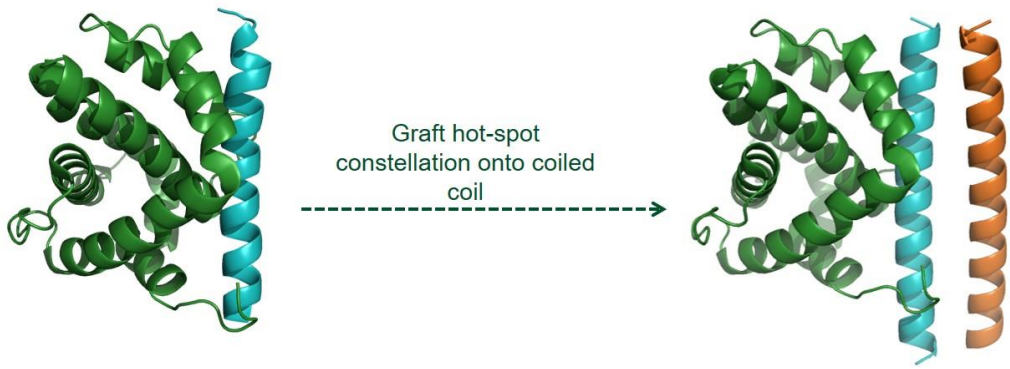


**Figure 2:** Schematic depicting the use of coiled coils as PPI inhibitors. Hot-resides from a helical epitope are grafted onto one face of a coiled-coil and this synthetic assembly is then used to inhibit the target PPI.

In summary, we have expanded understanding of helix mediated PPIs and the toolkit available for their inhibition. Future studies will focus on applying this understanding to the discovery of inhibitors of clinically relevant PPIs.

**Publications**

Bakail M., Rodriguez-Marin S., Hegedüs Z., Perrin M. E., Ochsenbein F. & Wilson A. J. (2018) Recognition of ASF1 Using Hydrocarbon Constrained Peptides, *ChemBioChem*, 10.1002/cbic.201800633.

dos Santos Rodrigues F. H., Firczuk, H, Breeze A. L., Cameron A. D., Walko M., Wilson A. J., Zanchin N. I. T. & McCarthy J. E. G. (2018) The Leishmania PABP1–eIF4E4 interface: a novel 5′–3′ interaction architecture for trans-spliced mRNAs, *Nucleic Acids Res.*, 10.1093/nar/gky1187.

Fletcher J. M., Horner K. A., Bartlett G. J. Rhys, G. R. Wilson A. J. & Woolfson D. N. (2018) De novo coiled-coil peptides as scaffolds for disrupting protein-protein interactions, *Chem. Sci.*, **9,** 7656-7665.

Hewitt S. H. & Wilson A. J. (2018) Generation of Dynamic Combinatorial Libraries Using Hydrazone Functionalized Surface Mimetics, *Eur. J. Org. Chem*., 1872-1879.

**Funding**

We acknowledge The University of Leeds, EPSRC, MRC, ERC, EU-H2020, and The Leverhulme Trust for financial support of this research.

**Collaborators**

*University of Leeds:* Alex Breeze
*External:* Dek Woolfson, Richard Sessions and Gail Bartlett (University of Bristol), Christian Ottmann (Eindhoven), John McCarthy and Alex Cameron (University of Warwick), Francoise Ochsenbein (CEA, Saclay, France)

## Chemical tools to study signal-receptor interactions at the host-microbe interface

Devon Legge, Stuart Warriner and Megan Wright

### Introduction

Host cells sense a complex array of molecules produced by microbes. Fuelled by advances in high-throughput sequencing, studies are increasingly linking specific microbes or genes to human disease. However, currently these studies are largely descriptive, leaving a significant gap in our understanding of the molecular mechanisms involved. Chemical tools have a unique ability to identify small molecule-protein interactions in native cellular environments without the need for genetic manipulation. A goal of our lab is to develop and apply chemical approaches to reveal new ligands, receptors and mechanisms operating at the host-microbe interface.

Formyl peptide receptors (FPRs), mammalian GPCRs, are candidate sensors of the microbiota due to their ability to sense bacterial ligands. But the three human FPRs sense a huge diversity of ligands, including self-derived signals, which has led to their implication in inflammatory disease and cancer. A complete lack of structural data together with the promiscuity of FPRs, compounds the challenge of understanding their biological roles. We are interested in developing new tools to study FPRs that will allow us to pinpoint ligand binding sites, identify new ligands and study receptor trafficking in real time.

### Results

To study how FPR1 interacts with its classical ligands, formylated bacterial peptides, we have developed synthetic routes to chemical probes that mimic these ligands. Probes are based on the key recognition sequence formyl-MLF and contain a photocrosslinking diazirine moiety and a terminal alkyne tag (Figure 1). Upon interaction of the probe with the receptor, UV light will be used to activate the diazirine and induce crosslink formation between the probe and the protein. Subsequent click reaction of the alkyne tag will enable labelling of the receptor-probe complex with fluorescent dyes for visualisation or affinity tags for enrichment. We have optimised the transient expression of FPR1 in Hek293 cells and crosslinking studies are ongoing. Future work will use mass spectrometry-based proteomics to analyse the binding site of formylpeptides on FPR1, and a long term goal is to apply these approaches to the less well-characterised isoforms, FPR2 and FPR3.

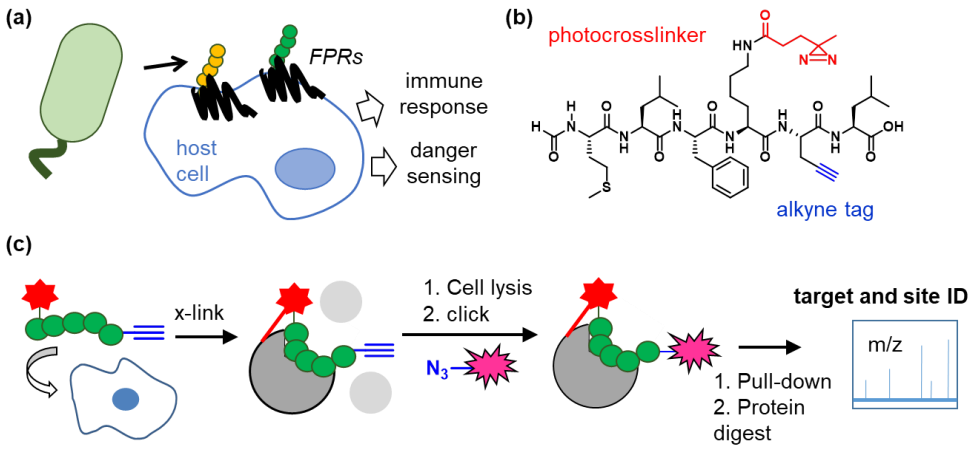


**Figure 1. a)** FPRs sense bacteria-derived ligands to regulate the host immune response. **b)** fMLF-inspired chemical probes. **c)** Photoaffinity-click workflow to identify binding partners of peptide-inspired probes.

### Publications

Wright, M.H. (2018) Chemical proteomics of host-microbe interactions. *Proteomics* **18**: 1700333.

### Funding

Thsi work was funded by the Royal Society and the University of Leeds.

## The structural mechanism of human DNA damage response and repair pathways for DNA double-strand breaks

Qian Wu

### Introduction

DNA damage is a constant threat towards the integrity of genomic information, and therefore functions, in cells. Unrepaired DNA damages can lead to cell death and genome instability, which is the hallmark of cancer. DNA double-strand breaks (DSBs) are the most toxic DNA damages and are repaired by two major repair pathways: Non-Homologous End Joining (NHEJ) and Homologous Recombination (HR). These two pathways repair DSBs with different speed, accuracy and cell cycle preference. Pathway choice between NHEJ and HR is essential for an appropriate balance between genome stability and diversity in order to achieve desired cellular functions. We studied the mechanism of NHEJ pathway and future research will focus on the choice of pathway for DNA damage response.

### Results

**NHEJ repair pathway:** The spatial architecture of protein complexes and their temporal arrangement at DNA damage sites are two essential aspects for understanding the structural mechanism of the NHEJ pathway. Previously, we have determined the structures of most key NHEJ proteins using X-ray crystallography and cryo-EM (in Tom Blundell's group). Through collaboration with Terence Strick's lab, we further expanded this research to explore the temporal property of the dynamic NHEJ protein assembly at damaged DNA ends using single-molecule methods. We have characterized the essential NHEJ components and time scale for forming stable DNA ends synapsis.

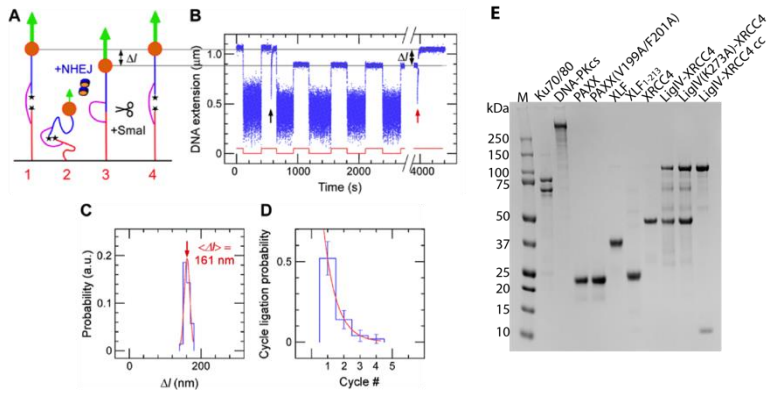


A) A 600 bp dsDNA segment (magenta) joins two 1.5 kbp dsDNA segments (blue, red), forming a construct in which two blunt ends face each other. Magnets located above the sample generate a controlled extending force on the DNA (green arrow), and the DNA end-to-end extension is determined in real time. B) Time trace obtained upon force modulation (red) in the presence of Ku, DNA-PKcs, PAXX, XLF, XRCC4 and ligase IV. Initially, DNA extension (blue points) is shown to alternate between a low and a high value upon force modulation. After addition of NHEJ components (black up arrow) and force modulation, the maximum extension displayed by the construct is reduced. After washing the sample with 0.2% SDS (break in time trace), addition of SmaI (red up arrow) results in an increase, ΔI, in DNA extension. C) Histogram of ΔI values. Red line is a fit to a Gaussian distribution, with a maximum at 161 ± 8 nm (s.d., n = 28 cleavage events). a.u., arbitrary units. D) DNA ligation probability per traction cycle. E) SDS-PAGE analysis of purified NHEJ components. 2 μg of each protein was loaded in each lane. "M" indicates protein ladder (kDa).

**DNA damage response pathway choice**: Recent cellular studies have revealed that DNA end resection is a key regulation factor for the repair pathway choice of DSBs. The Shieldin complex has very recently been identified through whole genome CRISPR-Cas9 screening in BRCA1-deficient breast cancer cells treated with PARP inhibitors (Steve Jackson's group). It binds to DSBs, preventing DNA end resection and therefore promotes DNA repair through

NHEJ. We have purified and characterized part of the Shieldin complex that binds to single-strand DNA. Future work will focus on the structure and function of this complex.

**Publications**

Nishi R., Wijnhoven PW. G., Kimura Y., Matsui M., Konietzny R., Wu Q., Nakamura K., Blundell T.L. & Kessler B.M. (2018) The deubiquitylating enzyme UCHL3 regulates Ku80 retention at sites of DNA damage. *Scientific Reports* **8**: 17891

Dev H., Chiang T.-W. W. W., Lescale C., de Krijger I., Martin A. G., Pilger D., Coates J., Sczaniecka-Clift M., Wei W., Ostermaier M., Herzog M., Lam J., Shea A., Demir M., Wu Q., Yang F., Fu B., Lai Z., Balmus G., Belotserkovskaya R., Serra V., O'Connor M. J., Bruna A., Beli P., Pellegrini L., Caldas C., Deriano L., Jacobs J. J. L., Galanty Y. & Jackson S. P. (2018) Shieldin complex promotes DNA end-joining and counters homologous recombination in BRCA1-null cells. *Nature cell biology* **20**: 954-965

Wang J. L., Duboc C., Wu Q., Ochi T., Liang S., Tsutakawa S. E., Lees-Miller S. P., Nadal M., Tainer J. A., Blundell T. L. & Strick T. R. (2018) Dissection of DNA double-strand-break repair using novel single-molecule forceps. *Nature structural & molecular biology* **25**: 482-487

**Funding**

Qian Wu was funded by Wellcome Trust (200814/Z/16/Z to Tom Blundell) for the work in these studies. Qian Wu's lab is currently funded by University Academic Fellowship, University of Leeds.

**Collaborators:**

*External:* Tom Blundell and Steve Jackson (University of Cambridge), Terence Strick (Institut Jacques Monod)

## Assembly, activation and function of BRCC36 deubiquitylating complexes

Miriam Walden, Safi Kani Masandi, Upasana Sykora and Elton Zeqiraj

### Introduction

Ubiquitylation of proteins serves as a post-translational signal to regulate virtually all cellular processes through the precise spatial and temporal control of protein stability, activity and/or localisation. Enzymes involved in the ubiquitin system are frequently dysregulated in cancer, neurodegeneration, autoimmunity and other human diseases. Ubiquitylation is a versatile post-translational modification aptly suited for a cellular communication system similar to other post-translational modifications (e.g. phosphorylation).

Ubiquitin (Ub) processing enzymes (E1, E2 and E3) write the Ub signalling code by adding Ub to substrates. A single Ub can be conjugated to lysine residues on the surface of substrate proteins (known as mono-ubiquitylation), or conjugated further to lysine residues on the surface of Ub itself, leading to poly-Ub chains with different topologies and unique signalling properties. Ub and poly-Ub chains can be “read out” by ubiquitin binding domains (UBDs), which allow signal decoding and transmission. Ubiquitylation is a reversible process and Ub is removed by deubiquitylating (DUB) enzymes. DUB actions produce monomeric Ub, recycle Ub from chains and reverse signalling events resulting from ubiquitylation.

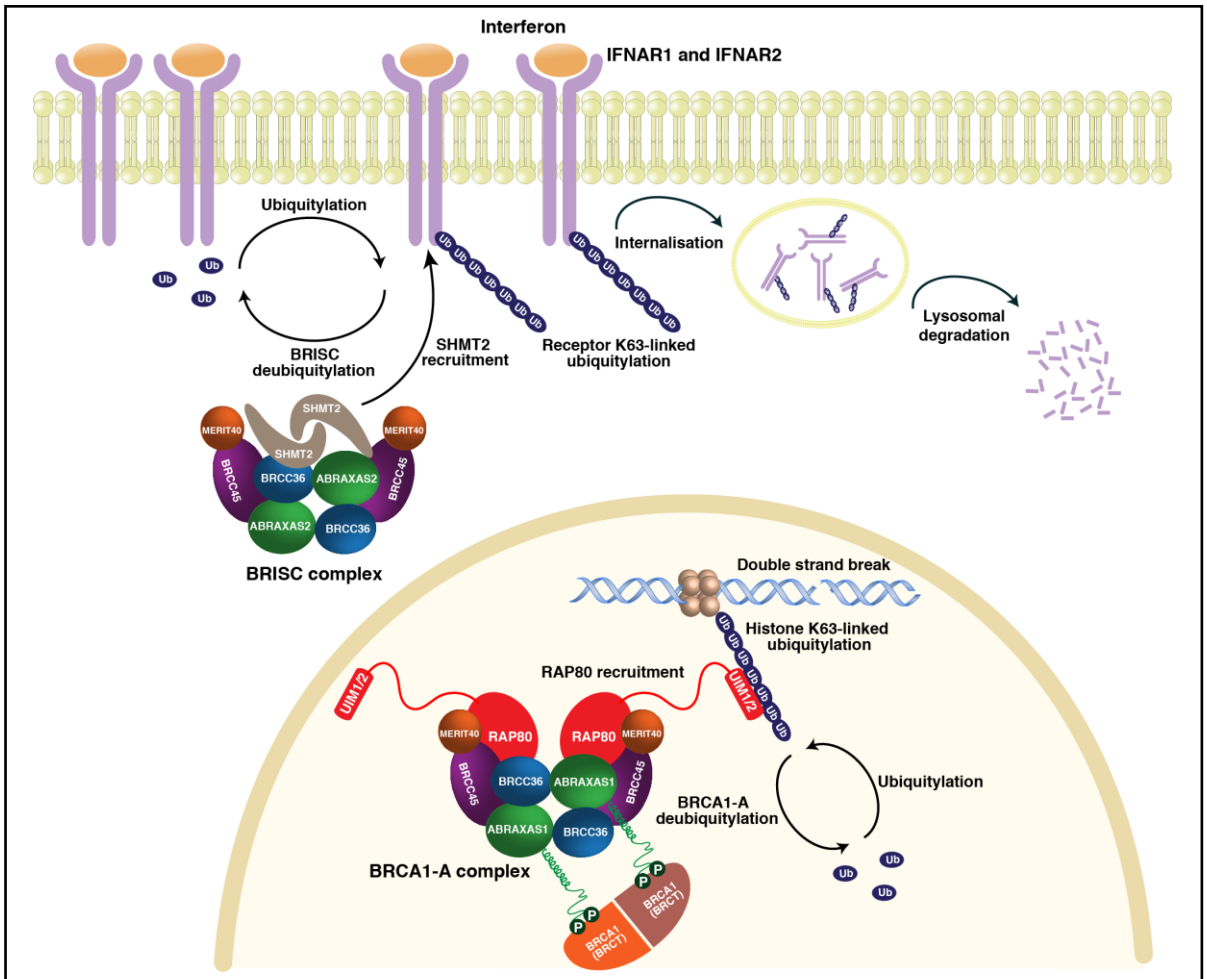


**Figure 1: BRCC36 functions in two protein complexes**
Illustration of the BRCC36 deubiquitylase (DUB) functions. Cytoplasmic BRCC36 regulates interferon receptor signalling as part of the BRISC complex. Nuclear BRCC36 takes part in DNA damage repair as the active DUB in the BRCA1-A complex. Pseudo-DUBs ABRAXAS1 and ABRAXAS2 are the main determinants for BRCC36 complex formation and subcellular localisation.

The active DUB BRCC36 is found in two macromolecular complexes (Fig. 1), depending on which inactive MPN⁻ pseudo-DUB it interacts with (ABRAXAS1 or ABRAXAS2). The BRCC36-ABRAXAS1 complex translocates to the nucleus and is part of a larger DUB complex called the BRCA1-A complex. This complex localises to sites of DNA damage (e.g. a double strand break) through RAP80 anchoring to K63-linked poly-Ub chains (Fig. 1). The BRCA1-A complex plays at least two roles in DNA damage repair: (1) binding and cleaving K63-linked poly-Ub chains and (2) recruitment of BRCA1 to sites of DNA damage.
In the cytoplasm, BRCC36 interacts with ABRAXAS2 and is part of a larger complex called BRISC-SHMT2 (Fig. 1). This cytoplasmic DUB complex interacts with and deubiquitylates interferon receptors 1 and 2 (IFANR1/2) and prevents the receptors from being prematurely endocytosed and entering the lysosomal degradation pathway. Thus, the BRISC-SHMT2 complex regulates interferon-dependent immune response by stabilising the interferon receptors and ensuring their availability at the membrane. BRISC deficiency in mice due to genetic deletion of the BRISC specific pseudo-DUB ABRAXAS2 resulted in resistance to bacterial lipopolysaccharide. Interestingly, the mice did not display any adverse phenotypes or deficiency in the DNA damage response, raising the possibility that BRISC inhibitors may have clinical utility against diseases stemming from elevated inflammatory cytokine signals.

## Results

BRCC36 resides in the BRISC-SHMT2 and BRCA1-A complexes and regulates different aspects of cell biology (Fig. 1). How do the different subunit compositions affect BRCC36 catalytic function, substrate recognition and regulation? How is each holoenzyme structurally organized? Is it possible to develop tool compounds that discriminate between complexes to selectively influence different arms of BRCC36 biology?

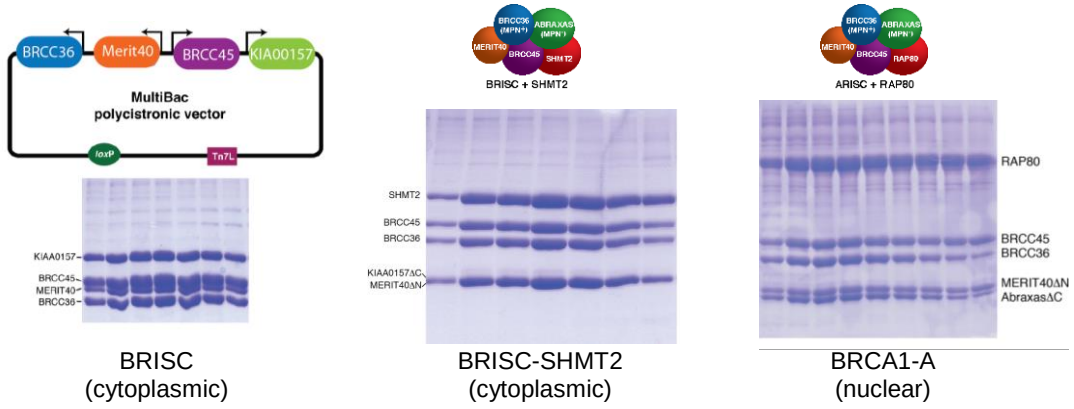


**Figure 2:** Large scale production of BRCC36-containing DUB complexes.
Schematic of a polycistronic vector for co-expression of the BRISC complex in insect cells and a Coomassie-stained gel of a co-purified BRISC complex *(left panel)*. Coomassie-stained gels of the indicated 5-subunit complexes *(middle and right panels)*.

To probe these questions at a biochemical and structural level, we have developed preparative expression systems for each multi-protein complex using the MultiBac insect cell/baculovirus system (Fig. 2). We are currently performing cryo-EM studies of these preparations to better understand complex assembly and BRCC36 mechanism of action.


## Funding

This work was funded by the Wellcome Trust and the Royal Society.


## Collaborators

*University of Leeds:* Emma Hesketh, Neil Ranson, Francesco Del Galdo, James Ault, Frank Sobott.
*External:* Roger Greenberg (Unviversity of Pennsylvania).

# Ultrasensitive detection and discrimination of DNA single-nucleotide polymorphisms using magnetic nanoparticle capture and poly-enzyme nanobead signal amplification

Lorico Lapitan, Yihan Xu, Yuan Guo and Dejian Zhou

## Introduction

Single-nucleotide polymorphisms (SNPs) are closely linked to many deadly human diseases, such as cancer, diabetes, vascular and neurodegenerative diseases. The ability to detect and quantify such SNPs is important not only to fundamental research but also clinical practices, allowing for early diagnosis of diseases, prediction of a patient's response to treatments and risk of disease relapse. However, disease related SNPs are often found at extremely low abundance in blood in an overwhelming background of wildtype genes, making them highly challenging targets to detect. Although PCR based techniques are widely used in SNP detection and can provide excellent sensitivity, they are often susceptible to contamination and amplification bias, limiting their accuracy and reliability. Significant efforts have thus been focused in developing PCR-free alternatives. Despite a number of different methods and significant progress being made over the past two decades, most methods can either offer limited sensitivity and/or SNP discrimination, making them unsuitable for early, non-invasive disease diagnosis via specific detection of disease related SNPs. To date, few methods has been able to offer simultaneous ultra-sensitivity and selectivity in SNP detection.

## Results

To address this challenge, we have previously developed a new magnetic nanoparticle (MNP)-enzyme sandwich assay which can convert each capture target-DNA into an active enzyme for signal amplification. We revealed that this strategy can specifically detect target-DNA down to the sub-pM range, although it remains uncompetitive against some of the most recent ultra-sensitive assays. Here we report a direct MNP-signal-DNA ligation to increase target-DNA to enzyme conversion efficiency. Moreover a new powerful poly-enzyme nanobead amplification strategy is introduced to convert each captured target-DNA into thousands of copies of enzymes for greatly enhanced signal amplification. We show that this strategy allows us to achieve ultra-sensitivity and excellent SNP discrimination simultaneously (Figure 1).

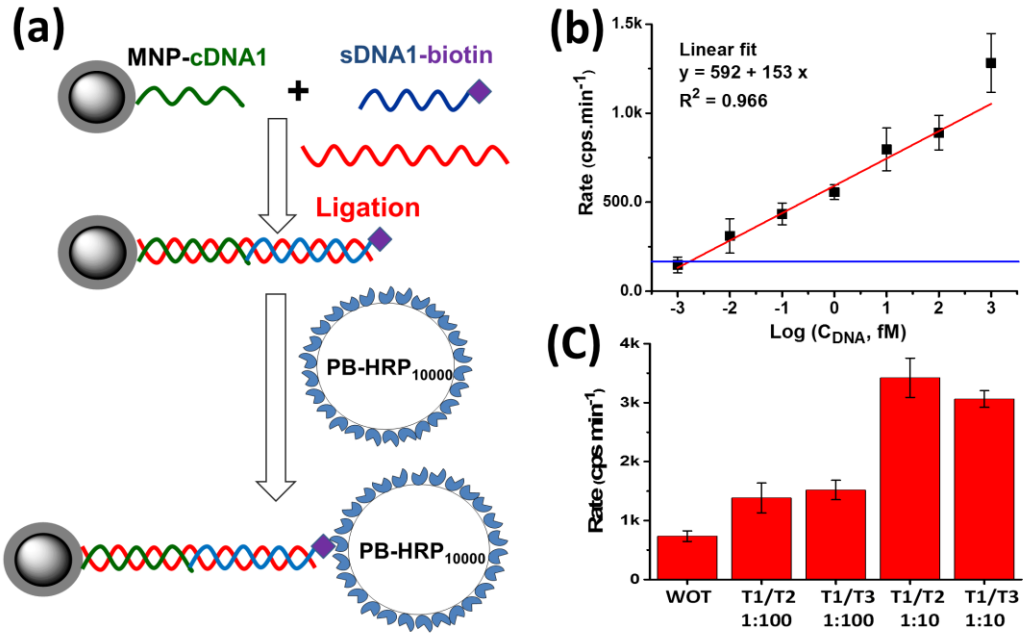


**Figure 1:** (a) Schematics of our MNP-polyenzyme nanobead DNA sensing strategy; (b) a typical calibration curve for detecting a perfect-match target-DNA (T1), blue line indicates the background + 3σ level; (c) detecting 1 fM full-match target-DNA (T1) in the presence of large excess (10 or 100 fold) of SNP targets (T2, T3), WOT: a control with 100 fM of T2 and T3 each but without T1.

Our sensing strategy is shown schematically in Figure 1a. A MNP linked capture-DNA (MNP-cDNA, 5'-phosphoriated) and a biotinylated signal-DNA (biotin-sDNA) are used to sandwich the target *via* specific sandwich hybridization. A ligation step is then applied to covalently link the sDNA-biotin to the MNP, forming a MNP-dsDNA-biotin. It is further treated with a polymer nanobead tagged with ~10,000 neutravidin-horseradish peroxidases (NAV-HRPs) to convert each MNP-linked biotin into ~10,000 HRPs. After washing to remove any unbound species, amplex red and $H_2O_2$ are introduced to initiate HRP-catalysed production of a strongly fluorescent product, resorufin, monitored on a fluorescence plate reader. The rate of fluorescence production, linear to the amount of MNP linked HRPs, is used to quantify the target-DNA concentration.

Figure 1b shows a typical calibration curve (based on the fluorescence production rate *v.s.* $\log C_{DNA}$) for detecting the perfect-match target-DNA (T1). A rather wide linear dynamic range over 6 orders of magnitude, from 1 aM to 1 pM ($R^2$ = 0.966), is obtained. Moreover, this strategy also gives an impressively low limit of detection (LOD) of 1.6 aM based on the interception point between the linear fit and the background + 3$\sigma$ level (horizontal blue line). Such levels of sensitivity are competitive with the most sensitive DNA biosensors ever reported in the literature. We attribute this ultra-sensitivity to the greatly increased signal amplification power offered by the poly-enzyme nanobead, each carrying ~$10^4$ copies of HRPs. As a result, it may be able to convert each captured full-match target-DNA into ~$10^4$ copies of HRPs (*versus* 1 in the earlier sandwich assay) for greatly enhanced sensitivity.

We further investigate the ability of our sensing strategy to detect low abundance full-match target-DNA (T1) in large excess of the SNP targets (T2, T3). The final concentrations are 1 fM for T1 and 10 fM (*i.e*.10-fold excess) or 100 fM (*i.e.* 100-fold excess) for each SNPs (T2, T3). Figure 1c reveals that the fluorescence signal is reduced with the increasing SNP:T1 ratio, presumably because the SNP targets (T2 or T3) can compete with T1 to sandwich hybridize to the capture-/signal-DNA strands, reducing the chance of a successful ligation templated by the full-match T1. Nevertheless, the signal from the sample containing just 1 fM T1 (1% that of T2/T3 SNP concentration) is clearly higher than that of control containing both SNP targets, suggesting that this strategy can specifically detect 1 fM full-match target even in the presence of 100 fold excess of SNP targets. This level of specificity for the perfect-match over its SNP targets places our approach among the very best DNA sensors reported in literature.

In summary, we have developed a new sensing strategy *via* sandwich hybridization followed by ligation to introduce covalently linked biotins to the MNP surface for subsequent enzymatic signal amplification which yields excellent SNP discrimination ratio. Moreover, a poly-enzyme nanobead amplification strategy to convert each captured target-DNA into thousands of copies of active enzymes has been developed, enabling the direct quantification of the target-DNA down to 1.6 aM with a linear dynamic range of 6 orders of magnitude, placing it among the most sensitive PCR-free DNA sensors. Furthermore, this sensor is highly specific and can positively detect 1% of the full-match target in a background of 100 fold excess SNP targets, suggesting it has great potential in broad biosensing and diagnostic applications.

**Publications**

Guo, Y., Turnbull, W.B. & Zhou, D. (2018) Probing Multivalent Protein–Carbohydrate Interactions by Quantum Dot-Förster Resonance Energy Transfer. *Methods Enzym*. **598:** 71-100.

**Funding**

This work was supported by the Wellcome Trust (097354/Z/11/Z) and the University of Leeds.

**Collaborators**

*University of Leeds:* Dr Nicole Hondow (School of Chemical and Process Engineering).

# Toward molecular mechanisms that trigger and control activation of the ER stress sensor Ire1

Samuel Dawes, Nicholas Hurst, Lukasz Wieteska and Anastasia Zhuravleva

## Introduction

The unfolded protein response (UPR) provides a mechanism to control protein folding capacity inside the endoplasmic reticulum (ER), an essential organelle in eukaryotic cells responsible for folding and maturation of the majority of secreted and membrane proteins. The trans-membrane stress sensor inositol requiring enzyme 1 alpha (Ire1) is the most conserved UPR branch. When unfolded proteins accumulate in the ER, Ire1 becomes active and triggers downstream signalling in the cytoplasm that in turn expands folding capacity of the ER. Growing evidence suggests that binding of unfolded protein substrates to the luminal domain (LD) of Ire1 triggers Ire1 oligomerization and consequent Ire1 activation, whilst interactions with the molecular chaperone BiP fine-tune the Ire1 oligomeric state and its activity. Despite significant progress in biochemical and structure characterization of the isolated Ire1-LD, the molecular mechanism(s) of Ire1-LD activation remain largely unidentified, mainly due to the multistate and dynamic nature of the activation process. We aim to obtain a detailed biophysical characterization of the Ire1-LD conformational landscape in the presence and the absence of model peptides (that mimic unfolded protein substrates) and BiP to elucidate the functional role(s) of BiP and unfoleded protein substrates on the Ire1 activation cascade.

## Results

The previously determined x-ray crystal structure of the luminal domain (LD) of human hIRE1α revealed that the N-terminal part of the protein (the core LD) comprises a unique β-sheet fold, whilist the C-terminal part of the protein (ca. 30% of hIRE1α-LD) is intrinsically disordered and not observed crystallogtaphycally. The disordered part comprises two large intinsically disordered regions (IDRs) connected by a short β-strand adjacent to the core LD. Similar to yeast Ire1-LD (yIRE1-LD) dimerization of human Ire1-LD (hIRE1α-LD) presumably creates an MHC-like groove at the interface. However, this groove is too narrow for substrate (a model peptide/unfolded protein) binding. In contrast to yIRE1-LD, peptide binding to the hIRE1α-LD groove is not required for its dimerization. However, peptide binding to dimeric hIRE1α-LD presumably induces allosteric changes in the protein that leads to its oligomerization.

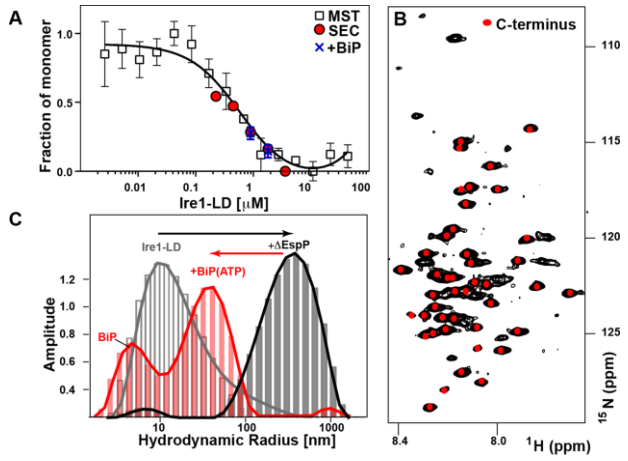


**Figure 1:** Biophysical characterization of the hIre1α-LD landscape. (A) The fraction of Ire1-LD monomer as a function of protein concentration, calculated from normalized MST (FITC-labelled Ire1-LD was titrated by unlabelled Ire1-LD) and SEC (calculated from the concentration-dependent retention volumes of IRE1-LD) data. SEC data in the presence of BiP are also shown as blue crosses. (B) Amide TROSY spectra of $^{15}$N labelled Ire1-LD recoded at 950 MHz; the peaks from the intrinsically disordered C-terminal region are highlighted in red. (C) DLS analysis of Ire1-LD size distribution in the presence and the absence model peptide EspP and ATP-bound BiP.

We employed microscale thermophoresis (MST), size exclusion chromatography (SEC), native mass spectrometry (MS) and nuclear magnetic resonance (NMR) to characterize the oligomeric state of hIRE1α-LD under different, near physiological conditions and thus elucidate how hIRE1α-LD activation is triggered and controlled (Figure 1). In a full agreement with previous results, we found that apo Ire1-LD forms dimers in a sub-μM range ($K_d$ ~0.2 μM, Figure 1A). The molecular chaperone BiP does not interfere with the dimerization process,

whilst binding to a model peptide ΔEspP results in hIRE1α-LD oligomerization (Figure 1C). To obtain molecular insights into the apo Ire1-LD dimeric conformation in solution (under near native conditions), we integrated ion mobility mass spectrometry (IM-MS) with structural modelling of hIRE1α-LD dimer. To model the hIRE1α-LD dimeric conformation, we combined the crystal structure of truncated monomeric hIRE1α-LD (PDB ID:2HZ6) with the x-ray structure of the dimeric yeast Ire1-LD; loops and intrinsically disordered regions were modelled, followed by 500ns MD simulations. The good correlation between the experimental collusion cross section measured by IM-MS (5295Å) and predicted from the model (5258Å) suggested that dimeric conformations of human and yeast Ire1-LD share the same structural features. NMR characterization of hIRE1α-LD revealed that the core hIRE1α-LD is invisible in amide and methyl NMR spectra (Figure 1B), suggesting unexpected conformational flexibility on the μs-ms time-scale. In contrast, the intrinsically disordered C-terminus is clearly observed in the NMR spectrum, suggesting that its conformational flexibility is independent (at least partially) from the core LD.

We found that hIRE1α-LD binding to a model peptide ΔEspP resulted in formation of high order oligomers, which became partially insoluble at higher protein and peptide concentrations (Figure 1C). Strikingly, the presence of the molecular chaperone BiP drastically decreased the size of hIRE1α-LD oligomers (Figure 1C, red). To deoligomerize hIRE1α-LD, BiP must be chaperone active, *i.e.* have ATPase activity and ability to interact with unfolded protein substrates. Indeed a significantly smaller (if any) effect on the hIRE1α-LD oligomeric state was observed either in the absence of ATP, for ATPase deficient BiP T229G, or for its V461F variant that lacks the ability to interact with substrates. Moreover, our NMR and SEC data revealed no evidence of the stable and/or long-lived complex formation between hIRE1α-LD and BiP under any experimental conditions up to sub-mM concentrations, suggesting that interactions between these two proteins are transient and dynamic. All together, these fundings suggest a plausible mechanism for how BiP controls hIRE1α-LD activity (Figure 2): oligomeric, substrate-bound hIRE1α-LD is a BiP substrate and its binding and release from BiP require BiP chaperone activity; in turn, these ATP-dependent transient interactions between hIRE1α-LD and BiP destabilize hIRE1α-LD oligomers and fine-tune Ire1 activity.

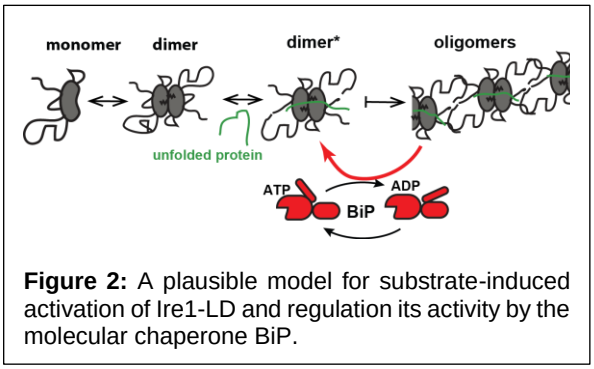


**Figure 2:** A plausible model for substrate-induced activation of Ire1-LD and regulation its activity by the molecular chaperone BiP.

**Funding:** BBSRC, EPSRC, BBSRC DTP, White Rose University Consortium.

**Collaborators:**
*University of Leeds:* Richard Bayliss, Frank Sobott
*External:* Beining Chen (University of Sheffield)

## ASTBURY SEMINARS 2018

**18th January**
*Unravelling the structure of toxic protein aggregates in situ*
Ruben Fernandez Busnadiego (Max Planck Institute of Biochemistry)

**1st February**
*RNP Complexes in RNA Metabolism: A View by Integrative Structural Biology*
Teresa Carlomagno (University of Hamburg)

**1st March**
*Changing the Compound Discovery Game with XChem Fragment Screening at Diamond*
Frank von Delft (The Structural Genomics Consortium, Oxford)

**5th April**
*Cellular ultrastructure and dynamics at the single molecule level*
Suliana Manley (University of Lausanne)

**3rd May**
*Functional Proteomics to Uncover Signaling Specificity and Cellular Responses*
Chiara Francavilla (University of Manchester)

**24th May**
*Chemical Physiology of Protein Conjugates and Natural Products*
Dr Gonçalo Bernades, University of Cambridge

**7th June**
*Probing molecular processes at the cell surface*
Yvonne Jones (University of Oxford)

**Astbury Annual Lecture 19th June**
*Protein Quality Control and Cell Stress Responses to Protect Cellular Health in Aging and Disease*
Richard Morimoto (Northwestern University, Illinois)

## PUBLICATIONS BY ASTBURY CENTRE MEMBERS 2018


Abbott W., Alber O., Bayer E., Berrin J.G., Boraston A., Brumer H., Brzezinski R., Clarke A., Cobucci-Ponzano B., Cockburn D.*, et al.* (2018) Ten years of cazypedia: A living encyclopedia of carbohydrate-active enzymes. *Glycobiology* **28**:3-8.

Abou-Saleh R.H., Hernandez-Gomez M.C., Amsbury S., Paniagua C., Bourdon M., Miyashima S., Helariutta Y., Fuller M., Budtova T., Connell S.D.*, et al.* (2018) Interactions between callose and cellulose revealed through the analysis of biopolymer mixtures. *Nat Commun* **9**:4538.

Adams P.G., Vasilev C., Hunter C.N. & Johnson M.P. (2018) Correlated fluorescence quenching and topographic mapping of light-harvesting complex ii within surface-assembled aggregates and lipid bilayers. *Biochim Biophys Acta Bioenerg* **1859**:1075-1085.

Agip A.N.A., Blaza J.N., Bridges H.R., Viscomi C., Rawson S., Muench S.P. & Hirst J. (2018) Cryo-EM structures of complex I from mouse heart mitochondria in two biochemically defined states. *Nat Struct Mol Biol* **25**:548-556.

Aimon A., Karageorgis G., Masters J., Dow M., Craven P.G.E., Ohsten M., Willaume A., Morgentin R., Ruiz-Llamas N., Lemoine H.*, et al.* (2018) Realisation of small molecule libraries based on frameworks distantly related to natural products. *Org Biolmol Chem* **16**:3160-3167.

Almeida-Souza L., Frank R.A.W, Garcia-Nafria J., Colussi A., Gunawardana N., Johnson C.M., Yu M., Howard G., Andrews B., Vallis Y., McMahon H.T. (2018) A flat BAR protein promotes actin polymerisation at the base of clathrin-coated pits. *Cell* **73**: 74, 325.

Amporndanai K., Johnson R.M., O'Neill P.M., Fishwick C.W.G., Jamson A.H., Rawson S., Muench S.P., Hasnain S.S. & Antonyuk S.V. (2018) X-ray and cryo-EM structures of inhibitor-bound cytochrome $bc_1$ complexes for structure-based drug discovery. *IUCrJ* **5**:200-210.

Ananth A., Genua M., Aissaoui N., Diaz L., Eisele N.B., Frey S., Dekker C., Richter R.P. & Gorlich D. (2018) Reversible immobilization of proteins in sensors and solid-state nanopores. *Small* **14**:e1703357

Aufderhorst-Roberts A., Baker D., Foster R.J., Cayre O., Mattsson J. & Connell S.D. (2018) Nanoscale mechanics of microgel particles. *Nanoscale* **10**:16050-16061.

Azam A.A., Kinder J.M., Khan G.N., Alase A., Ma P., Liu Y., Ault J.R., Henderson P.J.F., Chowdhry B.Z., Alexander B.D.*, et al.* (2018) Production of membrane proteins for characterisation of their pheromone-sensing and antimicrobial resistance functions. *Eur Biophys J* **47**:723-737.

Azinas S., Bano F., Torca I., Bamford D.H., Schwartz G.A., Esnaola J., Oksanen H.M., Richter R.P. & Abrescia N.G. (2018) Membrane-containing virus particles exhibit the mechanics of a composite material for genome protection. *Nanoscale* **10**:7769-7779.

Baggen J., Hurdiss D.L., Zocher G., Mistry N., Robert R.W., Slager J.J., Guo H.B., Van Vliet A.L.W., Wahedi M., Benschop K.*, et al.* (2018) Role of enhanced receptor engagement in the evolution of a pandemic acute hemorrhagic conjunctivitis virus. *Proc Natl Acad Sci USA* **115**:397-402.

Bakail M., Rodriguez-Marin S., Hegedüs Z., Perrin M. E., Ochsenbein F. & Wilson A. J. (2018) Recognition of ASF1 Using Hydrocarbon Constrained Peptides, *ChemBioChem*, 10.1002/cbic.201800633.

Bano F., Tammi M.I., Kang D.W., Harris E.N. & Richter R.P. (2018) Single-molecule unbinding forces between the polysaccharide hyaluronan and its binding proteins. *Biophys J* **114**:2910-2922.

Barroso A., Gimenez E., Konijnenberg A., Sancho J., Sanz-Nebot V. & Sobott F. (2018) Evaluation of ion mobility for the separation of glycoconjugate isomers due to different types of sialic acid linkage, at the intact glycoprotein, glycopeptide and glycan level. *J Proteomics* **173**:22-31.

Bartlett C., Curd A., Peckham M. & Harris M. (2018) Visualisation and analysis of hepatitis C virus non-structural proteins using super-resolution microscopy. *Scientific Reports* **8**:13604.

Batchelor M., Wolny M., Kurzawa M., Dougan L., Knight P. J. and Peckham M. (2018) Determining Stable Single Alpha Helical (SAH) Domain Properties by Circular Dichroism and Atomic Force Microscopy. *Methods Mol Biol* **1805**: 185-211

Batchelor M. & Paci E. (2018) Helical polyampholyte sequences have unique thermodynamic properties. *J Phys Chem B* **122**:11784-11791.

Bawazer L.A., Ihli J., Levenstein M.A., Jeuken L.J.C., Meldrum F.C. & Mcmillan D.G.G. (2018) Enzymatically-controlled biomimetic synthesis of titania/protein hybrid thin films. *J Mater Chem B* **6**:3979-3988.

Bayliss R. (2018) How protein phosphorylation shapes the mitotic spindle. *FEBS Open Bio* **8**:44-45.

Beales P.A., Ciani B. & Mann S. (2018) The artificial cell: Biology-inspired compartmentalization of chemical function. *Interface Focus* **8**:20180046

Bentley K., Cook J.P., Tuplin A.K. & Evans D.J. (2018) Structural and functional analysis of the roles of the HCV 5 ' NCR miR122-dependent long-range association and SLVI in genome translation and replication. *PeerJ* **6**:e5870.

Berdiell I.C., Warriner S.L. & Halcrow M.A. (2018) Silver(i) complexes of bis- and tris-(pyrazolyl)azine derivatives - dimers, coordination polymers and a pentametallic assembly. *Dalton Trans* **47**:5269-5278.

Bravo J.P.K., Borodavka A., Barth A., Calabrese A.N., Mojzes P., Cockburn J.J.B., Lamb D.C. & Tuma R. (2018) Stability of local secondary structure determines selectivity of viral RNA chaperones. *Nucleic Acids Res* **46**:7924-7937.

Bruce H.A., Du D.J., Matak-Vinkovic D., Bandyra K.J., Broadhurst R.W., Martin E., Sobott F., Shkumatov A.V. & Luisi B.F. (2018) Analysis of the natively unstructured RNA/protein-recognition core in the *Escherichia coli* RNA degradosome and its interactions with regulatory RNA/Hfq complexes. *Nucleic Acids Res* **46**:387-402.

Bunney T.D., Inglis A.J., Sanfelice D., Farrell B., Kerr C.J., Thompson G.S., Masson G.R., Thiyagarajan N., Svergun D.I., Williams R.L., *et al.* (2018) Disease variants of FGFR3 reveal molecular basis for the recognition and additional roles for Cdc37 in Hsp90 chaperone system. *Structure* **26**:446-458.

Burgess S.G., Mukherjee M., Sabir S., Joseph N., Gutierrez-Caballero C., Richards M.W.,

Huguenin-Dezot N., Chin J.W., Kennedy E.J., Pfuhl M.*, et al.* (2018) Mitotic spindle association of TACC3 requires Aurora-A-dependent stabilization of a cryptic α-helix. *EMBO J* **37**: e97902.

Bussey K.A., Lau U., Schumann S., Gallo A., Osbelt L., Stempel M., Arnold C., Wissing J., Gad H.H., Hartmann R.*, et al.* (2018) The interferon-stimulated gene product oligoadenylate synthetase-like protein enhances replication of Kaposi's sarcoma-associated herpesvirus KSHV) and interacts with the KSHV ORF20 protein. *PLoS Pathog* **14**:e1006937.

Cain R., Brem J., Zollman D., Mcdonough M.A., Johnson R.M., Spencer J., Makena A., Abboud M.I., Cahill S., Lee S.Y.*, et al.* (2018) *In silico* fragment-based design identifies subfamily b1 metallo-beta-lactamase inhibitors. *J Med Chem* **61**:1255-1260.

Calabrese A.N. & Radford S.E. (2018) Mass spectrometry-enabled structural biology of membrane proteins. *Methods* **147**:187-205.

Campuzano I.D.G., Sobott F. & Van Stipdonk M.J. (2018) Editorial and review: 30th ASMS Sanibel conference on mass spectrometry-computational modelling in mass spectrometry and ion mobility: Methods for ion structure and reactivity determination. *J Am Soc Mass Spectrom* **29**:2283-2286.

Charlton M.H., Aleksis R., Saint-Leger A., Gupta A., Loza E., De Pouplana L.R., Kaula I., Gustina D., Madre M., Lola D.*, et al.* (2018) N-leucinyl benzenesulfonamides as structurally simplified leucyl-tRNA synthetase inhibitors. *ACS Med Chem Lett* **9**:84-88.

Chavent M., Karia D., Kalli A.C., Domanski J., Duncan A.L., Hedger G., Stansfeld P.J., Seiradake E., Jones E.Y. & Sansom M.S.P. (2018) Interactions of the EphA2 kinase domain with pips in membranes: Implications for receptor function. *Structure* **26**:1025-1034.

Chen Z., Ye S.J., Evans S.D., Ge Y.H., Zhu Z.F., Tu Y.F. & Yang X.M. (2018) Confined assembly of hollow carbon spheres in carbonaceous nanotube: A spheres-in-tube carbon nanostructure with hierarchical porosity for high-performance supercapacitor. *Small* **14**:1704015.

Chow S., Liver S. & Nelson A. (2018) Streamlining bioactive molecular discovery through integration and automation. *Nat Rev Chem* **2**:174-183.

Cockburn J.J.B., Hesketh S.J., Mulhair P., Thomsen M., O'Connel M.J. & Way M. (2018) Insights into kinesin-1 activation from the crystal structure of KLC2 bound to JIP3. *Structure* **26**:1486-1498.

Cornwell O., Radford S.E., Ashcroft A.E. & Ault J.R. (2018) Comparing hydrogen deuterium exchange and fast photochemical oxidation of proteins: A structural characterisation of wild-type and delta n6 beta(2)-microglobulin. *J Am Soc Mass Spectrom* **29**:2413-2426.

Cottom J.W., Abellan P., Ramasse Q.M., Critchley K. & Brydson R. (2018) Systematic analysis of the coupling effects within supported plasmonic nanorod antenna arrays. *J Phys Chem C* **122**:22041-22053.

Davies H.S., Debarre D., El Amri N., Verdier C., Richter R.P. & Bureau L. (2018) Elastohydrodynamic lift at a soft wall. *Phys Rev Lett* **120**:198001.

Davies R.P.W., Liu B.B., Maude S., Carrick L.M., Nyrkova I., Mcleish T.C. & Harris S.A. (2018) Peptide strand length controls the energetics of self-assembly and morphology of β-sheet fibrils. *Pept Sci (Hoboken)* **110**:e23073.

De Backer J., Razzokov J., Hammerschmid D., Mensch C., Hafideddine Z., Kumar N., Van

Raemdonck G., Yusupov M., Van Doorslaer S., Johannessen C.*, et al.* (2018) The effect of reactive oxygen and nitrogen species on the structure of cytoglobin: A potential tumor suppressor. *Redox Biol* **19**:1-10.

De Pablo J.G., Armistead F.J., Peyman S.A., Bonthron D., Lones M., Smith S. & Evans S.D. (2018) Biochemical fingerprint of colorectal cancer cell lines using label-free live single-cell raman spectroscopy. *J Raman Spectrosc* **49**:1323-1332.

De Pablo J.G., Chisholm D.R., Steffen A., Nelson A.K., Mahler C., Marder T.B., Peyman S.A., Girkin J.M., Ambler C.A., Whiting A.*, et al.* (2018) Tandem fluorescence and raman (fluoraman) characterisation of a novel photosensitiser in colorectal cancer cell line SW480. *Analyst* **143**:6113-6120.

Defraine V., Liebens V., Loos E., Swings T., Weytjens B., Fierro C., Marchal K., Sharkey L., O'Neill A.J., Corbau R.*, et al.* (2018) 1-((2,4-dichlorophenethyl)amino)3-phenoxypropan-2-ol kills *Pseudomonas aeruginosa* through extensive membrane damage. *Front Microbiol* **9**:129.

Dev H., Chiang T.-W. W. W., Lescale C., de Krijger I., Martin A. G., Pilger D., Coates J., Sczaniecka-Clift M., Wei W., Ostermaier M., Herzog M., Lam J., Shea A., Demir M., Wu Q., Yang F., Fu B., Lai Z., Balmus G., Belotserkovskaya R., Serra V., O'Connor M. J., Bruna A., Beli P., Pellegrini L., Caldas C., Deriano L., Jacobs J. J. L., Galanty Y. & Jackson S. P. (2018) Shieldin complex promotes DNA end-joining and counters homologous recombination in BRCA1-null cells. *Nature cell biology* **20**: 954-965

Dilworth M.V., Piel M.S., Bettaney K.E., Ma P., Luo J., Sharples D., Poyner D.R., Gross S.R., Moncoq K., Henderson P.J.F.*, et al.* (2018) Microbial expression systems for membrane proteins. *Methods* **147**:3-39.

Doherty C., Young L., Karamanos T., Smith H., Jackson M., Radford S. & Brockwell D. (2018) A peptide-display protein scaffold to facilitate single molecule force studies of aggregation-prone peptides. *Prot. Sci.* ***27:***1205-1217.

Drulyte I., Johnson R.M., Hesketh E.L., Hurdiss D.L., Scarff C.A., Porav S.A., Ranson N.A., Muench S.P. & Thompson R.F. (2018) Approaches to altering particle distributions in cryo-electron microscopy sample preparation. *Acta Crystallogr D Struct Biol* **74**:560-571.

Easton V., Mcphillie M., Garcia-Dorival I., Barr J.N., Edwards T.A., Foster R., Fishwick C. & Harris M. (2018) Identification of a small molecule inhibitor of Ebola virus genome replication and transcription using in silico screening. *Antiviral Res* **156**:46-54.

Ebeed H.T., Stevenson S.R., Cuming A.C. & Baker A. (2018) Conserved and differential transcriptional responses of peroxisome associated pathways to drought, dehydration and aba. *Journal of Experimental Botany* **69**:4971-4985.

Elbaramawi S.S., Hughes C., Richards J., Gupta A., Ibrahim S.M., Lashine E.M., El-Sadek M.E., O'Neill A.J., Wootton M., Bullard J.M.*, et al.* (2018) Design, synthesis and microbiological evaluation of novel compounds as potential *Staphylococcus aureus* phenylalanine tRNA synthetase inhibitors. *Egypt J Chem* **61**:9-25.

Evans E.L., Cuthbertson K., Endesh N., Rode B., Blythe N.M., Hyman A.J., Hall S.J., Gaunt H.J., Ludlow M.J., Foster R.*, et al.* (2018) Yoda1 analogue (dooku1) which antagonizes yoda1-evoked activation of piezo1 and aortic relaxation. *British Journal of Pharmacology* **175**:1744-1759.

Farrell B. & Breeze A.L. (2018) Structure, activation and dysregulation of fibroblast growth factor receptor kinases: Perspectives for clinical targeting. *Biochemical Society Transactions* **46**:1753-1770.

Fearon D., Westwood I.M., Van Montfort R.L.M., Bayliss R., Jones K. & Bavetsias V. (2018) Synthesis and profiling of a 3-aminopyridin-2-one-based kinase targeted fragment library: Identification of 3-amino-5-(pyridin-4-yl)pyridin-2(1h)-one scaffold for monopolar spindle 1 (mps1) and aurora kinases inhibition. *Bioorganic & Medicinal Chemistry* **26**:3021-3029.

Fessl T., Watkins D., Oatley P., Allen W.J., Corey R.A., Horne J., Baldwin S.A., Radford S.E., Collinson I. & Tuma R. (2018) Dynamic action of the sec machinery during initiation, protein translocation and termination. *Elife* **7**:e35112.

Fletcher J.M., Horner K.A., Bartlett G.J., Rhys G.G., Wilson A.J. & Woolfson D.N. (2018) *De novo* coiled-coil peptides as scaffolds for disrupting protein-protein interactions. *Chem Sci* **9**:7656-7665.

Foster R.J., Damion R.A., Ries M.E., Smye S.W., Mcgonagle D.G., Binks D.A. & Radjenovic A. (2018) Imaging of nuclear magnetic resonance spin-lattice relaxation activation energy in cartilage. *Royal Society Open Science* **5**.

Foth M., Ismail N.F.B., Kung J.S.C., Tomlinson D., Knowles M.A., Eriksson P., Sjodahl G., Salmond J.M., Sansom O.J. & Iwata T. (2018) FGFR3 mutation increases bladder tumourigenesis by suppressing acute inflammation. *J Pathol* **246**:331-343.

Fowler C.A., Hemsworth G.R., Cuskin F., Hart S., Turkenburg J., Gilbert H.J., Walton P.H. & Davies G.J. (2018) Structure and function of a glycoside hydrolase family 8 endoxylanase from *Teredinibacter turnerae*. *Acta Crystallogr D Struct Biol* **74**:946-955.

Foyer C.H., Wilson M.H. & Wright M.H. (2018) Redox regulation of cell proliferation: Bioinformatics and redox proteomics approaches to identify redox-sensitive cell cycle regulators. *Free Radic Biol and Med* **122**:137-149.

Gatta A.T., Sauerwein A.C., Zhuravleva A., Levine T.P. & Matthews S. (2018) Structural insights into a StART-like domain in Lam4 and its interaction with sterol ligands. *Biochem Biophys Res Communications* **495**:2270-2274.

Gaule T.G., Smith M.A., Tych K.M., Pirrat P., Trinh C.H., Pearson A.R., Knowles P.F. & Mcpherson M.J. (2018) Oxygen activation switch in the copper amine oxidase of *Escherichia coli. Biochemistry* **57**:5301-5314.

Gomez Santiago, C., E. Paci and D. Donnelly (2018) A mechanism for agonist activation of the glucagon-like peptide-1 (GLP-1) receptor through modelling & molecular dynamics. *Biochem Biophys Res Commun* **498**: 359-365.

Guo Y., Turnbull W.B. & Zhou D.J. (2018) Probing multivalent protein-carbohydrate interactions by quantum dot-Forster resonance energy transfer. In *Chemical glycobiology, pt B: Monitoring glycans and their interactions*. Edited by Imperiali B. *Methods Enzymol* **598**:71-100.

Harborne S.P.D., Strauss J., Turku A., Watson M.A., Tuma R., Harris S.A. & Goldman A. (2018) Defining dynamics of membrane-bound pyrophosphatases by experimental and computational single-molecule FRET. In *Phosphatases*. Edited by Allen KN. *Methods Enzymol* **607**:93-130.

Harris M. & Duprex W.P. (2018) Whether you are a virus or a learned society-based virology journal, evolution is critical for success! *J Gen Virol* **99**:1-2.

Harrison, M.A. & Muench, S.P. (2018) The Vacuolar ATPase – A Nano-scale motor that drives cell biology. *Subcell Biochem*. **87**: 409-459.

Harvie A.J., Smith C.T., Ahumada-Lazo R., Jeuken L.J.C., Califano M., Bon R.S., Hardman S.J.O., Binks D.J. & Critchley K. (2018) Ultrafast trap state-mediated electron transfer for quantum dot redox sensing. *J Physl Chem C* **122**:10173-10180.

Hassan H., Marsden S.P. & Nelson A. (2018) Design and synthesis of a fragment set based on twisted bicyclic lactams. *Bioorg Med Chem* **26**:3030-3033.

Heath G.R., Harrison P.L., Strong P.N., Evans S.D. & Miller K. (2018) Visualization of diffusion limited antimicrobial peptide attack on supported lipid membranes. *Soft Matter* **14**:6146-6154.

Hemsworth G.R., Ciano L., Davies G.J. & Walton P.H. (2018) Production and spectroscopic characterization of lytic polysaccharide monooxygenases. In *Enzymes of energy technology*. Edited by Armstrong F. *Methods Enzymol* **613**:63-90.

Hesketh E.L., Saunders K., Fisher C., Potze J., Stanley J., Lomonossoff G.P. & Ranson N.A. (2018) The 3.3 Å structure of a plant geminivirus using cryo-EM. *Nat Commun* **9**:2369.

Hethershaw E.L., Adamson P.J., Smith K.A., Goldsberry W.N., Pease R.J., Radford S.E., Grant P.J., Ariens R.a.S., Maurer M.C. & Philippou H. (2018) The role of β-barrels 1 and 2 in the enzymatic activity of factor XIII A-subunit. *J Thromb Haemost* **16**:1391-1401.

Hewitt S. H. & Wilson A. J. (2018) Generation of Dynamic Combinatorial Libraries Using Hydrazone Functionalized Surface Mimetics, *Eur. J. Org. Chem*., 1872-1879.

Holmes N.A., Devine R., Qin Z.W., Seipke R.F., Wilkinson B. & Hutchings M.I. (2018) Complete genome sequence of *Streptomyces formicae* KY5, the formicamycin producer. *J Biotechnol* **265**:116-118.

Honda A., Kita T., Seshadri S.V., Misaki K., Ahmed Z., Ladbury J.E., Richardson G.P., Yonemura S. & Ladher R.K. (2018) FGFR1-mediated protocadherin-15 loading mediates cargo specificity during intraflagellar transport in inner ear hair-cell kinocilia. *Proc Natl Acad Sci USA* **115**:8388-8393.

Horne J.E., Walko M., Calabrese A.N., Levenstein M.A., Brockwell D.J., Kapur N., Wilson A.J. & Radford S.E. (2018) Rapid mapping of protein interactions using tag-transfer photocrosslinkers. *Angew Chem Int Ed Engl* **57**:16688-16692.

Hover S., Foster B., Fontana J., Kohl A., Goldstein S.A.N., Barr J.N. & Mankouri J. (2018) Bunyavirus requirement for endosomal $K^+$ reveals new roles of cellular ion channels during infection. *PLoS Pathog* **14**:e1006845.

Hunter R.W., Hughey C.C., Lantier L., Sundelin E.I., Peggie M., Zeqiraj E., Sicheri F., Jessen N., Wasserman D.H. & Sakamoto K. (2018) Metformin reduces liver glucose production by inhibition of fructose-1-6-bisphosphatase. *Nat Med* **24**:1395-1406.

Hurdiss D.L., Frank M., Snowden J.S., Macdonald A. & Ranson N.A. (2018) The structure of an infectious human polyomavirus and its interactions with cellular receptors. *Structure* **26**:839-847.

Iadanza M.G., Jackson M.P., Hewitt E.W., Ranson N.A. & Radford S.E. (2018) A new era for understanding amyloid structures and disease. *Nat Rev Mol Cell Biol* **19**:755-773.

Iadanza M.G., Silvers R., Boardman J., Smith H.I., Karamanos T.K., Debelouchina G.T., Su Y.C., Griffin R.G., Ranson N.A. & Radford S.E. (2018) The structure of a $\beta_2$-microglobulin fibril suggests a molecular basis for its amyloid polymorphism. *Nat Commun* **9**:4517.

Jardim A.C.G., Shimizu J.F., Rahal P. & Harris M. (2018) Plant-derived antivirals against hepatitis C virus infection. *Virol J* **15**:34.

Johnson R.M., Rawson S., Mcphillie M.J., Fishwick C.W.G. & Muench S.P. (2018) The growing role of electron microscopy in anti-parasitic drug discovery. *Curr Med Chem* **25**:5279-5290.

Jones L.M., Eves-Van Den Akker S., Hawle P.V., Atkinson H.J. & Urwin P.E. (2018) Duplication of hsp-110 is implicated in differential success of Globodera species under climate change. *Mol Biol Evol* **35**:2401-2413.

Joynt R. & Seipke R.F. (2018) A phylogenetic and evolutionary analysis of antimycin biosynthesis. *Microbiology* **164**:28-39.

Kalli A.C. & Reithmeier R.A.F. (2018) Interaction of the human erythrocyte band 3 anion exchanger 1 (AE1, SLC4A1) with lipids and glycophorin a: Molecular organization of the wright (Wr) blood group antigen. *PLoS Comput Biol* **14**:e1006284.

Karakus Y.Y., Goc G., Balci S., Yorke B.A., Trinh C.H., Mcpherson M.J. & Pearson A.R. (2018) Identification of the site of oxidase substrate binding in *Scytalidium thermophilum* catalase. *Acta Crystallogr D Struct Biol* **74**:979-985.

Kinoshita M., Lin Y.X., Dai I., Okumura M., Markova N., Ladbury J.E., Sterpone F. & Lee Y.H. (2018) Energy landscape of polymorphic amyloid generation of $\beta_2$-microglobulin revealed by calorimetry. *Chem Commun* **54**:7995-7998.

Knight P.D., Karamanos T.K., Radford S.E. & Ashcroft A.E. (2018) Identification of a novel site of interaction between ataxin-3 and the amyloid aggregation inhibitor polyglutamine binding peptide 1. *Eur J Mass Spectrom* **24**:129-140.

Krivov S.V. (2018) Protein folding free energy landscape along the committor - the optimal folding coordinate. *J Chem Theory Comput* **14**:3418-3427.

Kumar A., Gopalswamy M., Wolf A., Brockwell D., Hatzfeld M. & Balbach J. (2018) Phosphorylation-induced unfolding regulates p19INK4d during the human cell cycle. *Proc Natl Acad Sci USA*. **115**:3344-3349

Kumar V. & Turnbull W.B. (2018) Carbohydrate inhibitors of cholera toxin. *Beilstein J Org Chem* **14**:484-498.

Lenton S., Rhys N.H., Towey J.J., Soper A.K. & Dougan L. (2018) Temperature-dependent segregation in alcohol-water binary mixtures is driven by water clustering. *J Phys Chem B* **122**:7884-7894.

Lepannetier S., Gualdani R., Tempesta S., Schakman O., Seghers F., Kreis A., Yerna X., Slimi A., De Clippele M., Tajeddine N.*, et al.* (2018) Activation of trpc1 channel by metabotropic glutamate receptor mglur5 modulates synaptic plasticity and spatial working memory. *Frontiers in Cellular Neuroscience* **12**.

Lermyte F., Valkenborg D., Loo J.A. & Sobott F. (2018) Radical solutions: Principles and application of electron-based dissociation in mass spectrometry-based analysis of protein structure. *Mass Spectrom Rev* **37**:750-771.

Linkuviene V., Zubriene A., Manakova E., Petrauskas V., Baranauskiene L., Zaksauskas A., Smirnov A., Grazulis S., Ladbury J.E. & Matulis D. (2018) Thermodynamic, kinetic, and structural parameterization of human carbonic anhydrase interactions toward enhanced inhibitor design. *Q Rev Biophys* **51**:e10.

Liu Y.X., Kaljunen H., Pavic A., Saarenpaa T., Himanen J.P., Nikolov D.B. & Goldman A. (2018) Binding of EphrinA5 to RET receptor tyrosine kinase: An *in vitro* study. *Plos One* **13**:e0198291.

Liver, S., Masters, J., Nelson, A., (2018) "Function-driven Discovery of Bioactive Small Molecules", DOI: 10.1039/9781788012805-00138, in Chemical and Biological Synthesis, ed. Westwood N. J., Nelson, A., Royal Society of Chemistry, pp 138-152.

Llewellyn M.A., Gordon N.S., Abbotts B., James N.D., Zeegers M.P., Cheng K.K., Macdonald A., Roberts S., Parish J.L., Ward D.G.*, et al.* (2018) Defining the frequency of human papillomavirus and polyomavirus infection in urothelial bladder tumours. *Sci Rep* **8**:11290.

Lopata A., Hughes R., Tiede C., Heissler S.M., Sellers J.R., Knight P.J., Tomlinson D. & Peckham M. (2018) Affimer proteins for f-actin: Novel affinity reagents that label f-actin in live and fixed cells. *Sci Rep* **8**:6572.

Lykins J.D., Filippova E.V., Halavaty A.S., Minasov G., Zhou Y., Dubrovska I., Flores K.J., Shuvalova L.A., Ruan J.P., El Bissati K.*, et al.* (2018) CSGID solves structures and identifies phenotypes for five enzymes in *Toxoplasma gondii*. *Front Cell Infect Microbiol* **8**:352.

Macrae F.L., Duval C., Papareddy P., Baker S.R., Yuldasheva N., Kearney K.J., Mcpherson H.R., Asquith N., Konings J., Casini A.*, et al.* (2018) A fibrin biofilm covers blood clots and protects from microbial invasion. *J Clin Invest* **128**:3356-3368.

Majd H., King M.S., Palmer S.M., Smith A.C., Elbourne L.D.H., Paulsen I.T., Sharples D., Henderson P.J.F. & Kunji E.R.S. (2018) Screening of candidate substrates and coupling ions of transporters by thermostability shift assays. *Elife* **7**:e38821.

Majiya H., Adeyemi O.O., Herod M., Stonehouse N.J. & Millner P. (2018) Photodynamic inactivation of non-enveloped RNA viruses. *J Photochem Photobiol B* **189**:87-94.

Majiya H., Adeyemi O.O., Stonehouse N.J. & Millner P. (2018) Photodynamic inactivation of bacteriophage MS2: The A-protein is the target of virus inactivation. *J Photochem Photobiol B* **178**:404-411.

Manners O., Murphy J.C., Coleman A., Hughes D.J. & Whitehouse A. (2018) Contribution of the KSHV and EBV lytic cycles to tumourigenesis. *Curr Opin Virol* **32**:60-70.

Marklew C.J., Booth A., Beales P.A. & Ciani B. (2018) Membrane remodelling by a lipidated endosomal sorting complex required for transport-III chimera, *in vitro*. *Interface Focus* **8**:20180035.

Martin H.L., Bedford R., Heseltine S.J., Tang A.A., Haza K.Z., Rao A., Mcpherson M.J. & Tomlinson D.C. (2018) Non-immunoglobulin scaffold proteins: Precision tools for studying protein-protein interactions in cancer. *New Biotechnol* **45**:28-35.

Martir D.R., Cordes D.B., Slawin A.M.Z., Escudero D., Jacquemin D., Warriner S.L. & Zysman-Colman E. (2018) A luminescent Pd4Ru8 (24+) supramolecular cage. *Chem Commun* **54**:6016-6019.

Mata C.P., Mertens J., Fontana J., Luque D., Allende-Ballestero C., Reguera D., Trus B.L., Steven A.C., Carrascosa J.L. & Caston J.R. (2018) The RNA-binding protein of a double-stranded RNA virus acts like a scaffold protein. *J Virol* **92**:e00968-18.

Millington E.L., Dondas H.A., Fishwick C.W.G., Kilner C. & Grigg R. (2018) Catalytic bimetalic pd(0)/ag(i) heck-1,3-dipolar cycloaddition cascade reactions accessing spiro-oxindoles. Concomitant in situ generation of azomethine ylides and dipolarophile. *Tetrahedron* **74**:3564-3577.

Minard A., Bauer C.C., Wright D.J., Rubaiy H.N., Muraki K., Beech D.J. & Bon R.S. (2018) Remarkable progress with small-molecule modulation of trpc1/4/5 channels: Implications for understanding the channels in health and disease. *Cells* **7**.

Mistry D., Connell S.D., Mickthwaite S.L., Morgan P.B., Clamp J.H. & Gleeson H.F. (2018) Coincident molecular auxeticity and negative order parameter in a liquid crystal elastomer. *Nature Communications* **9**.

Moorcroft S.C.T., Jayne D.G., Evans S.D. & Ong Z.Y. (2018) Stimuli-responsive release of antimicrobials using hybrid inorganic nanoparticle-associated drug-delivery systems. *Macromolecular Bioscience* **18**.

Morgan E.L., Wasson C.W., Hanson L., Kealy D., Pentland I., Mcguire V., Scarpini C., Coleman N., Arthur J.S.C., Parish J.L.*, et al.* (2018) STAT3 activation by E6 is essential for the differentiation-dependent HPV18 life cycle. *PLoS Pathog* **14**:e1006975.

Morgentin R., Dow M., Aimon A., Karageorgis G., Kalliokoski T., Roche D., Marsden S. & Nelson A. (2018) Translation of innovative chemistry into screening libraries: An exemplar partnership from the European lead factory. *Drug Discov Today* **23**:1578-1583.

Muench S.P. & Van Der Laan M. (2018) No longer hidden secrets of proton pumping: The resolution revolution enlightens V-ATPases. *Mol Cell* **69**:921-922.

Mukherjee M., Sabir S., O'regan L., Sampson J., Richards M.W., Huguenin-Dezot N., Ault J.R., Chin J.W., Zhuravleva A., Fry A.M.*, et al.* (2018) Mitotic phosphorylation regulates Hsp72 spindle localization by uncoupling ATP binding from substrate release. *Sci Signal* **11**:eaao2464.

Naughton F.B., Kalli A.C. & Sansom M.S.P. (2018) Modes of interaction of pleckstrin homology domains with membranes: Toward a computational biochemistry of membrane recognition. *J Mol Biol* **430**:372-388.

Nishi R., Wijnhoven PW. G., Kimura Y., Matsui M., Konietzny R., Wu Q., Nakamura K., Blundell T.L. & Kessler B.M. (2018) The deubiquitylating enzyme UCHL3 regulates Ku80 retention at sites of DNA damage. *Scientific Reports* **8**: 17891

Novikova M., Adams L.J., Fontana J., Gres A.T., Balasubramaniam M., Winkler D.C., Kudchodkar S.B., Soheilian F., Sarafianos S.G., Steven A.C.*, et al.* (2018) Identification of a structural element in hiv-1 gag required for virus particle assembly and maturation. *MBio* **9**:e01567-18.

Nwogu N., Boyne J.R., Dobson S.J., Poterlowicz K., Blair G.E., Macdonald A., Mankouri J. & Whitehouse A. (2018) Cellular sheddases are induced by Merkel cell polyomavirus small tumour antigen to mediate cell dissociation and invasiveness. *PLoS Pathog* **14**: e1007276.

O'Brien, D. *et al.* (2018) A PQM-1-Mediated Response Triggers Transcellular Chaperone Signaling and Regulates Organismal Proteostasis. *Cell Rep.* **23,** 3905–3919.

Ocasio C.A., Warkentin A.A., Mcintyre P.J., Barkovich K.J., Vesely C., Spencer J., Shokat K.M. & Bayliss R. (2018) Type II kinase inhibitors targeting Cys-gatekeeper kinases display orthogonality with wild type and Ala/Gly-gatekeeper kinases. *ACS Chem Biol* **13**:2956-2965.

Okrugin B.M., Richter R.P., Leermakers F.a.M., Neelov I.M., Borisov O.V. & Zhulina E.B. (2018) Structure and properties of polydisperse polyelectrolyte brushes studied by self-consistent field theory. *Soft Matter* **14**:6230-6242.

Oldknow S., Martir D.R., Pritchard V.E., Blitz M.A., Fishwick C.W.G., Zysman-Colman E. & Hardie M.J. (2018) Structure-switching $M_3L_2$ Ir(III) coordination cages with photo-isomerising azo-aromatic linkers. *Chem Sci* **9**:8150-8159.

Oram, J., Jeuken, L.J.C. (2018) Tactic response of *Shewanella oneidensis* MR-1 towards insoluble electron acceptors, *mBio*, **10**, e02490-18.

Panou M.M., Prescott E.L., Hurdiss D.L., Swinscoe G., Hollinshead M., Caller L.G., Morgan E.L., Carlisle L., Muller M., Antoni M.*, et al.* (2018) Agnoprotein is an essential egress factor during BK polyomavirus infection. *Int J Mol Sci* **19**: E902.

Parker F., Batchelor M., Wolny M., Hughes R., Knight P.J. & Peckham M. (2018) A1603P and K1617del, mutations in β-cardiac myosin heavy chain that cause Laing early-onset distal myopathy, affect secondary structure and filament formation *in vitro* and *in vivo*. *J Mol Biol* **430**:1459-1478.

Parmar M., Rawson S., Scarff C.A., Goldman A., Dafforn T.R., Muench S.P. & Postis V.L.G. (2018) Using a SMALP platform to determine a sub-nm single particle cryo-EM membrane protein structure. *Biochim Biophys Acta Biomembr* **1860**:378-383.

Polasky D.A., Lermyte F., Nshanian M., Sobott F., Andrews P.C., Loo J.A. & Ruotolo B.T. (2018) Fixed-charge trimethyl pyrilium modification for enabling enhanced top-down mass spectrometry sequencing of intact protein complexes. *Anal Chem* **90**:2756-2764.

Polson E.S., Kuchler V.B., Abbosh C., Ross E.M., Mathew R.K., Beard H.A., Da Silva B., Holding A.N., Ballereau S., Chuntharpursat-Bon E.*, et al.* (2018) Khs101 disrupts energy metabolism in human glioblastoma cells and reduces tumor growth in mice. *Sci Transl Med* **10**:eaar2718.

Posner M.G., Upadhyay A., Ishima R., Kalli A.C., Harris G., Kremerskothen J., Sansom M.S.P., Crennell S.J. & Bagby S. (2018) Distinctive phosphoinositide- and $Ca^{2+}$-binding properties of normal and cognitive performance-linked variant forms of KIBRA C2 domain. *J Biol Chem* **293**:9335-9344.

Punch E.K., Hover S., Blest H.T.W., Fuller J., Hewson R., Fontana J., Mankouri J. & Barr J.N. (2018) Potassium is a trigger for conformational change in the fusion spike of an enveloped RNA virus. *J Biol Chem* **293**:9937-9944.

Pyle E., Kalli A.C., Amillis S., Hall Z., Lau A.M., Hanyaloglu A.C., Diallinas G., Byrne B. & Politis A. (2018) Structural lipids enable the formation of functional oligomers of the eukaryotic purine symporter UapA. *Cell Chem Biol* **25**:840-848.

Radom F., Pluckthun A. & Paci E. (2018) Assessment of *ab initio* models of protein complexes by molecular dynamics. *PLoS Comput Biol* **14**:e1006182.

Randall C.P., Gupta A., Utley-Drew B., Lee S.Y., Morrison-Williams G. & O'Neill A.J. (2018) Acquired nisin resistance in *Staphylococcus aureus* involves constitutive activation of an intrinsic peptide antibiotic detoxification module. *Msphere* **3**:e00633-18.

Rawson S., Bisson C., Hurdiss D.L., Fazal A., Mcphillie M.J., Sedelnikova S.E., Baker P.J., Rice D.W. & Muench S.P. (2018) Elucidating the structural basis for differing enzyme inhibitor potency by cryo-EM. *Proc Natl Acad Sci USA* **115**:1795-1800.

Remenyi R., Gao Y., Hughes R.E., Curd A., Zothner C., Peckham M., Merits A. & Harris M. (2018) Persistent replication of a chikungunya virus replicon in human cells is associated with presence of stable cytoplasmic granules containing nonstructural protein 3. *J Virol* **92**:e00477-18.

Richter R.P., Baranova N.S., Day A.J. & Kwok J.C.F. (2018) Glycosaminoglycans in extracellular matrix organisation: Are concepts from soft matter physics key to understanding the formation of perineuronal nets? *Curr Opin Struct Biol* **50**:65-74.

Richter R.P. & Lortat-Jacob H. (2018) Editorial overview: Carbohydrates: Menage a trois with glycosaminoglycans - a serious rendezvous, not a gag! *Curr Opin Struct Biol* **50**:IV-VI.

Ricketts K., Ahmad R., Beaton L., Cousins B., Critchley K., Davies M., Evans S., Fenuyi I., Gavriilidis A., Harmer Q.J.*, et al.* (2018) Recommendations for clinical translation of nanoparticle-enhanced radiotherapy. *Br J Radiol* **91**:20180325.

Ritzefeld M., Wright M.H. & Tate E.W. (2018) New developments in probing and targeting protein acylation in malaria, leishmaniasis and African sleeping sickness. *Parasitology* **145**:157-174.

Roach L., Ye S.J., Moorcroft S.C.T., Critchley K., Coletta P.L. & Evans S.D. (2018) Morphological control of seedlessly-synthesized gold nanorods using binary surfactants. *Nanotechnology* **29**:135601

Robinson J.I., Baxter E.W., Owen R.L., Thomsen M., Tomlinson D.C., Waterhouse M.P., Win S.J., Nettleship J.E., Tiede C., Foster R.J.*, et al.* (2018) Affimer proteins inhibit immune complex binding to FcγRIIIa with high specificity through competitive and allosteric modes of action. *Proc Natl Acad Sci USA* **115**:E72-E81.

Rostkova E., Burgess S.G., Bayliss R. & Pfuhl M. (2018) Solution NMR assignment of the C-terminal domain of human chTOG. *Biomolecular NMR Assignments* **12**:221-224.

Rubaiy H.N., Ludlow M.J., Siems K., Norman K., Foster R., Wolf D., Beutler J.A. & Beech D.J. (2018) Tonantzitlolone is a nanomolar potency activator of transient receptor potential canonical 1/4/5 channels. *Br J Pharmacol* **175**:3361-3368.

Sabbadin F., Hemsworth G.R., Ciano L., Henrissat B., Dupree P., Tryfona T., Marques R.D.S., Sweeney S.T., Besser K., Elias L.*, et al.* (2018) An ancient family of lytic polysaccharide monooxygenases with roles in arthropod development and biomass digestion. *Nat Commun* **9**:756.

Samson A., Bentham M.J., Scott K., Nuovo G., Bloy A., Appleton E., Adair R.A., Dave R., Peckham-Cooper A., Toogood G.*, et al.* (2018) Oncolytic reovirus as a combined antiviral and anti-tumour agent for the treatment of liver cancer. *Gut* **67**:562-573.

Samson A., Scott K.J., Taggart D., West E.J., Wilson E., Nuovo G.J., Thomson S., Corns R., Mathew R.K., Fuller M.J.*, et al.* (2018) Intravenous delivery of oncolytic reovirus to brain tumor patients immunologically primes for subsequent checkpoint blockade. *Sci Transl Med* **10**:eaam7577.

Sanfelice D., Koss H., Bunney T.D., Thompson G.S., Farrell B., Katan M. & Breeze A.L. (2018) Nmr backbone assignments of the tyrosine kinase domain of human fibroblast growth

factor receptor 3 in apo state and in complex with inhibitor pd173074. *Biomol NMR Assign* **12**:231-235.

Santiago C.G., Paci E. & Donnelly D. (2018) A mechanism for agonist activation of the glucagon-like peptide-1 (GLP-1) receptor through modelling & molecular dynamics. *Biochem Biophys Res Commun* **498**:359-365.

Schlichthaerle T., Eklund A.S., Schueder F., Strauss M.T., Tiede C., Curd A., Ries J., Peckham M., Tomlinson D.C. & Jungmann R. (2018) Site-specific labeling of affimers for DNA-paint microscopy. *Angew Chem Int Ed Engl* **57**:11060-11063.

Selvaraj M., Yegambaram K., Todd E., Richard C.A., Dods R.L., Pangratiou G.M., Trinh C.H., Moul S.L., Murphy J.C., Mankouri J.*, et al.* (2018) The structure of the human respiratory syncytial virus m2-1 protein bound to the interaction domain of the phosphoprotein p defines the orientation of the complex. *MBio* **9**:e01554-18.

Seneviratne R., Khan S., Moscrop E., Rappolt M., Muench S.P., Jeuken L.J.C. & Beales P.A. (2018) A reconstitution method for integral membrane proteins in hybrid lipid-polymer vesicles for enhanced functional durability. *Methods* **147**:142-149.

Sharkey L.K.R. & O'Neill A.J. (2018) Antibiotic resistance ABC-F proteins: Bringing target protection into the limelight. *ACS Infect Dis* **4**:239-246.

Skyrud W., Liu J., Thankachan D., Cabrera M., Seipke R.F. & Zhang W.J. (2018) Biosynthesis of the 15-membered ring depsipeptide neoantimycin. *ACS Chem Biol* **13**:1398-1406.

Solernou A., Hanson B.S., Richardson R.A., Welch R., Read D.J., Harlen O.G. & Harris S.A. (2018) Fluctuating finite element analysis (FFEA): A continuum mechanics software tool for mesoscale simulation of biomolecules. *PLoS Comput Biol* **14:**e1005897.

Southam H.M., Smith T.W., Lyon R.L., Liao C., Trevitt C.R., Middlemiss L.A., Cox F.L., Chapman J.A., El-Khamisy S.F., Hippler M.*, et al.* (2018) A thiol-reactive Ru(II) ion, not CO release, underlies the potent antimicrobial and cytotoxic properties of CO-releasing molecule-3. *Redox Biol* **18**:114-123.

Stakaityte G., Nwogu N., Dobson S.J., Knight L.M., Wasson C.W., Salguero F.J., Blackbourn D.J., Blair G.E., Mankouri J., Macdonald A.*, et al.* (2018) Merkel cell polyomavirus small t antigen drives cell motility via Ro-GTPase-induced filopodium formation. *J Virol* **92**:e00940-17.

Stakaityte G., Nwogu N., Lippiat J.D., Blair G.E., Poterlowicz K., Boyne J.R., Macdonald A., Mankouri J. & Whitehouse A. (2018) The cellular chloride channels CLIC1 and CLIC4 contribute to virus-mediated cell motility. *J Biol Chem* **293**:4582-4590.

Stertz S., Duprex W.P. & Harris M. (2018) A novel mutation in the neuraminidase gene of the 2009 pandemic H1N1 influenza A virus confers multidrug resistance. *J Gen Virol* **99**:275-276.

Strauss J., Wilkinson C., Vidilaseris K., Harborne S.P.D. & Goldman A. (2018) A simple strategy to determine the dependence of membrane-bound pyrophosphatases on $K^+$ as a cofactor. In *Phosphatases*. Edited by Allen K.N. *Methods Enzymol* **607**:131-156.

Suen K.M., Lin C.C., Seiler C., George R., Poncet-Montange G., Biter A.B., Ahmed Z., Arold S.T. & Ladbury J.E. (2018) Phosphorylation of threonine residues on Shc promotes ligand binding and mediates crosstalk between MAPK and Akt pathways in breast cancer cells. *Int J Biochem Cell Biol* **94**:89-97.

Talavera A., Hendrix J., Versees W., Jurenas D., Van Nerom K., Vandenberk N., Singh R.K., Konijnenberg A., De Gieter S., Castro-Roa D.*, et al.* (2018) Phosphorylation decelerates conformational dynamics in bacterial translation elongation factors. *Sci Adv* **4**: eaap9714.

Tanaka M., Suwatthanarak T., Arakaki A., Johnson B.R.G., Evans S.D., Okochi M., Staniland S.S. & Matsunaga T. (2018) Enhanced tubulation of liposome containing cardiolipin by MamY protein from magnetotactic bacteria. *Biotechnol J* **13**:1800087.

Tarn M.D., Sikora S.N.F., Porter G.C.E., O'Sullivan D., Adams M., Whale T.F., Harrison A.D., Vergara-Temprado J., Wilson T.W., Shim J.U.*, et al.* (2018) The study of atmospheric ice-nucleating particles via microfluidically generated droplets. *Microfluid Nanofluidics* **22**:52.

Tassi M., De Vos J., Chatterjee S., Sobott F., Bones J. & Eeltink S. (2018) Advances in native high-performance liquid chromatography and intact mass spectrometry for the characterization of biopharmaceutical products. *J Sep Sci* **41**:125-144.

Taylor S., Knipp S., Mavria G., Ladbury J., Bruning-Richardson A. & Short S. (2018) Finding the brake: Dissecting the Rhoa pathway regulating glioma cell migration. *Neuro Oncol* **20**:21-21.

Teare P., Smith C.F., Adams S.J., Anbu S., Ciani B., Jeuken L.J.C. & Peacock A.F.A. (2018) pH dependent binding in *de novo* hetero bimetallic coiled coils. *Dalton Trans* **47**:10784-10790.

Teixeira J.M.C., Skinner S.P., Arbesu M., Breeze A.L. & Pons M. (2018) Farseer-NMR: Automatic treatment, analysis and plotting of large, multi-variable NMR data. *J Biomol NMR* **71**:1-9.

Townsend D., Hughes E., Akien G., Stewart K.L., Radford S.E., Rochester D. & Middleton D.A. (2018) Epigallocatechin-3-gallate remodels apolipoprotein A-I amyloid fibrils into soluble oligomers in the presence of heparin. *J Biol Chem* **293**:12877-12893.

Townsend D., Hughes E., Stewart K.L., Griffin J.M., Radford S.E. & Middleton D.A. (2018) Orientation of a diagnostic ligand bound to macroscopically aligned amyloid-beta fibrils determined by solid-state NMR. *J Phys Chem Lett* **9**:6611-6615.

Turnbull W.B., Kumar V. (2018) Carbohydrate inhibitors of cholera toxin. *Beilstein J. Org. Chem.* **14**: 484-498.

Twarock R., Bingham R.J., Dykeman E.C. & Stockley P.G. (2018) A modelling paradigm for RNA virus assembly. *Curr Opin Virol* **31**:74-81.

Twarock R., Leonov G. & Stockley P.G. (2018) Hamiltonian path analysis of viral genomes. *Nat Commun* 9:2021.

Van Der Heul H.U., Bilyk B.L., Mcdowall K.J., Seipke R.F. & Van Wezel G.P. (2018) Regulation of antibiotic production in actinobacteria: New perspectives from the post-genomic era. *Nat Prod Rep* **35**:575-604.

Van Der Hoek L., Verschoor E., Beer M., Hoper D., Wernike K., Van Ranst M., Matthijnssens J., Maes P., Sastre P., Rueda P.*, et al.* (2018) Host switching pathogens, infectious outbreaks and zoonosis: A Marie Sklodowska-Curie innovative training network (HONOURS). *Virus Res* **257**:120-124.

Vasilca V., Sadeghpour A., Rawson S., Hawke L.E., Baldwin S.A., Wilkinson T., Bannister D., Postis V.L.G., Rappolt M., Muench S.P.*, et al.* (2018) Spherical-supported membranes as

platforms for screening against membrane protein targets. *Anal Biochem* **549**:58-65.

Vennard L.M., Atanasiu D., Saw W.T., Eisenberg R.J., Cohen G.H. & Fontana J. (2018) Recent insights into the structural characterization of herpes simplex virus fusion protein, gB. *Future Virol* **13**:5-7.

Vidilaseris K., Kellosalo J. & Goldman A. (2018) A high-throughput method for orthophosphate determination of thermostable membrane-bound pyrophosphatase activity. *Analytical Methods* **10**:646-651.

Walden M., Masandi S.K., Pawlowski K. & Zeqiraj E. (2018) Pseudo-dubs as allosteric activators and molecular scaffolds of protein complexes. *Biochem Soc Trans* **46**:453-466.

Wang, J. L., Duboc, C., Wu, Q., Ochi, T., Liang, S., Tsutakawa, S. E., Lees-Miller, S. P., Nadal, M., Tainer, J. A., Blundell, T. L. & Strick, T. R. (2018). Dissection of DNA double-strand-break repair using novel single-molecule forceps. *Nat. Struct. Mol. Biol* **25**, 482-487.

Werner M., Auth T., Beales P.A., Fleury J.B., Hook F., Kress H., Van Lehn R.C., Muller M., Petrov E.P., Sarkisov L.*, et al.* (2018) Nanomaterial interactions with biomembranes: Bridging the gap between soft matter models and biological context. *Biointerphases* **13:**028501.

Wetherill L.F., Wasson C.W., Swinscoe G., Kealy D., Foster R., Griffin S. & Macdonald A. (2018) Alkyl-imino sugars inhibit the pro-oncogenic ion channel function of human papillomavirus (HPV) e5. *Antiviral Res* **158**:113-121.

Willis L., Kumar A., Dobson J., Bond N., Lowe D., Turner R., Radford S., Kapur N. & Brockwell D. (2018) Using extensional flow to reveal diverse aggregation landscapes for three IgG1 molecules. *Biotech Bioeng* **115**:1216-1225.

Witkowska D., Cox H.L., Hall T.C., Wildsmith G.C., Machin D.C. & Webb M.E. (2018) Analysis of substrate binding in individual active sites of bifunctional human ATIC. *Biochim Biophys Acta-Proteins Proteom* **1866**:254-263.

Wooderchak-Donahue W., Farrell A., Johnson P., Mcdonald J., Thompson J., Velinder M., Ward A., Marth G. & Bayrak-Toydemir P. (2018) Unraveling the mystery: Analysis of the human genome with refus highlights the genetic complexity of hht. *Angiogenesis* **21**:151-152.

Wright M.H. (2018) Chemical proteomics of host-microbe interactions. *Proteomics* **18**.

Ye S.J., Wheeler M.C., Mclaughlan J.R., Tamang A., Diggle C.P., Cespedes O., Markham A.F., Coletta P.L. & Evans S.D. (2018) Developing hollow-channel gold nanoflowers as trimodal intracellular nanoprobes. *Int J Mol Sci* **19**:2327.

Yeoh S. & Bayliss R. (2018) New tools for evaluating protein tyrosine sulfation and carbohydrate sulfation. *Biochem J* **475**:3035-3037.

Yokoyama M., Stevens E., Laabei M., Bacon L., Heesom K., Bayliss S., Ooi N., O'neill A.J., Murray E., Williams P.*, et al.* (2018) Epistasis analysis uncovers hidden antibiotic resistance-associated fitness costs hampering the evolution of mrsa. *Genome Biol* **19**:94.

Zhurauski P., Arya S.K., Jolly P., Tiede C., Tomlinson D.C., Ferrigno P.K. & Estrela P. (2018) Sensitive and selective affimer-functionalised interdigitated electrode-based capacitive biosensor for Her4 protein tumour biomarker detection. *Biosens Bioelectron* **108**:1-8.

**The Astbury Centre for**
**Structural Molecular Biology**
University of Leeds
Leeds
LS2 9JT
Tel: 0113 343 3086
astbury@leeds.ac.uk
www.astbury.leeds.ac.uk

**UNIVERSITY OF LEEDS**
University of Leeds
Leeds, United Kingdom
LS2 9JT
Tel: 0113 243 1751
www.leeds.ac.uk